Scientific Research

JBiSE

ISSN: 1937-6871

Volume 3 Number 3 March 2010

Journal of Biomedical Science and Engineering

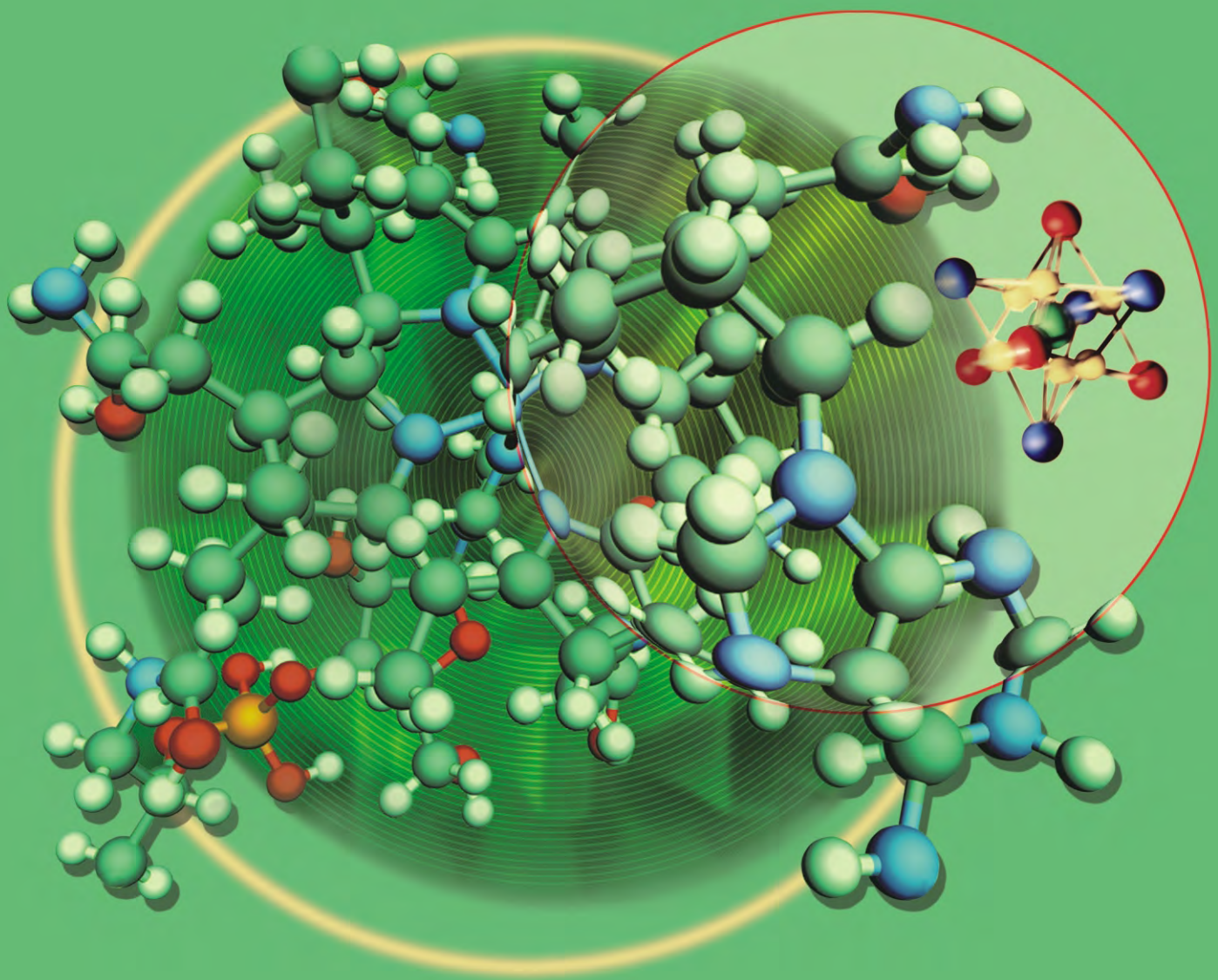

www.scirp.org/journal/jbise

Editor-in-Chief
Kuo-Chen Chou

Journal Editorial Board

ISSN 1937-6871 (Print) ISSN 1937-688X (Online)
http://www.scirp.org/journal/jbise

TABLE OF CONTENTS

Volume 3, Number 3, March 2010

Journal of Biomedical Science and Engineering (JBiSE)

Journal Information

SUBSCRIPTIONS

The *Journal of Biomedical Science and Engineering* (Online at Scientific Research Publishing, www.SciRP.org) is published monthly by Scientific Research Publishing, Inc., USA.

Subscription rates:

Print: $50 per issue.
To subscribe, please contact Journals Subscriptions Department, E-mail: sub@scirp.org

SERVICES

Advertisements
Advertisement Sales Department, E-mail: service@scirp.org

Reprints (minimum quantity 100 copies)
Reprints Co-ordinator, Scientific Research Publishing, Inc., USA.
E-mail: sub@scirp.org

COPYRIGHT

PRODUCTION INFORMATION

For manuscripts that have been accepted for publication, please contact:
E-mail: jbise@scirp.org

J. Biomedical Science and Engineering, 2010, 3, 227-240 **JBiSE**
doi:10.4236/jbise.2010.33031 Published Online March 2010 (http://www.SciRP.org/journal/jbise/).

Quantifying the effects of mutations on receptor binding specificity of influenza viruses

Wei Hu

Department of Computer Science, Houghton College, Houghton, USA.
Email: wei.hu@houghton.edu

Received 7 January 2010; revised 11 January 2010; accepted 15 January 2010.

ABSTRACT

Hemagglutinin (HA) of influenza viruses is a cylindrically shaped homotrimer, where each monomer comprises two disulfide-linked subdomains HA1 and HA2. Influenza infection is initiated by binding of HA1 to its host cell receptors and followed by the fusion between viral and host endosomal membranes mediated by HA2. Human influenza viruses preferentially bind to sialic acid that is linked to galactose by an α2,6-linkage (α2,6), whereas avian and swine influenza viruses preferentially recognize α2,3 or α 2,3/α2,6. For animal influenza viruses to cross host species barriers, their HA proteins must acquire mutations to gain the capacity to allow human-to-human transmission. In this study, the informational spectrum method (ISM), a bioinformatics approach, was applied to identify mutations and to elucidate the contribution to the receptor binding specificity from each mutation in HA1 in various subtypes within or between hosts, including 2009 human H1N1, avian H5N1, human H5N1, avian H1N1, and swine H1N2. Among others, our quantitative analysis indicated that the mutations in HA1 of 2009 human H1N1 collectively tended to reduce the swine binding affinity in the seasonal H1N1 strains and to increase that in the pandemic H1N1 strains. At the same time, they increased the human binding affinity in the pandemic H1N1 strains and had little impact on that in the seasonal H1N1 strains. The mutations between the consensus HA1 sequences of human H5N1 and avian H5N1 increased the avian binding affinity and decreased the human binding affinity in avian H5N1 while produced the opposite effects on those in human H5N1. Finally, the ISM was employed to analyze and verify several mutations in HA1 well known for their critical roles in binding specificity switch, including E190D/G225D in H1N1 and Q192R/ S223L/ Q226L/ G228S in H5N1.

Keywords: Binding Specificity; Discrete Fourier Transform; Electron-Ion Interaction Potential; Entropy; Hemagglutinin; Influenza; Informational Spectrum Method; Mutation; Receptor

1. INTRODUCTION

Influenza A viruses are classified into different subtypes based on the viral surface proteins hemagglutinin (HA) and neuraminidase (NA). The initial step in the influenza infection is the binding of HA to sialylated glycan receptors on the host cells. HA is also the primary target for the immune response in the infected host. Human and swine influenza viruses are derived from avian viruses, facilitated by regular close contact among humans, birds, and pigs [1]. The past three influenza pandemics, the Spanish flu (H1N1) in 1918, the Asian flu (H2N2) in 1957, and the Hong Kong flu (H3N2) in 1968, all had arisen from a reassortment from avian, swine, and human viruses. The current 2009 influenza pandemic was caused by a swine-origin H1N1 virus. The adaptation of the virus to a new host entails the compatibility between host and virus genetic requirements to allow efficient replication and sustained transmission. The host barrier for influenza viruses to transmit in humans is multigenic, however, the receptor specificity of HA proteins is a key determinant.

The binding preference of influenza virus HAs affects the host specificity for infection. In general, human influenza viruses bind preferentially to α2,6 receptors, avian influenza viruses tend to bind to α2,3 receptors, and swine influenza viruses can bind to either α2,6 receptors or both α2,6 and α2,3 receptors, primarily based on differences in the amino acids in the HA receptor binding domain (RBD). The RBD of HA in various influenza subtypes has three structural elements in common, one α-helix (190-helix) and two loops (130-loop and 220-loop). Different hosts express diverse SA isomers, *i.e.*, α2,3 linkages in the gut of waterfowl, α2,3 and α2,6 linkages in the lung and intestinal epithelium of chickens, and α2,6 linkages in the upper respiratory epithelium and α2,3 and α2,6 linkages in the lower respiratory epithelium of humans [2].

A change of binding preference is essential for cross species transfer, which involves mutations in HA to alter its glycan receptor preference [3]. It is hypothesized that

to facilitate efficient human transmission, mutations in HA are required to increase α2,5 binding and at the same time to decrease α2,3 binding [4]. A variety of mutations that can shift receptor preference of HA proteins have been identified.

In a study of receptor specificity of influenza A/H5 viruses [5], all but two isolates exhibited high affinity to α2,3 receptors. The two isolates with a unique S223N change in HA demonstrated decreased affinity to α2,3 and moderate affinity to α2,6 receptors. Another study showed that introduction of the mutation Q192R enhanced the binding of HA in H5N1 to α2,6 receptors, and introduction of both mutations Q192R and S223N increased the binding preference significantly. Residue 192 is close to the 190 helix, and residue 223 is part of the 220 loop, where it is feasible for them to influence the binding affinity [6]. As for the H2, H3, H4, and H9 HAs, two substitutions Q226L and G228S are mainly responsible for the switch from avian to human binding [3,7,8,9].

Residues 138, 186, 190, 194, 225, 226, and 228 can modulate the binding affinity of H1N1 HA proteins, and two residues 190 and 225 play key dominant roles in binding affinity [10,11]. The sequences of the RBD of avian H1 viruses maintain a Glu at position 190 and a Gly at 225 (H3 numbering), while the human H1 viruses generally have an Asp at both positions 190 and 225. It is known that E190D and G225D mutations in H1 viruses can shift binding patterns from avian to human type. In the five 1918 H1N1 HA sequences, three have a D190 and a D225 with α2,6 affinity, and two have a D190 and a G225 with mixed α2,6/α2,3 specificities [12]. In general, mutations D190/D225 favor α2,6 receptors in humans, D190/G225 like α2,6 and α2,3 receptors in swine, and E190/G225 prefer α2,3 receptors in avian [13]. The biochemical analysis in [14] quantified the multivalent HA-glycan interactions, and showed the effects of these mutations on glycan binding amplified by multivalency.

To date, the symptoms of 2009 H1N1 are mild. The fear is that the virus may continue to mutate to bring about another more lethal outbreak in the subsequent months as the 1918 Spanish flu. In [15] two representative 2009 H1N1 HA sequences, A/California/4/2009 and A/Hamburg/5/2009, were shown to bind to both α2,6 and α2,3 receptors with some minor differences in a carbohydrate microarray analysis, as predicted in [16]. There were three amino acid mutations between these HA sequences: S83P, A197T, and V321I, which might account for these differences in binding. These findings suggested that no major change in binding affinity is necessary for pandemic virus to acquire human binding patterns, and the dual binding to α2,6/α2,3 receptors is one contributor to the greater virulence of the pandemic virus than seasonal flu virus.

There were two other recent reports on the mutations of the 2009 H1N1 virus. The first report [17] located the potential mutations and strongly co-mutated positions in NA. The second report [18] focused on HA and the interaction between HA and NA. The mutations of HA in 2009 H1N1 were found and mapped to the 3D homology model of H1, and the mutations on the five epitope regions on H1 were identified. With help from the results of the first study, two co-mutation networks were uncovered, one in HA and one in NA, where each mutation in one network co-mutates with the mutations in the other network across the two proteins HA and NA. These two networks residing in HA and NA separately may provide a functional linkage between the mutations that can change the drug binding sites in NA and those that can affect the host immune response or vaccine efficacy in HA.

In references [19,20] the informational spectrum method (ISM) [21] was applied to investigate the interaction between HA and its receptors, which showed that HA1 of different flu subtypes encodes one highly conserved domain that might be determinants of HA binding affinity. The study in [22] extended the results in references [19,20] by identifying multiple domains in HA1 associated with each receptor interaction pattern. These conserved domains in HA1 might be used to identify new therapeutic targets for drug development.

In references [19,20] it was found that the consensus informational spectrum (CIS) of HA1 of influenza strains have the following characteristic dominant peaks at different IS frequencies as presented in Table 1. In this study, F(0.295) will be referred to as pandemic human H1N1 receptor interaction frequency, F(0.055) as swine receptor interaction frequency, F(0.076) as avian receptor interaction frequency, and F(0.236) as seasonal human H1N1 receptor interaction frequency. In addition to the dominant peak at IS frequencies in each subtype, there are secondary peaks at various IS frequencies [19,20,22].

Viral evolution can help influenza viruses surmount species barriers. Once adapted in a new host, they still need to continue their evolution to fit better in the new environment. In this study, we sought to investigate the effects of mutations in HA1, either within or between hosts, on binding preference shift through a quantitative analysis, the ISM. The analysis performed in this study was based on the observation that several influenza viruses display dual specific recognition of receptors with α2,6 or α2,3 linkages. Our goal was to utilize the ISM to uncover the amino acid polymorphisms in HA1 within or between hosts and to measure their contribution to the binding specificity switch quantitatively.

Table 1. Characteristic IS frequencies of HA proteins in 2009 H1N1, swine H1N1/H1N2, avian H5N1, and seasonal human H1N1.

Subtype	2009 H1N1	Swine H1N2/H1N1	Avian H5N1	Seasonal human H1N1
Frequency	F(0.295)	F(0.055)	F(0.076)	F(0.236)

2. MATERIALS AND METHODS

2.1. Sequence Data

All HA sequences were retrieved from the Influenza Virus Resource (http://www.ncbi/nlm.nih.giv/genomes/FLU/FLU.html) of the National Center for Biotechnology Information (NCBI) on November 20, 2009. Only the full length and unique sequences were selected. There were 450 HA sequences of human 2009 H1N1, 201 HA sequences of human H5N1 from 1979 to 2009, 1228 HA sequences of avian H5N1 from 1959 to 2009, 78 HA sequences of avian H1N1 from 1976 to 2008, and 83 HA sequences of swine H1N2 from 1980 to 2009. All the sequences used in the study were aligned with MAFFT [23].

2.2. Entropy

In information theory [24], entropy is a measure of disorder or randomness associated with a random variable. Let x be a discrete random variable that has a set of possible values $\{a_1, a_2, a_2, ...a_n\}$ with probabilities $\{p_1, p_2, p_3, ...p_n\}$ where $P(x = a_i) = p_i$. The entropy H of x is

$$H(x) = -\sum_i p_i \log p_i$$

In the current study, each of the n columns in a multiple sequence alignment of a set of HA sequences of N residues is considered as a discrete random variable x_i ($1 \le i \le N$) that takes on one of the 20 (n=20) amino acid types with some probability. $H(x_i)$ has its minimum value 0 if all the residues at position *i* are the same, and achieves its maximum if all the 20 amino acid types appear with equal probability at position *i*, which can be verified by the Lagrange multiplier technique. A position of high entropy means that the amino acids are often varied at this position. $H(x_i)$ measures the genetic diversity at position *i* in our current study. A brief overview of the extensive applications of entropy in sequence analysis, in particular the flu virus sequences, can be found in [17].

2.3. Important Sites in HA

Although there is a great variation due to high selection pressure in the HA1 sequences of various flu subtypes, the active site of HA1 is well conserved, which is located in a cleft composed of the residues 91, 150, 152, 180, 187, 191, and 192. The three amino acids at positions 187, 191 and 192 are a part of the 190 helix. The active site cleft of HA is formed by its right edge (131_GVTAA) and left edge (221_RGQAGR) (H1 numbering), which are also commonly referred to as the 130 loop and 220 loop, respectively [25,26].

3. RESULTS

3.1. Mutations within Hosts

3.1.1 2009 Human H1N1

After visual inspection of the alignment of 2009 human H1N1 HA1 sequences, there was either an Asp (single letter code D) at position 127 in the pandemic strains or a deletion at position 127 in the seasonal strains. Since Asp had the highest EIIP value of 0.128 [22], this deletion at position 127 might influence the DFT spectral distribution. Of the 450 HA1 sequences of 2009 human H1N1 collected, there were 345 pandemic H1N1 sequences with an Asp at position 127 and 105 seasonal H1N1 sequences with a deletion at position 127.

The CIS of the pandemic H1N1 HA1 sequences were plotted in **Figure 1(a)**, which have a dominant peak at frequency F(0.295) (pandemic human H1N1 binding), and the CIS of the seasonal H1N1 HA1 sequences were plotted in **Figure 1(b)**, which have a dominant peak at frequency F(0.055) (swine binding). According to the ISM concepts, this demonstrated the different receptor binding patterns of the 2009 pandemic and seasonal H1N1 strains. **Figure 2** illustrated the consensus sequences of the pandemic H1N1 strains (human binding preference) and seasonal H1N1 strains (swine binding preference), respectively.

There were 90 amino acid substitutions between the two consensus HA1 sequences of human and swine binding characteristics (**Figure 2** and **Table 2**). Based on

Table 2. Mutations between swine and human bindings in HA1 sequences of 2009 H1N1.

I3L	N35D	S36K	L43K	K45R	I47V	Q51H	N54K	S56N	V57I	L69S	I71S	S72T	K73A	E74S	K82T	P83S	N84S
P85S	E86D	H94D	A96I	E120T	-127D	S128T	V129N	T130K	S133T	S135A	S137P	N139A	E141A	S142K	R146K	L149I	T152V
G153K	N155G	G156N	L157S	N160K	A166I	N167D	E170G	V179I	P183S	N184T	I185S	V186A	K189Q	T190S	H193Q	T194N	E195A
N196D	S200F	V202G	H205R	R208K	T211K	K216I	I227M	L234V	T239K	I241T	N245T	I249V	A250V	L257M	S258E	G260N	F261A
N267I	N269D	A270T	M272V	D273H	K274D	D276N	A277T	K278T	Q283K	V295I	V298I	E302K	R308K	A310T	M314L	V315A	I321V

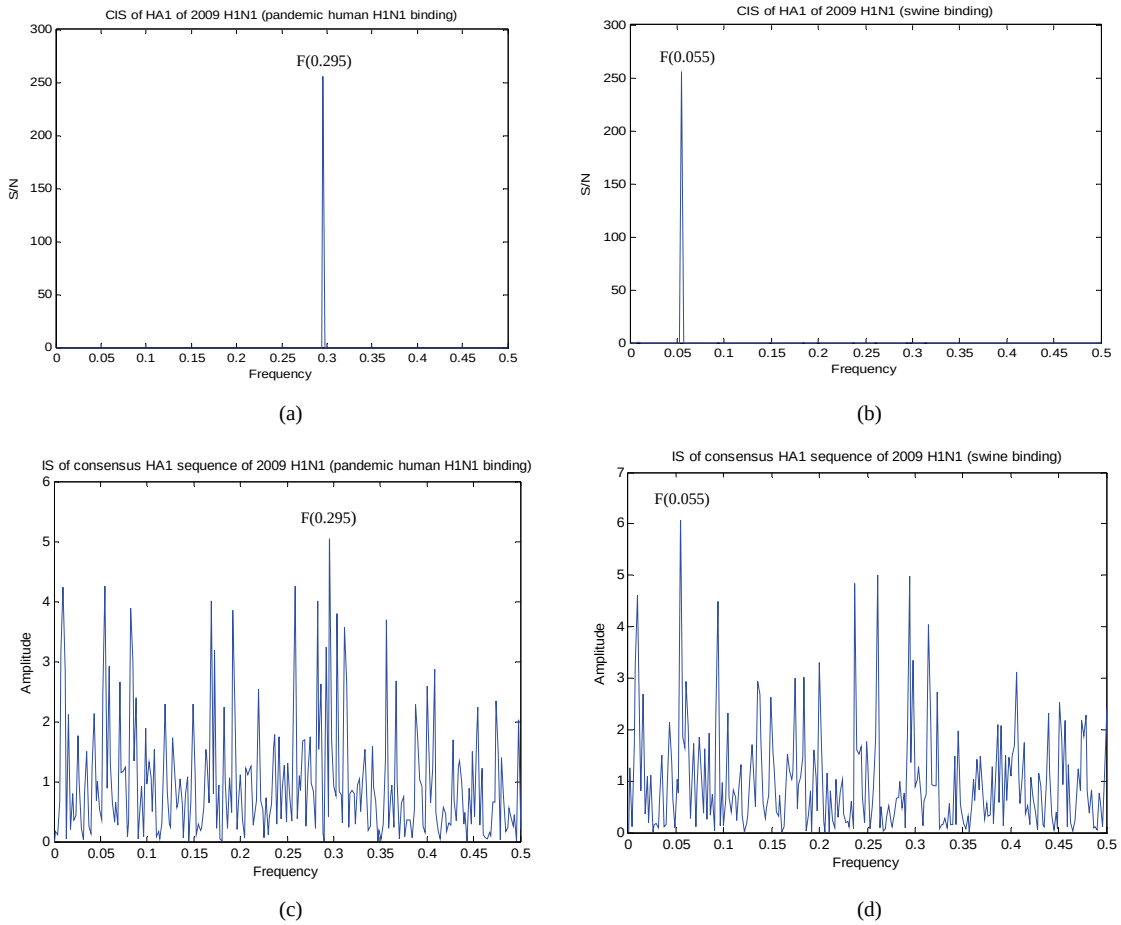

Figure 1. (a) CIS of HA1 of 2009 pandemic H1N1 (pandemic human H1N1 binding); (b) CIS of HA1 of 2009 seasonal H1N1 (swine H1N1 binding); (c) IS of HA1 of 2009 pandemic H1N1 (pandemic human H1N1 binding); (d) IS of HA1 of 2009 seasonal H1N1 (swine H1N1 binding).

the ISM theory, the mutations in HA1 that increased the amplitude of F(0.295) and decreased that of F(0.055) would contribute the switch of receptor binding affinity from swine to human type. The variation amount of the amplitudes of F(0.295) and F(0.055) was calculated for each of the 90 mutations applied to each consensus HA1 sequence, swine binding or human binding. The top 32 mutations that resulted in the amplitude change at frequency F(0.295) or F(0.055) (ΔA) more than 6% were listed in **Table 3**, suggesting that these mutations might be critical for modulating the binding preferences between swine and humans. In general, increasing the amplitude at one frequency F(0.295) or F(0.055) will decrease that at another frequency, but there were several exceptions. Three "hot spots", D94, D196, and D274, found in [19] contributed to the amplitudes at frequencies F(0.295) and F(0.055) with different amounts (**Table 3**). There were a mutation T152V at the binding site, and two mutations S133T and S135A at the right edge of the binding pocket, which were not listed in **Table 3** because their ΔA value was relatively small. **Table 3** also contained several mutations of interest, which were T130K and S137P near the right edge of the binding pocket, and P183S, N184T, I185S, H193Q, T194N, and N196D near the active site.

In [18], three networks of co-mutations in HA of 2009 H1N1 were uncovered. The first one had residues 269, 276, and 309, the second one had residues 34, 167, 195, and 268, and the third one had residues 129, 210, and 238, where each residue co-mutated with others in the same network. Two pairs of mutations N167D/E195A and N269D/D276N in **Table 2** were part of the aforementioned co-mutation networks discovered in [18]. Their individual and combined effects on ΔA were listed in **Table 4**, with the second pair having a much larger impact on the binding preference than the first. There were two clusters of mutations in **Table 2**, where the first was located at positions from 152 to 170, and the

second at positions from 257 to 278. The first cluster of mutations was contained in a pandemic human H1N1 receptor recognition domain (150:174) with the characteristic IS frequency at F(0.295) found in [22]. Prompted by this finding, we searched for a similar domain near the second cluster, and found a new domain (246:286) of swine binding characteristic with the IS dominant peak at frequency F(0.055) (**Figure 3**).

```
Swine Binding   DTICIGYHANNSTDTVDTVLEKNVTVTHSVNLLENSHNGKLCLLKGIAPLQLGNCSVAGW
Human Binding   DTLCIGYHANNSTDTVDTVLEKNVTVTHSVNLLEDKHNGKLCKLRGVAPLHLGKCNIAGW
                **:*********************************:.****** *:*:***:**:*.:***

Swine Binding   ILGNPECELLISKESWSYIVEKPNPENGTCYPGHFADYEELREQLSSVSSFERFEIFPKE
Human Binding   ILGNPECESLSTASSWSYIVETSSSDNGTCYPGDFIDYEELREQLSSVSSFERFEIFPKT
                ******** * : .*******.....:*******.* **********************

                                Right edge
Swine Binding   SSWPNH-TVTGVSASCSHNGESSFYRNLLWLTGKNGLYPNLSKSYANNKEKEVLVLWGVH
Human Binding   SSWPNHDSNKGVTAACPHAGAKSFYKNLIWLVKKGNSYPKLSKSYINDKGKEVLVLWGIH
                ****** : .**:*:*.* * .***:**:**. *.. **:***** *:* ********:*

                                                                Left edge
Swine Binding   HPPNIVDQKTLYHTENAYVSVVSSHYSRKFTPEIAKRPKVRDQEGRINYYWTLLEPGDTI
Human Binding   HPSTSADQQSLYQNADAYVFVGSSRYSKKFKPEIAIRPKVRDQEGRMNYYWTLVEPGDKI
                **.. .**:**:. :*** * **:**:**.**** **********:******:****.*

Swine Binding   IFEANGNLIAPRYAFALSRGFGSGIINSNAPMDKCDAKCQTPQGAINSSLPFQNVHPVTI
Human Binding   TFEATGNLVVPRYAFAMERNAGSGIIISDTPVHDCNTTCQTPKGAINTSLPFQNIHPITI
                ***.***:.******:.*. ***** *::*:..*::.****:****:******:**:**

Swine Binding   GECPKYVRSAKLRMVTGLRNIPSIQSR
Human Binding   GKCPKYVKSTKLRLATGLRNVPSIQSR
                *:*****:*:***:.*****:******
```

Figure 2. Alignment of two consensus HA1 sequences of 2009 pandemic H1N1 (pandemic human H1N1 binding) and 2009 seasonal H1N1 (swine binding). The binding sites in HA are colored in red, the left and right edges of the binding cleft in blue.

Table 3. Changes of amplitudes of IS frequencies by top 32 mutations with large ΔA value in HA1 of 2009 H1N1.

	Mutating Consensus HA1 Sequence of Swine Binding Patterns		Mutating Consensus HA1 Sequence of Human Binding Patterns	
Mutations	ΔA[F(0.055)]%	ΔA[F(0.295)]%	ΔA[F(0.055)]%	ΔA[F(0.295)]%
N35D	11.025	10.814	-12.123	-12.608
K45R	-6.935	2.2999	8.1835	-6.5807
S56N	-8.347	-9.5275	10.448	0.093211
L69S	1.1681	6.0652	-0.70212	-8.5586
I71S	7.0299	-9.42	-7.5854	4.8054
E74S	8.719	-3.4947	-9.8488	9.1621
K82T	-6.9799	-4.8104	8.282	-5.4234
P83S	-7.2536	7.4623	8.6929	-1.423
N84S	-7.7848	0.88042	9.617	10.047
H94D	6.739	5.3039	-7.8366	14.058
E120T	-9.7084	2.2202	11.954	-6.9883
T130K	-5.6997	7.272	5.909	5.7416
S137P	7.0562	8.6072	-8.3647	4.9132
T152V	0.49754	-6.8741	-3.6229	-9.9879
L157S	-9.3159	-5.0672	10.114	-9.6759
P183S	6.6852	7.4566	-8.2446	2.4515
N184T	10.495	0.64815	-11.043	-10.482
I185S	9.2299	-10.327	-8.6728	3.045
H193Q	-6.1179	4.6131	6.9435	3.7993
T194N	10.605	-4.89	-9.7841	10.506
N196D	-8.4752	-0.04744	6.2191	16.521
N245T	-5.3848	8.7494	9.7128	-10.596
L257M	9.7014	-7.2577	-10.573	10.05
S258E	-8.2999	-8.3169	8.7374	4.3745
N269D	-9.1545	8.9086	6.7895	-12.176
M272V	-3.1046	-9.3909	7.0087	9.0809
D273H	-6.1335	7.448	11.253	-0.73203
K274D	7.7964	-10.052	-10.303	12.443
D276N	-12.437	-3.5437	13.913	9.3104
A277T	5.1287	-7.8075	-4.4654	6.8946
R308K	-0.59247	7.761	3.5286	-6.9255
M314L	-7.2075	5.2935	6.3119	-5.2079
Total	-27.0553	0.9764	40.4485	29.9315

Table 4. Changes of amplitudes of IS frequencies by mutations contained in the co-mutation networks in 2009 H1N1 discovered in [18].

	Mutating Consensus HA1 Sequence of Swine Binding Patterns		Mutating Consensus HA1 Sequence of Human Binding Patterns	
Mutations	ΔA[F(0.055)]%	ΔA[F(0.295)]%	ΔA[F(0.055)]%	ΔA[F(0.295)]%
N167D	0	0	0	0
E195A	-2.674	-3.7307	2.1705	-0.36167
N167D, E195A	-2.6740	-3.7307	2.1705	-0.3617
N269D	-9.1545	8.9086	6.7895	-12.176
D276N	-12.437	-3.5437	13.913	9.3104
N269D, D276N	-20.8003	4.3377	21.7617	-3.6715

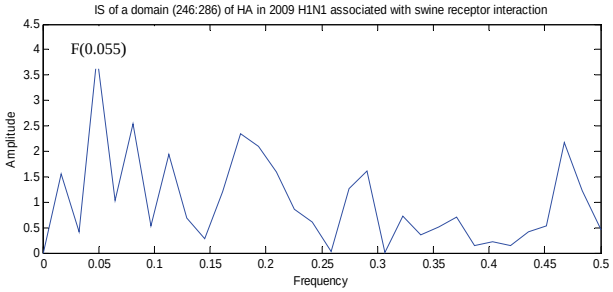

Figure 3. IS of one domain (246:286) of swine binding characteristic in HA1 of 2009 H1N1.

3.1.2. Avian H5N1

Although the whole set of HA1 sequences in avian H5N1 (n=1228) displayed the CIS dominant peak at frequency F(0.076) (**Figure 4(a)**), there were several

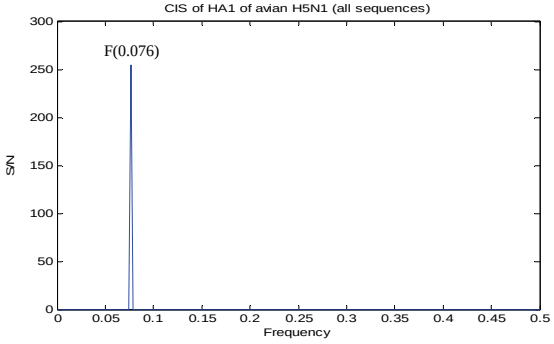

(a)

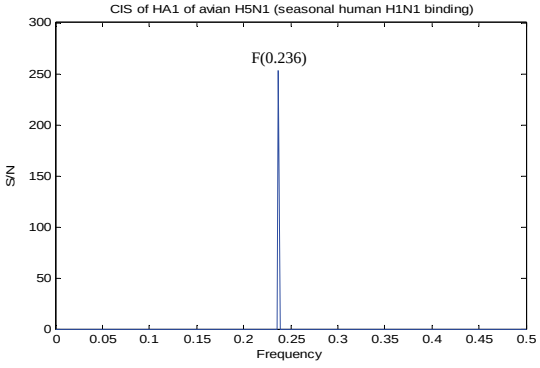

(b)

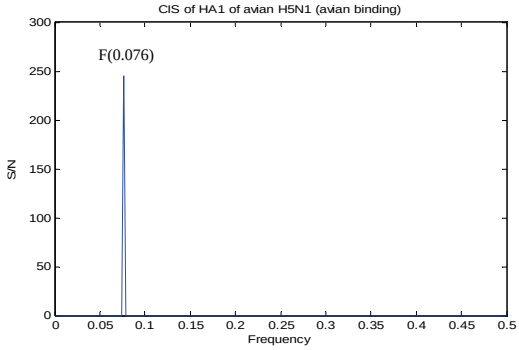

(c)

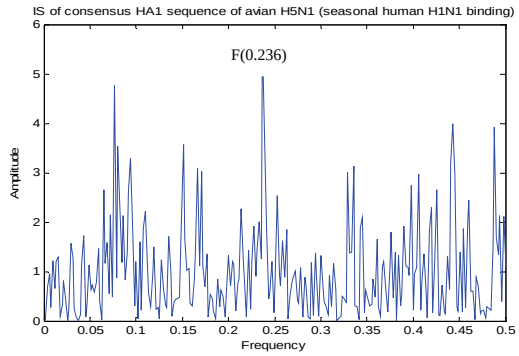

(d)

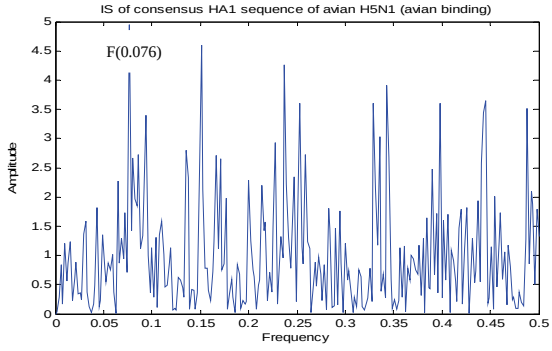

(e)

Figure 4. (a) CIS of consensus of all HA1 sequences of avian H5N1. (b) CIS of consensus HA1 sequence of avian H5N1 with seasonal human H1N1 binding. (c) CIS of consensus HA1 sequence of avian H5N1 with avian binding. (d) IS of consensus HA1 sequence of avian H5N1 with seasonal human H1N1 binding. (e) IS of consensus HA1 sequence of avian H5N1 with avian binding.

HA1 sequences in the dataset that had a higher IS peak at frequency F(0.236) than that at the frequency F(0.076). Bases on this observation, the whole set of HA1 sequences in avian H5N1 collected were divided into two subsets. One had the IS dominant peak at frequency F(0.076), referred to as avian binding subset (n=949), and the other had the IS dominant peak at frequency F(0.236), referred to as human binding subset (n=279). The CIS of these two subsets of HA1 sequences were plotted in (b) and (c) of **Figure 4**, and the IS of their consensus HA1 sequences were plotted in (d) and (e) of **Figure 4**, respectively. A total of 11 amino acid changes between the two consensus HA1 sequences of avian binding and human binding were found, and the resulting amplitude variation from each mutation was computed (**Table 5**). There were several mutations near the active site: D154N, N155S, A156T, and R189K.

3.1.3. Avian H1N1

For avian H1N1, we used the same strategy as for avian H5N1 to divide the whole set of HA1 sequences (n=78) in this subtype into two subsets according to different binding patterns (human (n=19) vs. avian (n=59)) as reflected by two different IS characteristic frequencies (F(0.295) vs. F(0.282))(**Figure 5**). Between the two consensus HA1 sequences of avian (F(0.282)) and human (F(0.295)) binding, there was only one mutation N121S (**Table 6**). The ISM was applied to quantify this mutation's contribution to the amplitude variation of the consensus HA1 sequence in each binding characteristics (**Table 6**).

For H1N1 viruses, the substitutions E190D/G225D were essential for avian virus HA to acquire human virus receptor specificity [13]. Here ISM was employed to verify this fact numerically (**Table 7**).

Table 5. Changes of amplitudes of IS frequencies by each mutation between avian and human binding patterns in HA1 of avian H5N1.

	Mutating Consensus HA1 Sequence of Avian Binding Patterns		Mutating Consensus HA1 Sequence of Human Binding Patterns	
Mutations	ΔA[F(0.076)]%	ΔA[F(0.236)]%	ΔA[F(0.076)]%	ΔA[F(0.236)]%
L71I	0	0	0	0
I83A	-2.7308	3.8849	2.6972	-3.2926
R140K	-7.8143	5.2052	8.2224	-4.3565
D154N	-14.371	5.9825	15.75	-3.3428
N155S	6.3122	9.7463	-5.5234	-8.0289
A156T	1.9481	4.9408	-1.3726	-3.7429
R189K	0.21422	-7.9896	0.36709	7.2805
N252Y	-5.9842	3.5318	6.173	-3.0255
T262A	0	0	0	0
I282M	4.7565	10.576	-4.6209	-8.6614
G323R	11.348	-8.0717	-10.859	7.048
Total	-6.3212	27.8086	10.8338	-20.1221

Table 6. Changes of amplitudes of IS frequencies by each mutation between avian and human binding patterns in HA1 of avian H1N1.

	Mutating Consensus HA1 Sequence of Avian Binding Patterns		Mutating Consensus HA1 Sequence of Human Binding Patterns	
Mutation	ΔA [F(0.282)]%	ΔA [F(0.295)]%	ΔA [F(0.282)]%	ΔA [F(0.295)]%
N121S	-15.7142	18.6251	18.6439	-15.7008

Table 7. Changes of amplitudes of IS frequencies by mutations E190D/G225D.

	Mutating Consensus HA1 Sequences of Avian H1N1		
Mutations	ΔA [F(0.282)]%	ΔA [F(0.295)]%	Dominant Peak Frequency
E190D	-13.2024	13.0862	F(0.282)
G225D	-10.4239	-0.6548	F(0.282)
E190D,G225D	-22.8997	11.7994	F(0.295)

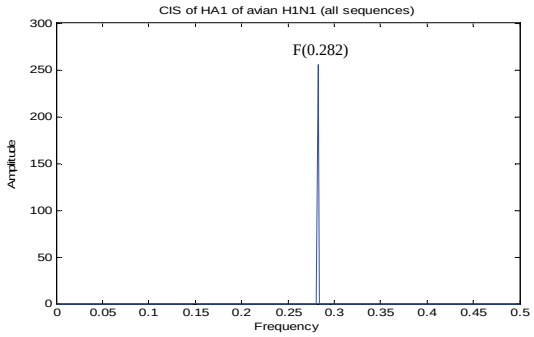

(a)

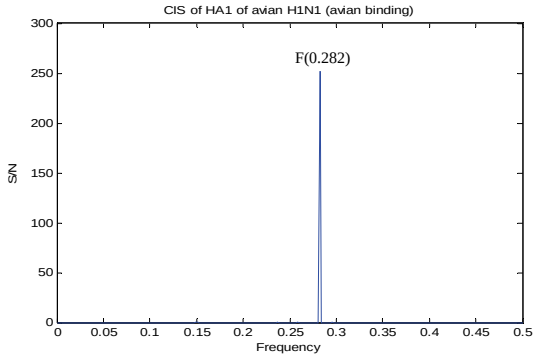

(b)

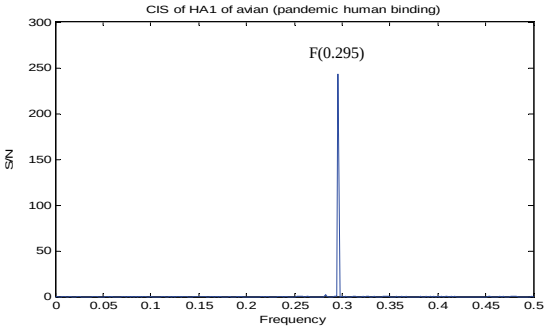

(c)

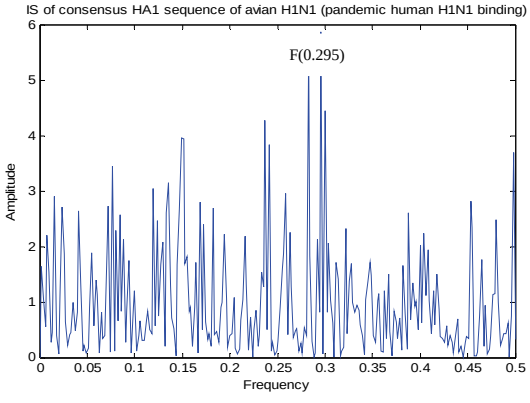

(d)

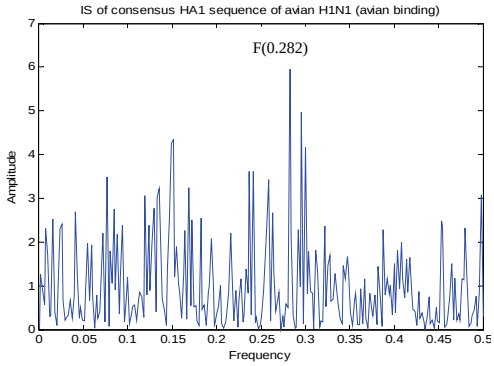

(e)

Figure 5. (a) CIS of consensus of all HA1 sequences of avian H1N1; (b) CIS of consensus HA1 sequence of avian H1N1 with pandemic human H1N1 binding; (c) CIS of consensus HA1 sequence of avian H1N1 with avian binding; (d) IS of consensus HA1 sequence of avian H1N1 with pandemic human H1N1 binding; (e) IS of consensus HA1 sequence of avian H1N1 with avian binding.

3.1.4. Swine H1N2

For swine H1N2, we used the same strategy as for avian H5N1 to divide the whole set of HA1 sequences (n=82) in this subtype into two subsets according to different binding patterns (human (n=45) vs. swine (n=37)) as reflected by two different IS characteristic frequencies (F(0.295) vs. F(0.055)) (**Figure 6**). The comparison of the two consensus HA1 sequences (human vs. swine) revealed 14 mutations, and the ISM was applied to quantify each mutation's contribution to the amplitude variation of the consensus HA1 sequence in each binding characteristics (**Table 8**). There were several mutations near the active site: N184T, R189Q, and T190S, and near the edges of the binding pocket: E127D, E224A, and R131K.

3.2. Mutations between Hosts

3.2.1. 2009 H1N1 and Swine H1N2

The 2009 H1N1 virus has its origin as a reassortant from a triple-reassortant virus circulating in North American swine and Eurasian avian-like swine H1N1, with its HA from the classical swine influenza viruses.

The comparison of the consensus HA1 sequences of 2009 H1N1 and swine H1N2 found 24 mutations. The ISM was applied to find the changes made by each mutation in the amplitude of IS of each consensus HA1 sequence (**Table 9**). Mutations K130R and E224A were near the edges of the binding pocket. There were three mutations at residues 71, 211, and 216 presented in Tables 3, 9, and 10, implying their importance in determining binding preferences of swine H1N2 and 2009 H1N1.

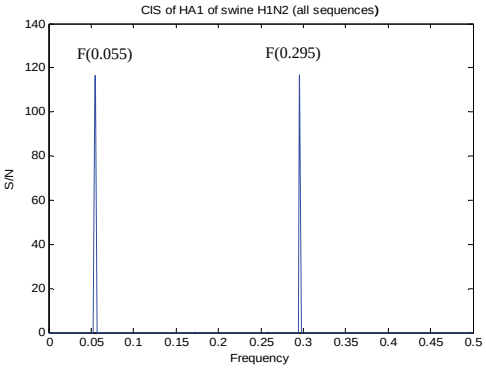

(a)

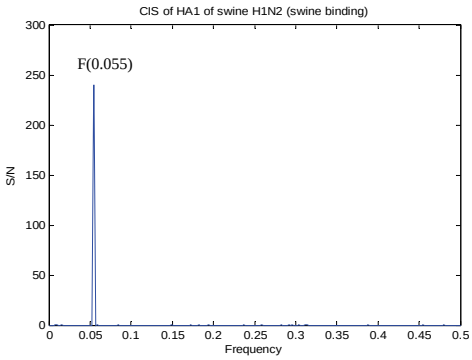

(b)

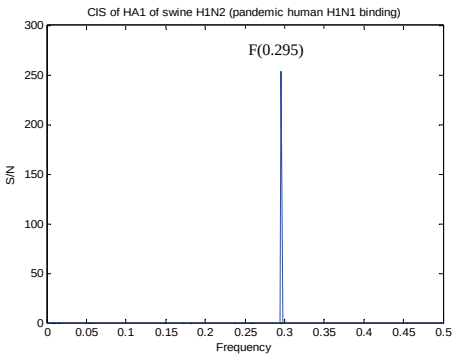

(c)

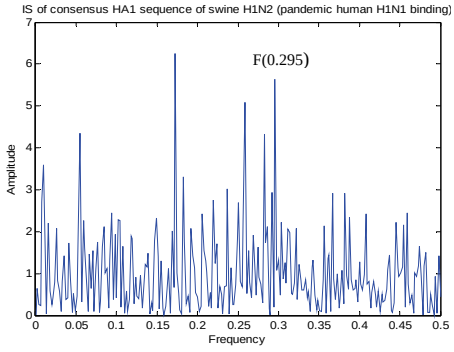

(d)

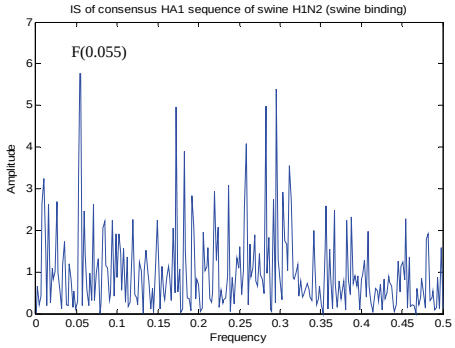

(e)

Figure 6. (a) CIS of consensus of all HA1 sequences of swine H1N2; (b) CIS of consensus HA1 sequence of swine H1N2 with pandemic human H1N1 binding; (c) CIS of consensus HA1 sequence of swine H1N2 with swine binding; (d) IS of consensus HA1 sequence of swine H1N2 with pandemic human H1N1 binding; (e) IS of consensus HA1 sequence of swine H1N2 with swine binding.

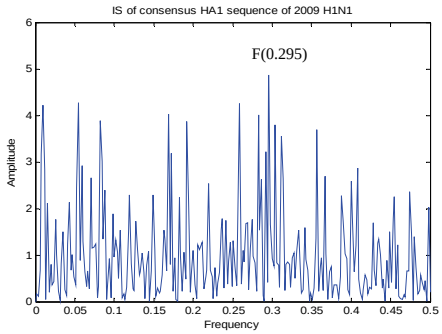

(a)

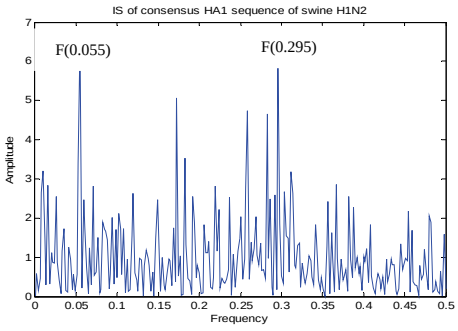

(b)

Figure 7. (a) IS of consensus HA1 sequence of 2009 H1N1. (b) IS of consensus HA1 sequence of swine H1N2.

Mutations in the binding site not only could modulate receptor specificity but also the antigenicity of the virus [27]. It was generally believed that the key residues at the binding site were not subject to selection, but recently a strong positive selection at position 190 in HA of H1N1 was detected in [13]. It was observed that there

Table 8. Changes of amplitudes of IS frequencies by each mutation between swine and human binding patterns in HA1 of swine H1N2.

	Mutating Consensus HA1 Sequence of Swine Binding Patterns		Mutating Consensus HA1 Sequence of Human Binding Patterns	
Mutations	ΔA [F(0.055)]%	ΔA [F(0.295)]%	ΔA [F(0.055)]%	ΔA [F(0.295)]%
V47I	-0.45253	-0.39918	0.61877	0.4217
I71F	-7.4498	3.7605	9.5403	-3.7394
E127D	-11.057	-1.2554	14.693	3.0055
R131K	0	0	0	0
G170E	0.014238	-0.07755	-0.01469	0.07289
N184T	-8.3652	-10.1	11.495	10.475
R189Q	-1.4448	-2.6783	1.6451	2.6875
T190S	-1.1476	0.1999	1.352	-0.09641
T211K	-6.1626	6.441	8.1349	-6.0602
K216T	-1.9443	7.4225	2.3502	-6.895
E224A	-0.10535	-1.9348	0.42226	1.7602
A250V	-1.1944	-3.5238	1.8901	3.4949
P271S	-2.8719	3.2365	3.4537	-3.3317
K278T	-0.95454	0.60359	2.0448	-0.81079
Total	-43.1358	1.6950	57.6254	0.9842

Table 9. Changes of amplitudes of IS frequencies by each mutation between consensus HA1 sequences of 2009 H1N1 and swine H1N2.

	Mutating Consensus HA1 Sequence of Swine H1N2		Mutating Consensus HA1 Sequence of 2009 H1N1	
Mutations	ΔA[F(0.055)]%	ΔA[F(0.295)]%	ΔA[F(0.055)]%	ΔA[F(0.295)]%
K36R	-5.6796	5.4297	7.2412	-4.7622
I61L	0	0	0	0
S71F	-0.75109	0.59143	0.90722	-0.85027
S84N	-7.0341	-8.3814	9.614	10.052
D97N	-4.8444	-9.6342	6.0451	9.9181
T120E	-8.911	5.4563	11.964	-7.0032
K130R	-4.3521	-4.4943	6.0754	5.9088
K142N	0.67563	-2.0369	-0.36048	2.8758
K146R	-5.7743	-2.0864	7.4097	1.4689
D168N	4.5193	-5.5381	-5.7447	4.824
G170E	0.011884	-0.07133	-0.01058	0.06883
R205H	1.7024	1.1275	-2.4361	-2.3933
K211T	6.5905	-5.7011	-7.8044	6.4193
I216K	-1.8394	3.6983	2.0037	-3.8566
E224A	-0.2376	-1.7644	0.61948	1.4082
K239T	-5.1394	0.52104	6.8924	0.89224
M257L	8.8688	-8.1637	-10.571	10.056
E258K	-2.8787	-2.2561	3.7825	2.0134
N260G	-0.05099	0.1242	0.071321	-0.12802
A261S	1.0216	0.76162	-0.593	-1.5978
I298V	0.093799	0.2947	-0.08087	-0.42787
K302E	-3.1322	1.8998	4.0108	-1.4074
L314M	-4.0997	6.3337	6.3078	-5.2087
V321I	-0.49821	-0.48678	0.6555	0.49537
Total	-31.7389	-27.3764	45.9990	28.7656

were two distinct evolutionary patterns in host-driven antigenic drift of human H1N1 HAs at positions 190 and 225, *i.e.*, the antigenic drift of 1918 pandemic HAs occurred at position 225, and that of epidemic HAs happened at position 190. In contrast to these two trends, the HAs in 2009 H1N1 took a different path, which were highly conserved at both positions 190 and 225, based on the 73 HA sequences of 2009 H1N1, as of July 10,

2009. In the present study, as of November 20, 2009, we had the following counts of various mutations at positions 190 and 225 in HA of 2009 H1N1 (**Table 10**). It appeared that the 2009 H1N1 HAs continued to keep this evolutionary pattern.

The alteration of receptor binding specificity was believed to be an essential step in host adaptation. Several studies on 1918 HA discovered that a single mutation D225G decreased the binding affinity of 1918 HA for α2,6 receptors and resulted in a mixed α2,6/α2,3 binding virus, furthermore, a double mutations D190E/D225G abolished the binding of 1918 HA to α2,6 and resulted in a α2,3 binding virus [28,29]. Our numerical analysis (**Table 11**) suggested that the mutations at positions 190 and 225 would produce similar binding affinity of 2009 H1N1 HA to that of 1918 HA. Mutation D190E decreased the amplitude at frequency F(0.295) more than that at frequency F(0.055), displaying the avian binding affinity, while mutation D225G produced the opposite effect, exhibiting the human binding specificity. The double mutations D190E/D225G showed avian binding preference.

Table 10. Mutation counts in HA1 sequences of 2009 H1N1.

Mutation	Counts
D190G	1
D190V	5
D225E	6
D225G	7
D225N	2

Table 11. Changes of amplitudes of IS frequencies by mutations observed in HA1 sequences of 2009 H1N1.

	Mutating Consensus HA1 Sequence of 2009 H1N1		
Mutations	ΔA [F(0.055)]%	ΔA [F(0.295)]%	Dominant Peak Frequency
D190E	-2.0061	-9.6206	F(0.282)
D190G	-2.0302	-9.6888	F(0.282)
D190N	-2.0789	-9.8255	F(0.282)
D190V	-2.0027	-9.6109	F(0.282)
D225E	-9.5672	-2.1233	F(0.295)
D225G	-9.6345	-2.1488	F(0.295)
D225N	-9.7694	-2.2003	F(0.295)
D190E,D225E	-10.5225	-12.3705	F(0.282)
D190E,D225G	-10.5836	-12.3981	F(0.282)
D190E,D225N	-10.7061	-12.4537	F(0.282)
D190G,D225E	-10.5392	-12.4420	F(0.282)
D190G,D225G	-10.6002	-12.4696	F(0.282)
D190G,D225N	-10.7226	-12.5253	F(0.282)
D190N,D225E	-10.5729	-12.5854	F(0.282)
D190N,D225G	-10.6338	-12.6131	F(0.282)
D190N,D225N	-10.7560	-12.6688	F(0.282)
D190V,D225E	-10.5201	-12.3603	F(0.282)
D190V,D225G	-10.5812	-12.3879	F(0.282)
D190V,D225N	-10.7037	-12.4435	F(0.282)

3.2.2. Avian H5N1 and Human H5N1

Most of the highly pathogenic avian H5N1 strains bind strongly to avian receptors. This specificity is normally a barrier to viral transmission from birds to humans. However, a few of them have been discovered to bind to human receptors as well as to avian receptors. The comparison of the consensus HA1 sequences of avian H5N1 and human H5N1 identified three mutations, R140K, R189K, and T263A, and their impact on the two characteristic frequencies F(0.076) and F(0.236) was illustrated in **Table 12**.

As demonstrated in the experiments conducted in references [5,6], substitutions Q192R and S223L could mediate a shift from avian to human binding preference in the H5N1 viruses. In references [30,31,32], mutations Q226L and G228S enhanced the human binding capacity while reduced avian binding capacity of the H5N1 viruses. Here the ISM was utilized to evaluate the outcome of these mutations (**Table 13**). **Figure 8** illustrated the effect of mutation S223L on the two characteristic frequencies F(0.076) and F(0.236).

4. DISCUSSION

Understanding the minimal adaptive changes necessary for viral adaptation to human host is of key importance in learning how pandemic influenza viruses emerge. Alteration of receptor recognition is a vital step in host adaptation, which is modulated directly by a subset of amino acids present in the HA protein. Other determinants of host adaptation include continued viral evolution to improve transmission and replication efficiency and optimize tissue tropism.

There are several well-known mutations in HA protein in different flu subtypes, playing critical roles in receptor binding preference shift. Besides mutations in HA, the glycosylation sites in HA might also impact the binding specificity of HA [32]. The mutations discovered in this study represent alternatives by which the HA can switch its substrate recognition. These mutations occur in nature, whereas those artificially engineered by wet lab techniques may have a very low probability to occur in nature. As evidenced by the study in [30] that mutations Q226L and G228S in HA proteins could alter the binding specificity of the H5N1 viruses. Nevertheless, it also pointed out that the likelihood to acquire the necessary nucleotide changes to produce these mutations in natural virus is small, which could explain in part why

Table 12. Changes of amplitudes of IS frequencies by each mutation between consensus HA1 sequences of avian H5N1 and human H5N1.

	Mutating Consensus HA1 Sequence of Avian H5N1		Mutating Consensus HA1 Sequence of Human H5N1	
Mutation	ΔA [F(0.076)]%	ΔA [F(0.236)]%	ΔA [F(0.076)]%	ΔA [F(0.236)]%
R140K	7.9425	-4.5900	-7.8143	5.2052
R189K	-0.5253	7.7370	0.2142	-7.9896
T263A	-3.7894	-6.0611	4.5619	6.8405
Total	3.6278	-2.9141	-3.0382	4.0561

Table 13. Changes of amplitudes of IS frequencies by mutations experimented in references [5,6,30,31,32].

	Mutating Consensus HA1 Sequence of Avian H5N1	
Mutations	ΔA [F(0.076)]%	ΔA [F(0.236)]%
Q192R	-3.2185	1.5596
S223L	-4.0399	10.8075
Q192R, S223L	-6.5711	11.6823
Q226L	0.9498	17.4463
G228S	7.3516	15.7656
Q226L, G228S	8.0339	16.9010

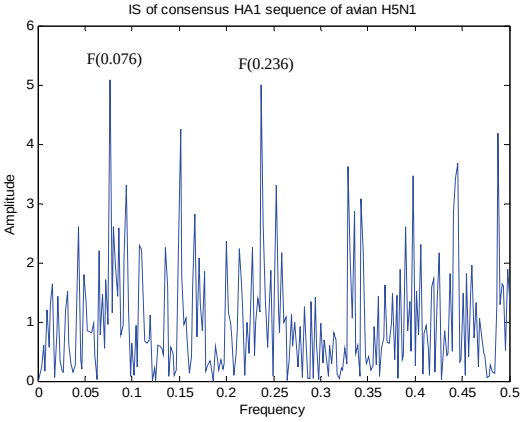

(a)

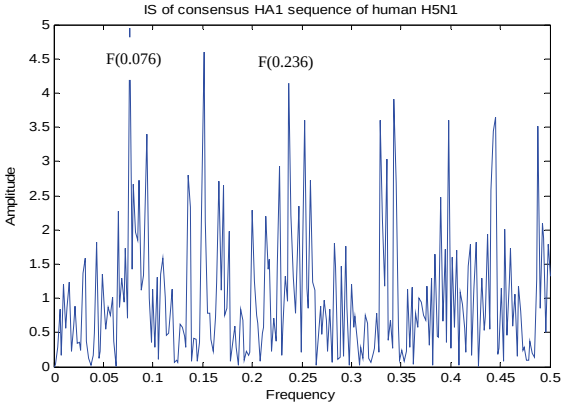

(b)

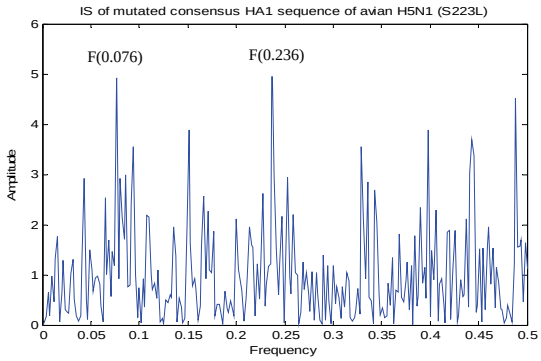

(c)

Figure 8. (a) IS of consensus HA1 sequence of avian H5N1; (b) IS of consensus HA1 sequence of human H5N1; (c) IS of consensus HA1 sequence of avian H5N1 mutated by S223L.

viruses such as H5N1 have not yet evolved into human transmissible strains to cause a human pandemic.

It appears that increased binding affinity for human influenza receptors alone is not sufficient for efficient human transmission, and additional molecular determinants are required. In [33], it was proposed that binding to long-chain α2-6 sialosides is a necessary requirement for viruses to efficiently replicate and transmit in humans. There is inadequacy in assessing the adaption to human receptor affinity from the analysis of a few influenza strains [30]. It showed that the effects of the same mutations, such as Q226L/G228S, on the binding preference of one strain were not the same on others strains in H5N1. Because lab experiments are labor intensive and costly, bioinformatics approaches offer reasonable alternatives in the analysis of binding specificity given the large number of virus sequences, which can process all strains with any combination of mutations within a subtype efficiently.

5. CONCLUSIONS

The increasing trend of direct transmission of avian/swine influenza viruses to humans underscores the need to understand further the mechanism of glycan receptor recognition and specificity switch. In this study, muta-

tions in HA1 within or between hosts in various flu subtypes were identified, and their contribution to binding preference was measured using the ISM. Our numerical analysis implied that the mutations in HA1 of 2009 human H1N1 collectively tended to reduce the swine binding affinity in the seasonal H1N1 strains and to increase that in the pandemic H1N1 strains. At the same time, they increased the human binding affinity in the pandemic H1N1 strains and had little impact on that in the seasonal H1N1 strains. The mutations in HA1 of avian H5N1 and avian H1N1 exhibited reduced avian binding in the strains of avian binding propensity while showed enhanced avian binding affinity in the strains with human binding propensity. They displayed the opposite effects on human binding. The mutations in HA1 of swine H1N2 reduced the swine binding affinity in the strains with swine binding propensity and enhanced that in the strains with human binding propensity. They showed little impact on the human binding affinity, which was different from the mutations in HA1 of 2009 H1N1. The mutations between the consensus HA1 sequences of 2009 H1N1 and swine H1N2 decreased both the human and swine binding affinities in swine H1N2 and increased those in 2009 H1N1. The mutations between the consensus HA1 sequences of human H5N1 and avian H5N1 increased the avian binding affinity and decreased the human binding affinity in avian H5N1 while produced the opposite effects on those in human H5N1.

The mutations discovered in the present study confirmed the potential for influenza viruses to adapt to human host, and furthermore, our numerical analysis detailed the extent of binding preference changes induced by each mutation. These mutations and their corresponding contribution to the binding specificity alteration yielded new clues to the mechanism of receptor recognition switch within and between hosts. The ISM offered a complementary and efficient approach to investigate the binding affinities of all HA sequences in various subtypes, a task difficult to accomplish experimentally.

6. ACKNOWLEDGMENTS

We thank Houghton College for its financial support.

REFERENCES

[1] Webster, R.G. (1999) 1918 Spanish influenza: The secrets remain elusive. *Proceedings of the National Academy of Sciences*, USA, **96(4)**, 1164-1166.

[2] Li, Q., Kash, J.C., Dugan, V.G., Wang, R.X., Jin, G.Z., Cunningham, R.E. and Taubenberger, J.K. (2009) Role of sialic acid binding specificity of the 1918 influenza virus hemagglutinin protein in virulence and pathogenesis for mice. *Journal of Virology*, **83(8)**, 3754-3761.

[3] Matrosovich, M.N., Klenk, H. D. and Kawaoka, Y. (2006) Receptor specificity, host-range, and pathogenicity of influenza viruses. In Yoshihiro Kawaoka (ed.) *Influenza Virology: Current Topics*, Caister Academic Press, 95-137.

[4] Zambon, M. (2007). Lessons from the 1918 influenza. *Nature Biotech*, **25**, 433-434.

[5] Gambaryan, A. Tuzikov, A., Pazynina, G., Bovin, N., Balish, A. and Klimov, A. (2006) Evolution of the receptor binding phenotype of influenza A (H5) viruses. *Virology*, **344(2)**, 432-438.

[6] Yamada, S., Suzuki, Y., Suzuki, T., Le, M. Q., Nidom, C. A., Sakai-Tagawa, Y., Muramoto, Y., *et al*. (2006) Haemagglutinin mutations responsible for the binding of H5N1 influenza A viruses to human-type receptors. *Nature*, **444(7117)**, 378-382.

[7] Matrosovich, M., Tuzikov, A., Bovin, N., Gambaryan, A., and Klimov, A., *et al*. (2000) Early alterations of the receptor-binding properties of H1, H2, and H3 avian influenza virus hemagglutinins after their introduction into mammals. *Journal of Virology*, **74(18)**, 8502-8512.

[8] Bateman, A.C., Busch, M.G., Karasin, A.I., Bovin, N., and Olsen, C.W. (2008) Amino acid 226 in the hemagglutinin of H4N6 influenza virus determines binding affinity for alpha2, 6-linked sialic acid and infectivity levels in primary swine and human respiratory epithelial cells. *Journal of Virology*, **82(16)**, 8204-8209.

[9] Wan, H., Sorrell, E.M., Song, H., Hossain, M.J., Ramirez-Nieto, G., *et al*. (2008) Replication and transmission of H9N2 influenza viruses in ferrets: Evaluation of pandemic potential. *PLoS ONE*, **3(8)**, e2923.

[10] Rogers, G.N. and D'Souza, B.L. (1989) Receptor binding properties of human and animal H1 influenza virus isolates. *Virology*, **173**, 317-322.

[11] Matrosovich, M.N., Gambaryan, A.S., Teneberg, S., Piskarev, V.E., Yamnikova, S.S., *et al*. (1997) Avian influenza A viruses differ from human viruses by recognition of sialyloligosaccharides and gangliosides and by a higher conservation of the HA receptor-binding site. *Virology*, **233(1)**, 224-234.

[12] Reid, A.H., Janczewski, T.A., Lourens, R.M., Elliot, A.J., Daniels, R.S., Berry, C.L., Oxford, J.S. and Taubenberger, J.K. (2003) 1918 influenza pandemic caused by highly conserved viruses with two receptor-binding variants. *Emerg Infect Disease*, **9(10)**, 1249-1253.

[13] Shen, J., Ma, J. and Wang, Q. (2009) Evolutionary trends of A(H1N1) influenza virus hemagglutinin since 1918. *PLoS ONE*, **4(11)**, e7789.

[14] Srinivasan, A., Viswanathan, K., Raman, R., Chandrasekaran, A., Raguram, S., Tumpey, T.M., Sasisekharan, V. and Sasisekharan, R. (2008) Quantitative biochemical rationale for differences in transmissibility of 1918 pandemic influenza A viruses. *Proceedings of the National Academy of Sciences*, **105(8)**, 2800-2805.

[15] Soundararajan, V., Tharakaraman, K., Raman, R., Raguram, S., Shriver, Z., Sasisekharan, V. and Sasisekharan R. (2009) Extrapolating from sequence–the 2009 H1N1 "swine" influenza virus. *Nature Biotechnology*, **27(6)**, 510-513.

[16] Childs, R.A., Palma, A.S., Wharton, S., Matrosovich, T., Liu, Y., Chai, W.G., Campanero-Rhodes, M.A., Zhang, Y.B., Eickmann, M., Kiso, M., Hay, A., Matrosovich. M. and Feizi, T. (2009) Receptor-binding specificity of

pandemic influenza A (H1N1) 2009 virus determined by carbohydrate microarray. *Nature Biotechnology*, **27 (9)**, 797-799.

[17] Hu, W. (2009) Analysis of correlated mutations, stalk motifs, and phylogenetic relationship of the 2009 influenza A virus neuraminidase sequences. *Journal of Biomedical Science and Engineering*, **2(7)**, 550-558.

[18] Hu, W. (2010) The Interaction between the 2009 H1N1 influenza A hemagglutinin and neuraminidase: Mutations, co-mutations, and the NA stalk motifs. *Journal of Biomedical Science and Engineering*, **3**, 1-12.

[19] Veljkovic, V., Niman, H.L., Glisic, S., Veljkovic, N., Perovic, V. and Muller C.P. (2009). Identification of hemagglutinin structural domain and polymorphisms which may modulate swine H1N1 interactions with human receptor. *BMC Structural Biology*, **9**, 62.

[20] Veljkovic, V., Veljkovic, N., Muller, C.P., Müller, S. Glisic, S., Perovic, V. and Köhler, H. (2009) Characterization of conserved properties of hemagglutinin of H5N1 and human influenza viruses: Possible consequences for therapy and infection control. *BMC Structural Biology*, **7**, 9-21.

[21] Cosic, I. (1997) The resonant recognition model of macromolecular bioreactivity, theory and application. Berlin: Birkhauser Verlag.

[22] Hu, W. (2010) Identification of highly conserved domains in hemagglutinin associated with the receptor binding specificity of influenza viruses: 2009 H1N1, avian H5N1, and swine. *Journal of Biomedical Science and Engineering*, **3**, 114-123.

[23] Katoh, K., Kuma, K., Toh, H. and Miyata, T. (2005) MAFFT version 5: Improvement in accuracy of multiple sequence alignment. *Nucleic Acids Research*, **33(2)**, 511-518.

[24] MacKay, D. (2003) Information theory, inference, and learning algorithms. Cambridge University Press.

[25] KováccaronOVá, A., Ruttkay-Nedecký, G., Karol HaverlíK, I. and Janecccaronek, S. (2002) Sequence similarities and evolutionary relationships of influenza virus A hemagglutinins, *Virus Genes*, **24(1)**, 57-63.

[26] Gamblin, S.J., Haire, L.F., Russell, R.J., Stevens, D.J., Xiao, B., Ha, Y., *et al*. (2004) The structure and receptor binding properties of the 1918 influenza hemagglutinin. *Science*, **303**, 1838-1842.

[27] Daniels, R.S., Douglas, A.R., Skehel, J.J., Wiley, D.C., Naeve, C.W., Webster, R.G., Rogers, G.N. and Paulson, J. C. (1984). Antigenic analyses of influenza virus haemagglutinins with different receptorbinding specificities. *Virology*, **138**, 174-177.

[28] Srinivasan, A., Viswanathan, K., Raman, R., Chandrasekaran, A., Raguram, S., *et al*. (2008) Quantitative biochemical rationale for differences in transmissibility of 1918 pandemic influenza A viruses. *Proceedings of the National Academy of Sciences*, **105**, 2800-2805.

[29] Stevens, J., Blixt, O., Glaser, L., Taubenberger, J.K. , Palese, P., *et al*. (2006) Glycan microarray analysis of the hemagglutinins from modern and pandemic influenza viruses reveals different receptor specificities. *Journal of Molecular Biology*, **355(5)**, 1143-1155.

[30] Ayora-Talavera, G., Shelton, H., Scull, M.A., Ren, J., Jones, I.M., *et al*. (2009) Mutations in H5N1 influenza virus hemagglutinin that confer binding to human tracheal airway epithelium. *PLoS ONE*, **4(11)**, e7836.

[31] Stevens, J., Blixt, O., Glaser, L., Taubenberger, J.K., Palese, P., *et al*. (2006) Glycan microarray analysis of the hemagglutinins from modern and pandemic influenza viruses reveals different receptor specificities. *Journal of Molecular Biology*, **355(5)**, 1143-1155.

[32] Stevens, J., Blixt, O., Chen, L.M., Donis, R.O., Paulson, J.C., *et al*. (2008) Recent avian H5N1 viruses exhibit increased propensity for acquiring human receptor specificity. *Journal of Molecular Biology*, **381(5)**, 1382- 1394.

[33] Chandrasekaran, A., Srinivasan, A., Raman, R., Viswanathan, K., Raguram, S., Tumpey, T.M., Sasisekharan, V. and Sasisekharan, R. (1008) Glycan topology determines human adaptation of avian H5N1 virus hemagglutinin. *Nature Biotechnology*, **26(1)**, 107-113.

J. Biomedical Science and Engineering, 2010, 3, 241-246 **JBiSE**
doi:10.4236/jbise.2010.33032 Published Online March 2010 (http://www.SciRP.org/journal/jbise/).

Evaluation of fast spin echo MRI sequence for an MRI guided high intensity focused ultrasound system for in vivo rabbit liver ablation*

Nicos Mylonas[1,2], Kleanthis Ioannides[3], Venediktos Hadjisavvas[1,4], Dimitris Iosif[2], Panayiotis A. Kyriacou[1], Christakis Damianou[2,4]

[1]City University, London, UK;
[2]Frederick University, Limassol, Cyprus;
[3]Polikliniki Ygia, Limassol, Cyprus;
[4]MEDSONIC LTD, Limassol, Cyprus.
Email: dalma@cytanet.com.cy; venedik@cytanet.com.cy; joseph.da@cytanet.com.cy; aktinodiagnostis@yahoo.com; cdamianou@cytanet.com.cy

Received 11 December 2009; revised 28 December 2009; accepted 6 January 2010.

ABSTRACT

The effectiveness of magnetic resonance imaging (MRI) to monitor thermal lesions created by High Intensity Focused Ultrasound (HIFU) in rabbit liver in vivo is investigated. The MRI sequences of T1-weighted, and T2-weighted fast spin echo (FSE) were evaluated. The main goal in this paper was to find the range of repetition time (TR) and range of echo time (TE) which maximizes the contrast to noise ratio (CNR). An ultrasonic transducer operating at 2 MHz was used, which is navigated using a positioning device. With T1W FSE the range of TR under which CNR is maximized ranges from 400 to 900 ms. The maximum contrast measured is approximately 25. With T2W FSE the range of TE that establishes maximum contrast is between 40 ms and 80 ms, with CNR of approximately 14. T1W FSE is much better than T2W FSE in detecting thermal lesions in liver. Both T1W and T2 W FSE were proven successful to image thermal lesions created by HIFU in rabbit liver in vivo.

Keywords: Ultrasound; Liver; MRI; Lesion; Ablation

1. INTRODUCTION

Surgical resection is considered the therapy of choice for liver cancer. However, the percentage of patients who are good candidates for surgery is low [1]. Surgical resection is only feasible in 10–20% of the patients resulting to 5-year survival rates in the region of 40% [1]. Moreover, the incidence of new metastases after resection is high, and the success rate after multiple resections is low [1]. Because of the above disadvantages of surgical resection the development of several less invasive local ablative therapies for liver tumors is imperative. These approaches have included percutaneous ethanol injection [2], cryotherapy [3], radiofrequency [4], microwave [5], and laser ablation [6,7]. These local therapies have produced survival rates similar to those with surgical resection in the treatment of metastases [8], but unfortunately high local recurrence rate is also reported [9].

Therefore thermal ablation methods could possibly become a main treatment option for liver cancer, especially if recurrence rate is minimized. Another ablative method that could be used for liver cancer treatment is High Intensity Focused Ultrasound (HIFU). HIFU is the only non-invasive local therapy to be proposed to date. If HIFU is proven equivalent to surgical resection, this minimally invasive approach may be able to replace surgery as the treatment of choice.

A lot of work has been done in many directions since the 80's in the area of liver ablation using HIFU. The threshold of intensity that is needed to cause irreversible damage in liver, was suggested by Frizell *et al*. 1987 [10] and Frizell 1988 [11]. This information is very useful, because the intensity needed to create lesions was defined. The thermal effects of HIFU in liver were well documented by ter Haar *et al*. 1989 [12], and Sibile *et al*. 1993 [13]. In the two studies by Chen *et al*. 1993 [14], and Chen *et al*. 1999 [15], the effect of HIFU ablation in liver and cancerous liver using histology were analysed extensively. The effective delivery of HIFU protocols in real oncologigal applications of liver was achieved by implanting tumour cells in liver [16,17,18,19,20].

*This work was supported by the Research Promotion Foundation (RPF of Cyprus under the contract ERYAN/2004/1, ΑΝΑΒΑ Θ ΜΙΣΗ/ΠΑΓΙΟ/0308/05, and ΕΠΙΧΕΙΡΗΣΕΙΣ/ ΕΦΑΡΜ /0308/01.

Since the 90's clinical work has been initiated for liver cancer. Vallancien *et al*. [21] treated two patients with solitary liver metastases prior to surgical resection. The team headed by Wu in 1999 reported a clinical study for treating 68 patients with liver malignancies [22]. The same group reported a clinical study with 474 patients with Hepatocelular Carcinoma (HCC) treated using HIFU in combination with transarterial chemo-embolisation [23]. HIFU ablation has also been used for palliation in 100 patients with advanced-stage liver cancer [24]. Following treatment, symptoms, such as pain and lethargy, were relieved in 87% of the patients.

Without an imaging system that allows for online monitoring of the deposition of ultrasound energy or the creation of induced lesion, it is impossible to predict the precise location of the HIFU beam, to monitor the temperature changes, or to control the deposited thermal dose. In the past, these major constraints limited the development of HIFU as a noninvasive surgical technique. In recent years, however, integration of HIFU with MRI, which allows high-sensitivity tumor detection and the ability to monitor temperature in real time, has increased the potentials of HIFU.

MRI-guided HIFU has generally been reserved for the treatment of uterine fibroids [25] and breast adenomas [26]. However, it is very likely that this mode of treatment monitoring and delivery will have a role in the treatment of liver tumours. Recently, a non-randomised clinical trial is under way [27] to assess the safety and efficacy of the MRI guided HIFU system ExAblate 2000 (InSightec, Haifa, Israel) in the treatment of liver tumours. It was reported that a small number of patients has been treated to date with promising results [27].

The first attempt to monitor the effect of HIFU using MRI in liver was reported by Rowland *et al*. 1997 [28], who demonstrated that monitoring of thermal lesions in liver is feasible. The MRI appearance of lesions in liver created using HIFU was also studied by Jolesz *et al*. 2004 [29] and Kopelman *et al*. 2006 [30].

In this paper the goal is to investigate the effectiveness of MRI to monitor therapeutic protocols of HIFU in rabbit liver *in vivo*. The two basic and most important MRI sequences of T1-weighted fast spin echo (FSE), and T2-weighted FSE are investigated. The goal was to create large lesions and use MRI to discriminate between liver tissue and lesion. With T1W FSE the signal intensity vs. repetition time (TR) is evaluated and based on this analysis, the contrast to noise ratio (CNR) is estimated, in order to find the range of TR that produces maximum contrast. Similarly for T2W FSE the range of echo time (TE) is found that maximizes the contrast. A spherically focused transducer operating at 2 MHz was used, which is navigated inside MRI using an MRI compatible robot.

2. METHODS

2.1. HIFU/MRI System

Figure 1 shows the block diagram of the HIFU/MRI system which includes the following subsystems:

a) HIFU system, b) MR imaging, c) Positioning device (robot) and associate drivers, and d) MRI compatible camera.

2.1.1. HIFU System

The HIFU system consists of a signal generator (HP 33120A, Agilent technologies, Englewood, CO, USA), a RF amplifier (250 W, AR, Souderton, PA, USA), and a spherically shaped bowl transducer made from piezoelectric ceramic of low magnetic susceptibility (Etalon, Lebanon, IN, USA). The transducer operates at 2 MHz, has focal length of 10 cm and diameter of 5 cm. The transducer is rigidly mounted on the MRI-compatible positioning system (MEDSONIC LTD, Limassol, Cyprus) which is described shortly.

2.1.2. MRI Imaging

The 3-d positioning device and the transducer were placed inside a MRI scanner (Signa 1.5 T, by General Electric, Fairfield, CT, USA). A spinal coil (USA instruments, Cleveland, OH, USA) was used to acquire the MRI signal.

2.1.3. Positioning Device/Robot Drivers

The robot has been developed initially for three degrees-of-freedom, but it can be easily developed for 5 degrees of motion. Since the positioning device is placed on the table of the MRI scanner its height is around 55 cm (bore diameter of the MRI scanner). The length of the positioning device is 45 cm and its width 30 cm. The weight of the positioning device is only 6 kg and therefore it can be considered portable. **Figure 2** shows the schematic the positioning device illustrating the 3 stages, transducer, and coupling method. The

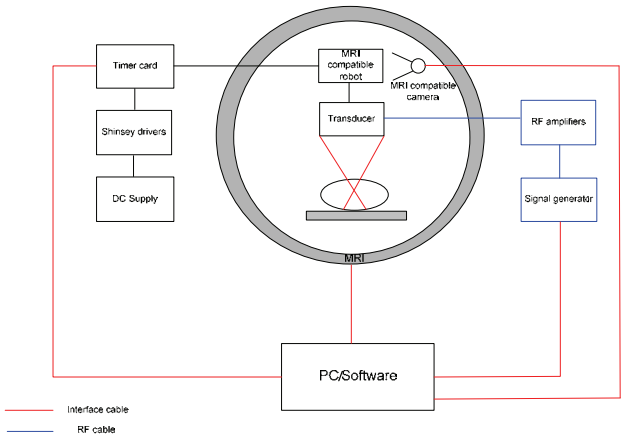

Figure 1. HIFU system under MRI guidance showing the various functionalities of the HIFU/MRI system.

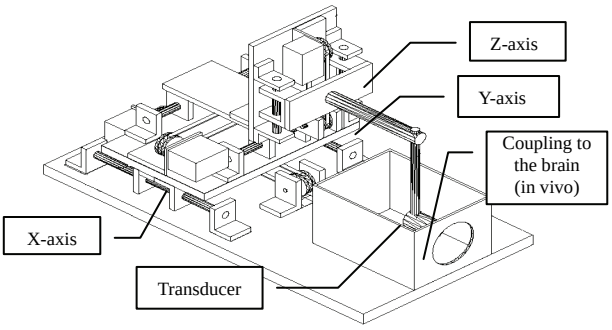

Figure 2. Schematic of the robot showing all of its stages.

positioning device operates by means of 3 piezoelectric motors (USR60-S3N, Shinsei Kogyo Corp., Tokyo, Japan). More details of this positioning device can be found in [31]. Moreover, the positioning system includes optoelectronic encoders (not shown in any of the figures) for providing signals indicating the relative positions of the movable elements in the positioning system. The resolution of all 3 axes of the positioning device is 0.1 mm.

The box hosting the motor drivers is placed outside the MRI room since magnetic materials are involved. A DC supply (24V, 6A) is used to drive the Shinsei drivers. Wires from the Shinsei drivers are connected to a PCI 6602 interface card (National instruments, Austin, Texas, USA) via a connecting block. The PCI 6602 interface card includes timing and digital I/O modules. The interface is connected in a PC (Dell Inc. Round Rock, Texas, USA).

2.1.4. MRI Compatible Camera

In order to monitor the condition of the animal or humans (future use), an MRI compatible camera (MRC Systems GmbH, Heidelberg, Germany) was mounted on the system. The camera was interfaced by means of a video card. With the aid of the MRI compatible camera, the researcher can monitor the welfare of the animal.

2.2. In Vivo Experiments

For the *in vivo* experiments, New Zealand adult rabbits were used weighting approximately 3.5-4 kg. Totally 7 rabbits were used in the experiments. The rabbits were anaesthetized using a mixture of 500 mg of ketamine (100 mg/mL, Aveco, Ford Dodge, IA), 160 mg of xylazine (20 mg/mL, Loyd Laboratories, Shenandoah, IA), and 20 mg of acepromazine (10 mg/mL, Aveco, Ford Dodge, IA) at a dose of 1 mL/kg. The animal experiments protocol was approved by the national body in Cyprus responsible for animal studies (Ministry of Agriculture, Animal Services).

2.3. HIFU Parameters

The *in situ* spatial average intensity was estimated based on the applied power and the half-power width of the beam of the transducer. The attenuation used was 4 Np/m-MHz. The half-power length of the beam is 15.6 mm and the half-power width is 1.2 mm. The details of the intensity estimation can be found in [32]. In order to create large lesions, a square grid pattern of 4x4 overlapping lesions was used. The spacing between successive transducer movements was 2 mm, which creates overlapping lesions for the intensity and pulse duration used. In all the exposures the ultrasound was turn on for 5 s. The *in situ* spatial average intensity used was 1000 W/cm^2. The delay between successive ultrasound firings was 10 s.

2.4. MRI Processing

The following parameters were used for T1-W FSE: TR was variable from 100-1000 ms, TE = 9 ms, slice thickness = 3 mm (gap 0.3 mm), matrix = 256 × 256, FOV = 16 cm, NEX = 1, and ETL = 8. For T2-W FSE: TR = 2500 ms, TE was variable from 10 ms to 160 ms, slice thickness = 3 mm (gap 0.3 mm), matrix = 256 × 256, FOV = 16 cm, NEX = 1, and ETL = 8.

The contrast to noise ratio (CNR) was obtained by dividing the signal intensity difference between the Region of Interest (ROI) in the lesion and in the ROI of normal liver tissue by the standard deviation of the noise in the ROI of normal liver tissue. The ROI was circular with diameter of 3 mm.

The tissue temperature change (ΔT) has been estimated using the proton resonance frequency method given by the equation stated in Chung *et al*. 1996 [33]:

$$\Delta\phi=\gamma B_0\alpha\Delta T\ \mathrm{TE} \quad (1)$$

where $\Delta\phi$ is the temperature-dependent phase shift which is the phase acquired before and during temperature elevation and which accumulates during the echo time TE using fast spoiled gradient (FSPGR). The other terms are γ which is the gyromagnetic ratio of proton, 42.58MHz/T, α is the average proton resonance frequency coefficient, and B_0 is the flux density of the static magnetic field. The measured temperature elevation can be added to the base-line temperature to obtain the absolute temperature. The average proton resonance frequency coefficient α for the frequency shift was taken to be -0.0105ppm/^{o}C as determined by the method described by Vykhodtseva *et al*. 2000 [33].

3. RESULTS

The goal in this study was to use T1W FSE using different TR (from 100 to 1000 ms) and then evaluate the effect of TR on the CNR. **Figure 3** shows a large lesion in liver *in vivo* using T1-w FSE (TR = 400 ms). This lesion was created using *in situ* spatial average intensity

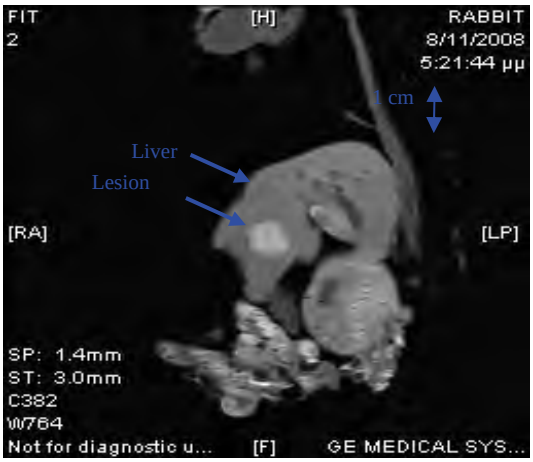

Figure 3. Large lesion in liver *in vivo* using T1-w FSE.

of 1000 W/cm^2 for 5 s. Since the step size of this 4 × 4 lesion was 2 mm, the size of this lesion is approximately 8 mm × 8mm. The MRI estimated maximum temperature in this lesion was 65°C. Since the estimated temperature is below 100°C, the occurrence of boiling was excluded. The thermal lesion appears bright and the contrast with liver tissue is excellent.

Figure 4 shows the photograph of the lesion of **Figure 3** after the animal was sacrificed in a plane perpendicular to the transducer face.

Figure 5 shows the CNR between lesion and liver plotted against TR for the MRI image of **Figure 3**. The same trend of CNR was seen in all the remaining 6 rabbits. Also the maximum CNR between liver and lesion of the other 6 rabbits was also close to 25, and thus we are confident that this typical graph represents the behaviour of CNR vs. TR for rabbit liver ablation *in vivo*. The relaxation time T1 of the lesion is 250 ms, and relaxation time T1 of the liver is 600 ms. The proton density of the lesion increases by 20 % compared to the host tissue.

Figure 6 shows the MRI image of the lesion of **Figure 3** using T1-w FSE demonstrating the excellent propagation deep in the liver (*i.e.* in plane parallel to the transducer beam axis).

The second goal in this study was to explore T2W FSE using different TE (from 10 to 140 ms) and then evaluate the effect of TE on the CNR. **Figure 7** shows the MRI images of the same lesion as in **Figure 3** using T2W FSE (TE = 60 ms).

Figure 8 shows the CNR between lesion and liver plotted against TE for the liver and lesion of the MRI image of **Figure 7**. The relaxation time T2 of lesion is 35 ms and the relaxation time T2 of the liver is 50 ms. The proton density of the lesion decreases by 5 % compared to the host tissue.

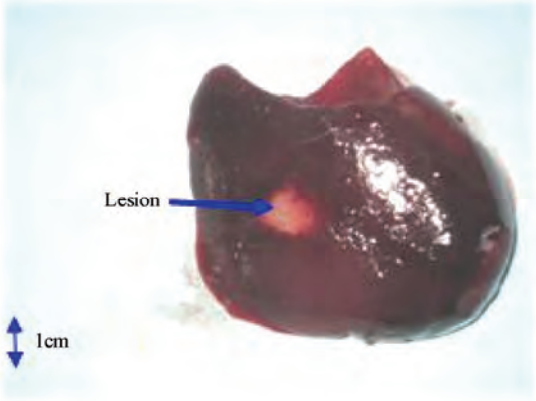

Figure 4. Photograph of the lesion of **Figure 3**.

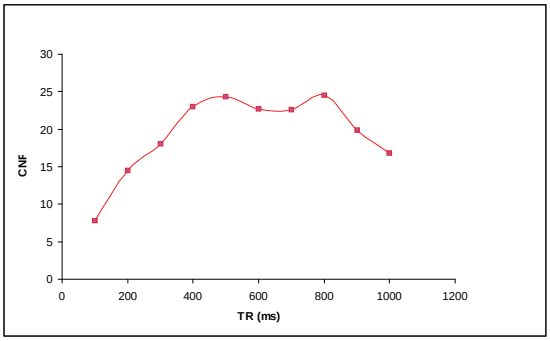

Figure 5. CNR vs TR.

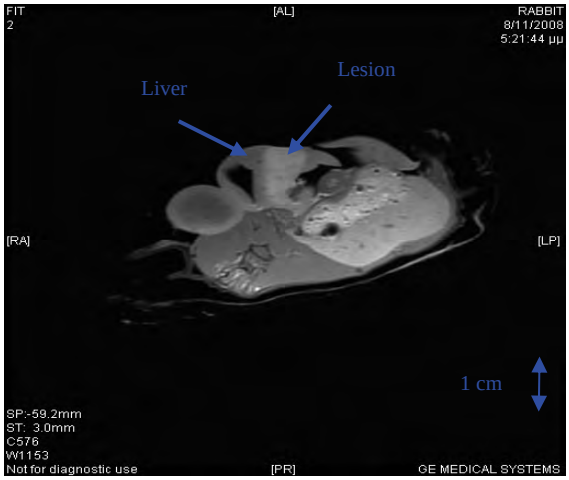

Figure 6. MRI image of the lesion of **Figure 3** using T1W FSE.

4. DISCUSSION

In this paper the goal was to measure the CNR of FSE MRI sequences in detecting thermal lesions created by HIFU in rabbit liver in vivo. Both T1-w FSE and T2-W FSE have been proven successfully for providing excellent contrast between liver and thermal lesion in rabbit in vivo.

The CNR with T1-w FSE is significantly higher than

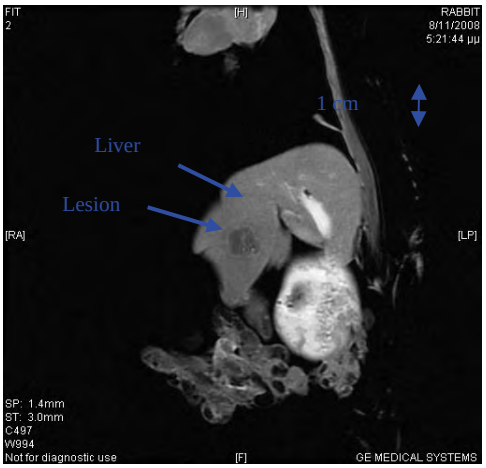

Figure 7. MRI images of the same lesion as in **Figure 3** using T2W FSE.

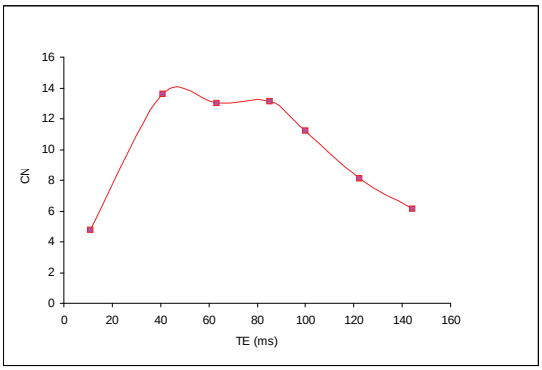

Figure 8. CNR vs TE for the MRI image shown in **Figure 7**.

T2-w FSE (25 with T1-w compared to 14 with T2-w). With T1W FSE the range of TR under which CNR is high and ranges from 400 to 900 ms. Obviously one should use TR of 400 ms in order to minimize the imaging time. Thus, the optimum TR to be used is 400 ms. The maximum contrast measured is approximately 25.

The maximum CNR obtained for liver is the highest we measured after 17 years of experience in this field. The relaxation time T1 of lesion (250 ms) is much lower than the T1 of the host tissue (liver) which is 600 ms. The greater the difference, the greater the CNR. However, one might not ignore the significant role that the value of proton density plays in the CNR. The proton density of the lesion is increased by 20%.

The trend of CNR vs TR starts to increase then it becomes flat and then at high TRs it starts to decrease again. This trend is justified because at low TR, the difference in signal intensity between lesion and liver is low at the beginning and therefore CNR is lower. At higher TR the signal intensity of lesion and tissue reaches their maxima and therefore the signal difference is lower and hence the CNR drops again.

With T2-w the range of TE that establishes maximum contrast is between 40 ms and 80 ms. This range was estimated by assuming that a CNR value of 10 is acceptable. Note that the maximum CNR value with T2-w FSE is around 14 which is much lower than the value obtained with T1-w FSE. The relaxation time T2 of lesion (35 ms) is lower than the T2 of the host tissue (liver) which is 50 ms. Therefore, in T2 W FSE the variation of signal intensity between lesion and liver is small (5%) and therefore the factor dominating the CNR in T2-w FSE is the T2 relaxation time. The trend of CNR vs TE starts to increase then it becomes flat and then at high TEs it starts to decrease again. The same explanation holds as in the case of T1-w FSE.

REFERENCES

[1] Grasso, A., Watkinson, A. F., Tibballs, J. M. *et al*. (2000) Radiofrequency ablation in the treatment of hepatocellular carcinoma-clinical viewpoint. *Journal of Hepatology*, **33**, 667-672.

[2] Livraghi, T., Lazzaroni, S., Meloni, F., Torzilli, G., and Vettori, C. (1995) Intralesional ethanol in the treatment of unresectable liver cancer. *World Journal of Surgery*, **19**, 801-806.

[3] McCall, J. L., Booth, M. W., and Morris, D. L. (1995) Hepatic cryotherapy for metastatic liver tumors. *British Journal of Hospital Medicine*; **54**, 378-381.

[4] Elias, D., De Baere, T., Smayra, T., Ouellet, J. F., Roche, A., and Lasser, P. (2002) Percutaneous radiofrequency thermoablation as an alternative to surgery for treatment of liver tumour recurrence after hepatectomy. *British Journal of Surg*, **89(6)**, 752-756.

[5] Yamanaka, N., Okamoto, E., Tanaka, T., Oriyama, T., Fujimoto, J., Furukawa, K., and Kawamura, E. (1995) Laparoscopic microwave coagulonecrotic therapy for hepatocellular carcinoma. *Surg Laparosc Endosc*, **5**, 444-449.

[6] Dick, E. A., Joarder, R., de Jode, M., Taylor-Robinson, S. D., Thomas H. C., Foster G. R., and Gedroyc, W. M. (2003) MR-guided laser thermal ablation of primary and secondary liver tumours, *Clinical Radiology*, **58(2)**, 112-120.

[7] Vogl, T. J., Straub, R., Eichler, K., Woitaschek, D., and Mack, M. G. (2002) Malignant liver tumors treated with MR imaging-guided laser-induced thermotherapy: Experience with complications in 899 patients (2,520 lesions). *Radiology*, **225(2)**, 367-377.

[8] Dodd, G. D., Soulen, M. C., Kane, R. A., Livraghi, T., Lees, W. R., Yamashita, Y., Gillams, A. R., Karahan, O. I., and Rhim, H. (2000) Minimally invasive treatment of malignant hepatic tumors: At the threshold of a major breakthrough. *Radiographics*, **20**, 9-27.

[9] Solbiati, L., Livraghi, T., Goldberg, S. N., Ierace, T., Meloni, F., Dellanoce, M., Cova, L., Halpern, E. F., Gazelle, G. S. (2001) Percutaneous radio-frequency ablation of hepatic metastases from colorectal cancer: long-term results in 117 patients. *Radiology*, **221**, 159-166.

[10] Frizzell, L., Linke, C., Carstensen, E., and Fridd, C. (1987) Thresholds for focal ultrasound lesions in rabbit kidney, liver and testicle. *IEEE Transactions on Biomedical Engineering*, **24(4)**, 393-396.

[11] Frizzell, L. (1988) Threshold dosages for damage to mammalian liver by high intensity focused ultrasound. *IEEE Transactions on Ultrasonics, Ferroelectrics and Frequency Control*, **UFFC-35**, 578-581.

[12] Ter Haar, G., Sinnett, D., and Rivens, I. (1989) High intensity focused ultrasound-a surgical technique for the teatment of discrete liver tumors. *Physics in Medicine and Biology*, **34(11)**, 1743-1750.

[13] Sibille, A., Prat, F., Chapelon, J. Y., Fadil, F. A., Henry, L., Theillere, Y., Ponchon, T., and Cathignol, D. (1993) Extracorporeal ablation of liver tissue by high-intensity focused ultrasound. *Oncology*, **50(5)**, 375-379.

[14] Chen, L., Rivens, I., ter Haar, G., Riddler, S., Hill, C. R., and Bensted, J. P. (1993) Histological changes in rat liver tumours treated with high-intensity focused ultrasound. *Ultrasound in Medicine & Biology*, **19(1)**, 67-74.

[15] Chen, L., ter Haar, G., Robertson, D., Bensted, J. P., and Hill, C. R., (1999) Histological study of normal and tumor-bearing liver treated with focused ultrasound. *Ultrasound in Medicine & Biology*, **25(5)**, 847-856.

[16] Yang, R., Reilly, C. R., Rescorla, F. J., Faught, P. R., Sanghvi, N. T., Fry, F. J., Franklin Jr, T. D., Lumeng, L., and Grosfeld, J. L. (1991) High-intensity focused ultrasound in the treatment of experimental liver cancer. *Archives of surgery*, **126(8)**, 1002-1210.

[17] Sibille, A., Prat, F., Chapelon, J. Y., abou el Fadil, F., Henry, L., Theilliere, Y., Ponchon, T., and Cathignol, D. (1993) Characterization of extracorporeal ablation of normal and tumor-bearing liver tissue by high intensity focused ultrasound. *Ultrasound in Medicine & Biology*, **19(9)**, 803-813.

[18] Prat, F., Centarti, M., Sibille, A., Fadil, F. A., Henry, L., Chapelon, J. Y., and Cathignol, D. (1995) Extracorporeal high-intensity focused ultrasound for VX2 liver tumors in the rabbit. *Hepatology*, **21(3)**, 832-836.

[19] Cheng, S. Q., Zhou, Z. D., Tang, Z. Y., Yu, Y., Wang, H. Z., Bao, S. S., and Qian, D. C. (1997) High intensity focused ultrasound in the treatment of experimental liver tumour. *Journal of Cancer Research and Clinical Oncology*, **123(4)**, 219-223.

[20] Chen, L., ter Haar, G., Hill, C.R., Eccles, S. A., and Box, G. (1998) Treatment of implanted liver tumors with focused ultrasound. *Ultrasound in Medicine & Biology*, **24(9)**, 1475-1488.

[21] Vallancien, G., Harouni, M., Veillon, B., Mombet, A., Prapotnich, D., Brisset, J. M., and Bougaran, J. (1992) Focused extracorporeal pyrotherapy: Feasibility study in man. *Journal of Endourology*, **6**, 173-181.

[22] Wu, F., Chen, W., and Bai, J. (1999) Effect of high- intensity focused ultrasound on patients with hepatocellular cancer–preliminary report. *The Chinese Journal of Ultrasonography*, **8**, 213-216.

[23] Wu, F., Wang, Z. B., Chen, W. Z., Zou, J. Z., Bai, J., Zhu, H., Li, K.Q., Xie, F. L., Jin, C. B., Su, H. B., *et al*. (2004) Extracorporeal focused ultrasound surgery for treatment of human solid carcinomas: Early Chinese clinical experience. *Ultrasound in Medicine & Biology*, **30**, 245-260.

[24] Li, C. X., Xu, G. L., Jiang, Z. Y., Li, J. J., Luo, G. Y., Shan, H. B., Zhang, R., and Li, Y. (2004) Analysis of clinical effect of high-intensity focused ultrasound on liver cancer. *World Journal of Gastroenterology*, **10**, 2201-2204.

[25] Stewart, E. A., Rabinovici, J., Tempany, C. M., Inbar, Y., Regan, L., Gostout, B., Hesley, G., Kim, H. S., Hengst, S., and Gedroyc, W. M. (2006) Clinical outcomes of focused ultrasound surgery for the treatment of uterine fibroids. *Fertility and Sterility*, **85(1)**, 22-29.

[26] Schmitz, A., Gianfelice, D., Daniel, B., Mali, W., and van den Bosch M. (2008) Image-guided focused ultrasound ablation of breast cancer: Current status, challenges, and future directions. *European Radiology*, **18**, 1431-1441.

[27] Gedroyc, W. M. (2006) Magnetic resonance guided focused ultrasound (MRgFUS) treatment of liver tumours. In: Coussios, C.C., Ed., *Proceedings of the 6th International Symposium on Therapeutic Ultrasound*, AIP, Oxford.

[28] Rowland, I. J., Rivens, I., Chen, L., Lebozer, C. H., Collins, D. J., ter Haar, G. R., and Leach, M. O. (1997) MRI study of hepatic tumours following high intensity focused ultrasound surgery. *British Journal of Radiology*, **70**, 144-153.

[29] Jolesz, F., Hynynen, K., McDannold, N., Freundlich, D., and Kopelman, D. (2004) Noninvasive Thermal Ablation of Hepatocellular Carcinoma by Using Magnetic Resonance Imaging-Guided Focused Ultrasound. *Gastroenterology*, **127**, S242-S247.

[30] Kopelman, D., Inbar, Y., Hanannel, A., Freundlich, D., Castel, D., Perel, A., Greenfeld, A., Salamon, T., Sareli, M., Valeanu, A., and Papa, M. (2006) Magnetic resonance-guided focused ultrasound surgery (MRgFUS): Ablation of liver tissue in a porcine model. *European Journal of Radiology*, **59**, 157-162.

[31] Damianou, C., Ioannides, K., and Milonas. (2008) Positioning device for MRI-guided high intensity focused ultrasound system. *Computer-Assisted Radiology and Surgery*, **2 (6)**, 335-345.

[32] Christakis, D., Pavlou, M., Velev, O., Kyriakou, K., and Trimikliniotis, M. (2004) High intensity focused ultrasound ablation of kidney guided by _RI. *Journal of Ultrasound in Medicine and Biology*, **30 (3)**, 397-404.

[33] Vykhodtseva, N., Sorrentino, V., Jolesz, F., Bronson, R. Hynynen, K. (2000) MRI detection of the thermal effects of focused ultrasound on the brain. *Ultrasound in Medicine & Biology*, **26 (5)**, 871-880.

J. Biomedical Science and Engineering, 2010, 3, 247-252 **JBiSE**
doi:10.4236/jbise.2010.33033 Published Online March 2010 (http://www.SciRP.org/journal/jbise/).

A comparison study between one-class and two-class machine learning for MicroRNA target detection

Malik Yousef[1,2,3*], Naim Najami[1,4], Waleed Khalifa[1*]

[1]The Institute of Applied Research-the Galilee Society, Shefa Amr, Israel;
[2]Computer Science, The College of Sakhnin, Sakhnin, Israel;
[3]Al-Qasemi Academic College, Baqa Algharbiya, Israel;
[4]The Academic Arab College of Education, Haifa, Israel.
Email: yousef@gal-soc.org; khwalid@hotmail.com; najamina@gmail.com

Received 9 September 2009; revised 2 November 2009; accepted 5 November 2009.

ABSTRACT

The application of one-class machine learning is gaining attention in the computational biology community. Different studies have described the use of two-class machine learning to predict microRNAs (miRNAs) gene target. Most of these methods require the generation of an artificial negative class. However, designation of the negative class can be problematic and if it is not properly done can affect the performance of the classifier dramatically and/or yield a biased estimate of performance. We present a study using one-class machine learning for miRNA target discovery and compare one-class to two-class approaches. Of all the one-class methods tested, we found that most of them gave similar accuracy that range from 0.81 to 0.89 while the two-class naive Bayes gave 0.99 accuracy. One and two class methods can both give useful classification accuracies. The advantage of one class methods is that they don't require any additional effort for choosing the best way of generating the negative class. In these cases one-class methods can be superior to two-class methods when the features which are chosen as representative of that positive class are well defined.

Keywords: MicroRNA; One-Class; Two-Class; Machine Learning

1. INTRODUCTION

MicroRNAs (miRNAs) are single-stranded, non-coding RNAs averaging 21 nucleotides in length. The mature miRNA is cleaved from a 70-110 nucleotide (nt) "hairpin" precursor with a double-stranded region containing one or more single-stranded loops. MiRNAs target messenger RNAs (mRNAs) for cleavage, primarily by repressing translation and causing mRNA degradation [1]. Although recent findings [2] suggest microRNAs may affect gene expression by binding to either 5' or 3' untranslated regions (UTRs) of mRNA, most studies have found that miRNA mark their target mRNAs for degradation or suppress their translation by binding to the 3'UTR and most target programs search there. These studies have suggested that the miRNA seed segment which includes 6-8 nt at the 5' end of the mature miRNA sequence is very important in the selection of the target site (see **Figure 1**).

Several computational approaches have been applied to miRNA gene prediction using methods based on sequence conservation and/or structural similarity [3,4,5, 6,7]. Those methods that used machine learning were based on the two-class approaches, while our new reported results are based on the one-class approaches.

Several additional methods for the prediction of miRNA targets have been subsequently developed. These methods mainly use sequence complementarities, thermodynamic stability calculations, and evolutionary conservation among species to determine the likelihood of a productive miRNA: mRNA duplex formation [8,9]. John *et al*., (2004) developed the miRanda [10] algorithm for miRNA target prediction. MiRanda uses dynamic programming to search for optimal sequence complementarities between a set of mature miRNAs and a given miRNA. Another algorithm RNAhybrid [8,9] is similar to a RNA secondary structure prediction algorithm like the Mfold program [11] but it determines the most favorable hybridization site between two sequences.

Lewis *et al*., (2005) developed TargetScanS [12]. TargetScanS scores target sites based on the conservation of the target sequences between five genomes (human, mouse, rat, dog and chicken) as evolutionarily conserved target sequences are more likely to be true targets. In testing, TargetScanS was able to recover targets for all 5300 human genes known at the time to be targeted by miRNAs.

PicTar [13] is a computational method to detect common miRNA targets in vertebrates, nematodes (*C. ele-*

```
3′ uagcgccaaauaugguuuacuua 5′ has-miR-579
   ||: |  |||||:  ||||||:|
5′ atttctttttatggaAAATGAGT 3′ LR1G3
```

Figure 1. Duplex partitioned into two parts for miRNA hsa-miR-579 and its target LRIG3, the seed part and the out-seed part. The seed part appears in capital letters.

gans), and insects (*Drosophila melanogaster*). PicTar is based on a statistical method applied to eight vertebrate genome-wide alignments (multiple alignments of orthologous nucleotide sequences (3' UTRs). PicTar was able to recover validated miRNA targets at an estimated 30% false-positive rate. In a separate study PicTar was applied to target identification in *D. melanogaster* [14]. These studies suggest that one miRNA can target 54 genes on average and that known miRNAs are projected to regulate a large fraction of all *D. melanogaster* genes (15%). This is likely to be a conservative estimate due to the incomplete input data.

TargetBoost [15] is a machine learning algorithm for miRNA target prediction using only sequence information to create weighted sequence motifs that capture the binding characteristics between miRNAs and their targets. The authors suggest that TargetBoost is stable and identifies more of the already verified true targets than do other existing algorithms.

Sung-Kyu *et al*., (2005), also reported the development of a machine learning algorithm using Support Vector Machine (SVM). The best reported results [16] were 0.921 sensitivity and 0.833 specificity. More recently Yan and others, used a machine learning approach that employs features extracted from both the seed and out-seed segments [17]. The best result obtained was an accuracy of 82.95% but it was generated using only 48 positive human and 16 negative examples, a relatively small training set to assess the algorithm.

In 2006, Thadani and Tammi [18] launched MicroTar, a novel statistical computational tool for prediction of miRNA targets from RNA duplexes which does not use sequence homology for prediction. MicroTar mainly relies on a quite novel approach to estimate the duplex energy. However, the reported sensitivity (60%) is significantly lower than that achieved using other published algorithms. At the same time, a miRNA pattern discovery method, RNA22 [19] was proposed to scan UTR sequences for targets. RNA22 does not rely upon cross-species conservation but was able to recover most of the known target sites with validation of some of its new predictions.

More recently, Yousef *et al*., (2007) described a target prediction method, (NBmiRTar [20]) using instead machine learning by a Naïve Bayes classifier. NBmiRTar does not require sequence conservation but generates a model from sequence and miRNA:mRNA duplex information derived from validated target sequences and artificially generated negative examples. In this case, both the seed and "out-seed" segments of the miRNA:mRNA duplexes are used for target identification. NBmiRTar technique produces fewer false positive predictions and fewer target candidates to be tested than miRanda [10]. It exhibits higher sensitivity and specificity than algorithms that rely only on conserved genomic regions to decrease false positive predictions.

This paper describes a comparison study of using one-class and two-class approaches for miRNA target detection. The advantage of one class methods is that they don't require any additional effort for choosing the best way of generating the negative class while it is clear that the two class approaches performances are outperform the one-class methods.

2. METHODS

2.1. Designing Duplex Structure and Sequence Features

Machine learning enables one to generate automatic rules based on observation of the appropriate examples by the learning machine. However, the selection and design of the features that will be considered in order to represent each example for the learning process are very important and influence the classifier performance. We have followed [20] for feature design. We have partitioned the duplex into two parts, the seed (5' 8nt of the miRNA) and out-seed (3' remainder) as described in **Figure 1**. For each of these parts the following features are extracted to give 57 structural features: 1) the number of paired bases (bp), 2) The number of bulges (inserts on one strand between paired bases), 3) the number of loops (unpaired bases opposite each other between paired bases), 4) the number of asymmetric loops (loops with unequal numbers of unpaired bases on the two strands), 5) eight features, each representing the number of bulges of lengths 1-7 and those with lengths greater than 7. 6) Eight features, each representing the number of symmetric loops with lengths 1-7 and those with lengths greater than 7, 7) eight features each representing the number of asymmetric loops with lengths 1-7 and those with lengths greater than 7, 8) the distance from the start of the seed (the 3' end) to the first paired base of the 5' start of the out-seed part is an additional feature that is extracted. For the sequence features, we define "words" as sequences having lengths equal to or less than 3. The frequency of each word in the seed part

is extracted to form a representation in the vector space.

2.2. One-Class Methods

In general a binary learning (two-class) approach to miRNA discovery considers both positive (miRNA) and negative (non-miRNA) classes by providing examples for the two-classes to a learning algorithm in order to build a classifier that will attempt to discriminate between them. The most common term for this kind of learning is *supervised learning* where the labels of the two-classes are known before hand. One-class uses only the information for the target class (positive class) building a classifier which is able to recognize the examples belonging to its target and rejecting others as outliers.

Among the many classification algorithms available, we chose five one-class algorithms to compare for miRNA discovery. We give a brief description of each one-class classifier and we refer the references [21,22] for additional details including a description of parameters and thresholds. The LIBSVM library [23] was used as implementation of the SVM (one-class using the RBF kernel function) and the DDtools [24] for the other one-class methods. The WEKA software [25] was used as implementation of the two-class classifiers.

2.3. One-Class Support Vector Machines (OC-SVM)

Support Vector Machines (SVMs) are a learning machine developed as a two-class approach [26,27]. The use of one-class SVM was originally suggested by [22]. One-class SVM is an algorithmic method that produces a prediction function trained to "capture" most of the training data. For that purpose a kernel function is used to map the data into a feature space where the SVM is employed to find the hyper-plane with maximum margin from the origin of the feature space. In this use, the margin to be maximized between the two classes (in two-class SVM) becomes the distance between the origin and the support vectors which define the boundaries of the surrounding circle, (or hyper-sphere in high-dimensional space) which encloses the single class.

2.4. One-Class Gaussian (OC-Gaussian)

The Gaussian model is considered as a density estimation model. The assumption is that the target samples form a multivariate normal distribution, therefore for a given test sample z in n-dimensional space, the probability density function can be calculated as:

$$p(z) = \frac{1}{(2\Pi)^{n/2}\left|\Sigma\right|^{1/2}} e^{(-1/2(z-\mu)^T \Sigma^{-1}(z-\mu)} \quad (1)$$

where μ and $\sum$ are the mean and covariance matrix of the target class estimated from the training samples.

2.5. One-Class Kmeans (OC-Kmeans)

Kmeans is a simple and well-known unsupervised machine learning algorithm used in order to partition the data into *k* clusters. Using the OC-Kmeans we describe the data as *k* clusters, or more specifically as *k* centroids, one derived from each cluster. For a new sample, *z*, the distance *d*(*z*) is calculated as the minimum distance to each centroid. Then based on a user threshold, the classification decision is made. If *d*(*z*) is less than the threshold the new sample belongs to the target class, otherwise it is rejected.

2.6. One-Class Principal Component Analysis (OC-PCA)

Principal component analysis (PCA) is a classical statistical method known as a linear transform that has been widely used in data analysis and compression. Mainly PCA is a projection method used for reducing dimensionality in a given dataset by capturing the most variance by a few orthogonal subspaces called principal components (PCs). For the one-class approach (OC-PCA) one needs to build the PCA model based on the training set and then for a given test example z the distance to the PCA(z) model is calculated and used as a decision factor for acceptance or rejection.

2.7. One-Class K-Nearest Neighbor (OC-KNN)

The one-class nearest neighbor classifier (OC-KNN) is a modification of the known two-class nearest neighbor classifier which learns from positive examples only. The algorithm operates by storing all the training examples as its model, then for a given test example z, the distance to its nearest neighbor *y*(*y*=*NN*(*z*)) is calculated as *d*(*z*,*y*). The new sample belongs to the target class when:

$$\frac{d(z,y)}{d(y,NN(y))} < \delta \quad (2)$$

where *NN*(*y*) is the nearest neighbor of y, in other words, it is the nearest neighbor of the nearest neighbor of *z*. The default value of δ is 1. The average distance of the *k* nearest neighbors is considered for the OC-KNN implementation.

3. TWO CLASS METHODS

3.1. Naïve Bayes

Naïve Bayes is a classification model obtained by applying a relatively simple method to a training dataset [28]. A Naïve Bayes classifier calculates the probability that a given instance (example) belongs to a certain class. It makes the simplifying assumption that the features

constituting the instance are conditionally independent given the class. Given an example X, described by its feature vector (x1,...,xn), we are looking for a class C that maximizes the likelihood: $P(X \mid C) = P(x_1,...,x_n \mid C)$. The (naïve) assumption of conditional independence among the features, given the class, allows us to express this conditional probability $P(X \mid C)$ as a product of simpler probabilities: $P(X \mid C) = \prod_{i=1}^{n} P(x_i \mid C)$.

We used the Rainbow program [29] to train the naïve Bayes classifier. To combine the numeric features identified in the miRNA-target duplex with the sequence features ("words") in the target candidate sequence, a dictionary of all the unique "words" was generated and the frequency of each "word" in the sequence is used.

3.2. Support Vector Machines (SVMs)

Support Vector Machines (SVMs) is a learning machine developed by Vapnik [27]. The performance of this algorithm, as compared to other algorithms, has proven to be particularly useful for the analysis of various classification problems, and has recently been widely used in the bioinformatics field [30,31,32]. Linear SVMs are usually defined as SVMs with linear kernel. The training data for linear SVMs could be linear non-separable and then soft-margin SVM could be applied. Linear SVM separates the two classes in the training data by producing the optimal separating hyper-plane with a maximal margin between the class 1 and class 2 samples. Given a training set of labeled examples (x_i, y_i), i = 1,…, ℓ where $x_i \in R^t$ and $y_i \in \{+1,-1\}$, the support vector machines (SVMs) find the separating hyper-plane of the form $w \cdot x + b = 0$ $w \in R^t, b \in R$. Here, w is the "normal" of the hyper-plane. The constant b defines the position of the hyper-plane in the space. One could use the following formula as a predictor for a new instance: $f(x) = sign(w \cdot x + b)$ for more information see Vapnik [27].

3.3. Random Forest

Random forests are a ensemble of tree predictors such that each tree depends on the values of a random vector sampled independently and with the same distribution for all trees in the forest [33]. The improvement in the classification accuracy is due to the growing or an ensemble of tress that vote for the most popular class. Random forests are becoming increasingly popular because their ability to deal with small sample size with high-dimensional space.

3.4. C4.5

C4.5 is a decision tree algorithm, developed by Quinlan (1993)[34]. A decision tree is a simple structure where non-terminal nodes represent tests on one or more attributes and terminal nodes reflect decision outcomes.

4. RESULTS

4.1. Data

A collection of 326 confirmed MicroRNA targets (human, mouse, fruit fly worm and virus) were downloaded from the TarBase [35] (TarBase_V4, Tarbase flat file data as of 04/2007) web-site to serve as positive examples and 1,000 negative examples chosen at random from the negative class pool generated at the study of NBmiRTar [20].

To evaluate classification performance, we used the data generated from the positive class and 1,000 negative examples. The negative class is not used for training of the one-class classifiers, but merely for estimating the specificity performance

Each one-class algorithm was trained using 90% of the positive class and the remaining 10% was used for sensitivity evaluation. The randomly selected 1,000 negative examples were used for the evaluation of specificity. The whole process was repeated 100 times in order to evaluate the stability of the methods. Additionally, the Matthews Correlation Coefficient (MCC) [36] measurement is used to take into account both over-prediction and under-prediction in imbalanced data sets. It is defined as:

$$MCC = \frac{(TpTn - FpFn)}{\sqrt{(Tp + Fp)(Tp + Fn)(Tn + Fn)(Tn + Fp)}}$$

5. DISCUSSION

The one-class approach in machine learning has been receiving more attention particularly for solving problems where the negative class is not well defined [37,38,39,40]; moreover, the one class approach has been successfully applied in various fields including text mining [41], functional Magnetic Resonance Imaging (fMRI) [42] ,signature verification [43] and miRNA gene discovery [44].

This paper describes a comparison study of using one-class and two-class approaches for miRNA target detection. The advantage of one class methods is that they don't require any additional effort for choosing the best way of generating the negative class while it is clear that the two class approaches performances are outperform the one-class methods.

Table 1 shows the performance of five one-class classifiers while **Table 2** shows the performances of two-class methods. The results of the one-class approaches show a slight superiority for OC-Kmeans over the other one class methods based on the average of the MCC measurement. The MCC measurement with value of +1 represents a perfect prediction while 0 value indicates an average random prediction. However, accuracy is less

Table 1. One-Class results.

Method	TP	TN	ACC	MCC
OC-SVM	0.91	0.779	0.81	0.69
OC-Gaussian	0.86	0.89	0.89	0.75
OC-Kmeans	0.90	0.87	0.87	0.77
OC-PCA	0.77	0.77	0.77	0.55
OC-Knn	0.87	0.89	0.89	0.76

Tbale 2. Two class results.

Method	TP	TN	Acc	MCC
Naïve Bayes	0.93	0.99	0.99	0.93
SVM	0.98	0.9974	99.3	0.977
KNN4	0.858	0.952	92.88	0.813
C4.5	0.912	0.978	96.23	0.89
Random Forest	0.958	0.993	98.44	0.951

than the two-class approaches. During the training stage of the one-class classifier we have set the 10% of the positive data, whose likelihood is furthest from the true positive data based on the distribution, as “outliers” in order to produce a compact classifier. This factor might cause a loss of information about the target class which might also result in reducing performance compared to the two class approach.

6. CONCLUSIONS

The current results show that it is possible to build up a classifier based only on positive examples yielding a reasonable performance. Moreover, more efforts are required to figure out more biological features to be used in the design of the one-class classifier to improve the performance. However, we hypothesize that taken 10% of the training data as “outlier” is the cause of reducing the one-class performance.

7. ACKNOWLEDGEMENTS

This project is funded in part under a grant with the ESHKOL scholarship program of the ministry of science culture and sport to support KW.

REFERENCES

[1] Bartel, D.P. (2004) MicroRNAs: Genomics, Biogenesis, Mechanism, and Function. *Cell*, **116**, 281-297.

[2] Lytle, J.R., Yario, T.A. and Steitz, J.A. (2007) Target mRNAs are repressed as efficiently by microRNA-binding sites in the 5²€ UTR as in the 3²€ UTR. *Proceedings of the National Academy of Sciences*, **104**, 9667-9672.

[3] Lim, L.P., Glasner, M.E., Yekta, S., Burge, C.B. and Bartel, D. P. (2003) Vertebrate MicroRNA Genes. *Science*, **299**, 1540.

[4] Lim, L.P., Lau, N.C., Weinstein, E.G., Abdelhakim, A., Yekta, S., Rhoades, M.W., Burge, C.B. and Bartel, D.P. (2003) The microRNAs of Caenorhabditis elegans. *Genes & Development*, **17**, 991-1008.

[5] Weber, M.J. (2005) New human and mouse microRNA genes found by homology search. *FEBS Journal*, **272**, 59-73.

[6] Lai, E., Tomancak, P., Williams, R. and Rubin, G. (2003) Computational identification of Drosophila microRNA genes. *Genome Biology*, **4**, R42.

[7] Grad, Y., Aach, J., Hayes, G.. D., Reinhart, B. J., Church, G.M., Ruvkun, G. and Kim, J. (2003) Computational and Experimental Identification of C. elegans microRNAs. *Molecular Cell*, **11**, 1253-1263.

[8] Bartel, D. P. (2004) MicroRNAs: Genomics, Biogenesis, Mechanism, and Function. *Cell*, **116**, 281.

[9] Lai, E. (2004) Predicting and validating microRNA targets. *Genome Biology*, **5**, 115.

[10] John, B., Enright, A.J., Aravin, A., Tuschl, T., Sander, C. and Marks, D.S. (2004) Human MicroRNA Targets. *PLoS Biology*, **2**, e363.

[11] Zuker, M. (2003) Mfold web server for nucleic acid folding and hybridization prediction. *Nucleic acids research*, **31 (13)**, 3406–3415.

[12] Lewis, B. P., Shih, I. H., Jones-Rhoades, M. W., Bartel, D. P. and Burge, C. B. (2003) Prediction of mammalian microRNA targets. *Cell*, **115**, 787.

[13] Krek, A. *et al*. (2005) Combinatorial microRNA target predictions. *Nature Genetics*, **37**, 495-500.

[14] Grun, D., Wang, Y.L., Langenberger, D., Gunsalus, K.C. and Rajewsky, N. (2005) MicroRNA target predictions across seven drosophila species and comparison to mammalian targets. *PLoS Computational Biology*, **1**, e13.

[15] SaeTrom, O.L.A., Snove, O.J. and SaeTrom, P.A.L. (2005) Weighted sequence motifs as an improved seeding step in microRNA target prediction algorithms. *RNA*, **11**, 995-1003.

[16] Sung-Kyu, K., Jin-Wu, N., Wha-Jin, L. and Byoung-Tak, Z. (2005) A kernel method for microrna target prediction using sensible data and position-based features. In computational intelligence in bioinformatics and computational biology. *Proceedings of the 2005 IEEE Symposiumon CIBCB*, 1-7.

[17] Yan, X., *et al*. (2007) Improving the prediction of human microRNA target genes by using ensemble algorithm. *FEBS Letters*, **581**, 1587.

[18] Thadani, R. and Tammi, M. (2006) MicroTar: Predicting microRNA targets from RNA duplexes. *BMC Bioinformatics*, **7**, S20.

[19] Miranda, K.C., Huynh, T., Tay, Y., Ang, Y.S., Tam, W.L., Thomson, A. M., Lim, B. and Rigoutsos, I. (2006) A pattern-based method for the identification of microrna binding sites and their corresponding. *Heteroduplexes*, **126**, 1203-1217.

[20] Yousef, M., Jung, S., Kossenkov, A.V., Showe, L.C. and Showe, M.K. (2007) Naive Bayes for microRNA target predictions machine learning for microRNA targetsed. Oxford University Press, 2987-2992.

[21] Tax, D.M.J. (2001) One-class classification; Concept-learning in the absence of counter-examples. Delft University of Technology ed.

[22] Schölkopf, B., Platt, J.C., Shawe-Taylor, J., Smola, A.J. and Williamson, R. C. (2001) Estimating the support of a

high-dimensional distribution. *Neural Computation*, **13**, 1443-1471.

[23] Chang, C.C. and Lin, C.J. (2001) LIBSVM: A library for support vector machinesed.

[24] Tax, D.M.J. (2005) DDtools, the data description toolbox for matlab. Delft University of Technology ed.

[25] Witten, I.H. and Frank, E. (2005) Data mining: Practical machine learning tools and techniques, Morgan Kaufmann, San Francisco.

[26] Schölkopf, B., Burges, C.J.C. and Smola, A.J. (1999) Advances in kernel methods. MIT Press, Cambridge.

[27] Vapnik, V. (1995) The Nature of Statistical Learning Theory, Springer.

[28] Mitchell, T. (1997) Machine Learning, McGraw Hill.

[29] McCallum, A.K. (1996) Bow: A toolkit for statistical language modeling, text retrieval, classification and clustering text retrieval, classification and clustering.

[30] Haussler, D. (1999) Convolution kernels on discrete structuresed, Technical Report UCSCCRL-99-10. Baskin School of Engineering, University of California, Santa Cruz.

[31] Pavlidis, P., Weston, J., Cai, J. and Grundy, W.N. (2001) Gene functional classification from heterogeneous data. *Proceedings of the* 5*th Annual International Conference on Computational Biology*, ACM Press, Montreal, 249-255.

[32] Donaldson, I. *et al.* (2003) PreBIND and Textomy-mining the biomedical literature for protein-protein interactions using a support vector machine. *BMC Bioinformatics*, **4**, 11.

[33] Breiman, L. (2001) Random Forests. Machine Learning **45**, 5-32.

[34] Quinlan, J.R. (1993) C4.5: Programs for machine learning Morgan Kaufmann Publishers Inc.

[35] Sethupathy, P., Corda, B. and Hatzigeorgiou, A.G. (2006) TarBase: A comprehensive database of experimentally supported animal microRNA targets. *RNA*, **12**, 192-197.

[36] Matthews, B. (1975) Comparison of the predicted and observed secondary structure of T4 phage lysozyme. *Biochim Biophys Acta*, **405(2)**, 442-451.

[37] Kowalczyk, A. and Raskutti, B. (2002) One class SVM for yeast regulation prediction. *SIGKDD Explorations*, **4**, 99-100.

[38] Spinosa, E.J. and Carvalho, A.C.P.L.F.d. (2005) Support vector machines for novel class detection. *Bioinformatics Genetics and Molecular Research*, **4**, 608-615.

[39] Crammer, K. and Chechik, G. (2004) A needle in a haystack: Local one-class optimization. *Proceedings of the* 21*st International Conference on Machine Learning*, Banff, 26.

[40] Gupta, G. and Ghosh, J. (2005) Robust one-class clustering using hybrid global and local search. *Proceedings of the* 22*nd International Conference on Machine Learning*, ACM Press, Bonn, 273-280.

[41] Manevitz, L.M. and Yousef, M. (2001) One-class SVMs for document classification. *Journal of Machine Learning Research*, 139-154.

[42] Thirion, B. and Faugeras, O. (2004) Feature characterization in fMRI data: The information bottleneck approach. *Medical Image Analysis*, **8**, 403.

[43] Koppel, M. and Schler, J. (2004) Authorship verification as a one-class classification problem. *Proceedings of the* 21*st International Conference on Machine Learning*, ACM Press, Banff, 62.

[44] Yousef, M., Jung, S., Showe, L. and Showe, M. (2008) Learning from positive examples when the negative class is undetermined-microRNA gene identificationed. *Algorithms for Molecular Biology*, **3**, 2.

J. Biomedical Science and Engineering, 2010, 3, 253-261 **JBiSE**
doi:10.4236/jbise.2010.33034 Published Online March 2010 (http://www.SciRP.org/journal/jbise/).

Extracting a seizure intensity index from one-channel EEG signal using bispectral and detrended fluctuation analysis

Pegah Tayaranian Hosseini[1]*, Reza Shalbaf [2]*, Ali Motie Nasrabadi[3]

[1]Biomedical Engineering Department, Amirkabir University of Technology, Tehran, Iran;
[2]Electrical Engineering Department, Iran University of Science and Technology, Tehran, Iran;
[3]Biomedical Engineering Department, Faculty of Engineering, Shahed University, Tehran, Iran.
Email: p_hosseini@aut.ac.ir; rshbme@yahoo.com

Received 7 December 2009; revised 20 December 2009; accepted 28 December 2009.

ABSTRACT

Epilepsy is a medical condition that produces seizures affecting a variety of mental and physical functions. Seizures can last from a few seconds to a few minutes. They can have many symptoms, from convulsions and loss of consciousness to blank staring, lip smacking, or jerking movements of arms and legs. If early warning signals of an upcoming seizure (diagnosis of preictal period) are detected, proper treatment can be applied to the patient to help prevent the seizure. In this research, an epileptic disorder has been divided into three subsets: Normal, Preictal (just before the seizure), and Ictal (during seizure). By using Detrended Fluctuation Analysis (DFA), Bispectral Analysis (BIS), and Standard Deviation (SD) three features from single-channel EEG signals have been derived in the foresaid groups. A fuzzy classifier is used to separate the three groups which can successfully separate them with a separation degree of 100% and further a fuzzy inference engine is used to extract a Seizure Intensity Index (SII) from the Electroencephalogram (EEG) signals of the three different states. One can apparently see the distinction of SII amounts between the three states. It is more important when one remembers that these results are just from single-channel EEG signal.

Keywords: Epilepsy; Fuzzy Inference Engine; Bispectrum; Detrended Fluctuation Analysis

1. INTRODUCTION

Epilepsy is a brain disorder in which clusters of nerve cells or neurons in the brain, sometimes, signal abnormally. In epilepsy, the normal pattern of neuronal activity becomes disturbed, causing strange sensations, emotions, and behavior or sometimes convulsions, muscle spasms, and loss of consciousness. Epilepsy is a disorder with many possible causes. Epilepsy may develop because of an abnormality in brain wiring, an imbalance of nerve signaling chemicals called neurotransmitters, or some combination of these factors. EEGs and brain scans are common diagnostic tests for epilepsy.

Once epilepsy is diagnosed, it is important to begin treatment as soon as possible. For about 80 percent of those diagnosed with epilepsy, seizures can be controlled with modern medicines and surgical techniques. Some antiepileptic drugs can interfere with the effectiveness of oral contraceptives. Scientists are studying potential antiepileptic drugs with the goal of enhancing treatment for epilepsy. Once a seizure is predicted, antiepileptic drugs could be injected to prevent the seizure.

In this research, the brain situation of an epileptic patient has been divided into 3 states: Normal (normal brain state), Preictal (just before the seizure), and Ictal (during seizure). Here, a technique to calculate a two digit index that can distinctly separate these three states during patient monitoring is seeked: a two digit index that can represent the brain state of the patient.

Bispectral (BIS) analysis is an advanced signal processing technique that quantifies quadratic nonlinearities (phase-coupling) among the components of a signal. There are only a few reports concerning the bispectrum of electroencephalogram (EEG). Barnett *et al*. first reported the bispectral analysis of EEG in 1971. Sigl and Chamoun introduced the detailed principle and concept of bispectral analysis in 1994. Ning and Bronzino reported the changes of bispectrum of the rat EEG during various vigilance states. Muthuswamy *et al*. reported the bispectral analysis of burst patterns in EEG. This information is represented in [1]. In [2] bispectrum is used to predict epileptic seizures. Tallach *et al*. tried to monitor seizures using bispectral index in [3] and Ye *et al*. represented an anesthesia index using bispectral analysis in [4]. There are, therefore, not many researches concerning bispectrum for seizure detection. This analysis has been introduced in this article and it has been used to extract a BIS feature. One can further see the application

*The two authors contributed equally to this work.

of this feature in Seizure Intensity Index (SII) calculation.

Nonlinear dynamical analysis has emerged as a novel method for the study of complex systems in the past few decades. Besides BIS, a nonlinear technique called Detrended Fluctuation Analysis (DFA) is introduced and this method is used to derive another feature from single-channel EEG for SII computation process. DFA was invented by Peng [5] and established as an important tool for the detection of long-range (auto-) correlations in time series with non-stationarities. In [6] DFA is used to extract a depth of anesthesia index. It is also used in [7] to measure the depth of anesthesia. One of DFA's most important recent applications is in anesthesia index detection while there is no significant record showing its application in epileptic seizure detection or prediction.

These two features (BIS and DFA) are used separately along with Standard Deviation (SD) to classify the three mentioned groups in this research. A fuzzy classifier with distinct characteristics is utilized to well classify the three states. A fuzzy inference engine is further used to produce a Seizure Intensity Index (SII).

Using the database of Andrzejak [8] and a leave-Bone-out technique, we came to 100% separation between the three classes for SD and DFA combination and 98% for SD and BIS combination. We further extract the mentioned index that can well represent the different states of the brain especially in case of SD and DFA combination. These results become more considerable when we remember that the dataset includes single-channel EEG signals. This means that monitoring of seizure situation can be easily performed with a two-electrode EEG recorder.

The outline of the paper is as follows: in the next section, the complete information of the used database is presented. Section 3 describes the algorithms applied on the mentioned database. The results and a conclusion of the whole article are represented in Sections 4 and 5, respectively.

2. DATABASE

In this research, the data described in [8] is used, which is publicly available. In this section, we restrict ourselves to only a short description and refer to [8] for further details. The complete dataset consists of five sets (denoted A-E), each containing 100 single-channels EEG signals of 23.6s with sample frequency of 173.6Hz.

Sets A and B have been taken from surface EEG recordings of five healthy volunteers with eyes open and closed, respectively. Signals in two sets have been measured in seizure-free intervals from five patients in the epileptogenic zone (D) and from the hippocampal formation of the opposite hemisphere of the brain (C). Set E contains seizure activity, selected from all recording sites exhibiting ictal activity. Sets A and B have been recorded extra cranially whereas sets C, D, and E have been recorded intra cranially.

In the present study, the three datasets (A, C, E) of the complete database are classified.

3. PROPOSED ALGORITHMS

The major algorithms which are utilized in this study are described in the following subsections. The explanations are represented along with our specified amounts of the parameters in the whole research.

3.1. Detrended Fluctuation Analysis

In the analysis of EEG data, different chaotic measures such as correlation dimension, Lyapunov exponent and entropy have been used in recent years. These methodologies have been under question for several reasons. In general, the brain as a complex system is not expected to produce an activity which can be described by a low dimensional dynamic. Furthermore, if the existence of a sufficiently low-dimensional attractor is assumed, for a reliable estimation of the fractal dimension, a time series must satisfy the requirements such as stationarity, a sufficiently large number of data points, and a reasonable signal-to-noise ratio. It is very improbable that these necessities are simultaneously met in the case of the EEG signal.

However, as the statistical characteristics of biological signals often change with time, and are typically highly irregular and non-stationary, analyses of such systems are complicated. To overcome these limitations we have focused on the long-range power-law correlations, which have been discovered in a wide variety of systems, including those that are physiological. The quantification of power-law correlations, with a critical exponent, may give useful information on understanding the properties of the nonlinear dynamic systems. In this paper, we have proposed an optimal nonlinear analysis algorithm for processing the EEG signals without being concerned about the non-stationarity and finite length of the signal. The fractal-scaling exponents that quantify the power-law correlations are computed by DFA which is known for its robustness against nonstationarity in [6].

According to [6] and [9], the stepwise algorithm of DFA is as follows:

1) n is set to 3.

2) 10s epoch of EEG signal x is considered. Its size N is 10×173.6 samples.

3) The average of the epoch is subtracted from each sample of the epoch.

4) An integral of the signal is calculated using (1):

$$y(j)=\sum_{i=1}^{j} x(i) \tag{1}$$

5) y is divided into n-sample epochs without overlapping. So y is divided into $K=N/n$ epochs and each epoch is named as y_k.

6) The linear trend of y_k (k = 1,…,K) is calculated and named as y_{fit}.

7) y_{fit} is subtracted from y_k and the variance of the resulted amounts is calculated as (2):

$$F^2(k)=\frac{1}{n}\sum_{i=1}^{n}\left(y_k(i)-y_{\text{fit}}(i)\right)^2 \quad (2)$$

8) The fluctuations of n is computed as the average of variances using (3):

$$F(n)=\left(\frac{1}{k}\sum_{k=1}^{K}F^2(k)\right)^{1/2} \quad (3)$$

9) n is increased one unit and the steps from 5 to 8 are repeated till n = 30.

10) The curve of lg($F(n)$) via lg(n) is plotted and the slope of this curve is considered as the DFA feature of the 10s epoch.

11) The next 10s epoch is extracted without overlapping and the steps 3 to 10 are repeated till we get to the end of EEG signal.

The steps explained above are shown consecutively in **Figure 1** and **Figure 2**. **Figure 1(a)** represents the original signals, **Figure 1(b)** shows the integral of original signals using (1), and **Figure 1(c)** displays the signals in 1(b) along with their linear trends (y_k and y_{fit}) for 50-point epochs. **Figure 2** represents the curves of F_n via n. These slopes of these curves are the DFA features.

This should be noted that, in each 10s epoch, for different amounts of n, if the last epoch has fewer samples than n, this epoch is eliminated and is not considered in future calculations.

3.2. Bispectral Analysis

Bispectral (BIS) analysis is an advanced signal processing technique that quantifies quadratic nonlinearities (phase-coupling) among the components of a signal. There are only a few reports concerning the bispectrum of electroencephalogram (EEG) [1]. The number of articles concerning the bispectrum of EEG in seizure analysis is rare [2,3]. In this paper, the BIS analysis is used to derive a feature from single-channel EEG signal. This feature is further used to produce an index for seizure situation in epileptic patients.

Each bispectrum value is calculated as follows:

$$TP_j(f_1,f_2)=X_j(f_1).X_j(f_2).X_j^*(f_1+f_2) \quad (4)$$

$$B(f_1,f_2)=\left|\sum_j TP_j(f_1,f_2)\right| \quad (5)$$

Complex numbers, $X(f_1)$, $X(f_2)$, and $X(f_1+f_2)$ are power spectrum components by FFT. $X^*(f)$ is the conjugate of $X(f)$. TP_j is called triple product. The summation in (5) is the heart of the bispectral analysis [1].

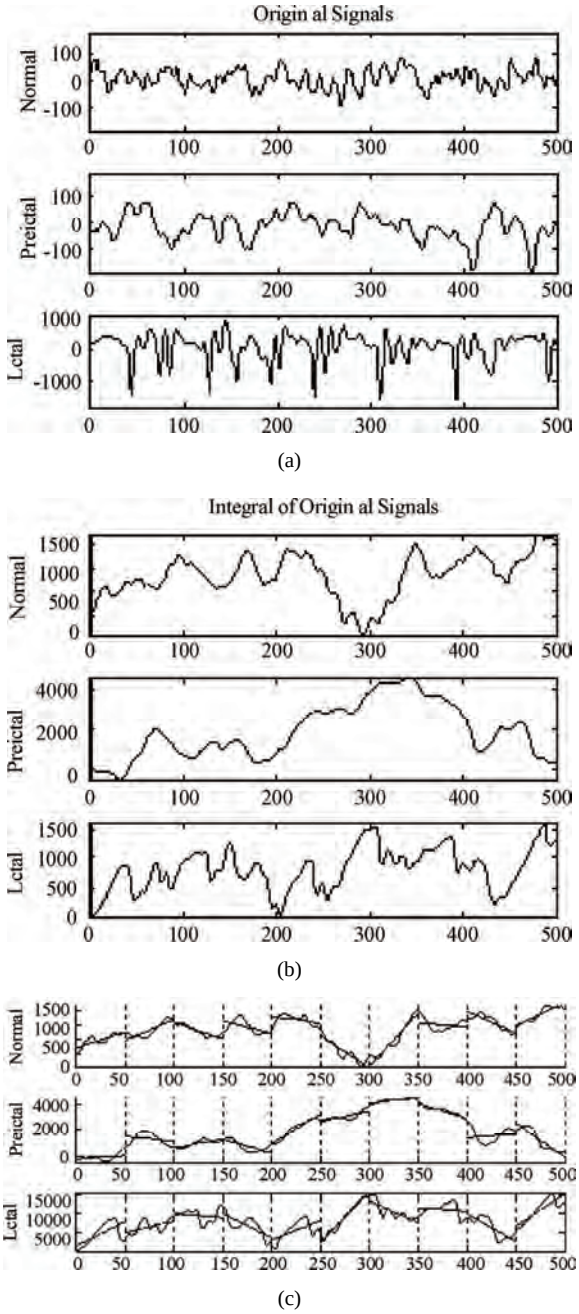

(a)

(b)

(c)

Figure 1. (a) Original EEG signals; (b) Integral of signals in 1(a); (c) the signals in 1(b) along with their linear trends for 50-point epochs.

For each group of signals (Normal, Preictal, and Ictal) the bispectrum scheme was similar for different signals. It means the coordinates of higher peaks were approximately in the same position for different signals in one group.

Inspiring from [4], for each signal, the 10 higher peaks are selected. Among these 10 peaks, the peaks that have an amount more than 15% of the highest peak are chosen. The Euclidean distances of the chosen peaks

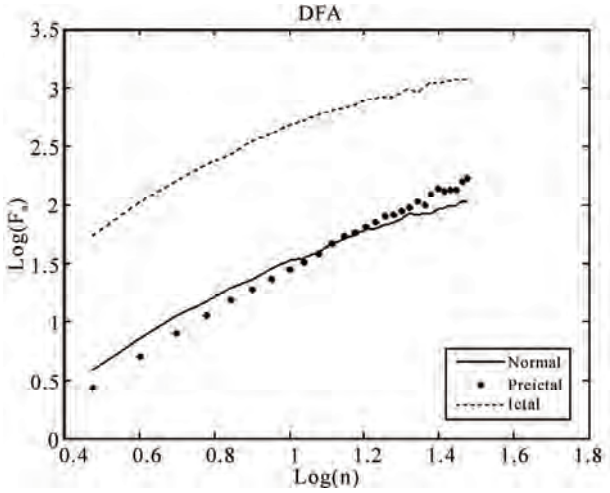

Figure 2. The F_n curves of the EEG signals of **Figure 1(a)** for different n's. Their slopes are the final DFA features.

from zero are calculated and summed together. The final amount is considered as the BIS feature of that signal.

3.3. Fuzzy Inference Engine

In this section, we briefly describe the fuzzy classification method based on fuzzy if-then rules proposed in [10,11,12,13].

Designing membership functions (MF's) is the fundamental stage in constructing a fuzzy classifier. MF's should partition the input space efficiently such that the different subsets of training patterns can be well learned by the classifier [13]. In the present study, input membership functions are designed with respect to the data distribution pattern over each dimension (the box plots of the obtained features are represented in Section 4).

Figure 3 shows the membership functions that were used for BIS, DFA, and SD inputs. As described later, the proposed fuzzy procedure has 2 inputs. Once the inputs are DFA and SD and the other time they are BIS and SD.

The proposed fuzzy rule-based classification system consists of N fuzzy if-then rules each of which has a form as in (6):

$$\begin{aligned} &Rule\ R_j: If\ x_1\ is\ A_{j1}\ and\ ...\ and\ x_n\ is \\ &A_{jn}\ then\ class\ is\ C_j\ with\ CF_j,\ j=1,2,...,N, \end{aligned} \tag{6}$$

where R_j is the label of the j-th fuzzy if-then rule, $A_{j1},\ldots$, A_{jn} are antecedent fuzzy sets on the input range, C_j is the consequent class (*i.e.* one of the M given classes), and CF_j is the grade of certainty of the fuzzy if-then rule R_j.

There are two steps in the generation of fuzzy if-then rules: specification of antecedent part and determination of consequent class C_j and the grade of certainty CF_j. The antecedent part of fuzzy if-then rules is specified manually. Then the consequent part (*i.e.* consequent class and the grade of certainty) is determined from the given training patterns [12].

Let us assume that m training patterns x_p= (x_{p1}, …, x_{pn}), p=1 ,…, m, are given for an n-dimensional C-class pattern classification problem. It is also assumed that a weight w_p, p=1, …, m, is assigned to each training pattern a priori. The consequent class C_j and the grade of certainty CF_j of the if-then rule are determined in the following manner:

Step 1: Calculate $\beta_{Class\ h}(j)$ for Class $\hat{h}$ as (7):

$$\beta_{Class\ h}(j)=\sum_{x_p\in Class\ h}\mu_j(x_p)\cdot w_p \tag{7}$$

where,

$$\mu_j(x_p)=\mu_{j1}(x_{p1})\times\ldots\times\mu_{jn}(x_{pn}) \tag{8}$$

and μ_{jn} is the membership function of the fuzzy set A_{jn}. In this paper, the fuzzy sets are used as in **Figure 3**.

Step 2: Find the Class h that has the maximum value of $\beta_{Class\ h}(j)$:

$$\beta_{Class\ \hat{h}}(j)=\max_{1\le k\le M}\{\beta_{Class\ k}(j)\} \tag{9}$$

This should be noted that this fuzzy rule generation method can also be applied to the standard pattern classification problem where there are no pattern weights. In this case, the class and the grade of certainty are determined from training patterns by specifying a pattern weight as w_p=1 for p=1,…, m.

If two or more classes take the maximum value, the consequent class C_j of the rule R_j cannot be determined uniquely. In this case, specify C_j as C_j= ϕ. If a single class $\hat{h}$ takes the maximum value, let C_j be class $\hat{h}$. The grade of certainty CF_j is determined as (10):

$$CF_j=\frac{\beta_{Class\ \hat{h}}(j)-\overline{\beta}}{\sum_h\beta_{Class\ h}(j)} \tag{10}$$

with:

$$\overline{\beta}=\frac{1}{c-1}\sum_{h\neq\hat{h}}\beta_{Class\ h}(j) \tag{11}$$

After both the consequent class C_j and the grade of certainty CF_j are determined for all N rules, a new pattern x=(x_1 ,…, x_n) can be classified by the following procedure. Calculate $\alpha_J(x)$ for j =1,…, N, as:

$$\alpha_J(x)=\max\{\mu_j(x)\cdot CF_j\,|\,C_j\} \tag{12}$$

in which J is the number of winner rule. The class of the new pattern would be the C_J *i.e.* the class that has been assigned to rule number J.

If two or more classes take the maximum value, then the classification of x is rejected (*i.e.* x is left as an

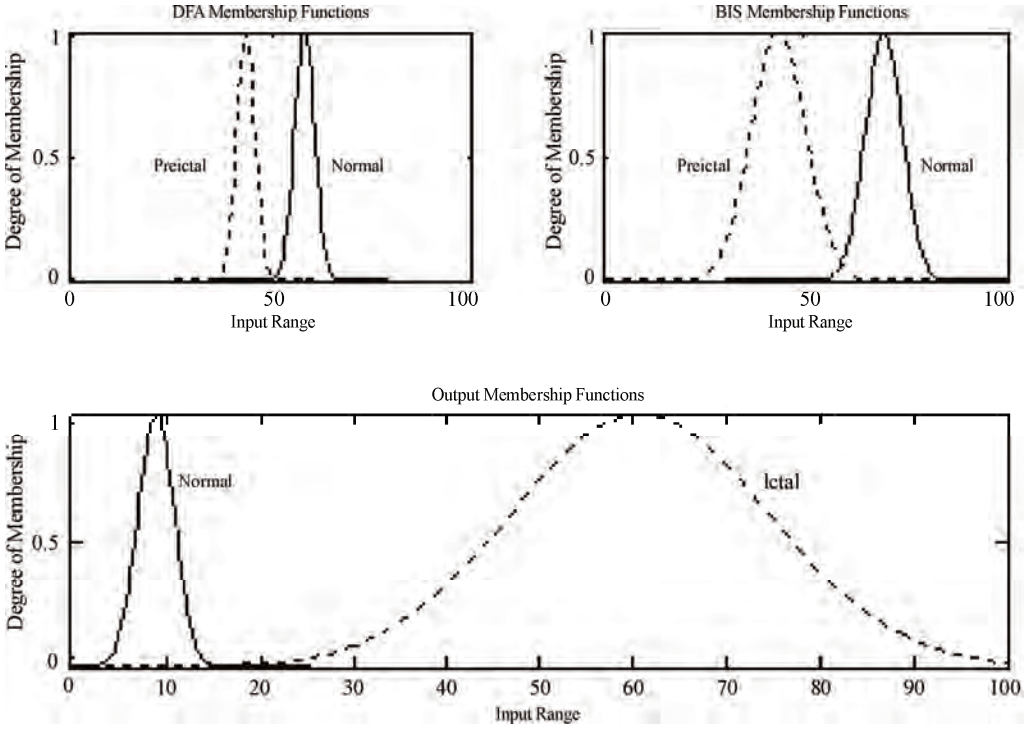

Figure 3. Membership Functions of different inputs.

unclassifiable pattern), otherwise assign *x* to Class *h´*.

In addition to a four-class classification, we intend to derive an index in [0 100] that reflects the level of epilepsy. 0 shows Ictal and 100 shows Normal state. Consequently, in this stage, the whole rule set is used instead of just one winner rule. In order to infer a result from a set of rules, a fuzzy inference engine must be added to the proposed system. The product inference engine with the following properties has been chosen regarding to [13]: individual-rule base inference, union combination of results, Mamdani's product implication, algebraic product for all T-norm operations, and maximum for all S-norm operations. In the other hand, to derive a crisp number representing the measure of epilepsy, it is essential to design an appropriate membership function for output space and to choose a defuzzification method as well. In this way, 3 membership functions corresponding to 3 classes of Ictal, Preictal, and Normal has been put in the output section and values of 100, 50, and 0 has been assigned to their membership function centers respectively as **Figure 4**. Also, centriod defuzzifier is used to obtain SII.

4. EXPERIMENTAL RESULTS

As mentioned previously, the used dataset has 100 23.6s-epoch single-channel signals for each set (A, C, and E); besides, at least 10s of data is needed to best extract DFA and BIS features. So, 3.6 seconds of the end of each signal was eliminated, the rest 20 seconds where divided into two 10s epochs, and BIS, DFA, and SD were extracted from each epoch.

The DFA amounts relate extremely to the range of n because the slope of F_n via n differs significantly based on the part of the curve chosen. We tested different ranges and calculated the separation percents. The DFA amounts for some different ranges are displayed in **Figure 5** and the classification percents for these ranges are represented in **Table 1**.

Increasing n increases the separation between Normal and Preictal states but the speed of computation should

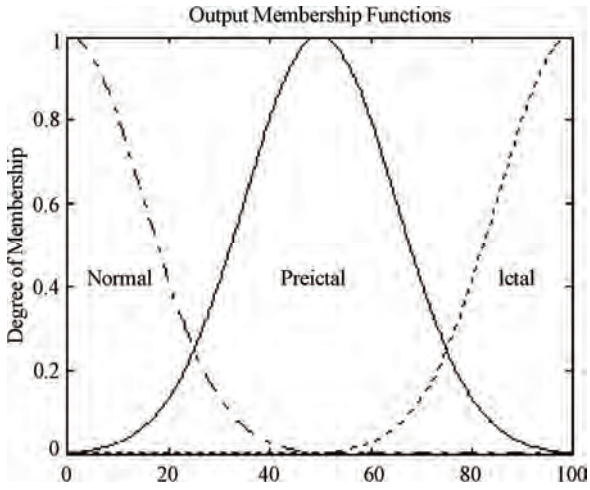

Figure 4. Output membership functions.

Table 1. Classification percents of three states using DFA and SD changes with different ranges of n.

Range of n	Classification Percent
3 < n < 10	97.23
3 < n < 15	99.13
3 < n < 30	100
3 < n < 50	100

also be considered especially when we speak of using this method in patient monitoring and index calculation. After lots of observations, the best range for n is chosen to be [3,30].

After computation of DFA with the best range, an 8-point moving average is applied on each feature of each set, so the first 7 features of each group are omitted. In the end, there are 193 3-feature vectors for each group (A, C, and E). The BIS, DFA, and SD features of these 193 vectors are represented separately for each set of data along with their box plots in **Figure 6**.

From **Figure 6**, it is obvious that SD along with just one of the other features is enough to make a good separation between three states. As mentioned in Section 3.3, a fuzzy classifier with membership functions of **Figure 3** is used to separate the three sets A, C, and E.

The p-values of each pair of DFA, BIS, and SD features are represented separately in Tables 2 to 4. $P < 0.05$ means that the two groups have similar amounts for that specific feature and cannot be separated easily using that feature. The represented values are relevant to the results in **Figure 6**.

A leave-one-out technique is applied to the data in classification process. It means that the classification performed 193 × 3 times. Each time, one of the samples is used as a test and the whole other samples are used as train. At the end, an average of all classification percents of these 193 × 3 tries is declared as the classification percent of the whole system. The classification percent for SD and BIS is 99.82% and for SD and DFA is 100%. **Table 5** is a comparison of the proposed method with previous works on the same data.

The important part of this study is the index extraction. Along with SD feature, DFA and BIS can separately well classify the three states, so they are used separately as the inputs of the fuzzy inference engine. The used inference engine is the product engine and the input and output membership functions are as displayed in **Figures 3 and 4**. A centroid defuzzifier is applied to the output to compute the final index which is called SII. The index is programmed to be between 0 and 100. Zero means the patient is in Normal situation and 100 means he is in Ictal situation. Convenient ranges for these amounts are specified to better interpret the medical situation of the patient. **Table 6** is exposed to suggest a range for different states.

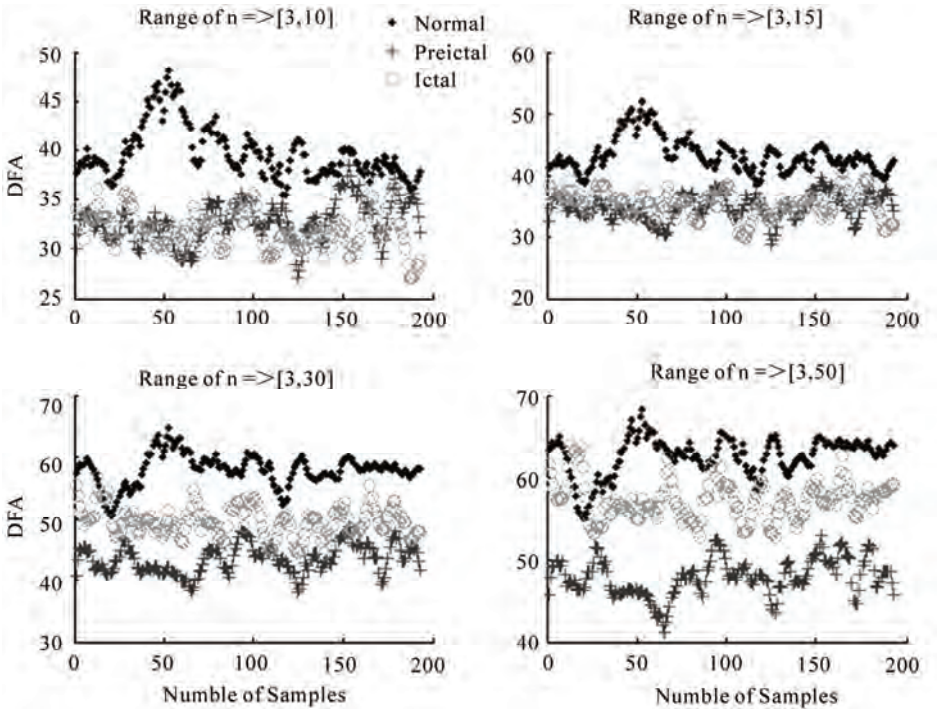

Figure 5. Different Ranges for *n* produces different DFAs.

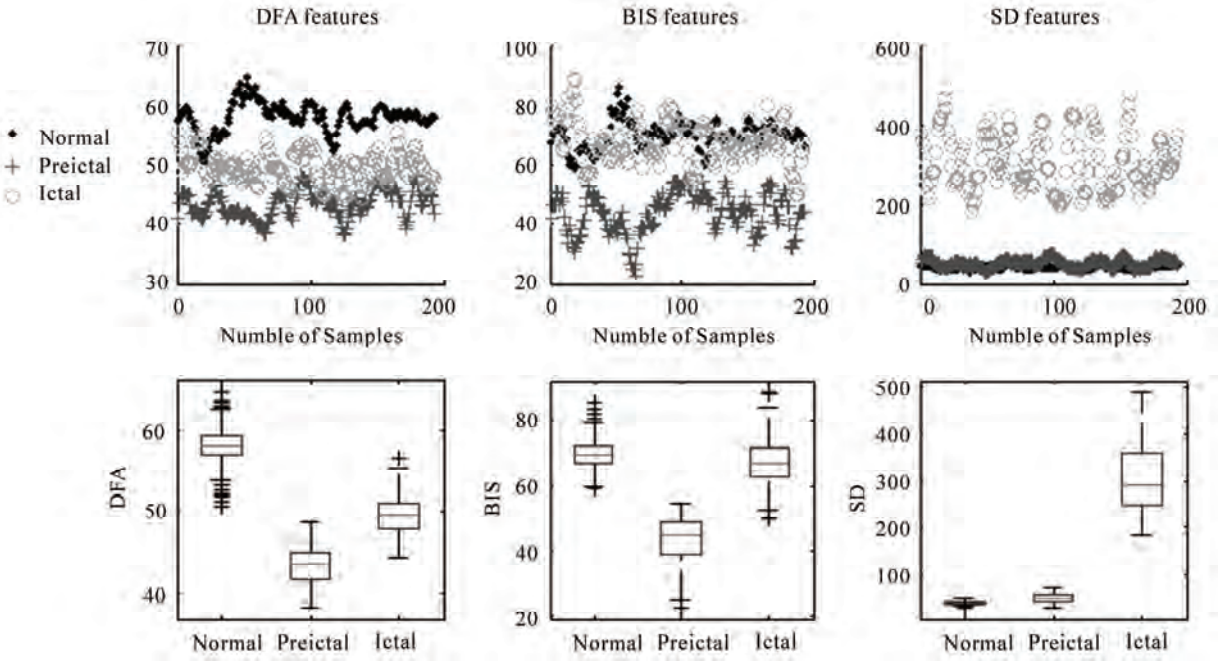

Figure 6. (a) DFA; (b) BIS; (c) SD features of 3 sets and their box plots.

Table 2. P-values of different DFA vectors.

DFA p-values	Normal	Preictal	Ictal
Normal	0	0.3476	0.1198
Preictal	0.34762	0	0.0049
Ictal	0.11982	0.0049	0

Table 3. P-values of different BIS vectors.

BIS p-values	Normal	Preictal	Ictal
Normal	0	0.8421	0.0019
Preictal	0.8421	0	0.8019
Ictal	0.0019	0.8019	0

Table 4. P-values of different SD vectors.

SD p-values	Normal	Preictal	Ictal
Normal	0	3.4814e-005	0.62488
Preictal	3.4814e-005	0	0.12001
Ictal	0.62488	0.12001	0

First, the inputs of the engine are SD and BIS and then the inputs are SD and DFA. The output of both systems is the desired index SII. There are 193 values for each feature in each set. We feed all 579 values of each feature to each system and come to the results shown in **Figure 7**. The vertical lines separate the samples of each set (A, C, and E). One can obviously see the well separation in index amounts for different states of both DFA and BIS.

Both of these methods are fast and their algorithms are not complex although DFA is faster and less complex. Though, the proposed methods can easily be used in patient monitoring of epileptic patients. As the output index is a two digit number, the system can be manufactured completely user friendly and the interpretation of the results is so easy for the physicians. The important point is that just one channel of EEG signal has been used.

5. CONCLUSIONS

Epilepsy is a brain disorder in which clusters of nerve cells, or neurons, in the brain sometimes signal abnormally. In epilepsy, the normal pattern of neuronal activity becomes disturbed, causing strange sensations, emotions, and behavior or sometimes convulsions, muscle spasms, and loss of consciousness. Though, once epilepsy is diagnosed, it is important to begin treatment as soon as possible. Scientists are studying potential antiepileptic drugs with the goal of enhancing treatment for epilepsy. Once a seizure is predicted, antiepileptic drugs can be injected to prevent the seizure.

We have divided the brain situation of an epileptic patient into 3 states: Normal (normal brain state), Preictal (just before the seizure), and Ictal (during seizure). In this research, we are seeking a technique to calculate an index that can distinctly separate these three states.

The dataset used is a public dataset which is described thoroughly in the text. This database includes 5 sets in every which there are 100 single-channel EEG signals of a specific state of epileptic patients' brains (A to E).

In this paper, three features are extracted from single-

Table 5. Proposed method and previous works.

Features	Classifiers	Used datasets	Classification Percents (%)
Spectral and embedding entropies [14]	ANFIS	A and E	92
Lyapunov Exponent [15]	Neural Network	A,D, and E	96.79
Wavelet [16]	Neural Network	A and E	95
Chaotic features [17]	Neural Network	A, C, and E	96.7
FFT [18]	Decision Tree	A and E	98.72
Welch (FFT) and PCA [19]	AIRS with fuzzy	A and E	100
BIS and SD (Proposed Method)	Fuzzy	A, C, and E	99.82
DFA and SD (Proposed Method)	Fuzzy	A, C, and E	100

Table 6. The appropriate ranges for differnt states.

State	Range
Normal	0 < SII < 30
Preictal	30 < SII < 70
Ictal	70 < SII < 100

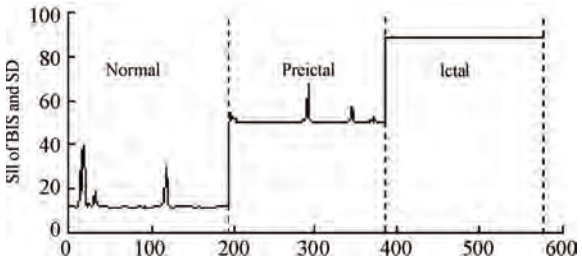

(a) Number of Samples

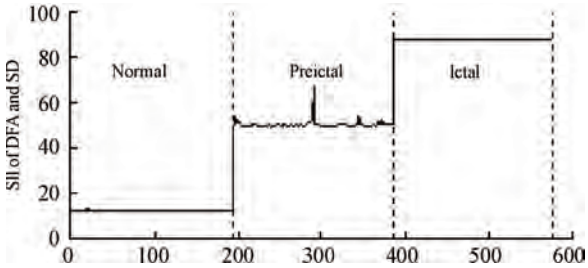

(b) Number of Samples

Figure 7. SII index using. (a) BIS and SD; (b) DFA and SD.

channel EEG signals: BIS (Bispectral feature), DFA (Detrended Fluctuation Analysis feature), and SD (Standard Deviation). The first and second features are discussed completely in the paper. For classification and index extraction, fuzzy classifier and fuzzy inference engine are used.

In classification process, first, BIS and SD are used and the three states can be separated with 99.82% accuracy. Then, using DFA and SD, Normal, Preictal, and Ictal are separated with 100% classification percent. In comparison with previous works which are discussed in the paper, our results are much higher.

Using the product engine as the fuzzy inference engine, a Seizure Intensity Index (SII) is calculated once with BIS and SD and once with DFA and SD as the inputs. In both cases, the index is completely separable for the three sets (A, C, and E). The index stands between 0 and 100. Zero means the patient is in the Normal situation and 100 means he is experiencing seizure. We can specify a range for the index. If the index is between 30 and 70, the patient is in the preictal period and the antiepileptic drugs should be injected.

The proposed methods are fast and simple and may easily run a user friendly system. Our research can be used vastly in medical care sections because it works with single-channel EEG signal and it can significantly help the physicians understand the situation of an epileptic patient and apply an appropriate treatment based on the patient situation.

REFERENCES

[1] Hagihira, S., Takashina, M., Mori, T., Mashimo, T. and Yoshiya, I. (2001) Practical issues in bispectral analysis of electroencephalographic signals. *Journal of Anesthesia Analge*sia, **93**, 966-970.

[2] Huang, L., Sun, Q., Cheng, J. and Huang, Y. (2003) Prediction of epileptic seizures using bispectrum analysis of electroencephalograms and artificial neural network. *Proceedings of* 25*th Annual International Conference of the IEEE Engineering in Medicine and Biology Society*, **3**, 2947-2949.

[3] Tallach, R., Ball, D. and Jefferson, P. (2004) Monitoring seizures with the bispectral index. *Journal of Anesthesia*, **59,** 1033-1034.

[4] Ye, S., Park, J., Kim, J., Jung, J., Jeon, A., Kim, I., Son, J., Nam, K., Baik, S., Ro, J. and Jeon G. (2009) Development for the Evaluation Index of an Anesthesia Depth using the Bispectrum Analysis. *International Journal of*

Biological and Medical Sciences, **4**, 67-70.

[5] Peng, C., Buldyrev, S., Havlin, S., Simons, M., Stanley, H. and Goldberger, A. (1994) Mosaic organization of DNA nucleotides. *Journal of Physical Review E*, **49**, 1685-1689.

[6] Gifani, P., Rabiee, H., Hashemi, M., Taslimi, P. and Ghanbari, M. (2007) Optimal fractal-scaling analysis of human EEG dynamic for depth of anesthesia quantification. *Journal of the Franklin Institute*, **344**, 212-229.

[7] Jospin, M., Caminal, P., Jensen, E., Litvan, H., Vallverdu, M., Struys, M., Vereecke, H. and Kaplan, D. (2007) Detrended fluctuation analysis of EEG as a measure of depth of anesthesia. *IEEE Transactions on Biomedical Engineering*, **54**, 840-846.

[8] Andrzejak, R., Lehnertz, K., Rieke, C., Mormann, F., David, P. and Elger, C. (2001) Indications of nonlinear deterministic and finite dimensional structures in time series of brain electrical activity: Dependence on recording region and brain state. *Journal of Physical Review E*, **64**, 061907.

[9] Kantelhardta, J., Bundea, E., Regoa, H., Havlinb, S. and Bundea, A. (2001) Detecting long-range correlations with detrended Fluctuation analysis. *Journal of Physica A*, **295**, 441-444.

[10] Ishibuchi, H., Nozaki, K., Yamamoto, N. and Tanaka, H. (1995) Selecting fuzzy if-then rules for classification problems using genetic algorithms. *IEEE Transactions on Fuzzy Systems*, **3**, 260-270.

[11] Ishibuchi, H. and Nakashima, T. (2001) Effect of rule weights in fuzzy rule-based classification systems. *IEEE Transactions on Fuzzy Systems*, **9**, 506-515.

[12] Nakashima, T., Yokota, Y. and Ishibuchi, H. (2005) Learning fuzzy if-then rules for pattern classification with weighted training patterns. *Proceedings of* 4*th Conference of the European Society for Fuzzy Logic and Technology and* 11*th Rencontres Francophones sur la Logique Floue et ses Applications*, 1064-1069.

[13] Esmaeili, V., Assareh, A., Shamsollahi, M., Moradi, M. and Arefian, N. (2008) Estimating the depth of anesthesia using fuzzy soft computation applied to EEG features. *Journal of Intelligent Data Analysis*, **12**, 393-407.

[14] Kannathal, N., Choo, M., Acharya, U. and Sadasivan, P. (2005) Entropies for detection of epilepsy in EEG. *Journal of Computer Methods and Programs in Biomedicine*, **80**, 187-194.

[15] Guler, N., Ubeyli, E. and Guler, I. (2005) Recurrent neural networks employing Lyapunov exponents for EEG signals classification. *Journal of Expert Systems with Applications*, **29**, 506-514.

[16] Subasi, A. (2007) EEG signal classification using wavelet feature extraction and a mixture of expert model. *Journal of Expert Systems with Applications*, **32**, 1084- 1093.

[17] Dastidar, S., Adeli, H. and Dadmehr, N. (2007) Mixed-band wavelet-chaos-neural network methodology for epilepsy and epileptic seizure detection. *IEEE Transactions on Biomedical Engineering*, **54**, 1545-1551.

[18] Polat, K. and Gunes, S. (2007) Classification of epileptiform EEG using a hybrid system based on decision tree classifier and fast Fourier transform. *Journal of Applied Mathematics and Computation*, **187**, 1017-1026.

[19] Polat, K. and Gunes, S. (2008) Artificial immune recognition system with fuzzy resource allocation mechanism classifier, principal component analysis and FFT method based new hybrid automated identification system for classification of EEG signals. *Journal of Expert Systems with Applications*, **34**, 2039-2048.

J. Biomedical Science and Engineering, 2010, 3, 262-267 **JBiSE**
doi:10.4236/jbise.2010.33035 Published Online March 2010 (http://www.SciRP.org/journal/jbise/).

Mutation pattern in human adrenoleukodystrophy protein in terms of amino-acid pair predictability

Shao-Min Yan[1], Guang Wu[2]*

[1]National Engineering Research Center for Non-food Biorefinery, Guangxi Academy of Sciences, Nanning, China;
[2]Computational Mutation Project, DreamSciTech Consulting, Shenzhen, China; *Corresponding author.
Email: hongguanglishibahao@yahoo.com

Received 28 December 2009; revised 5 January 2010; accepted 8 January 2010.

ABSTRACT

The mutation pattern in protein is a very important feature and is studied through various approaches including the study on mutation pattern in domains where amino acids are converted into numbers from letters. In this study, we converted the amino acids in human adrenoleukodystrophy protein with its 128 missense mutations into random domain using the amino-acid pair predictability, and then we studied their mutation patterns. The results show 1) the mutations are more likely to target the amino-acid pairs whose actual frequency is larger than their predicted one, 2) the mutations are more likely to form the amino-acid pairs whose actual frequency is smaller than their predicted frequency, 3) mutations are more likely to occur at unpredictable amino-acid pairs, and 4) mutations have the trend to narrow the difference between predicted and actual frequencies of amino-acid pairs.

Keywords: Adrenoleukodystrophy;
Amino-Acid Pair Predictability; Mutation Pattern

1. INTRODUCTION

The public-accessible protein databases provide us not only the possibility of tracking the history of protein family as well as other important topics, but also the possibility of analyzing the protein evolution from various angles. Of many facts that influence the protein evolution is the mutation, which has been the objective of many studies.

One way to study the mutation is to find out its pattern, for example, the "hotspot" sites in a protein have been defined as to be sensitive to endogenous and exogenous mutagens [1,2,3]. This approach and others such as multi-sequence comparison and alignment work in the domain of amino-acid sequence, that is, we directly analyze the mutation patterns in terms of the letters, which represent amino acids in a protein.

Another approach, which is extremely powerful and widely used in other research fields, is to analyze the issue of interest in numeric domains, which also paves the ways to use more sophisticated mathematical tools to analyze the mutation patterns. For example, we can use the physicochemical property of amino acids to represent a protein sequence, and analyze the protein sequence in physicochemical domain as a numeric sequence [4].

However, we should not stop here because the physicochemical property and other parameters borrowed from physics and chemistry were developed for the purpose of other types of studies, but may not for the purpose of studying mutations. Our group has developed three approaches since 1999 to study protein mutation in a random domain [5,6,7,8] not only because pure chance is now considered to lie at the very heart of nature [9] but also because our approaches are more sensitive to the protein length, amino-acid composition and position, neighboring amino acids etc. In particular, our approaches are sensitive to mutations because they can give different values before and after mutation [5,6,7,8].

In this study, we will analyze the mutation pattern in the adrenoleukodystrophy protein (ALDP), which is a transporter in the peroxisome membrane and belongs to the ATP-binding cassette transporter superfamily [10,11, 12,13]. This protein is involved in the transport of coenzyme A esters of very-long-chain fatty acids from the cytoplasm into the peroxisomal lumen [14,15]. Mutations in the gene *ABCD*1 mapping to Xq28 can result in the defects of adrenoleukodystrophy protein that are the cause of a severe X-linked disease, called X-linked adrenoleukodystrophy [16,17]. This disease is the most common peroxisomal disorder [18] with a minimal incidence of 1:21000 males [19]. It is characterized by the characteristic accumulation of saturated very long-chain fatty acids and disorder of peroxisomal beta-oxidation [20,21,22,23,24]. The clinical outcomes of adrenoleu-

kodystrophy vary strikingly and unpredictably [13,14,15, 16,17,18,19,20,21,22,23,24,25,26]. The phenotypes include the rapidly progressive childhood cerebral form (CCALD), the milder adult form, adrenomyeloneuropathy (AMN), and variants without neurologic involvement. There is no apparent correlation between genotype and phenotype [24,25,26,27].

Besides the importance mentioned above, there are currently 132 mutations documented in human adrenoleukodystrophy protein, which is statistically sufficient for pattern analysis.

2. MATERIALS AND METHODS

2.1. Data

The amino-acid sequence of human adrenoleukodystrophy protein and its 132 mutations were obtained from the UniProtKB/Swiss-Prot (accession number P33897). Among the mutations, 128 are missense point mutations and the rest are small deletions or insertions [28].

2.2. Conversion of Adrenoleukodystrophy Protein into Random Domain

We use the amino-acid pair predictability as a measurement for the randomness of adjacent amino-acid pairs in a protein, and this simple measure can serve as an indicator to the complicity of protein construction, which leads to many our studies [29,30,31,32,33,34,35,36,37, 38,39].

The human adrenoleukodystrophy protein consists of 745 amino acids. The first and second amino acids are an adjacent amino-acid pair, the second and third as another amino-acid pair, the third and fourth, until the 744th and 745th, thus there are 744 adjacent amino-acid pairs.

Then, we can use the permutation to define if an amino-acid pair is predictable. For example, there are 80 alanines (A) and 57 valines (V) in human adrenoleukodystrophy protein: if the permutation works, then the amino-acid pair AV would appear 6 times ($80/745 \times 57/744 \times 744 = 6.12$); actually we do find six AV pairs in this protein, so the appearance of AV is predictable, because the actual frequency is equal to its predicted one.

On the other hand, there are 59 arginines (R) in human adrenoleukodystrophy protein, if the permutation works, the predicted frequency of AR appearance would be 6 ($80/745 \times 59/744 \times 744 = 6.34$); however, the pair AR appears 9 times in realty, so the appearance of AR is unpredictable, because the actual frequency is larger than its predicted one.

Also, we can find the case, where the actual frequency is smaller than its predicted one. For example, there are 94 leucines (L) and 55 glutamic acids (G) in human adrenoleukodystrophy protein so that the predicted frequency of pair LG is 7 ($94/745 \times 55/744 \times 744 = 6.94$), however, its actual frequency is only 2.

2.3. Mutations in Terms of Predictable and Unpredictable Amino-Acid Pairs

A point missense mutation would lead to the change in two amino-acid pairs if the mutation would not occur at terminals. For instance, a mutation at position 484 substitutes proline (P) to arginine (R), which impairs the protein dimerization [40]. This mutation leads amino-acid pairs TP and PS to change to TR and RS, because threonine (T) is located at position 483 and serine (S) is located at position 485. Nevertheless, this mutation would be reflected in terms of predicted frequency, actual frequency and their difference (see **Table 1**).

This mutation changed the difference between predicted frequency (PF) and actual frequency (AF) of affected amino-acid pairs, $\sum$(PF–AF). Before mutation, $\sum(PF - AF) = (1 - 1) + (2 - 4) = -2$ for TP and PS, and $\sum(PF - AF) = (2 - 0)+(4 - 4) = 2$ for TR and RS. After mutation, $\sum(PF - AF) = (1 - 0) + (2 - 3) = 0$ for TP and PS, and $\sum(PF - AF) = (2 - 1) + (4 - 5) = 0$ for TR and RS. Needless to say, there would construct a certain mutation pattern if we analyze sufficient mutations.

2.4. Statistics

The data were presented as median with an interquartile. The Mann-Whitney *U*-test and *Chi*-square test were used for comparisons, and $P < 0.05$ is considered statistically significant.

3. RESULTS

As there are 20 kinds of amino acids, they can theoretically construct 400 types of amino-acid pairs, which serve us as a reference for comparison with human adrenoleukodystrophy protein. Of 400 types of amino-acid pairs, 118 are absent including 44 predictable and 74 unpredictable. Consequently 744 amino-acid pairs in human adrenoleukodystrophy protein include only 282 types of amino-acid pairs (400 – 118 = 282), which means these 282 types would host all mutations occurred in the protein. Of those 282 types, 98 are predictable and 184 are unpredictable; while of 744 amino-acid pairs 175 and 569 pairs are predictable and unpredictable because some types of amino-acid pairs appear more than once.

The first mutation pattern is the amino-acid pairs tar-

Table 1. Predicted frequency, actual frequency and their difference of amino-acid pairs affected by T485S mutant of human adrenoleukodystrophy protein.(PF: Predicted frequency, AF: actual frequency; T: threonine, P: praline, R: arginine, S: serine.).

Amino-acid pair	Before mutation			After mutation		
	PF	AF	PF–AF	PF	AF	PF–AF
TP	1	1	0	1	0	1
PS	2	4	–2	2	3	–1
TR	2	0	2	2	1	1
RS	4	4	0	4	5	–1

geted by mutations, or we might call them as hotspots. **Table 2** details the substituted amino-acid pairs in terms of the relationship between actual and predicted frequencies. Here, the mutations are more likely to target the amino-acid pairs whose actual frequency is larger than their predicted one, for example, 47 mutations targeted these amino-acid pairs; by contrast, the mutations are less likely to target the amino-acid pairs whose actual frequency is smaller than their predicted one, for example, only 5 mutations targeted these amino-acid pairs. The *Chi*-square test indicates remarkable statistical difference before and after mutation (P=<0.001).

The second mutation pattern is the amino-acid pairs formed after mutations. **Table 3** details the substituting amino-acid pairs in terms of the relationship between actual and predicted frequencies. The *Chi*-square test indicates remarkable statistical difference before and after mutation (P=<0.001). **Table 3** has the same format as those in **Table 2**, thus we can easily find out the second mutation pattern by comparing two tables. For example, the data in the fourth column in both tables are almost in totally opposite orders, that is, mutations are more likely to target the amino-acid pairs whose actual frequency is larger than their predicted frequency, while mutations are more likely to form the amino-acid pairs whose actual frequency is smaller than their predicted frequency. Again, the data in the seventh column in both tables appear somewhat similar.

Meanwhile, **Tables 2** and **3** also reveal the third mutation pattern that is mutations are more likely to occur at unpredictable amino-acid pairs (lines 4–8 in both tables).

The above three mutation patterns are mainly related to the relationship in amino-acid pair between actual and predicted frequencies. In fact, the difference between predicted and actual frequencies can also provide us with further mutation patterns. **Figure 1** shows the difference between predicted and actual frequencies related to amino-acid pairs identical to substituted and substituting amino-acid pairs before and after mutation, and their statistical results are shown in **Figure 2**, which highlights the fourth mutation pattern.

Before mutation, the median of difference between predicted and actual frequencies is –2 in substituted amino-acid pairs, suggesting that the mutations occur in the amino-acid pairs, which appear more than their predicted frequency. Meanwhile, the corresponding value is 1 in substituting amino-acid pairs, indicating that the mutations lead to the appearance of the amino-acid pairs that appear less than their predicted frequency.

After mutation, the median of difference between predicted and actual frequencies is 0 in substituted amino-acid pairs, suggesting that these amino-acid pairs are

Table 2. Amino-acid pairs identical to substituted amino-acid pairs before and after mutations. (AF: actual frequency; PF: predicted frequency. There is a remarkable statistical difference before and after mutation (*Chi*-square = 47.841 with 5 degrees of freedom, P = <0.001).

Amino-acid pairs			Before Mutation			After Mutation		
	Pair I	Pair II	Number	%	Total %	Number	%	Total %
Predictable	AF=PF	AF=PF	21	16.41	16.41	14	10.94	10.94
Unpredictable	AF>PF	AF>PF	47	36.72	83.59	14	10.94	89.06
	AF>PF	AF=PF	29	22.66		20	15.63	
	AF>PF	AF<PF	20	15.63		30	23.44	
	AF<PF	AF=PF	6	4.69		27	21.09	
	AF<PF	AF<PF	5	3.91		23	17.97	

Table 3. Amino-acid pairs identical to substituting amino-acid pairs before and after mutations (AF: actual frequency; PF: predicted frequency. There is a remarkable statistical difference before and after mutation (*Chi*-square = 54.114 with 5 degrees of freedom, P = <0.001).

Amino-acid pairs			Before Mutation			After Mutation		
	Pair I	Pair II	Number	%	Total %	Number	%	Total %
Predictable	AF=PF	AF=PF	11	8.59	8.59	9	7.03	7.03
Unpredictable	AF>PF	AF>PF	6	4.69	91.41	39	30.47	92.97
	AF>PF	AF=PF	24	18.75		40	31.25	
	AF>PF	AF<PF	29	22.66		25	19.53	
	AF<PF	AF=PF	34	26.56		8	6.25	
	AF<PF	AF<PF	24	18.75		7	5.47	

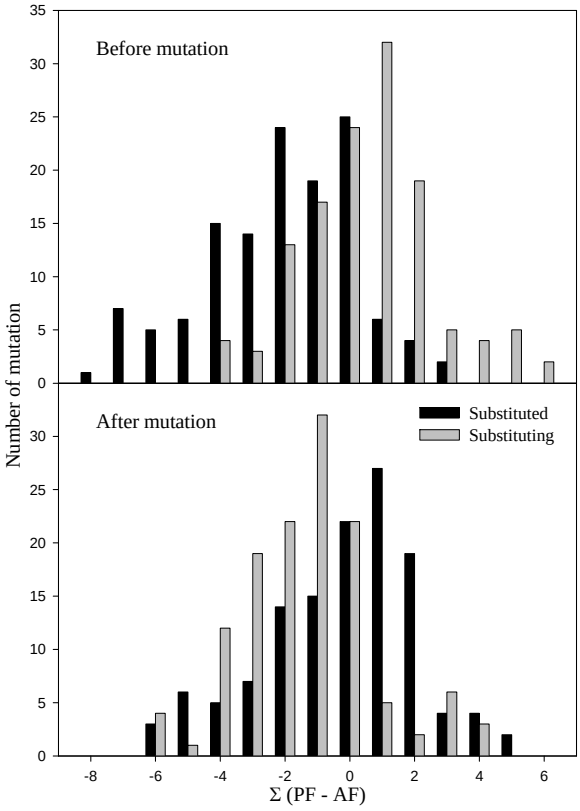

Figure 1. Difference between predicted frequency (PF) and actual frequency (AF) related to amino-acid pairs identical to substituted and substituting amino-acid pairs before and after mutation.

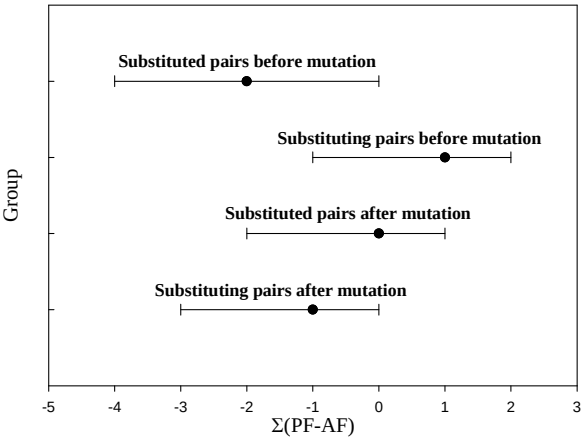

Figure 2. Sum of difference between predicted and actual frequencies [Σ(PF – AF)] of substituted and substituting amino-acid pairs before and after mutation in human adrenoleukodystrophy protein. The data are presented by median with an interquatile interval. There is a statistically significant difference between corresponding groups ($P < 0.001$, Mann-Whitney *U*-test).

more randomly constructed in the mutant adrenoleukodystrophy proteins, as their predicted and actual frequencies are about the same. However, the corresponding value is –1 in substituting amino-acid pairs, indicating that the mutations are favor the amino-acid pairs that already exist in the protein. Striking statistical difference is found between the corresponding groups ($P < 0.001$).

4. DISCUSSION

In this study, we analyze the mutation patterns in numerical domain rather than word descriptions because it is far much easy to find repeatable patterns in numerical domain. Actually there are many ways to analyze the mutation patterns in numerical domain, for example, we can use the physicochemical property to replace amino acids in a protein, and then we can analyze the mutation patterns in physicochemical property domain, which would be an interesting topic for pursuit.

The numerical domain in our approach is random whose rationale has been given in the Introduction, its biological implications would include the followings: 1) Nature follows parsimony, which suggests to construct a protein with minimal time and energy, thus the predictable amino-acid pairs in our approach confirm the nature parsimony, while the unpredictable amino-acid pairs suggest that nature deliberately spends more time and energy to construct them, which could be functional sites. 2) The difference between predicted and actual frequencies in amino-acid pairs can be regarded as a force driving mutation. Although there are uncountable factors driving mutations, their effect in fact is the difference between predicted and actual frequencies. 3) The basic effect of mutation in our sense is to narrow the difference between predicted and actual frequencies in targeted amino-acid pairs: most mutations do have such effects. However, the new formed amino-acid pairs could create new unpredictable amino-acid pairs, which once again have the difference between predicted and actual frequencies leading to new mutation so the evolution can continue.

As the difference between predicted and actual frequencies is a measure of random construction of amino-acid pairs in a protein, thus the smaller the difference is, the more random the construction of amino-acid pairs is. In particular, a) the larger the positive difference is, the more randomly unpredictable amino-acid pairs are absent; and b) the larger the negative difference is, the more randomly unpredictable amino-acid pairs are present.

Therefore, this study highlights the mutation patterns in terms of amino-acid pair predictability in human adrenoleukodystrophy protein. In future, we hope to incorporate these mutation patterns in random domain into the changes in the secondary structure contents and consequently affect biological functions of the protein [41,42].

5. ACKNOWLEDGEMENTS

This study was partly supported by National Basic Research Program of China (2009CB724703), Guangxi Science Foundation (0991080)

and Guangxi Academy of Sciences (09YJ17SW07).

REFERENCES

[1] Rideout, W.M., Coetzee, G.A., Olumi, A.F. and Jones, P.A. (1990) 5-Methylcytosine as an endogenous mutagen in human LL receptor and p53 genes. *Science*, **249**, 1288-1290.

[2] Montesano, R., Hainaut, P. and Wild, C.P. (1997) Hepatocellular carcinoma: From gene to public health. *Journal of the National Cancer Institute*, **89**, 1844-1851.

[3] Hainaut, P. and Pfeifer, G.P. (2001) Patterns of p53 G→T transversions in lung cancers reflect the primary mutagenic signature of DNA-damage by tobacco smoke. *Carcinogenesis*, **22**, 367-374.

[4] Fasman, G.D. (1976) Handbook of biochemistry: Section D physical chemical data. 3rd Edition, CRC Press, London and New York.

[5] Wu, G., and Yan, S. (2002) Randomness in the primary structure of protein: methods and implications. *Molecular Biology Today*, **3**, 55-69.

[6] Wu, G. and Yan, S. (2006) Mutation trend of hemagglutinin of influenza A virus: A review from computational mutation viewpoint. *Acta Pharmacologica Sinica*, **27**, 513-526.

[7] Wu, G. and Yan, S. (2006) Fate of influenza A virus proteins. *Protein and Peptide Letters*, **13**, 377-384.

[8] Wu, G. and Yan, S. (2008) Lecture Notes on Computational Mutation. Nova Science Publishers, New York.

[9] Everitt, B.S. (1999) Chance rules: An informal guide to probability, risk, and statistics. Springer, New York.

[10] Efferth, T. (2001) The human ATP-binding cassette transporter genes: From the bench to the bedside. *Current Molecular Medicine*, **1**, 45-65.

[11] Pohl, A., Devaux, P.F. and Herrmann, A. (2005) Function of prokaryotic and eukaryotic ABC proteins in lipid transport. *Biochimica and Biophysica Acta*, **1733**, 29-52.

[12] Oswald, C., Holland, I.B. and Schmitt, L. (2006) The motor domains of ABC-transporters. What can structures tell us? *Naunyn-Schmiedeberg's Archives of Pharmacology*, **372**, 385-399.

[13] Kim, J.H. and Kim, H.J. (2005) Childhood X-linked adrenoleukodystrophy: Clinical-pathologic overview and MR imaging manifestations at initial evaluation and follow-up. *Radiographics*, **25**, 619-631.

[14] Shimozawa, N. (2007) Molecular and clinical aspects of peroxisomal diseases. *Journal of inherited metabolic disease*, **30**, 193-197.

[15] Wanders, R.J., Visser, W.F., van Roermund, S., Kemp, C.W. and Waterham, H.R. (2007) The peroxisomal ABC transporter family. *Pflügers Archiv European Journal of Physiology*, **453**, 719-734.

[16] Moser, H., Dubey, P. and Fatemi, A. (2004) Progress in X-linked adrenoleukodystrophy. *Current opinion in neurology*, **17**, 263-269.

[17] Moser, H.W., Mahmood, A. and Raymond, G.V. (2007) X-linked adrenoleukodystrophy. *Nature Clinical Practice. Neurology*, **3**, 140-151.

[18] Wanders, R.J. and Waterham, H.R. (2005) Peroxisomal disorders I: Biochemistry and genetics of peroxisome biogenesis disorders. *Clinical Genetics*, **67**, 107-133.

[19] Bezman, L., Moser, A.B., Raymond, G.V., Rinaldo, P., Watkins, P.A., Smith, K.D., Kass, N.E. and Moser, H.W. (2001) Adrenoleukodystrophy: Incidence, new mutation rate, and results of extended family screening. *Annals of Neurol*, **49**, 512-517.

[20] Elgersma, Y. and Tabak, H.F. (1996) Proteins involved in peroxisome biogenesis and functioning. *Biochimica and Biophysica Acta*, **1286**, 269-283.

[21] Hettema, E.H. and Tabak, H.F. (2000) Transport of fatty acids and metabolites across the peroxisomal membrane. *Biochimica and Biophysica Acta*, **1486**, 18-27.

[22] Clayton, P.T. (2001) Clinical consequences of defects in peroxisomal beta-oxidation. *Biochemical Society Transactions*, **29**, 298-305.

[23] Hargrove, J.L., Greenspan, P. and Hartle, D.K. (2004) Nutritional significance and metabolism of very long chain fatty alcohols and acids from dietary waxes. *Experimental Biology and Medicine*, **229**, 215-226.

[24] Kemp, S. and Wanders, R.J. (2007) X-linked adrenoleukodystrophy: Very long-chain fatty acid metabolism, ABC half-transporters and the complicated route to treatment. *Molecular Genetics and Metabolism*, **90**, 268-276.

[25] Takano, H., Koike, R., Onodera, O. and Tsuji, S. (2000) Mutational analysis of X-linked adrenoleukodystrophy gene. *Cell Biochemistry and Biophysics*, **32**, 177-185.

[26] Berger, J. and Gärtner, J. (2006) X-linked adrenoleukodystrophy: Clinical, biochemical and pathogenetic aspects. *Biochimica and Biophysica Acta*, **1763**, 1721- 1732.

[27] Kemp, S., Pujol, A., Waterham, H.R., van Geel, B.M., Boehm, C.D., Raymond, G.V., Cutting, G.R., Wanders, R.J.A. and Moser, H.W. (2001) ABCD1 mutations and the X-linked adrenoleukodystrophy mutation database: Role in diagnosis and clinical correlations. *Human Mutation*, **18**, 499-515.

[28] Bairoch, A. and Apweiler, R. (2000) The SWISS-PROT protein sequence data bank and its supplement TrEMBL in 2000. *Nucleic Acids Research*, **28**, 45-48.

[29] Wu, G. (1999) The first and second order Markov chain analysis on amino acids sequence of human haemoglobin -chain and its three variants with low O_2 affinity. *Comparative Haematology International*, **9**, 148-151.

[30] Wu, G. (2000) The first, second, third and fourth order Markov chain analysis on amino acids sequence of human dopamine-hydroxylase. *Molecular Psychiatry*, **5**, 448-451.

[31] Wu, G. and Yan, S.M. (2001) Prediction of presence and absence of two- and three-amino-acid sequence of human monoamine oxidase B from its amino acid composition according to the random mechanism. *Biomolecular Engineering*, **18**, 23-27.

[32] Wu, G. and Yan, S.M. (2002) Estimation of amino acid pairs sensitive to variants in human phenylalanine hydroxylase protein by means of a random approach. *Peptides*, **23**, 2085-2090.

[33] Wu, G. and Yan, S. (2003) Determination of amino acid pairs sensitive to variants in human-glucocerebrosidase by means of a random approach. *Protein Engineering Design and Selection*, **16**, 195-199.

[34] Wu, G. and Yan, S. (2004) Fate of 130 hemagglutinins from different influenza A viruses. *Biochemical and Bio-Physical Research Communications*, **317**, 917-924.

[35] Wu, G. and Yan, S. (2005) Prediction of mutation trend in hemagglutinins and neuraminidases from influenza A viruses by means of cross-impact analysis. *Biochemical and Bio-Physical Research Communications*, **326**, 475-482.

[36] Wu, G. and Yan, S. (2006) Timing of mutation in hemagglutinins from influenza A virus by means of amino-acid distribution rank and fast Fourier transform. *Protein and Peptide Letters*, **13**, 143-148.

[37] Wu, G. and Yan, S. (2007) Prediction of mutations in H1 neuraminidases from North America influenza A virus engineered by internal randomness. *Molecular Diversity*, **11**, 131-140.

[38] Wu, G. and Yan, S. (2008) Prediction of mutations engineered by randomness in H5N1 neuraminidases from influenza A virus. *Amino Acids*, **34**, 81-90.

[39] Yan, S. and Wu, G. (2009) Describing evolution of hemagglutinins from influenza A viruses using a differential equation. *Protein and Peptide Letters*, **16**, 794-804.

[40] Zhou, H.X. (2004) Improving the understanding of human genetic diseases through predictions of protein structures and protein-protein interaction sites. *Current Medicinal Chemistry*, **11**, 539-549.

[41] Kuvaniemi, H., Tromp, G. and Prockop, D.J. (1997) Mutations in fibrillar collagens (types I, II, III, and IV), fibril-associated collagen (type IV), and network-forming collagen (type X) cause a spectrum of diseases of bone, cartilage, and blood vessels. *Human Mutation*, **9**, 300-315.

[42] Kashtan, C.E. (2000) Alport syndromes: Phenotypic heterogeneity of progressive hereditary nephritis. *Pediatric Nephrology*, **14**, 502-512.

J. Biomedical Science and Engineering, 2010, 3, 268-273 **JBiSE**
doi:10.4236/jbise.2010.33036 Published Online March 2010 (http://www.SciRP.org/journal/jbise/).

Sedative effects of peanut (*Arachis hypogaea* L.) leaf aqueous extracts on brain ATP, AMP, Adenosine and Glutamate/GABA of rats

Xiao-Yan Zu, Zhen-Ya Zhang*, Ji-Qiang Liu, Hong-Hai Hu, Guo-Qing Xing, Ying Zhang, Di Guan

Graduate School of Life and Environmental Sciences, Tsukuba University, Tsukuba, Japan; *Corresponding author.
Email: tyou6688@sakura.cc.tsukuba.ac.jp

Received 26 December 2009; revised 10 January 2010; accepted 17 January 2010.

ABSTRACT

Peanut (*Arachis hypogaea* L.) leaf aqueous extracts (PLAE) has been reputed to be a type of sleep-aid in China. To investigate the sedative effects and effect pathways of PLAE, rats (n = 31) were employed in two experiments and intragastrically administrated of (1) distilled water, PLAE (500 mg/kg body weight (BW)) and peanut stem aqueous extracts (PSAE, 500 mg/kg BW); (2) 0, 100 or 500 mg/kg BW of PLAE, respectively for at least 14 days. Six relevant neurotransmitters were measured finally. Experiment-1 (n = 16) results showed that the brain Lactate were significantly elevated (p < 0.05) in rat cerebrums after PLAE administrations, compared with Control and PSAE groups. In respect of brain energy system, significant degradations of the brain adenosine triphosphate (ATP) (p < 0.05) were observed in the brainstems and even the whole brains of rats though PLAE treatments. Moreover, we found that the brain Adenosine monophosphate (AMP) were clearly decreased (p < 0.05) in rat cerebrum and brainstem regions, while the brain Adenosine revealed an increasing propensity (p = 0.076) in the cerebrums of freely behaving rats. After experiment-2 (n = 15), the γ-aminobutyric acid (GABA) concentrations were statistically (p < 0.05) enhanced and the ratios of Glutamate/GABA were simultaneously reduced (p < 0.05) in rat brainstems, no matter which one dose (100 or 500 mg/kg BW) of PLAE were used. Results indicated that PLAE could influence the target neurotransmitters that related to rat circadian rhythms in the specific brain regions, possessing the potentialities as a sedative or sleep-aid for hypnic therapy purposes.

Keywords: *Arachis Hypogaea* L. Leaf Aqueous Extracts; Sedative Effects; Rats; Neurotransmitters

1. INTRODUCTION

Given the high prevalence of insomnia and hypnotics addiction worldwide, herb sedatives have attracted increasing research interests in terms of substituting the drug-addictive hypnotics. However, to our best knowledge, most of herb-sedative studies remain inconclusive in support of their effectiveness [1]. Therefore, a novel herb medicine that is demonstratively available to alleviate insomnia or sleep disorders is highly desired nowadays.

Peanut (*Arachis hypogaea* L.) leaf aqueous extracts (PLAE) have received a long reputation in china as an abirritative remedy to ease various sleep disorders [2], and clinically validated by modernistic medical approaches [3,4]. However, many those researches only focus on the clinical effects, and relevant studies on their deep effect mechanisms are still lacking. Our studies therefore carried out two rat experiments which lied in clarifying PLAE effects and pathways in the sleep regulation as well as evaluating their efficacies on spontaneous circadian rhythms of freely behaving rats.

By understanding how the animal circadian rhythms are influenced via brain nerve system and neurotransmitters [5,6], in our researches, PLAE efficacy can be identified though brain neurotransmitter variation and thereby we expect that its effect mechanisms can be revealed to some extent though this way. Thus, after intragastric (i.g.) drug administrations we separated rat brain tissues and then measured six neurotransmitters of Lactate, Adenosine triphosphate (ATP), Adenosine monophosphate (AMP), Adenosine (Ad), γ-aminobutyric acid (GABA), and Glutamate (Glu) using HPLC (High performance liquid chromatography) or Auto Amino Acid Analyzer, to evaluate the hypnotic effects of PLAE and further elucidate their effect roles correlated to PLAE on rat sleep modulation.

2. MATERIALS AND METHODS

2.1. Animals, Plant Extracts and Reagents

Male Sprague-Dawley rats (8 weeks of age, weight of 270 ± 30 g) were used as research animals. They were

housed at ambient circumstance of 25°C with 12 h light/dark cycles (light on 08:00, light off 20:00), and approached food and water *ad libitum*. All rat experiments were carried out in a humane manner after receiving approval from Institutional Animal Experiment Committee of the Tsukuba University (Japan), and in accordance with the regulations for Animal Experiments and fundamental guidelines under the jurisdiction of the Japanese Ministry of Education, Culture, Sports, Science and Technology. The PLAE and peanut stem aqueous extracts (PSAE) were extracted respectively from 98 °C water (3 h, twice), following a filtration to remove the residues. Their brown powders were obtained though rotary evaporation and freeze drying. The regents of ATP, AMP and Ad were purchased from Sigma Chemical Co. (St. Louis, MO, USA). Other chemicals used were purchased from Wako Pure Chemical Industries, Ltd. (Japan).

2.2. Experimental Protocols

Experiment-1: Sixteen rats were habituated in an animal lab for at least 7 days, then randomly divided into the following groups: Control (n = 5, distilled water), PLAE (n = 6) and PSAE (n = 5). As described before [7], all drug administrations were conducted intragastrically (i.g.) for 14 days in a dose of 500 mg/kg body weight (BW) before 8:00 (prior to the beginning of the light phase). Experiment-2: After habituated for 7 days, the rats (n = 15) employed were equally divided into three groups, fed with 0, 100 or 500 mg/kg BW of PLAE (i.g.) respectively for at least 14 days. After trials, the rats were anaesthetized by Urethane (intra-peritoneal (i.p.) injection, 200 mg/ml, 0.5 ml/100g BW), and dissected rapidly to separate their whole brains. To verify the neurotransmitter variation in diverse brain regions, the whole brain was separated into three parts of cerebrum region, brainstem region (midline involving thalamus and hypothalamus) and cerebellum region. Considering the brain responses to nucleoside and nucleotide synthesis, we froze those brain tissues immediately and stored them at –80°C till the target neurotransmitters were analyzed.

2.3. Neurotransmitter Analysis

After experiment-1, samples were firstly thawed and homogenized with 4 °C saturated trichloroacetic acid (TCA) in the sample volume of 25% (v/v), followed a centrifugation to remove the protein sediments. The pH values in cooled supernatants were then neutralized to 5-6 by NaOH. After filtered (0.45 μm membrane), the supernatants were analyzed by the HPLC (Japanese Jasco International Co., Ltd). Brain Lactates were measured though RI detector of HPLC on the basis of the methods described before (Hallstrom *et al*., 1989), and 0.1% H_3PO_4 were used as the mobile phase. Analyzing brain neurotransmitters of ATP, AMP and Ad, were performed according to the methods reported previously [8] with minor modifications. Simply, the samples were analyzed by the HPLC with Capcell-Pak C_{18} column (4.6 mm I.D. × 150 mm, particle size of 5 μm) in a flow rate of 1 ml/min at the detection wavelength of 254 nm. During testing, the mobile phase was 0.01 mol/L phosphate buffer solution (PBS, pH 6.5) that mixed with methanol (99.7%) in a ratio of 85/15 (v/v). Concentrations of ATP and its metabolites were calculated by comparing peak areas with appropriate standards.

After experiment-2, the brain samples homogenized were mixed with sulfosalicylic acid (3%) for 15 min prior to centrifugation. The pH value of supernatants were then adjusted to 2-3 using LiOH (3 mol/L). Brain GABA and Glu in samples were determined by an auto amino acid analyzer (JLC-500/V2, *Jeol* Ltd., Tokyo, Japan) in accordance with the manufacturer's specifications. Briefly, it was an ionic exchange chromatography with a stepwise elution of free amino acids, and detection with ninhydrine. The final results were calculated on the basis of the corresponding standards, and expressed as concentrations of nmol/mg in brain tissues.

2.4. Statistical Analysis

The obtained data were analyzed using a two-tailed Student's t-test, and results were expressed as mean ± SD. Statistic difference was considered to be significant at $p < 0.05$(*).

3. RESULTS

3.1. Brain ATP

As results shown in **Figure 1**, the ATP of control (Con.) group in the cerebrum, brainstem, and whole brain were 0.114 ± 0.020, 0.109 ± 0.015 and 0.134 ± 0.022 nmol/ mg, respectively. Contrasted to Control (Con.) Groups, the brain ATP declined in both of the whole brain and the single brain region after PLAE administrations. In detail, The ATP from PLAE groups were slightly reduced in cerebrums, while significant degradations were observed ($p < 0.05$) in the brainstems and whole brains on comparison with Con. groups. In the case of PSAE treatments, the enhancements of ATP were occurred in all brain regions, especially in the cerebrums.

3.2. Brain AMP

In experiment-1, we also obtained the AMP concentrations of 0.072 ± 0.013, 0.078 ± 0.005, 0.082 ± 0.007 nmol/mg respectively in the cerebrum, brainstem, and whole brain from Con. groups. As can been seen from **Figure 2,** after PLAE treated, the AMP were decreased in almost all brain regions (cerebellum results were not showed in this figure), particularly reduced ($p < 0.05$) in the cerebrum and brainstem regions. The AMP from PSAE groups showed no statistic changes compared

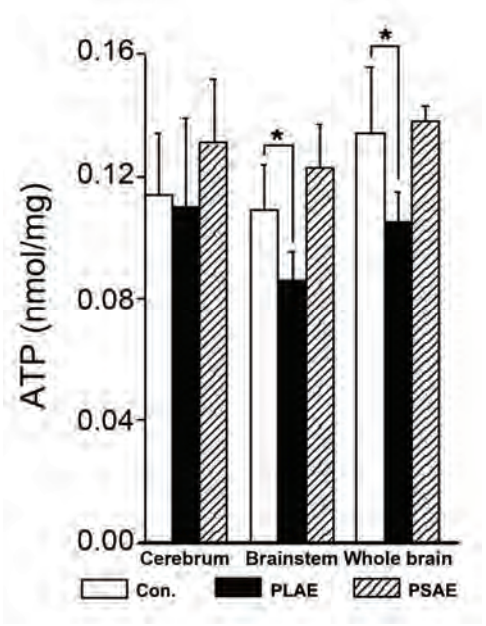

Figure 1. ATP concentrations in the cerebrum, brainstem and whole brain of freely behaving rats at experiment-1. Open bars, Con. (Control, distilled water); closed bars, PLAE (500 mg/kg BW); diagonal bars, PSAE (500 mg/kg BW). Data were expressed as mean ± SD of 5-6 independent samples (*p < 0.05, vs. Con.).

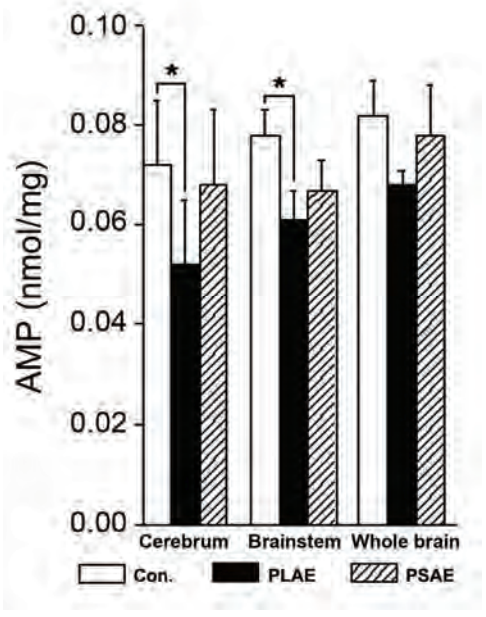

Figure 2. AMP concentrations in the cerebrum, brainstem and whole brain of freely behaving rats at experiment-1. Open bars, Con. (Control, distilled water); closed bars, PLAE (500 mg/kg BW); diagonal bars, PSAE (500 mg/kg BW). Data were expressed as mean ± SD of 5-6 independent samples (*p < 0.05, vs. Con.).

with group Con. though the trails, although the declines were observed as well.

3.3. Brain Ad and Lactate

Figure 3 showed the results of Ad and lactate in Cerebrum, and revealed that the Lactate changes were consistent with Ad in cerebrum after PLAE administrations in Experiment-1. As can be seen, compared with group Con. and PSAE, the Ad amelioration (p = 0.076) in PLAE group was occurred in cerebrum where played the main roles on modulating animal sleepiness. And the Lactate was elevated (p < 0.05) in cerebrum simultaneously after PLAE treated. On the other hand, PSAE results presented only slight differences in contrast to the Con. groups.

3.4. Brain GABA

Brain GABA of PLAE-0 group were 0.767±0.180 and 0.767 ± 0.079 nmol/mg respectively in the brainstem and Whole brain. And the GABA results of cerebrums and cerebellums were monotonous and eliminated from **Figure 4**. In the results, we found that the GABA concentrations exceeded statistically (p < 0.05) than PLAE-0 group in brainstems at both PLAE-100 and PLAE-500 groups. The GABA from PLAE-500 group showed significant improvement (p < 0.05) even in the whole brain of the experimental rats.

3.5. Brain Glu

After experiment-2, we investigated the brain Glu contents in different brain regions simultaneously. As **Figure 5**

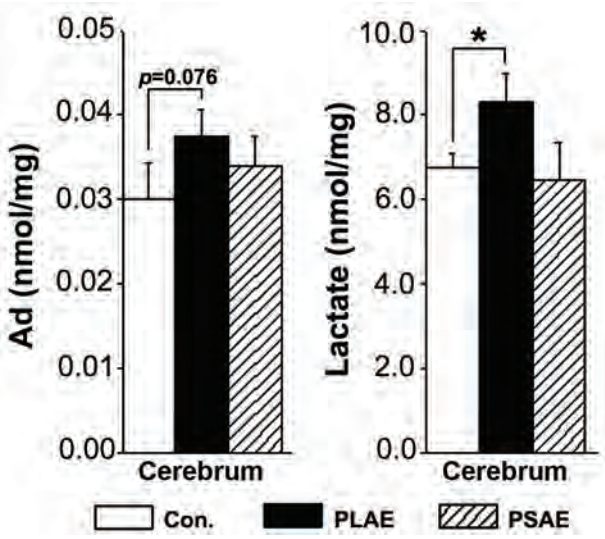

Figure 3. Concentrations of Ad and Lactate in the cerebrum of freely behaving rats at experiment-1. Open bars, Con. (Control, distilled water); closed bars, PLAE (500 mg/kg BW); diagonal bars, PSAE (500 mg/kg BW). Data were expressed as mean ± SD of 5-6 independent samples (*p < 0.05, vs. Con.).

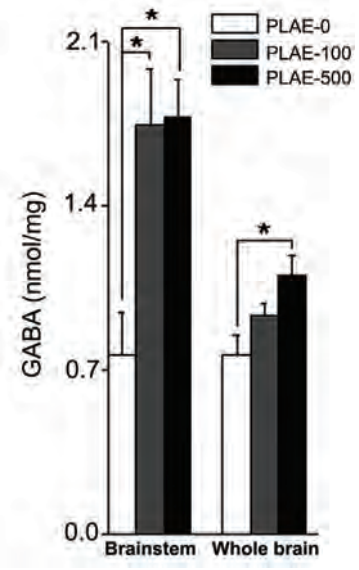

Figure 4. GABA concentrations in the brainstem and whole brain of freely behaving rats at experiment-2. Open bars, PLAE-0 (Control, without PLAE); gray bars, PLAE-100 (100 mg/kg BW of PLAE); closed bars, PLAE-500 (500 mg/kg BW of PLAE). Data were expressed as mean ± SD of five independent samples (*$p < 0.05$, vs. PLAE-0).

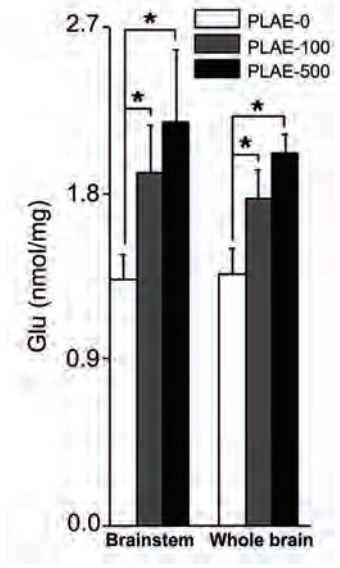

Figure 5. Glu concentrations in the brainstem and whole brain of freely behaving rats at experiment-2. Open bars, PLAE-0 (Control, without PLAE); gray bars, PLAE-100 (100 mg/kg BW of PLAE); closed bars, PLAE-500 (500 mg/kg BW of PLAE). Data were expressed as mean ± SD of five independent samples (*$p < 0.05$, vs. PLAE-0).

shown, the Brain Glu in the brainstem and whole brain were 1.330 ± 0.139 and 1.361 ± 0.141 nmol/mg respectively, which elucidated that the rats in PLAE-0 group possessed the higher contents of initial brain Glu than the brain GABA. Moreover, on comparison with PLAE-0 groups, the Glu concentrations were greatly raised ($p < 0.05$) in the brainstem as well as the whole brain, no matter which one dosage (100 or 500 mg/kg BW) of PLAE were administered in experiment-2.

3.6. The ratio of Glu/GABA

Considering the results in **Figure 4** and **5**, the ratios of Glu/GABA was important to evaluate the excitatory or suppressive state of the rat brain, we thereby calculated it and presented the results in **Figure 6**. Available variances have not been observed in the whole brains of the three groups. Moreover, compared to the PLAE-0 groups, the ratio of Glu/GABA in PLAE-100 and PLAE-500 groups were specifically decreased ($p < 0.05$) in brainstems where showed important relations with the two neurotransmitters.

4. DISCUSSION

4.1. Effects of PLAE and PSAE on Brain Energy Metabolism

ATP is the direct energy source of life activities. Its decline (**Figure 1**) in rat brain on our investigations re flected

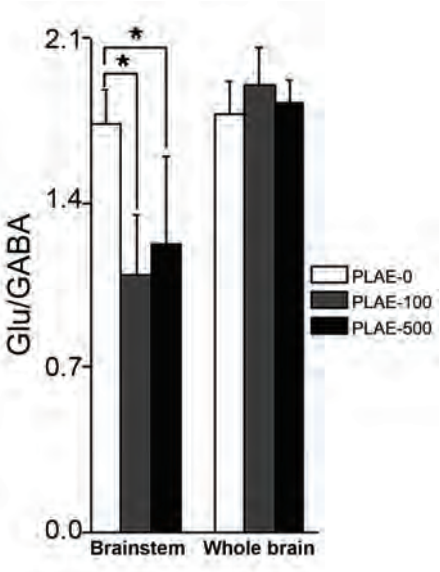

Figure 6. Ratios of Glu/GABA in the brainstem and whole brain of freely behaving rats at experiment-2. Open bars, PLAE-0 (Control, without PLAE); gray bars, PLAE-100 (100 mg/kg BW of PLAE); closed bars, PLAE-500 (500 mg/kg BW of PLAE). Data were expressed as mean ± SD of five independent samples (*$p < 0.05$, vs. PLAE-0).

the requirement of energy reserves, and indicated the potential of rat sleepiness. AMP can transfer into ATP or degraded into Ad [9]. According to the deficiency of ATP in the results, the reduction of AMP (**Figure 2**) in group PLAE elucidated the tendency of its breaking down to Ad. As reported previously, Ad is a critical neurotransmitter in brain sleep system [10], which accumulates in the cholinergic basal forebrain of cerebrum, has been proposed as one of the important homeostatic sleep factors [11]. In our researches, as a result of the deficiency of high-energy phosphates, the observed increases of Ad concentrations in cerebrums reflected a bio-energetic stress of animals. Energy depletion can build up the sleep pressure [7] and it is an available pathway and measure to explain the PLAE induced sleep propensity. From experiment-1, the great decrease of the ATP and AMP strongly indicated that the PLAE was promising in driving homeostatic sleeps of freely behaving rats. Besides, the insignificant accumulation of Ad in the PLAE group suggested a mild effect of PLAE on sleep ameliorating.

Lactate, an end product of metabolic system, can be regarded as an additional metabolic marker of the sleep pressure. Our results (**Figure 3**) illuminated that Lactate changed together with Ad, in agreement with those reported previously [12] and indicative of the PLAE contributions in sedative or hypnic propensities.

In all PSAE investigations, the rat brain energy system presented the great enhancement of ATP in cerebrum compared with Control and PLAE groups. However, such variations were disadvantageous for establishing the sleep pressure and meliorating the sleep of our experimental rats.

4.2. Effects of PLAE on Brain GABA, Glu and the Ratio of Glu/GABA

GABA is a type of inhibitory neurotransmitter amino acid in brain. To clarify the PLAE effects on brain GABA, fifteen rats were employed in experiment-2 and randomly divided into three groups, and treated with PLAE in diverse dosages for 14 days. The GABA-contained neurons in brainstem and thalamic nucleus released GABA neurotransmitters [13,14], which can response for inhibiting target neurons of the arousal systems in brainstem [15] and play an important role in meliorating rats' sleep [6]. Thus, the GABA increase in our studies (**Figure 4**) not only suggested the specific effect region (brainstem) of GABA-neurotransmitter, and also testified the sedative efficacy of PLAE.

It is well demonstrated that Glu play an excitatory role in animal brain, and then drives the animals to arousal. Glu receptors, expressed in the basal forebrain [16,17], stimulate gamma and theta electroencephalographic (EEG) activities of arousal and then suppress rat sleepiness [18,19]. In these researches, we found that PLAE also aroused the neurons to release Glu neurotransmitters (**Figure 5**) for exciting the rat brains.

In deed, GABA can be formed from Glu primarily via the action of Glu decarboxylase [20]. Glu/GABA in brainstem is a type of available parameters that can characterize the state of sleep-wake system [21]. Since GABA is inhibitory and Glu is excitatory, both of them control many tranquilizing or exciting processes in rat brain. Apparently, PLAE we used stimulated both the brain Glu and the brain GABA. However, the sleep-modulation effects of Glu sited specifically in perifornical-lateral hypothalamic area [22] of the brainstem which is the main region that releases GABA to inhibit the arousal of animal. Hence, the Glu/GABA decrease in this area (**Figure 6**) indicated superior GABA efficacy than Glu, and preferred to drive rats into drowsiness. On the other hand, as a mild tranquilizer, it was not surprising that PLAE significantly elevated GABA-mediated neurotransmission, and reduced Glu/GABA in target brain region. Thus, in profile, it was still suggested the PLAE efficacy on spontaneous sleep improvement.

In summary, PLAE resulted in the great ATP consumption, slight Ad accumulation, as well as the significant decrease of Glu/GABA in corresponding brain areas. It revealed a mild hypnotic effect of PLAE on sleep ameliorations. In the case of sedatives, the PSAE was considered to be ineffective on meliorating rats' sleeps at least view the matter from our investigations. On the other hand, in these researches, more detailed works on the effect components of such PLAE are desired to be determined in the future. Moreover, apart from the aqueous extracts of peanut leaves and stems, alcohol extracts of them are needed as well to as the contrasts in further investigations.

REFERENCES

[1] Diana, M.T., Carol, A.L., Heidi, P. and Michael, V.V. (2007) A systematic review of valerian as a sleep aid: Safe but not effective. *Sleep Medicine Reviews*, **11**, 209-230.

[2] Wang, Q.C., Xu, J. and Shi, M. (2001) Clinical efficacy of Groundnut leaves on insomnia treatments. *Shanghai Journal of Traditional Chinese Medicine*, **5**, 8-10.

[3] Hu, P.F., Fan, R.P., Li, Y.P. and Pang, C.Y. (2001) Studies on pharmacological action of Luohuashengzhiye extracts. *Chinese Traditional Patent Medicine*, **23**, 919-920.

[4] Wang, Y.F., Li, H.F., Xu, Y.F., Zhang, Y.L., Xu, D.S., Xiao, L.M. and Li, X.M. (2001). Clinical confirmation of preparation from the branch and leaf of peanut in treating insomnia. *Shanghai Journal of Traditional Chinese Medicine*, **35**, 8-10.

[5] Saper, C.B., Scammell, T.E. and Lu, J. (2005) Hypothalamic regulation of sleep and circadian rhythms. *Nature*, **437**, 1257-1263.

[6] Jones, B.E. (2005) From waking to sleeping: Neuronal and chemical substrates. *Trends in Pharmacological Sciences*, **26,** 578-586.

[7] Thakkar, M.M., Engemann, S.C., Walsh, K.M. and Sahota, P.K. (2008) Adenosine and the homeostatic control of sleep: Effects of A1 receptor blockade in the perifornical lateral hypothalamus on sleep-wakefulness. *Neuroscience*, **153**, 875-880.

[8] Schweinsberg, P.D. and Loo, T.L. (1980) Simultaneous analysis of ATP, ADP, AMP, and other purines in human erythrocytes by high-performance liquid chromatography. *Journal of Chromatography*, **181**, 103-107.

[9] Dworak, M., Diel, P., Voss, S., Hollmann, W.K. and Strüder, H. (2007) Intense exercise increases adenosine concentrations in rat brain: Implications for a homeostatic sleep drive. *Neuroscience*, **150**, 789-795.

[10] Huang, Z.L., Urade, Y. and Hayaishi, O. (2007) Prostaglandins and adenosine in the regulation of sleep and wakefulness. *Current Opinion in Pharmacology*, **7**, 33-38.

[11] Kalinchuk, A.V., Urrila, A.S., Alanko, L., Heiskanen, S., Wigren, H.K., Suomela, M., Stenberg, D. and Porkka-Heiskanen, T. (2003) Local energy depletion in the basal forebrain increases sleep. *European Journal of Neuroscience*, **17**, 863-869.

[12] Wigren, H.K., Schepens, M., Matto, V., Stenberg, D. and Porkka-Heiskanen, T. (2007) Glutamatergic stimulation of the basal forebrain elevates extracellular adenosine and increases the subsequent sleep. *Neuroscience*, **147**, 811-823.

[13] Maloney, K.J., Mainville, L. and Jones, B.E. (1999) Differential c-Fos expression in cholinergic, mono-aminergic and GABAergic cell groups of the pontomesencephalic tegmentum after paradoxical sleep deprivation and recovery. *Neuroscience*, **19**, 3057-3072.

[14] Maloney, K.J., Mainville, L. and Jones, B.E. (2000) c-Fos expression in GABAergic, serotonergic and other neurons of the pontomedullary reticular formation and raphe after paradoxical sleep deprivation and recovery. *Neuroscience*, **20**, 4669-4679.

[15] Sherin, J.E., Shiromani, P.J., McCarley, R.W. and Saper, C. B. (1996) Activation of ventrolateral preoptic neurons during sleep. *Science*, **271**, 216-219.

[16] Martin, L.J., Blackstone, C.D., Levey, A.I., Huganir, R. L. and Price, D.L. (1993) Cellular localizations of AMPA glutamate receptors within the basal forebrain magnocellular complex of rat and monkey. *Neuroscience*, **13**, 2249-2263.

[17] Page, K.J. and Everitt, B.J. (1995) The distribution of neurons coexpressing immunoreactivity to AMPA-sensitive glutamate receptor subtypes (GluR1-4) and nerve growth factor receptor in the rat basal forebrain. *European Journal of Neuroscience*, **7**, 1022-1033.

[18] Cape, E.G. and Jones, B.E. (2000) Effects of glutamate agonist versus procaine microinjections into the basal forebrain cholinergic cell area upon gamma and theta EEG activity and sleep-wake state. *European Journal of Neuroscience*, **12**, 2166-2184.

[19] Fournier, G.N., Materi, L.M., Semba, K. and Rasmusson, D.D. (2004) Cortical acetylcholine release and electroencephalogram activation evoked by ionotropic glutamate receptor agonists in the rat basal forebrain. *Neuroscience*, **123**, 785-792.

[20] Bown, A.W. and Shelp, B.J. (1997) The metabolism and functions of γ-aminobutyric acid. *Plant Physiology*, **115**, 1-5.

[21] Schousboe, A., Westergaard, N., Sonnewald, U., Petersen, S.B., Yu, A.C. and Hertz, L. (1992) Regulatory role of astrocytes for neuronal biosynthesis and homeostasis of glutamate and GABA. *Progress in Brain Research*, **94**, 199-211.

[22] Alam, M.A. and Mallick, B.N. (2008) Glutamic acid stimulation of the perifornical-lateral hypothalamic area promotes arousal and inhibits non-REM/REM sleep. *Neuroscience Letters*, **439**, 281-286.

J. Biomedical Science and Engineering, 2010, 3, 274-284 **JBiSE**
doi:10.4236/jbise.2010.33037 Published Online March 2010 (http://www.SciRP.org/journal/jbise/).

Mathematical model for the ubiquitin activating enzyme E1

Francisco Javier López-Cánovas[1], Francisca Cánovas[2], María Antonia Günther Sillero[1], Antonio Sillero[1]

[1]Departamento de Bioquímica, Instituto de Investigaciones Biomédicas Alberto Sols UAM/CSIC, Facultad de Medicina, Madrid, Spain;
[2]Departamento de Matemáticas e Informática, Escuela Técnica Superior de Ingenieros de Caminos, Canales y Puertos, Universidad Politécnica de Madrid, Madrid, Spain.
Email: antonio.sillero@uam.es

Received 21 December 2009; revised 4 January 2010; accepted 8 January 2010.

ABSTRACT

The ubiquitin-activating enzyme E1 (EC 6.3.2.19) represents the first step in the degradation of proteins by the ubiquitin proteasome pathway. E1 transfers ubiquitin from the ubiquitinated E1 to the ubiquitin carrier proteins (E2), ubiquitin-protein ligases (E3) and proteins. This process is rather complex, and known from the work of Haas, Ciechanover, Hershko, Rose and others. The occurrence of 19 hypothetical intermediate enzyme forms (EFs) and 22 different reactions were considered in the presence of ubiquitin (Ub), ATP, adenosine 5'-tetraphosphate (p_4A), pyrophosphate (P_2), and tripolyphosphate (P_3) as substrates, and iodoacetamide (IAA) and dithiothreitol (DTT) as inhibitors. Inspired by the work of Cha (Cha (1968) J. Biol. Chem., 243, 820-825) we have treated these reactions in two complementary ways: in rapid equilibrium and in steady state. The kinetics of both types of reactions were simulated and solved with a system of ordinary differential equations using the Mathematica Program. The ubiquitination of E1 has been also theoretically coupled to the ubiquitination of E2, E3 and proteins. This makes the model useful to predict the theoretical influence of inhibitors (or of changes in some parameters of the reaction) on the ubiquitination of proteins. The Program responds to changes in the concentration of ATP or ubiquitin and has predictive properties as shown by the influence of AMP on the synthesis of p_4A, calculated theoretically and confirmed experimentally.

Keywords: Dinucleoside Polyphosphates; Adenosine Tetraphosphate; Tripolyphosphate; Proteasome; Mathematical Model

1. INTRODUCTION

The work here presented deals with the development of a mathematical model for the ubiquitin activating enzyme E1 (EC 6.3.2.19) and is based on the following grounds, A, B, C, D:

1) Ligases catalyze the synthesis of diadenosine tetraphosphate (Ap_4A) and other (di)nucleoside polyphosphates through the general reactions a) and b), where X is a co-substrate of a ligase [1]

a) E + X + ATP <-----> E-X-AMP + P_2

b) E-X-AMP + ATP -----> Ap_4A + X + E

As reaction a) is reversible, the synthesis of Ap_4A is greatly favored in the presence of pyrophosphatase (PPase). In our experience, reaction b) is rather unspecific and the AMP residue of the E-X-AMP complex may react with the terminal phosphate of almost any molecule containing an intact terminal pyrophosphate, such as ATP, GTP, adenosine tetra phosphate (p_4A), tri, tetra, penta phosphate (P_3, P_4, P_5) [2].

2) The ubiquitin-activating enzyme E1 is a particular ligase using ubiquitin (Ub) and ATP (reaction c), or p_4A (reaction d) as substrates for the synthesis of the AMP derivative of the enzyme and, by the same token, uses P_2 or P_3 in the reverse reactions; p_4A and P_3 act as analogs of ATP and P_2, respectively [3].

c) E + Ub + ATP <-----> E-Ub-AMP + P_2

d) E + Ub + p_4A <-----> E-Ub-AMP + P_3

The reactions of E1 with ubiquitin and ATP as substrates and iodoacetamide (IAA), dithiothreitol (DTT) and pyrophosphatase as modifiers of the reaction constitute a complex metabolic pathway thoroughly explored by the groups of Ciechanover, Hershko, Rose and others [4,5,6,7]. The knowledge developed by these authors on this system is the cornerstone of the work shown below. We have recently approached the reactions catalyzed by E1 using ATP, P_3 and p_4A as substrates and iodoacetamide and dithiothreitol as inhibitors of the reaction [3].

3) Two main processes can be considered in the ubiquitin proteasome system for degradation of proteins: a) ubiquitination of proteins and b) proteolytic cleavage of the tagged proteins by the 26 S proteasome complex. In the initial conjugative phase the ubiquitin activating en-

zyme E1 catalyzes the formation of a high-energy thioester bond between the C-terminal of ubiquitin and a cysteine residue of E1; one of the several E2 enzymes (ubiquitin-carriers or ubiquitin conjugating enzymes) transfers the activated ubiquitin moiety from E1, via an additional high energy thioester intermediate, to the substrate that is specifically bound to a member of the ubiquitin-protein ligase family E3. The ubiquitinated protein is degraded by the proteasome with liberation of peptides and ubiquitin monomers [7,8,9,10,11].

4) Finally, as shown below, we have applied our previous experience in the mathematical modeling of metabolic pathways of glucose [12], and purine nucleotide metabolism in rat brain [13] and *Saccharomyces cerevisiae* [14] to the ubiquitin proteasome system.

On the above bases, we have tried to develop a mathematical model of the reactions catalyzed by E1 in order to get new insights into the proteasome system in general, and on the role of E1 in this system. The description of the reactions catalyzed by E1 are presented (**Figure 1**) in a way that facilitates their mathematical writing with the powerful Mathematica Program [15]. The theoretical and experimental results can be compared, so that the analysis of some physiological aspects of E1, difficult to be explored *in vivo* or *in vitro*, can be attempted with the mathematical approach. In our view, the mathematical method here described may serve as a guide to explore other complex metabolic situations, changes in the concentration of intermediate enzyme forms of E1 (**Figure 1**), as well as to approach the mechanism of action of potential inhibitors of the enzyme. As an example of its predictive properties, the effect of AMP on the synthesis of p_4A by E1 was studied theoretically and confronted with the experimental results.

2. EXPERIMENTAL PROCEDURES

2.1. Nomenclature

Ubiquitin (abbreviated as Ub, U, u or u) is a small 76-residue polypeptide containing a C-terminal glycine, to which an adenylated residue can be covalently bound. The ubiquitin-activating enzyme will be named as E1, E or $_{HS}$E. The two functional regions or areas of this enzyme will be written at the left and at the right side of the letter E. The area at the left, corresponding to the U region (acronym of ubiquitin), may contain a molecule of ubiquitin covalently bound, by a thioester bond, to a cysteine residue of the enzyme ($_{UbS}$E); this area is also called the ubiquitin donating area, as this ubiquitin can be donated to E2. The area at the right of E1 corresponds to the region named as A-u (acronym of AMP and ubiquitin), where the ubiquityl-adenylate (AMP-Ub) complex is tightly, but not covalently, bound to E1. The AMP-Ub complex is formed by the reaction between

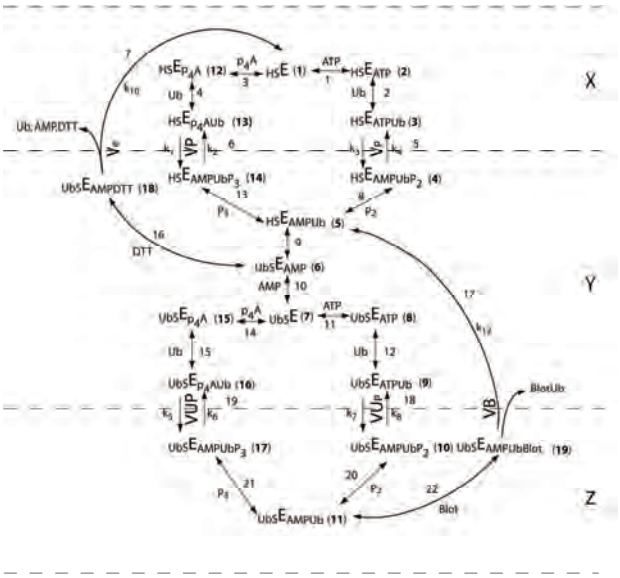

Figure 1. Scheme of the reactions considered for the ubiquitin activating enzyme E1. The following reactants were involved: ATP, adenosine 5'-tetraphosphate (p_4A), pyrophosphate (P_2), tripolyphosphate (P_3), ubiquitin (Ub), iodoacetamide (IAA), dithiothreitol (DTT), ubiquitin carrier-proteins (E2), ubiquitin protein-ligases (E3) and proteins to be ubiquitinated (E2 + E3 + proteins = Blot in the Figure). The enzyme forms (EFs) of E1 with the potential reactants are also indicated with a number in bold face and between brackets. The reactions between two EFs have been indicated in regular face numbers from 1 to 22. Three Boxes were contemplated: X, Y and Z. The reactions within each one of these Boxes are considered: in rapid equilibrium, reversible and indicated with two opposing arrow heads. The reactions between boxes are considered in steady state. For more details on nomenclature see the text.

one OH-residue of the phosphate moiety of AMP and the C-terminal of ubiquitin. The ubiquitin moiety of this complex is in an activated state, but it will not be donated to E2; the A-u area is also called the ubiquitin activating area. The different forms of the enzyme will be named as EF followed by a number in bold face. The reactions between two different EFs are designated with numbers from 1 to 22. The dissociation constants are named with two to five letters. The letters x, y or z indicate that the reaction belongs to Box X, Y or Z, respectively (see below, Subsection 3.1.1); the other letters of the constant name indicate the substrate involved, as indicated between brackets: a (ATP); A (p_4A); u, U or u (ubiquitin); p (P_2); P (P_3); e (AMP); d (DTT); B (Blot or the sum of E2 + E3 + Protein). The order of those letters indicates, in general, the sequence in which the reactants are bound to the enzyme complex. Forward reactions (**Table 1**, Appendix B) refer to those in the direction of the synthesis of EF 11, the enzyme form donating ubiquitin to E2; they have kinetic constants sub-indexed with uneven numbers; the contrary applies to the reverse reactions.

2.2. Computation

The solving of the equations and the plotting of the solutions have been carried with a personal laptop computer Intel® Pentium® M processor 1.70 GHz with the help of the Mathematica 5.0 Program [15].

3. RESULTS AND DISCUSSION

3.1. The System

The complete set of reactions catalyzed by E1, using ATP, p_4A, P_2, P_3, AMP, ubiquitin, and E2 as substrates and IAA and DTT as inhibitors are presented in **Tables 1** and **2** and schematically shown in **Figure 1**. The reactions have been numbered from 1 to 22. Those reactions identified with two opposing arrow heads indicate binding of substrates to E1 or rearrangement of substrates within the enzyme complex; they are considered in rapid equilibrium, following Michaelis-Menten postulates. The reactions noted with a simple arrow head, involving transformation of the bound substrate(s), are considered rate-limiting reactions and treated as being in steady state. The dissociation constants and the equilibrium constant (yue) are indicated in **Table 1**. The enzyme forms (EF) are expressed with the potential reactants or simply with a number in bold face, between brackets. As noted in Experimental procedures, the parts at the left and right side of E1 correspond to the U (acronym of ubiquitin) and to the A-u (acronym of AMP and ubiquitin) areas, respectively. The U area of E1 is the ubiquitin donating area to E2. The reactions depicted in **Figure 1** can be dissected into two parts.

The one at the right side of **Figure 1** represents the classical reactions previously described [7] using ATP, P_2 and ubiquitin as substrates. In summary, ATP and ubiquitin are joined to E1 (reactions 1 and 2); the bound ATP is split into AMP + P_2 (reaction 5), the bound P_2 is liberated (reaction 8) and ubiquitin is displaced from the A-u to the U region of the enzyme, with concomitant liberation of AMP (reactions 9 and 10). Once ubiquitin is covalently joined to the U region of E1, another moiety of ubiquitin is bound to the A-u area of the enzyme (using ATP as co-substrate) through a sequence of reactions (reactions 11, 12, 18, 20) similar to those previously described (reactions 1, 2, 5, 8). The enzyme form (EF 11) is already prepared to serve as donor of ubiquitin from the U area of E1 to E2 (named as "Blot" in **Figure 1**). The EF 9 generated in this step is ready to repeat the cycle, catalyzed by reactions 9-12, 18, and 20 and to afford the ubiquitin molecules needed for the processing of the proteins by the proteasome.

The part at the left side of **Figure 1** shows similar reactions to those just described with the exception that p_4A serves as a source of energy instead of ATP (compare reactions 1 and 11 with reactions 3, 14, respectively), and a molecule of P_3, instead of P_2, is involved in the process (compare reactions 8 and 20 with reactions 13 and 21, respectively). Treatment of this part of **Figure 1** is based on previous publications from our laboratory [3],

Table 1. Reactions in rapid equilibrium inside boxes X, Y, and Z. (**Figure 1**). The number, substrates and product of the reactions are as indicated in the Table and in **Figure 1**. The dissociation (equilibrium) constants were named according to the following rules: the binding of a reactant to the A-u area of E1 is represented with a letter between brackets: P_2 (p), P_3 (P), ATP (a), p_4A (A), Ub (u), AMP (e), DTT (d) or Blot (B); x, y or z indicates their location in boxes X, Y or Z; u represents the oscillation of ubiquitin from the A-u to the U area of E1; U represents ubiquitin bound to a –SH group of the U area of E1. For more details on the nomenclature of the constants see Experimental procedures. Dissociation constants are defined as the product of the concentration of the substrates divided by the concentration of the bound complex (product EF); for example, constant xa= $_{HS}E$ x ATP/$_{HS}E_{ATP}$. The equilibrium constant yue is defined as $_{UbS}E_{AMP}/_{HS}E_{AMPUb}$. Numeric values for these constants have either been taken from the literature or tuned (#) to reflect available experimental data. To facilitate location of the reactions in **Figure 1**, EFs are also indicated by their assigned numbers (in bold characters between brackets).

	Reaction		Constant value (μM)
	Number	Substrates, dissociation constant, product	
Box X	1	$_{HS}E$ **(1)** + ATP ⟷ $_{HS}E_{ATP}$ **(2)**	(ATP) 4.9 [8,23]
	2	$_{HS}E$ **(1)** + p_4A ⟷ $_{HS}E_{p4A}$ **(12)**	(p_4A) 150.0#
	3	$_{HS}E_{ATP}$ **(2)** + Ub ⟷ $_{HS}E_{ATPUb}$ **(3)**	(Ub) 2.0 [8,23]
	4	$_{HS}E_{p4A}$ **(12)** + Ub ⟷ $_{HS}E_{p4AUb}$ **(13)**	(Ub) 2.0 [8,23]
Box Y	8	$_{HS}E_{AMPUb}$ **(5)** + P_2 ⟷ $_{HS}E_{AMPUbP2}$ **(4)**	(P_2) 550#
	13	$_{HS}E_{AMPUb}$ **(5)** + P_3 ⟷ $_{HS}E_{AMPUbP3}$ **(14)**	(P_3) 2800 [8]
	9	$_{HS}E_{AMPUb}$ **(5)** ⟷ $_{UbS}E_{AMP}$ **(6)**	2.0 [5]
	10	$_{UbS}E$ **(7)** + AMP ⟷ $_{UbS}E_{AMP}$ **(6)**	(AMP) 5 [5]
	16	$_{UbS}E_{AMP}$ **(6)** + DTT ⟷ $_{UbS}E_{AMPDTT}$ **(18)**	2250#
	11	$_{UbS}E$ **(7)** + ATP ⟷ $_{UbS}E_{ATP}$ **(8)**	(ATP) 4.9 [8,23]
	14	$_{UbS}E$ **(7)** + p_4A ⟷ $_{UbS}E_{p4A}$ **(15)**	(p_4A) 150.0#
	12	$_{UbS}E_{ATP}$ **(8)** + Ub ⟷ $_{UbS}E_{ATPUb}$ **(9)**	(Ub) 2.0 [8,23]
	15	$_{UbS}E_{p4A}$ **(15)** + Ub ⟷ $_{UbS}E_{p4AUb}$ **(16)**	(Ub) 2.0 [8,23]
Box Z	20	$_{UbS}E_{AMPUb}$ **(11)** + P_2 ⟷ $_{UbS}E_{AMPUbP2}$ **(10)**	(P_2) 550#
	21	$_{UbS}E_{AMPUb}$ **(11)** + P_3 ⟷ $_{UbS}E_{AMPUbP3}$ **(17)**	(P_3) 2800 [8]
	22	$_{UbS}E_{AMPUb}$ **(11)** + Blot ⟷ $_{UbS}E_{AMPUbBlot}$ **(19)**	33000#

Table 2. Rate constant values (simplified procedure) of the steady state reactions. The constants with uneven or even numbers indicate forward or reverse direction, respectively, towards formation of $_{UbS}E_{AMPUb}$ (EF 11, the enzyme complex donating Ub to the ubiquitin carrier proteins E2).

Constants	Reactions	Value (s^{-1})	References
k1=k3	Vp; VP	0.75 x k5	[4]
k2=k4	Vp; VP	0.75 x k6	[4]
k5=k7	VUp; VUP	0.13	Tuned
k6=k8	VUp; VUP	6.25 x k5	[4]
k10	Ve	0.57	Tuned
k12	VB	3.3	Tuned

with the assumption that the binding of p_4A and P_3, behave similarly to the binding of ATP and P_2, respectively.

3.1.1. Kinetics Considerations

The kinetic treatment followed here is based on the general consensus on how to handle rapid equilibrium and steady state reactions of uni-reactant enzymes [16] and on the simplifications introduced by Cha [17]. He showed that the calculation of rates of equations of complex enzyme systems could be simplified by treating all the enzyme forms, implying binding of a substrate to an enzyme within a rapid equilibrium segment, as a single entity. On the contrary, reactions involving transformation of the previously bound substrates are considered rate-limiting reactions and treated as being in a steady state.

Following these criteria three set of reactions, considered in rapid equilibrium among themselves, were arranged in Boxes X, Y and Z. Reactions 1-4, in which binding of ATP, p_4A, or Ub, to E1 take place, were grouped in Box X; Reactions 8-12 and 14-15, implying the binding of P_2, P_3, AMP, ATP, p_4A and ubiquitin to E1, were grouped in Box Y. Reactions 20-22, catalyzing binding of P_2, or P_3 to E1 and transfer of ubiquitin from E1 to E2 were grouped in Box Z.

The reactions considered as being in steady state were those implying cleavage of ATP (reactions 5 and 18) or of p_4A (reactions 6 and 19) (**Figure 1**). These reactions interconnect Boxes X-Y and Boxes Y-Z).

3.1.2. Reactions in the Presence of Added Dithiothreitol (DTT), Iodoacetamide (IAA), Blot or Pyrophosphatase

As shown by Haas [6], DTT does not split the ubiquityl adenylate complex if it is tightly bound to the A-u area of E1 (as in EF 5). However, DTT breaks the thioester bond between Ub and a cysteine of E1 (**Figure 1**, EF 6), with formation of DTT-Ub. This last complex is rather unstable due either to the ability of ubiquitin itself to monitor its own C-terminal for the occurrence of thioester bond or to a possible contaminant thiolesterase present in the sample of E1 [6]. Iodoacetamide (IAA) binds covalently to -SH group(s) here indicated (schematically) at the left side of all the EFs (**Figure 1**). Particularly important, in the context of this work, is the reaction between IAA and the -SH residue of EF 5, to which ubiquitin is linked prior to its transference to E2. The effect of IAA (as it blocks reaction 9) results in a displacement of all the enzyme forms (EFs) of **Figure 1** towards those above EF 5, with the subsequent disappearance of EFs 6-11 and 15-17.

With respect to the effect of E2 on E1, E1 can also be viewed as the first enzymatic step for the ubiquitination of proteins and further degradation by the proteasome. To simulate the whole ubiquitination process a hypothetical reactant named Blot (from Blotting of ubiquitin) has been introduced. Blot is the sum of ubiquitin carrier proteins (E2), ubiquitin protein ligases (E3) and protein(s) to be ubiquitinated, and represents the destiny for all the ubiquitin molecules activated by E1. To simulate physiological conditions, Blot is supposed to be in large excess over E1. The reaction between EF 11 and the entity Blot has been named 22 and was considered in rapid equilibrium (**Figure 1**).

Finally, the effect of the addition of PPase to the system has been easily simulated by the following reaction, assumed to have Michaelis-Menten kinetics:

$$PPase + P_2 \longleftrightarrow PPaseP_2 \longrightarrow PPase + 2\ P_i$$

Thus, PPase hydrolyzing the P_2 liberated in reaction 8 (between EFs 4-5) and 20 (between EFs 10-11) displaces the equilibrium towards EF 5 and EF 11, respectively (**Figure 1**).

3.2. Mathematical Model

The mathematical model, a symbolic expression of the enzyme reactions assumed above (**Figure 1** and **Tables 1** and **2**), was developed with the help of the Mathematica Program according to the following steps:

3.2.1. Application to the Rapid Equilibrium Reactions Inside Boxes X, Y and Z (Supplemental Data, Appendix A)

The concentrations of the enzyme forms in rapid equilibrium were calculated following a similar procedure in each one of the Boxes: 1) each dissociation constant was equalled to its corresponding value according to the substrates and products involved; 2) the sum of the EFs contained in Boxes X, Y and Z were equalled to X, Y and Z, respectively; 3) the values of the 19 EFs to be calculated (5 in Box X; 10 in Box Y and 4 in Box Z) were requested with the command "Solve" of the Mathematica Program (Supplemental data, Appendix A). The rather cumbersome resulting equations, were disentangled with the command "Simplify" and used in the following step.

3.2.2. Steady State Reactions between Boxes X-Y and Y-Z (Supplemental Data, Appendix B)

The resulting equations for the 10 EFs involved in the steady state reactions were used to determine the actual net velocities: Vp (between EFs 3 and 4); VP (between EFs 13 and 14); VUp (between EFs 9 and 10); VUP (between EFs 16 and 17); Ve (between EF 18 and 1) and VB (between EFs 19 and 5). The velocities Ve and VB were also included to cope with situations described below, where the presence of dithiothreitol and E2 are contemplated. Those six velocities (Vp, VP, VUp, VUP, Ve and VB), were calculated as functions of the concentrations of EFs (as determined in Appendix A), the rate constants (k1-k8, k10, k12), and taking into account the forward (towards the synthesis of EF 11) and the reverse reactions (Supplemental data, Appendix B, a). In part b of Appendix B, the values of the 19 enzyme forms cal-

culated in Appendix A are presented; note that these values are grouped into two sections: 1) comprising those values directly involved in the steady state situation, and 2) the values implicit in the anterior formulas and needed for their solutions. In part c of Appendix B the statements needed for the solution of the equations are given: the total enzyme is defined as the sum of the amount of enzyme in Boxes X, Y and Z; by application of the steady state treatment suggested by Cha to the diagram of reactions (**Figure 1**), the net flux between boxes X and Y (VP + Vp-Ve) and between boxes Y and Z (VUP + VUp-VB) is set equal to zero and, finally, the unknowns to be solved are listed.

3.2.3. Ordinary Differential Equations System (Supplemental Data, Appendix C)

The changes in the concentration of reactants (or even of EFs) with the incubation time can be calculated with a system of differential equations performed with the Command "NDSolve" of the Mathematica Program, once the expression of the velocities are known. The syntax for this procedure admits many variants depending on the entity to be clarified. As an example, changes in the concentrations of ATP, p_4A, P_3, P_2, AMP, Blot or BlotUb are presented in Supplemental data, Appendix C. The Program admits other requested variants. The parameter values, initial assay conditions, and time of the reaction must also be included. Concerning the parameter values, two Procedures have been employed: Comprehensive and Simplified. The Comprehensive Procedure allows the theoretical calculation of all the variables of the system (19 EFs) as a function of: a) the total amount of E1, b) the value of the 15 dissociation constants and of the equilibrium constant yue, c) the value of the 10 rate constants, and d) the concentration of the reactants. This can be contemplated as an ideal scenery, helpful for example, to handle reactions that can not be performed experimentally, to investigate the role of each constant on the system and to calculate the concentrations of EFs and of the reactants under different experimental conditions, etc. However, given the scarcity of available experimental data, we considered it more convenient to introduce the Simplified Procedure (**Table 2**) with the following assumptions: the dissociation constant values for the binding of ATP, p_4A, P_2, P_3, Ub, AMP to any EF were set equal for each substrate, irrespective of the enzyme form (EFs) to which they bind (**Figure 1**, **Tables 1** and **2**); the values of the dissociation constants were taken from the literature, calculated as the average of different reported values (when this was the case) or tuned to fit the experimental results when no data on a particular constant had been reported (**Tables 1** and **2**); the constant UzueB (dissociation constant between EF 11 and EF 19 (**Figure 1**) was chosen arbitrarily as equal to 33 mM, since Blot is an hypothetical substrate that represents the sum of E2 + E3 + proteins (theoretically considered in large excess over E1); ii) the rate constants of each one of the pairs (k1, k3), (k2, k4), (k5, k7) and (k6, k8) were given the same value, as they correspond to similar catalyzed reactions (**Table 2**); from some experimental data [3,4] it can be deduced that the values of (k1, k3) and (k2, k4) are 75% of those of (k5, k7) and (k6, k8), respectively (**Table 1** and **2**) (**Figure 1**); finally, a previous study [4] specifically calculated that k7/k8 = 0.16; rate constant k5 was tuned to 0.13 s^{-1}; rate constant k12 was arbitrarily made equal to 3.3 s^{-1}, as we only wanted to compare the effect of different assay conditions in the ubiquitination rate of Blot. All these data are sufficient to fix one of the eight rate constants, allowing the rest of the seven constants to be calculated automatically by the program

3.3. Experimental Test of the Mathematical Model

Once the mathematical model was established and simplified, it was critical to confront it with the experimental results. As the mathematical scanning of the plethora of experimental results available on E1 would be beyond the scope of the present study, only the reactions taking place in the presence of ubiquitin, ATP, p_4A and P_3 and the influence of DTT, IAA, pyrophosphatase and Blot (E2 + E3 + proteins) on these reactions are considered. The advantage of P_3 over P_2 concerning the evaluation of the experimental results should be stressed. Whereas in the presence of ATP ($\pm P_2$) synthesis or degradation of ATP is observed [5] (*i.e.* no new compound is synthesized and the reaction could be studied mainly using radioactive substrates), in the presence of ATP ($\pm P_3$) the rate of synthesis of a new compound (p_4A) can be used as a tool to follow the course of the reaction.

3.3.1. Effect of Dithiothreitol (DTT)

According to the experimental findings reported by Haas [6], the effect of DTT has been here mathematically reproduced through the rapid equilibrium binding of DTT to EF 6, consequent breakage of the thioester bond between Ub and a cysteine located in the U region of the enzyme, formation of EF 1 and final liberation of AMP, DTT and Ub to the medium (**Figure 1**). The effect of DTT is theoretically clear: the synthesis of AMP from ATP is produced and AMP is liberated irreversibly to the reaction medium with displacement of the reactions toward the enzyme forms located above EF 6 in the scheme shown in **Figure 1**; the synthesis of p_4A takes place both through reaction 3, between EF 12 and EF 1 (Box X), and through reaction 14, between EF 15 and EF 7 (Box Y). As a consequence of the disappearance of the enzyme forms located below EF 6 by the effect of DTT, changes in the rate of synthesis of p_4A in the presence of DTT would be indicative of the relative rate of synthesis of p_4A by reaction 6 (between Boxes X-Y)

versus reaction 19 (between Boxes Y-Z). The experimental and theoretical rates of syntheses of AMP and p_4A (from ATP and P_3), in the absence of DTT or in the presence of increasing concentrations of DTT, are represented in **Figure 2**. The rate of synthesis of AMP clearly increased in the presence of DTT whereas the rate of synthesis of p_4A decreased slightly (about 8%) [3], indicating that the synthesis of p_4A takes place (in the absence of DTT) preferentially by reaction 3 (between EF 12 and EF 1). The experimental and the theoretical results agree quite well. The strict linearity of the experimental approach (in the upper panels of **Figure 2** reflects the fact that only one experimental point was considered. The theoretical maximum velocities were always calculated from the information provided by the suppliers on the amount of protein, enzyme activity and molecular weight of E1. Concerning the synthesis of p_4A (panels at the right), the apparent discrepancies between the experimental and theoretical results are attributable to the amount of active enzyme actually present in that assay. The effect of DTT on the ubiquitination of E2 (Blot) will be presented further on.

3.3.2. Effect of Iodoacetamide (IAA)

The experimental results (**Figure 3**) obtained with IAA

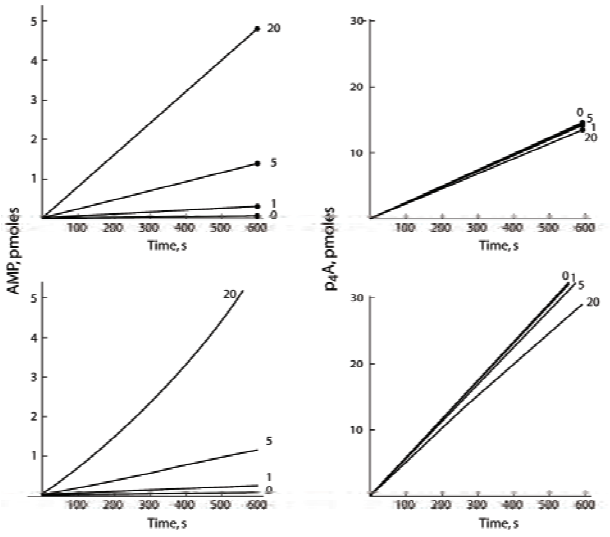

Figure 2. Influence of dithiothreitol (DTT) on the synthesis of AMP (panels on the left, A) and on the synthesis of p_4A (panels on the right, B): experimental results (upper panels) and theoretical calculation (lower panels). Initial assay conditions: 0.02 mM ATP; 6 µM ubiquitin; 0.8 mM P_3; 0.05 µg PPase; 0; 1; 5 and 20 mM DTT as indicated, and 1 pmol of E1. Time of the reaction 600 s. Experimental data were taken from [3] and theoretical calculations were obtained with the Mathematica Program as indicated in the text. Note that the synthesis of AMP is undetectable in the absence of DTT, both in experimental and theoretical conditions.

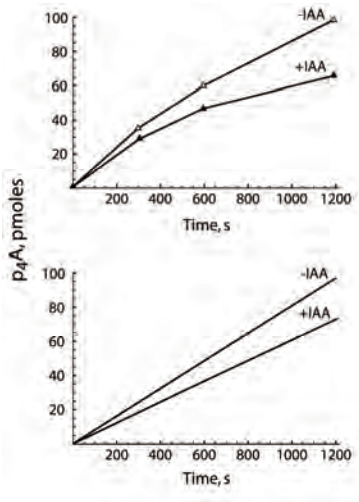

Figure 3. Influence of iodoacetamide (IAA) on the synthesis of p_4A and (not represented) on the synthesis of AMP: experimental and theoretical results. E1 at a final concentration of 0.75 nmol/ml (1.5 pmol of E1) was incubated in the presence of: 50 mM Tris–HCl, pH 7.5, and 1 mg/ml BSA for 30 min at 37 ºC and in the absence or presence of 0.5 mM IAA. Initial assay conditions were 0.02 mM ATP; 6 µM ubiquitin; 0.8 mM P_3; 0.05 µg PPase. DTT was omitted. Time of the reaction was 1200 s. Experimental data (upper panel) are taken from [3]. Theoretical results (lower panel) were obtained with the Mathematica Program. Synthesis of AMP was undetectable by both procedures and therefore is not represented in the Figure.

were performed with E1 previously incubated with IAA [5]. According to [4,5], IAA reacts covalently with a critical -SH residue located in the U region of E1, blocking its reaction with ubiquitin. This inhibition was simulated mathematically by giving the value zero to the equilibrium constant yue (**Figure 1**, reaction 9, between EF 5 and EF 6). Although the effect of IAA and DTT on E1 may seem apparently similar (both split the scheme of reactions presented in **Figure 1** into two parts, above and below a specific enzyme form: EF 5 and EF 6, respectively), the consequences are drastically different concerning the synthesis of AMP. Whereas DTT stimulates, IAA completely inhibits the synthesis of AMP, as EF 6 is not formed in the presence of IAA (see **Figure 3** and its legend). Following a similar reasoning as above, the effect of DTT and IAA on the synthesis of p_4A could be expected to be inhibitory. The experimental results pointed in that direction, with IAA being a more potentinhibitor of the synthesis of p_4A (25 %, **Figure 3**) than DTT (8%, **Figure 2**) [3].

3.3.3. Influence of Pyrophosphatase

In the presence of Ub, ATP, and P_3, synthesis of P_2 takes place (**Figure 1**) in reactions 5 and 8 (with the participa-

tion of EFs 3-5) and in reactions 18 and 20 (with participation of EFs 9-11); P_2 is a substrate for the synthesis of ATP in the same reactions as above, acting in the reverse direction. In the presence of PPase, P_2 is degraded and reactions 8 and 20 cannot proceed in the reverse direction (**Figure 4**). Consequently, in the presence of PPase and P_3 the synthesis of p_4A is favored, by displacement of the E1 cycle towards the left part of **Figure 1**, *i.e.* toward the synthesis of p_4A. Previous results from this laboratory [3] had shown that the addition of PPase to a reaction mixture containing P_3, almost doubled the rate of synthesis of p_4A and slightly inhibited the synthesis of AMP. The theoretical and experimental results on the influence of PPase on the synthesis of AMP and p_4A are shown in **Figure 4**.

3.3.4. p_4A as Substrate of the Reaction

This experiment was performed by allowing a complete transformation of [a-^{32}P]ATP into labeled [a-^{32}P]p_4A in the presence of Ub, P_3 and PPase [3]. Further incubation of this reaction mixture converted gradually the synthesized p_4A into AMP thanks to the effect of DTT. The experimental and theoretical results are shown in **Figure 5**, demonstrating that p_4A is a substrate for the synthesis of AMP through EFs 12-14, 5, 6, 18 and 1. In this way, when the final equilibrium is reached, AMP is the only destiny for all the ATP initially present in the assay mixture. The small differences between the experimental and theoretical results might be related to the inactivation of the enzyme after prolonged times of incubation (**Figure 5**).

3.3.5. Influence of E2

In the presence of only ATP and ubiquitin, the enzyme catalyzes a rapid pre-steady state situation where only two equivalents of ATP per equivalent of enzyme are hydrolyzed [4]. The hydrolysis of ATP can be stimulated by the addition of P_3 (as in previous sections) or by the addition of an ubiquitin acceptor (**Figure 1**). This last situation is here simulated by the addition of Blot, a mixture of E2 + E3 + proteins, representing a sink for the activated ubiquitin. The main reaction in the presence of Blot is represented by:

$_{UbS}E_{AMPUb}$ (EF 11) + Blot <—> $_{UbS}E_{AMPUbBlot}$ (EF 19) —> $_{HS}E_{AMPUb}$ (EF 5)+ BlotUb

These steps have been simulated by one reversible reaction in rapid equilibrium (reaction 22 between EF 11 and EF 19) and one reaction in steady state (VB). This last reaction (17) is considered irreversible because of the physiological large excess of (E2 + E3 + proteins) over E1 (**Figure 1**). The complete cycle for the hydrolysis of ATP in the presence of Blot is composed of reactions 22, 17, 9-12, 18, 20 (**Figure 1**). The influence of Blot (at 0, 0.5, 1, 2, 5, 15 mM) on the reaction catalyzed by E1 is represented in **Figure 6** panels a and b. In the absence of Blot changes in the concentration of ATP, or synthesis of AMP (not represented) are undetectable (**Figure 6 (a)**); the rate of disappearance of ATP increased with increasing concentrations of Blot, with an apparent activation constant of about 1.5 mM for Blot in

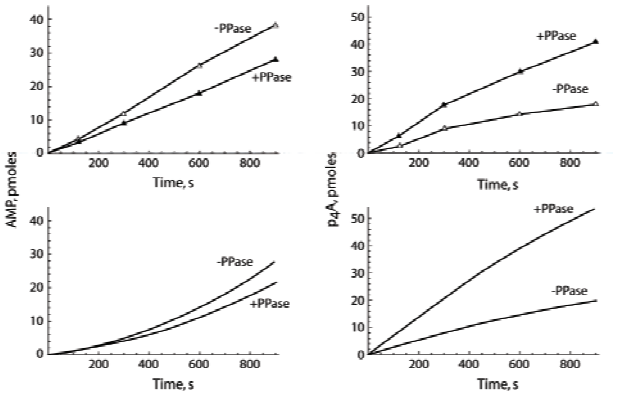

(a) (b)

Figure 4. Influence of PPase on the synthesis of AMP (left-hand panels A) and p_4A (right-hand panels, B): experimental and theoretical results. Initial assay conditions: 0.02 mM ATP; 6 μM Ub; 0.8 mM P_3; 20 mM DTT; 1.5 pmol E1 and, when indicated, 0.05 μg PPase. Reaction time: 900 s. Experimental data were taken from [3] and represented in the upper part of both panels. The theoretical results are represented in the lower panels.

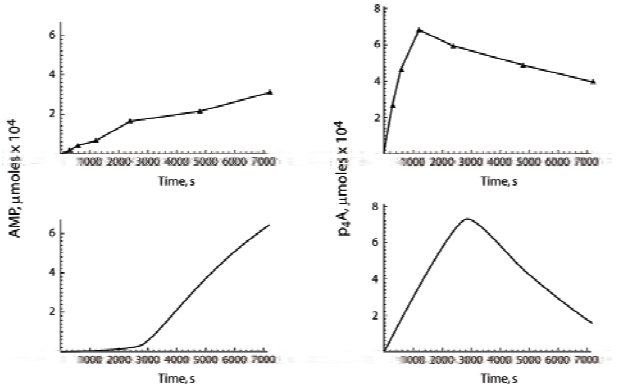

(a) (b)

Figure 5. Adenosine 5'-tetraphosphate (p_4A) as substrate for the synthesis of AMP: experimental and theoretical results. Initial assay conditions: 0.04 mM ATP; 12 μM Ub; 0.8 mM P_3; 0.05 μg PPase; 2 mM DTT and 4 pmol E1. The reaction time was increased to 7200 s (2 hours) in order to consume all the ATP in the assay. In this way, the synthesis and posterior degradation of p_4A towards formation of AMP can be observed, as a function of incubation time. Experimental data were taken from [3] and represented in the upper part of both panels. Theoretical results obtained for the synthesis of AMP and p_4A are represented in the lower panels.

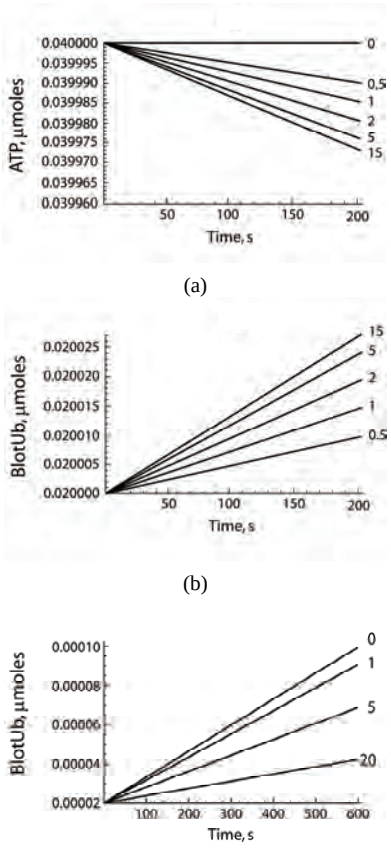

Figure 6. Theoretical approach for ubiquitination of Blot (E2+E3+proteins) by E1 and inhibition of this process by DTT. The pre-established theoretical conditions in the upper panels were: 2 mM ATP; 6 µM Ub; 1.5 pmol E1; 0.05 µg PPase and Blot (0; 0.5; 1; 2; 5 and 15 mM). Time of reaction: 200 s. In the absence of Blot and DTT, the concentrations of ATP remain constant. Upon addition of increasing concentrations of the Blot reactant (which represents a sink for activated ubiquitin) consumption of ATP (panel a) and formation of ubiquitinated Blot (BlotUb) (panel b) can be observed. In panel c, the pre-established theoretical conditions are as above, except that AMP (0.8 mM) and Blot (65 mM), were included to simulate physiological conditions; DTT was included at theoretical concentrations of 0, 1, 5 and 20 mM as indicated. Time of reaction: 600 s.

these theoretical conditions (**Figure 6 (a)**). The influence of the concentration of Blot on the synthesis of BlotUb followed a similar pattern to that observed for the degradation of ATP (**Figure 6 (b)**). Finally, the influence of DTT on the ubiquitination process was tested in the presence of physiological concentrations of ATP (2 mM), AMP (0.8 mM) and Blot (E2 + E3 + protein) (65 mM). Inhibition rates for the ubiquitination of Blot of 10, 32 and 57 % were calculated in the presence of 1, 5 and 20 mM DTT (**Figure 6 (c)**). This inhibition by DTT was due to the displacement of the equilibrium of the system away from $_{UbS}E_{AMPUb}$ (EF 11), the enzyme form donating Ub to E2.

3.3.6. Responsiveness and Predictability of the System

Metabolic control analysis [18] deals mainly with the steady state of a system of enzymes that connect series of metabolites. In our view, this theory is not directly applicable in the case of the E1 ubiquitin system composed only of one enzyme, with different enzyme forms. Nevertheless some of the concepts developed for metabolic control analysis could be of application to the E1 system. Hence, the response of the system to changes in the concentration of ATP or ubiquitin was tested. Considering the rate of ubiquitination of Blot (**Figure 1**, reaction 17) as the final flux, representation of ln ATP (**Figure 7 (a)**) or ln Ubiquitin (**Figure 7 (b)**) *versus* ln rate of synthesis of BlotUb, a good correlation among those parameters were obtained showing the responsiveness of the theoretical approach. The apparent elasticity coefficient of E1 towards ATP and ubiquitin were near 0 and 0.29, respectively at the concentration points used routinely in the assays, 20 µM and 6 µM, respectively.

The predictability of the system was tested with a situation not contemplated in the previous kinetics treatment: the influence of the concentration of AMP on the synthesis of p_4A in the presence of ATP and ubiquitin. That influence on AMP, predicted using the Mathematica Program (**Figure 7 (c)**) was later approached experiment-

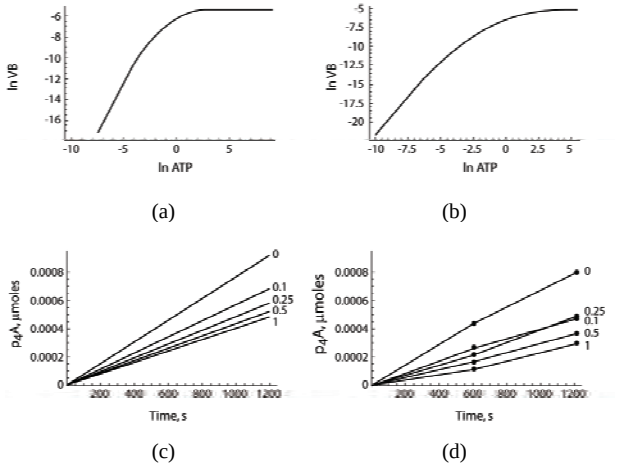

Figure 7. Responsiveness and predictability of the E1 system. As a measure of the responsiveness of the system, the influence of the concentration of ATP (panel a) or ubiquitin (panel b) on the ubiquitination of Blot are represented as a double-logarithmic plot. The elasticities of E1 towards ATP or ubiquitin are the slopes of the tangents of the corresponding curves. The predictability of the system was tested in two complementary ways. That influence on AMP on the synthesis of p_4A, predicted using the Mathematica Program (**Figure 7 (c)**), was later approached experimentally with identical results (**Figure 7 (d)**).

tally with identical results (**Figure 7 (d)**). In both cases AMP accelerated the rate of synthesis of p_4A. The physiological implications of this finding will be explored elsewhere in another study.

4. CONCLUDING REMARKS

The above results may be considered from different perspectives. The ubiquitin activating enzyme E1 has been treated as a complex enzyme system comprising 8 reactants, 2 inhibitors/effectors, and 19 enzyme forms (EFs) (**Figure 1**). Calculation of the rate equations of this type of reactions has been approached with the King and Altman method [19] and/or with the simplifications introduced in [20,21] and in [17]. For a general comment on these procedures, see [22]. Although these methods may appear mathematically simple they present great difficulties due to the potential errors introduced during the process of manual operations. Fortunately, with the introduction of computer methods of calculation, performed here with the Mathematica Program [15], treatment of the concerned equations has been greatly simplified. The only difficulty is how to feed the computer with the appropriate information. The simplifications introduced by Cha [17] have been of great help for the mathematical treatment of the postulated reactions catalyzed by the ubiquitin activating enzyme, a system that seemed to be particularly appropriated for this mathematical treatment. Cha [17] postulated that when an enzyme-catalyzed reaction consists of more than one step, and one or more portions of the whole reaction are significantly faster than the over-all reaction, the partial reactions in such segments have almost reached equilibrium when the over-all reaction reaches a steady state. As shown in **Figure 1**, clusters of reactions of the E1 system involving binding of substrates were considered in rapid equilibrium, were grouped in boxes X, Y and Z, and treated as three single entities; another group of reactions involving modification of the bound substrates were treated as in a steady state situation. Altogether, the panorama is similar to the one presented by Cha to develop his methodology [17]. In our view, other complex enzyme situations can be approached in the same way, and the kinetics treatment of E1, here shown, can be taken as an example. Presently we are applying Cha's approach to the mathematical treatment of the signal transductions involved in glycogen metabolism.

Although P_3 and p_4A are here exclusively considered as a kinetic tool to unravel the set of reactions catalyzed by E1, they also have physiological significance by themselves. Inorganic polyphosphates are probably present in every cell [23,24,25] and are particularly abundant in yeast extracts where P_3 and P_4 have been described at mM concentrations [23]. As previously pointed out [3,26], the potential effects exerted by polyphosphates can be considered under two different aspects: Either caused by their presence at high concentration and frequently condensed in organelles or caused by their occurrence at low concentration in different cellular compartments. Although their role in the last case is not clear, there is a widespread concern about the possibility of polyphosphates playing more general and universal functions in biology [23,24]. In the case of E1, it is difficult for us to envisage the physiological role of P_3, considering its high apparent K_m value in the reactions here described [3]. The occurrence of p_4A has been described in chromaffin granules of the adrenal medulla [27], in skeletal and cardiac muscle [28,29], in the aqueous humor of rabbits [30] and in yeast [31]. p_4A has been involved in yeast sporulation [31] and as a modulator of cardiac vascular tone [29]. p_4A could also indirectly modulate the levels of Ap_4A and Ap_4N (nucleotides with apparently elusive physiological roles [32, 33]), by inhibiting (K_i, nM) the activity of the *(assymetrical)* dinucleoside tetraphoshatase (EC 3.6.1.17) [34].

The present study can also be viewed as pertinent to the so-called System Biology aiming to understand general principles of the complexity of living cells [35,36, 37]. This complexity is so astonishing that restricted approaches to simple networks could pave the way for the uncovering of some general principles governing higher organisms. Examples are the study of signal transductions, gene expression, evolution and selforganization, understanding the cell cycle, fluxes in metabolic pathways, neural networks, modeling of biological processes, etc. Study of metabolic processes is one of the main topics of modern System Biology and the work presented here can be considered as an example on how the conjugation of a theoretical and an experimental approach to a particular topic, may help to jump from a mere reductionism to a more global vision of that problem.

The present study has to be considered as an example rather than a framework for the mathematical treatment of complex biological systems. This work may be important to understand the ubiquitin proteasome system itself. This system is the center of a vast arrangement of cellular processes including: cell cycle, transcription control, regulation of enzyme levels, antigen presentation, rate for disposing of unfolded or damaged proteins and controlling life span of regulatory proteins, etc. Alteration of the ubiquitin proteasome system is also responsible for the genesis of malignant diseases and neurodegenerative disorders.

In summary, as shown above this work deals only with the ubiquitin activating enzyme (E1). The reactions catalyzed by E1 are well known from studies developed by Haas, Ciechanover, Hersko, Rose and others [4,5,6], mainly in crude extracts. The present report, greatly inspired by their work, has been carried out with purified, and commercially available E1. The use of P_3 as substrate of the enzyme has greatly helped to follow the

steps of the intermediary reactions (see above). Two mathematical methods have been used for that purpose: Comprehensive and Simplified methods. Some of the kinetic constants involved in these reactions, implicit in the Comprehensive Method, are not yet known and have been tuned; in addition, a simplification of the Comprehensive method has been introduced. The corner-stone of the mathematical treatment of any of these systems is that the experimental and the theoretical results must be consistent. When this is so, the theoretical approach can be used with more confidence and new questions can be theoretically proposed and contrasted with experimental results. In this regard, the effect of potential drugs acting on E1 [38] can be explored in the presence of ATP, P_3 and ubiquitin, and the experimental results contrasted with the theoretical approach developed here aiming to pinpoint their precise mode of drug action.

5. CONCLUSSIONS

The aim of this work was to investigate the reactions catalyzed by the ubiquitin activating enzyme (E1) using ubiquitin, ATP, adenosine tetraphosphate (p_4A), pyrophosphate, tripolyphosphate, and ubiquitin activating enzyme (E2) as substrates and iodoacetamide dithiothreitol, as inhibitors of the reaction. A total of 19 different hypothetical enzyme forms (EF) of E1 and 22 different enzyme reactions were established and the equations relating the enzyme forms approached with a system of ordinary differential equations and solved with the help of the Mathematica Program. This study can be view a) as a way to treat a complex biological system, b) as a possibility to follow the steps of the intermediate reactions and the theoretical concentrations of the intermediate enzyme forms; c) as a method to study the effects of possible inhibitors on E1 and by extrapolation on the proteasome system itself. Note: the Supplemental Data is available on request from Antonio Sillero at: antonio.sillero@uam.es.

6. ACKNOWLEDGEMENTS

This investigation was supported by grants from Dirección General de Investigación Científica y Técnica (BFU 2008-00666 and BFU2009-08977). We thank Anabel de Diego, Antonio Fernández and Javier Pérez for very capable technical assistance and Professor José Gonzalez Castaño and Dr. Gabriela Morreale de Escobar for helpful suggestions and critical reading of the manuscript.

REFERENCES

[1] Sillero, A. and Günther Sillero, M.A. (2000) Synthesis of dinucleoside polyphosphates catalyzed by firefly luciferase and several ligases. *Pharmacology and Therapeutics*, **87**, 91-102.

[2] Ortiz, B., Sillero, A. and Günther Sillero, M.A. (1993) Specific synthesis of adenosine(5')tetraphospho(5') nucleoside and adenosine(5')oligophospho(5')adenosine (n > 4) catalyzed by firefly luciferase. *European Journal of Biochemistry*, **212**, 263-270.

[3] Günther Sillero, M.A., de Diego, A., Silles, E. and Sillero, A. (2005) Synthesis of (di)nucleoside polyphosphates by the ubiquitin activating enzyme E1. *FEBS Letter*, **579**, 6223-6229.

[4] Haas, A.L. and Rose, I.A. (1982) The mechanism of ubiquitin activating enzyme. A kinetic and equilibrium analysis. *Journal of Biological Chemistry*, **257**, 10329-10337.

[5] Haas, A.L., Warms, J.V., Hershko, A. and Rose, I.A. (1982) Ubiquitin-activating enzyme. Mechanism and role in protein-ubiquitin conjugation. *Journal of Biological Chemistry*, **257**, 2543-2548.

[6] Haas, A.L., Warms, J.V. and Rose, I.A. (1983) Ubiquitin adenylate: Structure and role in ubiquitin activation. *Biochemistry*, **22**, 4388-4394.

[7] Hershko, A. and Ciechanover, A. (1998) The ubiquitin system. *Annual review of biochemistry*, **67**, 425-479.

[8] Baumeister, W., Walz, J., Zuhl, F. and Seemuller, E. (1998) The proteasome: Paradigm of a self-compartmentalizing protease. *Cell*, **92**, 367-380.

[9] Ciechanover, A., Orian, A. and Schwartz, A.L. (2000) The ubiquitin-mediated proteolytic pathway: Mode of action and clinical implications. *Journal of Cell Biochemistry Supply*, **34**, 40-51.

[10] Glickman, M.H. and Ciechanover, A. (2002) The ubiquitin-proteasome proteolytic pathway: Destruction for the sake of construction. *Physiological reviews*, **82**, 373–428.

[11] Lee, I. and Schindelin, H. (2008) Structural insights into E1-catalyzed ubiquitin activation and transfer to conjugating enzymes. *Cell*, **134**, 268-278.

[12] Selivanov, V.A., Puigjaner, J., Sillero, A., Centelles, J.J., Ramos-Montoya, A., Lee, P.W. and Cascante, M. (2004) An optimized algorithm for flux estimation from isotopomer distribution in glucose metabolites. *Bioinformatics*, **20**, 3387-3397.

[13] Torrecilla, A., Marques, A.F., Buscalioni, R.D., Oliveira, J.M., Teixeira, N.A., Atencia, E.A., Günther Sillero, M.A. and Sillero, A. (2001) Metabolic fate of AMP, IMP, GMP and XMP in the cytosol of rat brain: An experimental and theoretical analysis. *Journal of Neurochemistry*, **76**, 1291-1307.

[14] Osorio, H., Carvalho, E., del Valle, M., Günther Sillero, M.A., Moradas-Ferreira, P. and Sillero, A. (2003) H_2O_2, but not menadione, provokes a decrease in the ATP and an increase in the inosine levels in *Saccharomyces cerevisiae*. An experimental and theoretical approach. *European Journal of Biochemistry*, **270**, 1578-1589.

[15] Wolfram, S. (1996) The Mathematica Book. Cambridge University Press, Cambridge.

[16] Segel, I.H. (1975) Enzyme kinetics: Behavior and analysis of rapid equilibrium and steady state enzyme systems. Wiley, New York.

[17] Cha, S. (1968) A simple method for derivation of rate equations for enzyme-catalyzed reactions under the rapid equilibrium assumption or combined assumptions of equilibrium and steady state. *Journal of Biological Chemistry*, **243**, 820-825.

[18] Fell, D. (1997) Understanding the control of metabolism, Portland Press, MiamiBrookfield.

[19] King, E.L. and Altman, C. (1956) A schematic method for deriving the rate laws for enzyme-catalyzed reactions. *The Journal of Physical Chemistry*, **60**, 1357-1378.
[20] Wong, J.T. and Hanes, C.S. (1962) Kinetic formulations for enzymic reactions involving two substrates. *Canadian journal of biochemistry and Physiology*, **40**, 763-804.
[21] Volkenstein, M.V. and Goldstein, B.N. (1966) Allosteric enzyme models and their analysis by the theory of graphs. *Biochimica et Biophysica Acta*, **115**, 471-477.
[22] Cornish-Bowden, A. (1995) Fundamental of enzyme kinetics. Portland Press, London.
[23] Kulaev, I.S. and Vagabov, V.M. (1983) Polyphosphate metabolism in micro-organisms. *Advances in Microbial Physiology*, **24**, 83-171.
[24] Wood, H.G. and Clark. J.E. (1988) Biological aspects of inorganic polyphosphates. *Annual Review of Biochemistry*, **57**, 235-260.
[25] Kornberg, A., Rao, N.N. and Ault-Riche, D. (1999) Inorganic polyphosphate: A molecule of many functions. *Annual Review of Biochemistry*, **68**, 89-125.
[26] Günther Sillero, M.A., de Diego, A., Silles, E., Osorio, H. and Sillero, A. (2003) Polyphosphates strongly inhibit the tRNA dependent synthesis of poly(A) catalyzed by poly(A) polymerase from *Saccharomyces cerevisiae*. *FEBS Letter*, **550**, 41-45.
[27] Günther Sillero, M.A., Del Valle, M., Zaera, E., Michelena, P., Garcia, A.G. and Sillero, A. (1994) Diadenosine 5',5''-P1,P4-tetraphosphate (Ap_4A), ATP and catecholamine content in bovine adrenal medulla, chromaffin granules and chromaffin cells. *Biochimie*, **76**, 404-409.
[28] Small, G.D. and Cooper, C. (1966) Studies on the occurrence and biosynthesis of adenosine tetraphosphate. *Biochemistry*, **5**, 26-33.
[29] Westhoff, T., *et al.* (2003) Identification and characterization of adenosine 5'-tetraphosphate in human myocardial tissue. *The Journal of Biological Chemistry*, **278**, 17735-17740.
[30] Pintor, J., Pelaez, T. and Peral, A. (2004) Adenosine tetraphosphate, Ap4, a physiological regulator of intraocular pressure in normotensive rabbit eyes. *Journal of Pharmacology and Experimental Therapeutics*, **308**, 468-473.
[31] Jakubowski, H. (1986) Sporulation of the yeast *Saccharomyces cerevisiae* is accompanied by synthesis of adenosine 5'-tetraphosphate and adenosine 5'-pentaphosphate. *Proceedings of the National Academy of Sciences*, **83**, 2378-2382.
[32] McLennan, A.G. (2000) Dinucleoside polyphosphates-friend or foe? *Pharmacology and Therapeutics*, **87**, 73-89.
[33] Mc Lennan, A.G., *et al.* (2001) Recent progress in the study of the intracellular functions of diadenosine polyphosphates. *Drug Development Research*, **52**, 249-259.
[34] Lobatón, C.D., Vallejo, C.G., Sillero, A. and Sillero, M.A. (1975) Diguanosinetetraphosphatase from rat liver: Acitivity on diadenosine tetraphosphate and inhibition by adenosine tetraphosphate. *European journal of Biochemistry*, **50**, 495-501.
[35] Alon, U. (2006) An introduction to system biology. Design principles of biological circuits. CRC Press, Taylor & Francis Group, London.
[36] Klipp, E., Herwig, R., Kowald, A., Wierling, C. and Lehrach, H. (2005) System biology in practice. Concepts, implementation and application, Wiley-VCH Verlag GmbH & Co., Weinhein.
[37] Fell, D. (1997) Undersatnding the control of metabolism, Portland Press, London.
[38] Yang, Y., *et al.* (2007) Inhibitors of ubiquitin-activating enzyme (E1), a new class of potential cancer therapeutics. *Cancer Research*, **67**, 9472-9481.

J. Biomedical Science and Engineering, 2010, 3, 285-290 **JBiSE**
doi:10.4236/jbise.2010.33038 Published Online March 2010 (http://www.SciRP.org/journal/jbise/).

Z-Scan technique: To measure the total protein and albumin in blood

A. N. Dhinaa, P. K. Palanisamy*

Department of Physics, Anna University Chennai, Chennai, India.
Email: profpkpannauniv@yahoo.co.in

Received 19 December 2009; revised 28 December 2009; accepted 4 January 2010.

ABSTRACT

Z-scan technique is an effective tool for measuring the optical nonlinearity of the materials. By using this technique the measurement was made for total protein and albumin. The nonlinear refractive index of the total protein and albumin were found to vary linearly with concentration. Hence by calculating the nonlinear refractive index it is possible to measure their concentration in the sample. The values measured thus are found in equivalence with conventional colorimetric method.

Keywords: Z-scan Technique; Nonlinear Refractive Index; Total Protein; Albumin

1. INTRODUCTION

Protein is an essential nutrient made up of building-block chemicals called amino acids. Protein provides energy and is needed for the body to make new cells, to maintain and rebuild muscles, to carry other nutrients, to act as messengers in the body, and to support the immune system. A total serum protein test measures the total amount of protein in the blood. It also measures the amounts of two major groups of proteins in the blood: albumin and globulin.

Albumin is made mainly in the liver. It helps keep to the blood from leaking out of blood vessels. Albumin also helps to carry some medicines and other substances through the blood and is important for tissue growth and healing.

Globulin is made up of different proteins called alpha, beta, and gamma types. Some globulins are made by the liver, while others are made by the immune system. Certain globulins bind with hemoglobin. Other globulins transport metals such as iron in the blood and help fight infection.

Low total protein levels can suggest a liver disorder, a kidney disorder, or a disorder in which protein is not digested or absorbed properly. Low levels may be seen in severe malnutrition and with conditions that cause malabsorption, such as Celiac disease or inflammatory bowel disease (IBD). High total protein levels may be seen with chronic inflammation or infections such as viral hepatitis or HIV. They may be caused by bone marrow disorders such as multiple myeloma.

Measurements of protein may reflect liver disease, nutritional state, kidney disease and others. A decreased value of total protein may indicate liver or kidney disease. If levels of albumin are low, there is a possibility of primary liver disease, kidney disease, tissue damage or inflammation, and malnutrition [1,2]. In chronic liver diseases like “cirrhosis” or “nephrotic syndrome” the level is decreased. Poor nutrition or protein catabolism may cause “hypoalbuminaemia”. Measurement of serum-total protein is useful in conditions relating to changes in plasma or fluid volumes, such as shock and dehydration. In these conditions concentration of serum-total protein is elevated indicating hemoconcentration. Haemodilution is reflected as relative hypoproteinemia, which occurs with water intoxication or salt retention syndrome, during massive intravenous infusions.

The most widely accepted assays so far for proteins are the Biuret [3], Lowry [4], Bradford [5,6], Bromophenol Blue [7] and Bromocresol Green[8] methods. In this Biuret reaction is highly susceptible to interference by non-protein substances [9,10,11,12]. The bromocresol green method for determination of serum albumin is the most specific and sensitive of the dye binding techniques [13]. The glyoxylic acid method measures tryptophan content which represents 8-10% albumin and 90-91% globulin. Since the bromocresol green method is specific and simple, it is the method of choice for albumin determination [14].

The Z-scan technique was extended to study the optical nonlinearity has been reported for LDL-Cholesterol [15,16]. Some more reports are on characterization of lipids in body fluid [17,18], study of the nonlinear refraction of vitreous humor in human and rabbit [19], determination of nonlinear refractive index of retinal derivatives [20]. In this present investigation total protein and albumin are subjected to the Z-scan technique to cal-

culate the nonlinear refractive index (n_2). Already work has been done on measurement of glucose [21], total cholesterol and triglycerides [22].

The single beam Z-scan analysis, which was developed by Mansoor Sheik Bahae *et al.* [23], is a simple and effective tool for determining nonlinear optical properties of materials [24,25,26,27]. This approach has been now a day widely used in optical characterization of different materials. Nonlinear refractive index is proportional to the real part of the third-order susceptibility Re[$\chi(3)$]. Basically, the Z-scan method consists in translating a nonlinear sample through the focal plane of a tightly focused Gaussian laser beam and monitoring the changes in the far field intensity pattern. For a purely refractive nonlinearity, the light field induces an intensity dependent nonlinear phase and, as consequence of the transverse Gaussian intensity profile, the sample presents a lens-like behavior. The induced self-phase modulation has the tendency of defocusing or recollimating the incident beam, depending on its Z position with respect to the focal plane. By monitoring the transmittance change through a small circular aperture placed at the far field position, it is possible to determine the nonlinear refractive index. In the present study, we have measured total protein and albumin levels in blood by calculating the nonlinear refractive index (n_2) value using a single beam Z-scan method.

2. METHODOLOGY

2.1. Preparation of Total Protein Sample

For sample preparation (Total Protein-Biuret method - a kit supplied by Transasia Bio-medicals Ltd, Baddi, Himachal Pradesh, India) was used. To 20 microliter of the serum one milliliter of total protein reagent was added and incubated for 10 minutes at 37 ^{o}C. The principles involved for this reaction is that the peptide bonds of protein react with copper II ions in alkaline solution to form blue-violet complex (Biuret reaction). Each copper ion complexes with 5 or 6 peptide bonds. Tartrate is added as a stabilizer whilst Iodide is used to prevent auto-reduction of the alkaline copper complex. The color formed is proportional to the protein concentration.

2.2. Preparation of Albumin Sample

For sample preparation (Albumin-BCG method - a kit supplied by Transasia Bio-medicals Ltd, Baddi, Himachal Pradesh, India) was used. To 10 microliter of the serum one milliliter of albumin reagent was added and incubated for 1 minute at 37^{o}C. The principle involved in this reaction is that the albumin binds with Bromocresol green (BCG) at pH 4.2 causing a shift in absorbance of the yellow BCG dye. The Blue green color formed is proportional to the concentration of albumin.

2.3. Nonlinear Refractive Index

The Z-scan experiments were performed using a 532 nm Nd: YAG (SHG) CW laser beam (COHERENT–Compass 215M-50 diode-pumped laser) and He-Ne laser beam (RESEARCH ELECTRO OPTICS–30995 cylindrical helium-neon laser) focused by a lens of 35 mm focal length. The experimental set up is shown in **Figure 1**.

A typical closed-aperture Z-scan curve for the standard total protein solution at incident intensity Io = 7.824 kW/cm^2. Likewise the Z-scan curve for standard albumin solution at incident intensity Io = 1.758 kW/cm^2. This normalized transmittance curves are characterized by a pre-focal peak followed by a post-focal valley. This implies that the nonlinear refractive indices of total protein, albumins are negative ($n_2 < 0$). The defocusing effect shown in Z-scan curve can be attributed to a thermal nonlinearity resulting from absorption of radiation at 532 nm and 633 nm respectively. Localized absorption of a tightly focused beam propagating through an absorbing sample medium produces a spatial distribution of temperature in the sample solution and consequently, a spatial variation of the refractive index, that acts as a thermal lens resulting in phase distortion of the propagating beam.

The nonlinear refractive index (n_2) is calculated using the standard relations [18].

$$\Delta T_{p-v} = 0.406\,(1 - S)^{0.25}\,\left|\Delta\Phi_0\right| \qquad (1)$$

where ΔT_{p-v} can be defined as the difference between the normalized peak and valley transmittances $(T_p - T_v)$, $\left|\Delta\Phi_0\right|$ is the on-axis phase shift at the focus.

The linear transmittance of the aperture is given by

$$S = 1 - exp\,(-2r_a^2 / w_a^2) \qquad (2)$$

where r_a is the radius of the aperture and w_a is the beam radius at the aperture.

$$n_2 \approx \frac{\Delta\Phi_0}{kI_0L_{eff}} \qquad (3)$$

where n_2 is the nonlinear refractive index, k is the wave number($k = \frac{2\pi}{\lambda}$) and

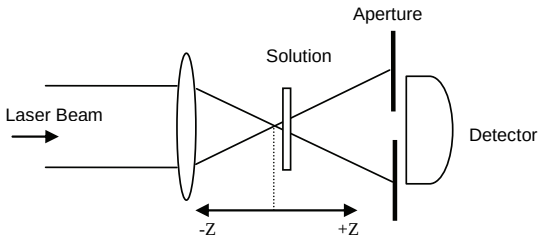

Figure 1. Experimental setup for Z-scan technique.

$$L_{eff} = \frac{1-e^{-\alpha L}}{\alpha}$$

$I_0 = \frac{2P}{\pi w_0^2}$ is defined as the peak intensity within the sample at the focus. L is the thickness of the sample, α is the linear absorption coefficient.

An additional experiment was performed with a conventional colorimetric method following the standard procedure of A. G. Gornall *et al.* [3] and R. L. Rodkly *et al.* [8] for total protein and albumin samples respectively. This involves measurement of optical density variation with respect to concentration. These results are compared with the results calculated with the Z-scan technique.

2.4. Statistical Analysis

The error involved in the measurements was determined by *t* test, $P < 0.01$.These statistical analysis was conducted using SPSS commercial statistical package (SPSS, version 10.0 for windows, SPSS Inc., Chicago, U.S.A).

3. RESULTS AND DISCUSSION

3.1. Measurement of Absorbance Spectra

The absorption spectra were measured using UV-Vis spectrophotometer (SHIMADZU- UV-2401PC), and the spectra for both total protein and albumin were found to be broad banded as depicted in **Figure 2**. Hence for further study 532 nm Nd:YAG laser for total protein and 633 nm He-Ne laser for albumin were used.

3.2. Measurement of Nonlinear Refractive Indices

The results of typical Z-scan normalized transmittance measurement for total protein and albumin are shown in **Figure 3**. As the concentration of the total protein and albumin increases, the normalized transmittance peak increases whereas the valley decreases respectively. The graph in **Figure 4 (a)** and **(b)** shows that the ΔTp-v value linearly increases with concentration of standard total protein and albumin solutions. Similarly in **Figure 4 (c)** and **(d)** refractive index value linearly increases with concentration of standard total protein and albumin solutions.

In addition experiment based on optical density is

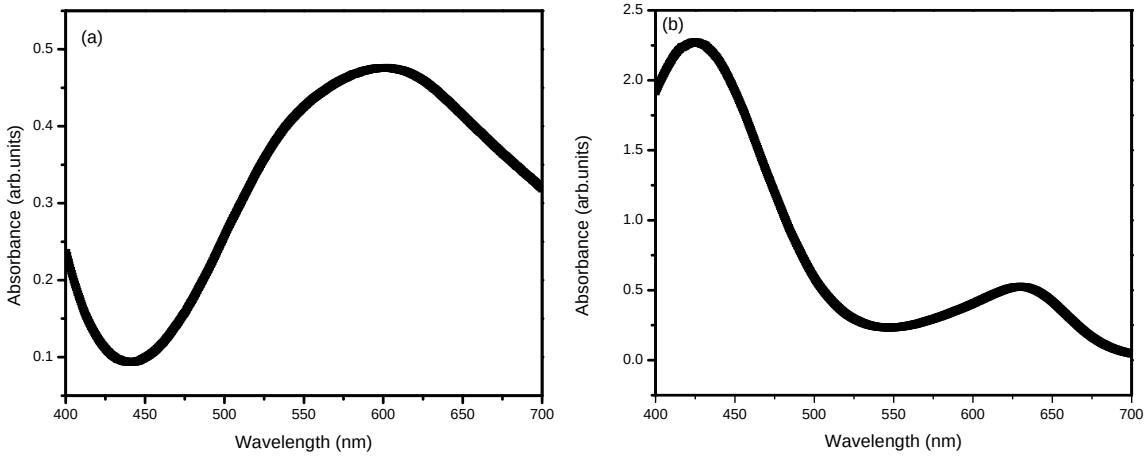

Figure 2. UV-Vis Spectra of standard (a) total protein (b) albumin with reagent.

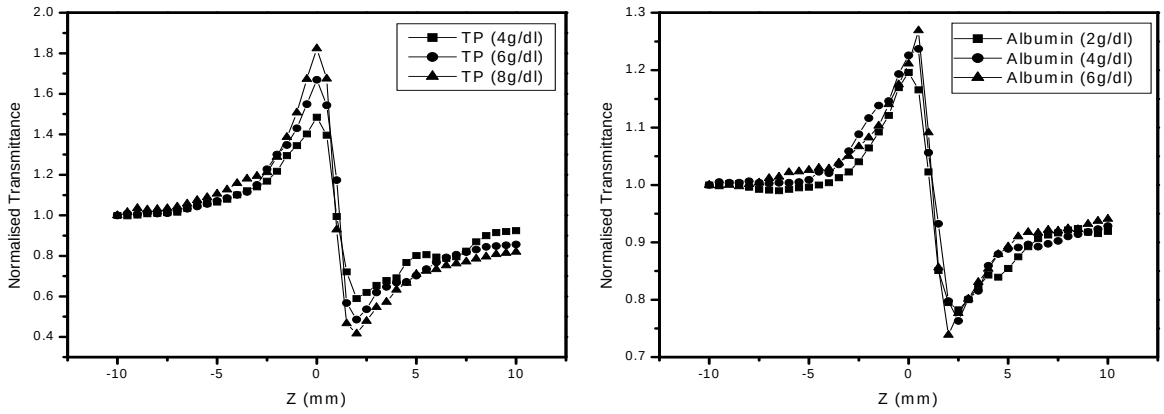

Figure 3. Z-scan data of the standard total protein (TP) and albumin.

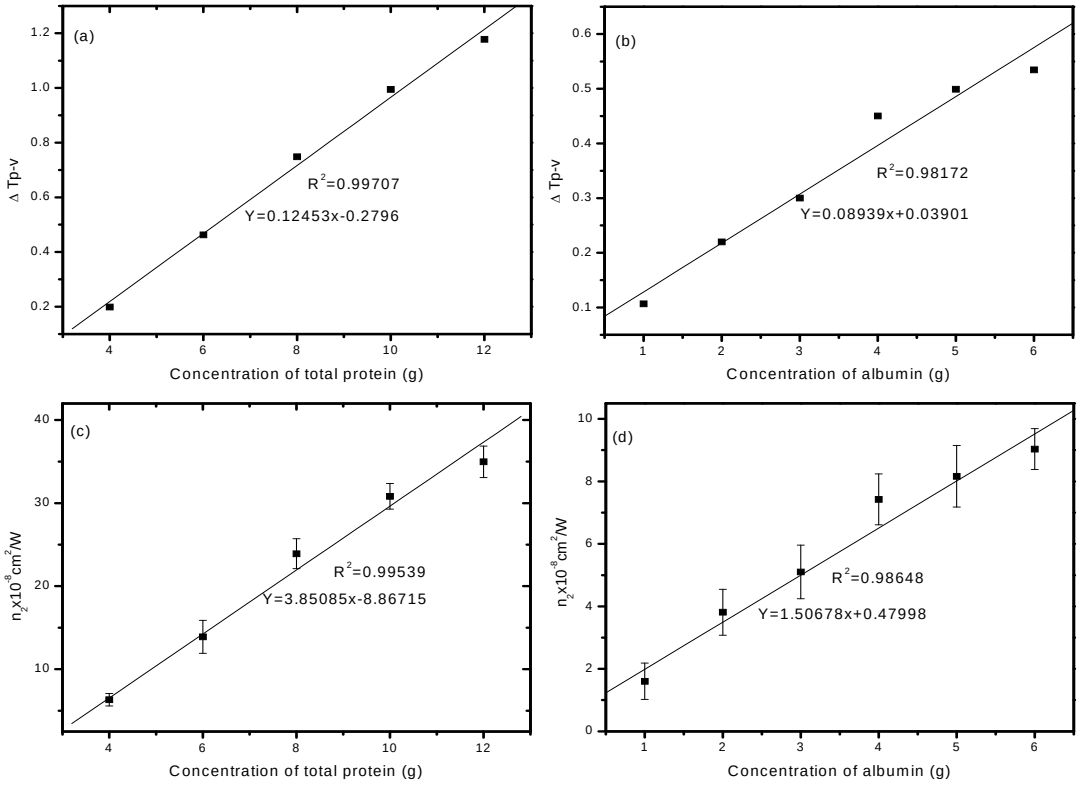

Figure 4. Linear variation of T p-v and nonlinear refractive index (n_2) with concentration of total protein (a,c) and albumin (b,d) by Z-scan method.

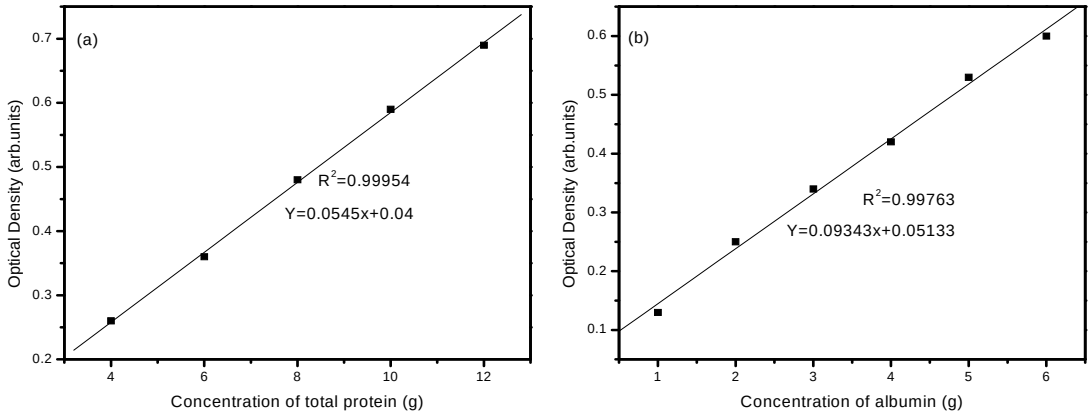

Figure 5. Linear variation of optical density of total protein (a) and albumin (b) by colorimetric method.

given in **Figure 5 (a)** and **(b)**. The experiments were repeated five times and the mean value of the nonlinear refractive index (n_2) was calculated from the normalized transmittance values. This calculated value was assumed to be the standard for measurement of unknown total protein and albumin content present in blood sample. This can be arrived by plotting a linear graph of total protein and albumin concentration Vs nonlinear refractive index. The nonlinear refractive index value was first measured against the reagent blank solution. The calibration was made with the conventional colori-metric method and the results are tabulated in **Table 1** for total protein and in **Table 3** for albumin. The normal level of total protein in serum is in the range of 6–8.3 g/dl, and serum albumin normal level is in the range of 3.2–5 g/dl.

For estimating the total protein and albumin levels, one need not plot full Z-scan curve every time. Once, experimental setup explained above is established, one needs to note down peak and valley values of the transmittance curve translating the sample holder continu-

ously along Z-axis. The difference in these two values Tp–Tv, $|\Delta\Phi_0|$ when substituted in Equation (3) yields the nonlinear refractive index value.

Consequently by the results of Z-scan method, we infer that the n_2 value is to be in the range of 13.90 ± 1.98 to 23.01 × 10^{-8} cm^2/W for normal level of total protein in serum. Likewise, n_2 value for normal level of albumin in serum is to be in the range of 5.26 to 8.16 ± 0.98 × 10^{-8} cm^2/W.

3.3. Valuation with Conventional Method

Many trials were performed to measure the total protein and albumin level with Z-scan method. The blood samples were collected from five volunteers. We could see that the results arrived are in good agreement with those of the conventional colorimetric method for total protein as shown in **Table 2** and for albumin **Table 4**. Hence we could clearly ascertain that the Z-scan method is on par with the conventional colorimetric method. By calculating the total protein and albumin values we can also calculate the globulin level in serum. (Globulin = Total Protein–Albumin) is tabulated in **Table 5**.

Table 1. Nonlinear refractive index (n_2) values for standard total protein.

Standard total protein Concentration (g/dl)	Nonlinear refractive index $n_2 \times 10^{-8}$ (cm^2/W)
4	06.32 ± 0.74
6	13.90 ± 1.98
8	23.91 ± 1.79
10	30.81 ± 1.53
12	34.97 ± 1.89

Table 2. Comparative analysis of serum total protein measurement using colorimetric method and Z-scan method.

Total Protein level	Concentration of total protein (g/dl)	
	Colorimetric method	*Z-scan method*
Normal	6.33	6.22
Normal	6.83	6.90
Normal	6.50	6.54
Normal	7.83	7.79
Normal	7.33	7.26

Table 3. Nonlinear refractive index (n_2) values for standard albumin.

Standard albumin concentration (g/dl)	Nonlinear refractive index $n_2 \times 10^{-8}$ (cm^2/W)
1	1.60 ± 0.58
2	3.81 ± 0.73
3	5.10 ± 0.85
4	7.42 ± 0.81
5	8.16 ± 0.98
6	9.03 ± 0.65

Table 4. Comparative analysis of serum albumin measurement using colorimetric method and Z-scan method.

Albumin level	Concentration of albumin (g/dl)	
	Colorimetric method	*Z-scan method*
Normal	3.42	3.49
Normal	3.85	3.78
Normal	3.68	3.75
Normal	4.20	4.13
Normal	4.02	4.08

Table 5. Globulin concentration calculated from colorimetric method and Z-scan method.

Concentration of globulin (g/dl)	
Colorimetric method	*Z-scan method*
2.91	2.73
2.98	3.12
2.82	2.79
3.63	3.66
3.31	3.18

4. CONCLUSIONS

The Z-scan measurements indicate that the total protein's and albumin's standard sample and serum sample exhibit nonlinear optical properties. We have measured the nonlinear refractive index values for total protein and albumin present in the serum sample by Z-scan method with 532 nm Nd:YAG CW laser and 633 nm He-Ne laser respectively. Comparative analysis of these values with the one obtained by conventional colorimetric method shows that they are in good agreement. Hence, apart from existing techniques, Z-scan technique can also be used for the measurement bioanalytes in serum.

REFERENCES

[1] Tietz, N.W. (1991) Clinical guide to laboratory tests, 2nd Edition, Saunders Co.

[2] Friedman, R.B and Young, D.S (1997) Effects of disease on clinical laboratory tests, 3rd Edition, AACC Press, Washington, DC.

[3] Gornall, A.G., Bardawill, C.J. and David, M.N. (1949) Determination of serum proteins by means of the Biüret reaction. *The Journal of Biological Chemistry*, **177**, 751-766.

[4] Lowry, O.H., Rosebrough, N.J., Farr, A.L. and Randall, R.J. (1951) Protein measurement with the folinphenol reagent, *Journal of Biological Chemistry*, **193**, 265-275.

[5] Bradford, M.M. (1976) A rapid and sensitive method for the quantitation of microgram quantities of protein utilizing the principle of protein-dye binding. *Analytical Biochemistry*, **72**, 248-254.

[6] Zor, T. and Selinger, Z. (1996) Linearization of the bradford protein assay increases its sensitivity: Theoretical and experimental studies. *Analytical Biochemistry*, **236**, 302-308.

[7] Flores, R. (1978) A rapid and reproducible assay for quantitative estimation of protein using bromophenol blue. *Analytical Biochemistry*, **88**, 605-611.

[8] Lee Rodkly, F. (1964) Binding of bromocresol green by human serum albumin. *Archives of Biochemistry and Biophysics*, **108**, 510-513.

[9] Caraway, W.T. and Kammeyer, C.W. (1972) Chemical interference by drugs and other substances with clinical laboratory test procedures. *Clinica Chimica Acta*, **41**, 395-434.

[10] Elking, M.P. and Kabat, H.F. (1968) Drug induced modifications of laboratory test values. *American Journal of Hospital Pharmacy*, **25**, 485-519.

[11] Parvin, R., Pande, S.V. and Venkitasubramanian, T.A. (1965) On the colorimetric biuret method of protein determination. *Analytical Biochemistry*, **12**, 219-229.

[12] De Ia Huerga, J., Smetters, G.W. and Sherrick, J.C. (1964) Colorimetric determination of serum proteins: The biuret reaction. In: Sunderman, F.W., Jr., Eds., *Serum Proteins and the Dysproteinemias*, Lippincott, Philadelphia, 52-62.

[13] Doumas, B.T. and Biggs, H.G. (1972) Standard Methods of Clinical Chemistry, Academic Press, New York, **7**.

[14] Doumas, B.T., Watson, W.A. and Biggs, H.G. (1971) Albumin standards and the measurement of serum albumin withbromocresol green. *Clinica Chimica Acta*, **31**, 87-96.

[15] Kroll, M.H. and Chesler, R. (1998) The nonlinearity seen for ldl-cholesterol with lyophilized material is a matrix effect. *Clinical Chemistry*, **44**, 1770-1771.

[16] Kroll, M.H. and Chesler, R. (1994) Nonlinearity of high-density lipoprotein cholesterol determinations is matrix dependent. *Clinical Chemistry*, **40**, 389-394.

[17] G´omez, S.L., Turchiello, R.F., Juradoc, M.C., Boschcov, P., Gidlund, M. and Figueiredo Neto, A.M. (2004) Characterization of native and oxidized human low-density *Physics of Lipids*, **132**, 185-195.

[18] G´omez, S.L., Turchiello, R.F., Juradoc, M.C., Boschcov, P, Gidlund, M. and Figueiredo Neto, A.M. (2006) Thermallens effect of low density lipoprotein lyotropic-like aggregates investigated by using the Z-scan technique. *Liquid Crystal Today*, **15**, 1-3.

[19] Rockwell, B.A., Roach, W.P., Rogers, M.E., Mayo, M.W., Toth, C.A., Cain, C.P. and Noojin, G.D. (1993) Nonlinear refraction in vitreous humor. *Optics Letter*, **18**, 1792-1794.

[20] Bezerra, A.G., Jr., Gomes, A.S.L., de Melo, C.P. and de Arafijo, C.B. (1997) Z-scan measurements of the nonlinear refraction in retinal derivatives. *Chemical Physics Letters*, **276**, 445-449.

[21] Dhinaa, A.N., Ahmad, Y.N., Murali, K. and Palanisamy, P.K. (2008) Z-Scan Technique as a Tool for the Measurement of Blood Glucose. *Laser Physics*, **8**, 1212-1216.

[22] Dhinaa, A.N. and Palanisamy, P.K. (2009) Z-scan technique for measurement of total cholesterol and triglycerides in blood. *Journal of Innovative Optical Health Sciences*, **2**, 295-301.

[23] Sheik Bahae, M., Said, A.A., Wei, T.H., Hagan D.J. and Vanstryland, E.W. (1990) Sensitive measurement of optical nonlinearities using a single beam. *Quantum Electron*, **26**, 760-769.

[24] Qusay, M.A. and Palanisamy, P.K. (2005) Investigation of nonlinear optical properties of organic dye by Z-scan technique using He-Ne laser. *Optik*, **116**, 515-520.

[25] Madhanasundari, R. and Palanisamy, P.K. (2006) Optical nonlinearity of a triphenyl methane dye as studied by Z-scan and self-diffraction techniques. *Modern Physics Letter B*, **20**, 887-897.

[26] Qusay, M.A. and Palanisamy, P.K. (2006) Z-scan determination of the third order optical nonlinearity of organic dye nileblue chloride. *Modern Physics Letter B*, **20**, 623-632.

[27] Dhinaa, A.N., Ahmad, Y.N. and Palanisamy, P.K. (2007) Nonlinear optical properties of acid orange 10 dye by Z-scan technique using Ar^+ laser. *Journal of nonlinear Optical Physics and Materials*, **16**, 359-366.

J. Biomedical Science and Engineering, 2010, 3, 291-299 **JBiSE**
doi:10.4236/jbise.2010.33039 Published Online March 2010 (http://www.SciRP.org/journal/jbise/).

Covariation of mutation pairs expressed in HIV-1 protease and reverse transcriptase genes subjected to varying treatments

David King, Roger Cherry, Wei Hu*

Department of Computer Science, Houghton College, Houghton, USA.
Email: wei.hu@houghton.edu.

Received 7 October 2009; revised 27 November 2009; accepted 4 December 2009.

ABSTRACT

A previous study, focused on the correlation of mutation pairs of synonymous (S) and asynonymous (A) mutations, distinguished only between the treated and untreated data of protease and reverse transcriptase (RT) of HIV-1 subtype B. It is well known that single mutation patterns in HIV-1 are treatment-specific. It logically follows that covariation between mutations will also be treatment specific. Thus, our motivation is to give a more in depth study of the covariation between mutation pairs, analyzing not only treated and untreated, but what specific treatments were used, and how they affected the covariation between the mutations differently. We intended to further deepen this study by analyzing the covariation of mutations in protease and RT in different subtypes of HIV-1. We found that virus samples subjected to antiretroviral Protease- and RT-inhibitors do show different patterns of mutation covariation in B-subtype protease and RT of HIV-1, while maintaining the same overall trend. <A, A> covariation will tend to be higher and more distinct from <A, S> and <S, S> covariation after treatment. The same trend continues in protease and RT regardless of subtype. We also found the highly covaried codon positions, position pairs, and position-covariation clusters in protease, affected by different treatments. Most of them are well known major drug-resistance sites for these treatments.

Keywords: HIV; Covariation; Synonymous Mutation; Asynonymous Mutation; Protease; Reverse Transcriptase; Drug Resistance

1. INTRODUCTION

Analysis of mutations in human immunodeficiency virus type one (HIV-1) has become a vital component of treatment development. This is largely due to the ability of mutations to alter the effectiveness of retroviral drugs in treatment.

In particular, the study of correlation, or covariation, between mutations has been a focus. A particularly strong correlation between amino acids can be seen as evidence of a functional link between those amino acids. Studying the covariation of these mutations will help both our understanding of the HIV-1 virus, and our ability to treat it.

There is more than one type of mutation which HIV undergoes. However, the changes in the HIV-1 genome, which is a string of nucleotides, do not necessarily lead to changes in the amino acids a particular portion of the genome generates. Asynonymous mutations, or mutations that affect the viral amino acid sequences, have been the focus of much research. In a previous study [1], there has been shown to be a significant increase in the covariance of asynonymous (A) mutations after treatment. The other mutation type, synonymous (S), those mutations which do not affect the viral amino acid sequence, has not shown as extreme change due to treatment. Previous studies [1] have also shown that on the average, the correlation between two mutations decreases as the physical distance between the mutations increased.

These studies are hindered by the scarcity of data for many subtypes of HIV and several varieties of antiretroviral drugs, since clinical tests are administered according to the needs of the patients, not the desire for data. Genetic records primarily focus on subtype B HIV, the most prevalent variety of the virus in the western world, so most research in turn focuses on mutations in HIV-1, subtype B.

Previous studies [1,2,3,4,5] in this field have been limited in scope, focusing mainly on sequences of subtype B, and mainly distinguishing between treated and untreated sequences without considering the specific treatment involved.

Our current study expands upon that research. We have run analysis of datasets of HIV-1 sequences, distinguishing based on the specific drug administered. In addition, we have run analysis on other subtypes of HIV-1, in order to get a more complete picture of the ways treatment, protease inhibitors (PIs) and nucleotide

reverse transcriptase inhibitors (NRTIs), affects the covariation of HIV-1 mutations.

2. METHODS

2.1. HIV-1 Sequence Datasets

We used datasets from the Stanford HIV Drug Resistance Database (http://hivdb.stanford.edu/). All reference sequences were taken from the Los Alamos HIV Sequence Database (http://www.hiv.lanl.gov/content/index). All data were in FASTA-format nucleotide sequences.

A reference sequence, in this study, is a consensus sequence, found to be normative of a given genomic region and subtype. We used one reference sequence for each genomic region and each subtype. A mutation is considered to be a deviation from this reference sequence.

We used two categories of datasets. Our primary dataset, the treatment-specific, consisted only of B-subtype protease and RT, downloaded exclusively from the Stanford database. Only data sets of significant size (100 or more) were used. We used two datasets of protease sequences, both of subtype B, one treated with the drug IDV (642 sequences) and another treated with NFV (899 sequences). The RT datasets were also of subtype B exclusively, and included a set of sequences treated with the drug AZT (361 sequences), and one with a common combination of drugs, AZT, 3TC, and EFV (114 sequences).

Our second set of datasets was of treated/untreated protease and RT of different subtypes. B-subtype, C-subtype, and recombinant subtype AE were obtained for both datasets. Of these, there were 8335 untreated B-subtype protease sequences, 8138 treated. There were 8364 treated B-subtype RT sequences, 5880 untreated. C-subtype had 1112 sequences untreated protease, 1565 treated protease, 650 treated RT, and 2202 untreated RT. Due to lack of data, Recombinant subtype AG was obtained for protease only. Also due to lack of data, we analyzed only the RT of subtype A (106 sequences treated, 1519 sequences untreated).

2.2. Covariation Measurements in Specific Mutation Pairs

We used covariation measure D' to determine the amount of non-random association between the mutations considered in a pair. D' is a well known measure for determining non-random association, and was used in several previous studies, including [1]. The formula and complete procedure of computing D' can be found in [6].

We chose D' as a measure above other covariation measures because of its symmetry: the D' value, which is a value between –1 and 1, provides an equal scale for evaluating both negative and positive correlation. This allows us to study both positive and negative correlation of mutation pairs.

The D' value of a given mutation pair containing mutations X and Y relies on a 2 × 2 contingency table consisting of N_{XY}, N_X, N_Y, and N_O, where N_{XY} is the number of sequences in the dataset which contain both mutations, N_X, is the number of sequences in the dataset which contain only mutation X, N_Y, is the number of sequences in the dataset which contain only mutation Y, and N_O, is the number of sequences in the dataset which contain neither mutation. N is the total number of sequences in the dataset.

As in [1], we also used a value $\theta = (N_{xy}*N_O)/(N_X*N_Y)$ which is a maximum likelihood estimator for independence of mutations X and Y. When $\theta = 1$, there is complete independence of X and Y.

We used this θ value as a cutoff when plotting our curves. By using this value to cutoff some of the outlier points which throw the curves off, we create more clear and reliable plots. In our plots, we only allowed data points with $\theta > 1.5$ or $\theta < 0.5$.

In each dataset, a singular cutoff was utilized, such that mutations which occur only once in the dataset were not used in the calculation of D'.

2.3. Counting Paradigm for Specific Mutation Pairs

The collection and calculation of the mutation pairs are handled at the same time by the following algorithm.

Data preprocessing and alignment is just as important to the algorithm as the central process itself. In preprocessing, we ensured that each sequence was correctly aligned to the reference sequence of the same genomic region and subtype. Each reference sequence was taken from the Los Alamos HIV Database. If an individual sequence couldn't be aligned with the reference sequence, it was not used, as a single unaligned sequence within a dataset can drastically affect the output of the D' analysis.

Gaps were not allowed in the reference sequences, but were allowed in the data sequences provided they aligned properly with the reference sequence. If a data sequence was properly aligned, but longer than the reference sequence, we only analyzed the portion of the sequence which could be compared with the reference sequence.

2.4. D' Values According to Codon Position

The collection and calculation of the mutation pairs are handled by a simple counting mechanism. We compared all nucleotide sequences of our dataset against a consensus sequence, and made not of each nucleotide substitution, and whether that substitution constituted a synonymous or asynonymous mutation. For each sequence in the dataset, we record all valid pairs of mutations. Mutations pairs that involve both asynonymous mutations were labeled as <A, A>, those that involve one asynonymous and one synonymous mutation were labeled <A, S>, and those that involve two synonymous mutations are <S, S>. Then, we take frequency counts on all mutation pairs across all sequences in order to calculate the D' of each mutation pair.

For display, we use a sliding window curve. This enhances the readability and reliability of the curve. Simply graphing this data such that each physical position is an average of all D' values at that physical position give an unsteady curve towards the greater physical distances. As the physical distance increases, the number of data points available for that physical distance decreases, leading to greater oscillation as the plot goes on.

A sliding window has the same amount of data going into each point on the graph, and is thus more reliable. Our sliding window curves each use 3% of the data in the set per window, with a 50% overlap.

2.5. D' According to Genomic Position

We analyzed D' according to amino acid position within the genomic region as in [1]. This gives us information on how specific codon positions interact with one another within the gene, particularly in response to different treatments.

We also performed a pair-wise analysis of these specific mutation positions in order to reveal more on the differences between <A, A>, <A, S>, and <S, S> mutation pairs.

Using this data, we generated covariation histograms. In these histograms, the value at each codon position is the sum of the D' value for all mutation pairs associated with that position. Each mutation pair will contribute total D' value to the positions of its two mutations. In this manner, positions which are either the site of great amounts of mutation or high covariance will stand out, with positions which are both high in mutation amount and covariance being seen as peeks.

In order to further explore the relationships between the amino acid positions, we cast our histograms into two dimensional contour plots, which reveal clusters of covariation. To generate these plots, we form a square two dimensional table with a length equal to the number of amino acid positions in a given dataset. Each mutation pair is then mapped to a position on this table, based on the position of that pair's mutations. For example, the mutation pair L10I and Q20V would be mapped to position x = 10, y = 20.

The value of each position in the table is the sum of all D' values of the pairs assigned to that position. This provides a visual representation of the relationships between positions, with higher values representing positions which are highly correlated with one another, and the lower values representing unrelated positions.

3. RESULTS

3.1. Effects of Specific Treatment on the Covariation of B-Subtype Protease and RT

First, in order to discover the effects of specific treatments on the covariation of HIV-1 mutation pairs, we ran a D' analysis on data sets of B-subtype protease and RT with known treatment types. For reference, we also included the generically treated and untreated datasets of B-subtype protease and RT, in order to see how the different treatments effected the genomes and, and how the compare to the effects of overall treatments.

Our findings revealed that covariation between mutations is, as we expected, treatment dependent. In comparing IDV- and NFV-treated protease, these results become clear. The plots in **Figure 1**, show the results of the analysis according to physical distance, display clearly different patterns in their covariation. The average D' values of <A, A> pair covariation are just at 0.3 for both datasets, however we can clearly see peaks of high covariance in different positions on the <A, A> curves. If we compare these two treatment-specific plots against D' values generated from the set of generically treated HIV-1 sequences (those sequences that have received treatment of any sort, plot not pictured), we can see that the differences even more pronounced. The average D' of <A, A> mutation pairs in protease which has seen any sort of treatment whatsoever is much higher—a value just at 0.4, and yet a different set of peaks within the curve. We see similar results in RT. The curves generated by RT treated with the drug AZT are considerably different than the generically treated RT, as can be seen in **Figure 2**.

The generic trends of covariation, however, were largely the same despite what specific treatments were used. <A, A> covariation tended to be higher than <A, S> or <S, S> covariation in all datasets. In addition, we also noticed that on average, <A, S> covariation tended to be higher than <S, S>. This separation was even present in the untreated dataset.

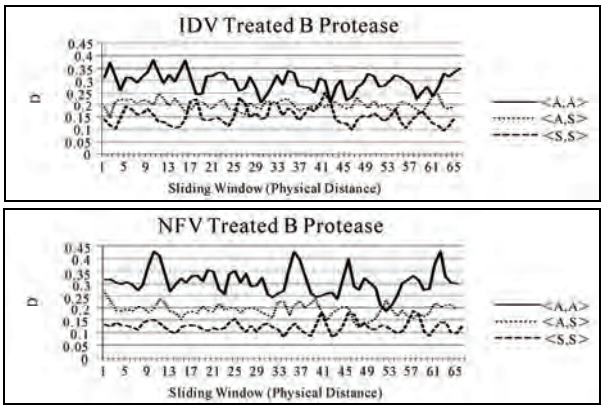

Figure 1. Different treatments lead to different patterns of covariation. These two sliding window plots display the D' analysis of two different treatment types. The top displays results derived from IDV-based treatment, and the bottom plot displays those derived from NFV. Clearly, the different treatments induce quite different <A, A> covariation patterns in the sliding window curves. The different treatments do not seem to significantly affect the <A, S> or <S, S> curves.

We also found that, in agreement with previous results [1], <A, A> covariation increased when subjected to any form of treatment. In **Figure 3**, we can see the changes made by specific drug treatments, both before and after treatment. There is a clear pattern of increase in the <A, A> category.

There were instances where <A, S> or <S, S> covariation was decreased, and other instances where the <A, S> or <S, S> covariation was increased.

To ensure that these were typical results that were caused by treatment of HIV, we retrieved a dataset from Stanford that contained sequences from the same set of patients, 470 sequences of both before and after treatment. Numerical analysis revealed the treatment both increased the amount of <A, A> covariation from an average value of 0.278 to 0.308 and increased the overall separation of the curves. Before treatment, the average difference between <A, A> and <A, S> covariation was a value of0.085 from 0.278 to 0.193, and the average difference between <A, S> and <S, S> was 0.051 from 0.193 to 0.142. After treatment, the difference between <A, A> and <A, S> was 0.104 from 0.308 to 0.204, and the difference between <A, S> and <S, S> 0.066 from 0.204 to 0.138. These results, and the typical trends these results show, can be seen in **Figure 4**.

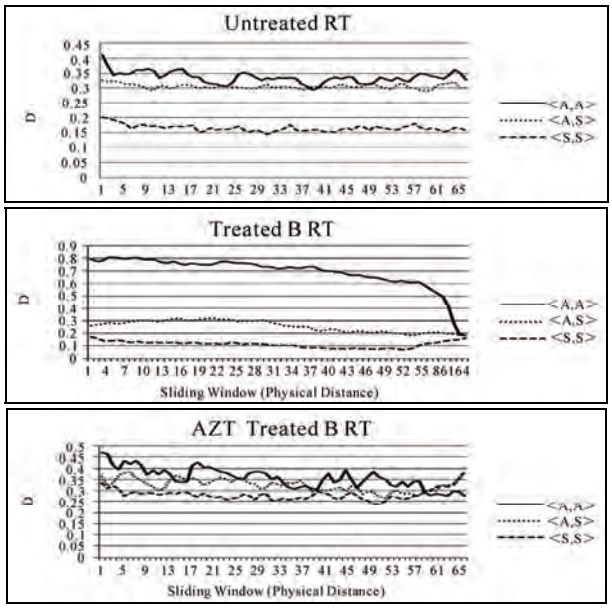

Figure 2. Treatment specific RT. These graphs display the analysis of B-type RT before and after treatment. The top plot displays the results from the analysis of untreated B-subtype RT. The middle plot displays the results derived from any RT sequences which have received any NRTI treatment whatsoever, and the bottom plot displays the results derived from those sequences treated only with the specific drug AZT. Clearly, the AZT-specific treatment had a different effect than the overall treatment. The curves for the overall treatment are very well separated, whereas the AZT-specific curves are not as well separated, but still somewhat distinct. The average values of the three curves are seperated. <A, A> has an average of 0.359, <A, S> has 0.326, and <S, S> has 0.284.

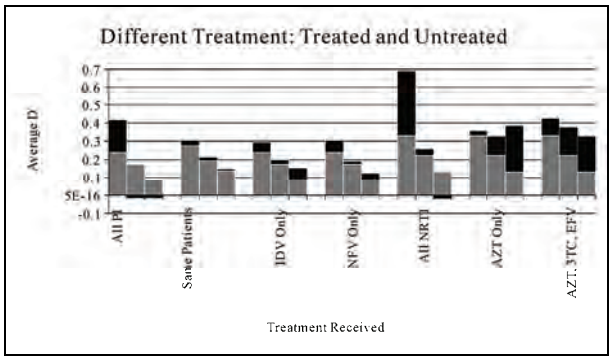

Figure 3. Before and after treatment for different drug treatments. This chart shows the effects of specific treatments on B-subtype protease and reverse transcriptase. The values here are averaged from the three curves in the sliding window plots we generated. In each group, the first column is <A, A> covariation, the second is <A, S>, the third is <S, S>. The gray portions represent the average D' before treatment. The black portions represent the change in D' from the treatment. If they are above the gray, the D' value increased with treatment. If they are below the gray, the D' decreased. The column labeled 'Same Patients' is the dataset containing the exact same group of patients, both before and after treatment.

We also analyzed <A, A> mutation pairs according to their codon positions, rather than physical distance. This analysis can be seen in **Figure 4**.

The top plot shows a control analysis of generally treated subtype B protease. In this plot, we show the thirty positions which were most significantly affected by the treatment, and what their total D' value was prior to and after treatment. This plot shows that, in almost all significantly affected positions, there was an increase in <A, A> covariation. In addition, we can see that several of the most affected positions are also medically significant, according the Stanford HIV database.

The second plot shows a comparison between the IDV and NFV treated datasets. Again, we can see that the two treatments cause different patterns in the covariation pattern. Certain codon positions have roughly the same amount of covariation after treatment, but others, including several medically significant positions, seen in the bottom plot, have significantly different covariation values, such as positions 20, 46, and 82.

3.2. D' Results from Treated/Untreated Datasets of Different Subtypes

For this portion of the study, we did not distinguish based on treatment type, but rather only invested in distinguishing between 'treated' and 'untreated' sequences. Selecting a specific treatment type limited the larger treated datasets into subsets too small for proper analysis.

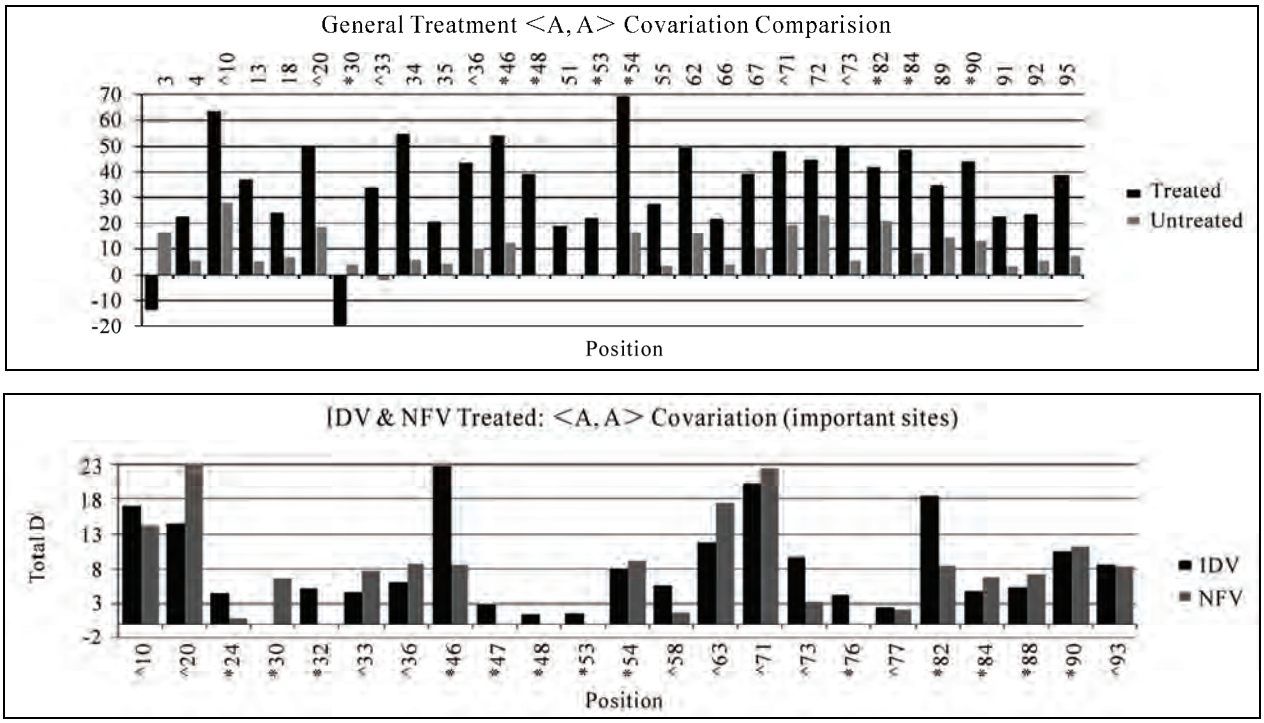

Figure 4. Site-specific Analysis for B-subtype Protease. The top plot shows the thirty postitions who's covariation was most affected by the application of generic treatment ot B-subtype protease. The positions with * or ^ next to them are the major or minor positions respectively that are associated with drug resistance according to the Stanford HIV Database. The bottom plot contrasts the difference between the IDV- and NFV-treated datasets on medically significant sites.

For use in the analysis of protease and RT, we selected HIV-1 subtypes A, B, and C, as well as recombinant subtypes AE, and AG. Subtype AG was only analyzed for protease, and subtype A was only analyzed for RT, due to lack of data.

With the treatment-specific datasets, we analyzed all datasets, and generated sliding window curves for all of them, mapping the relationship of D' values of mutation pairs and their physical distances.

Our results showed that different subtypes yield different patterns of covariation, and that once again the typical trends were maintained on average. There was a clear seperation of <A, A>, <A, S> and <S, S> covaration, both before and after treatment, although treatment in most cases improved the separation. There was one exception to this: subtypes A and C RT displayed a significant increase in<A, A> covariation, but similar increases in <A, S> and <S, S> covariation lead to them having less-separated curves after treatment.

There was also increase in <A, A> covariation after treatment in all datasets. While this increase in <A, A> covariation is consistent for all datasets, we did notice that subtype-B protease and RT had a considerably larger increase in covariation than any other subtype. **Figure 5** shows a summary of the findings in this section.

3.3. Pair-Wise Mutation Analysis and Clustering

Results of the pair-wise analysis revealed that there is a clear-and-distinct difference between the position-based covariance of <A, A> mutation pairs, <A, S> mutation pairs, and <S, S> mutation pairs.

There tended to be far greater <A, A> covariance at certain positions than <A, S> or <S, S> covariance in general. Additionally, these peaks of high <A, A> covariance tended to be close to one another, creating clusters or areas of high <A, A> covariance within the genome. By contrast, <A, S> covariation was less clustered, and <S, S> not clustered at all. This can be seen in **Figure 6**.

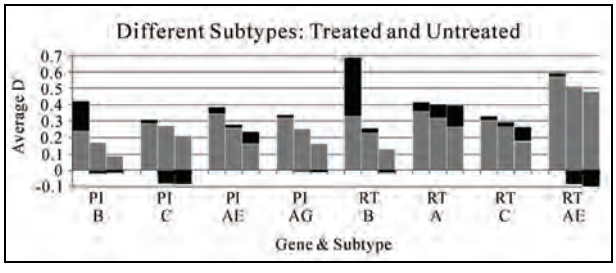

Figure 5. Before and after treatment for different subtypes. This chart shows the effects of treatment on different subtypes of protease and RT. For the most part, data followed expected patterns. Subtype A RT does not have a clear distinction between <A, A>, <A, S> and <S, S>, but beyond that, plots behave normally.

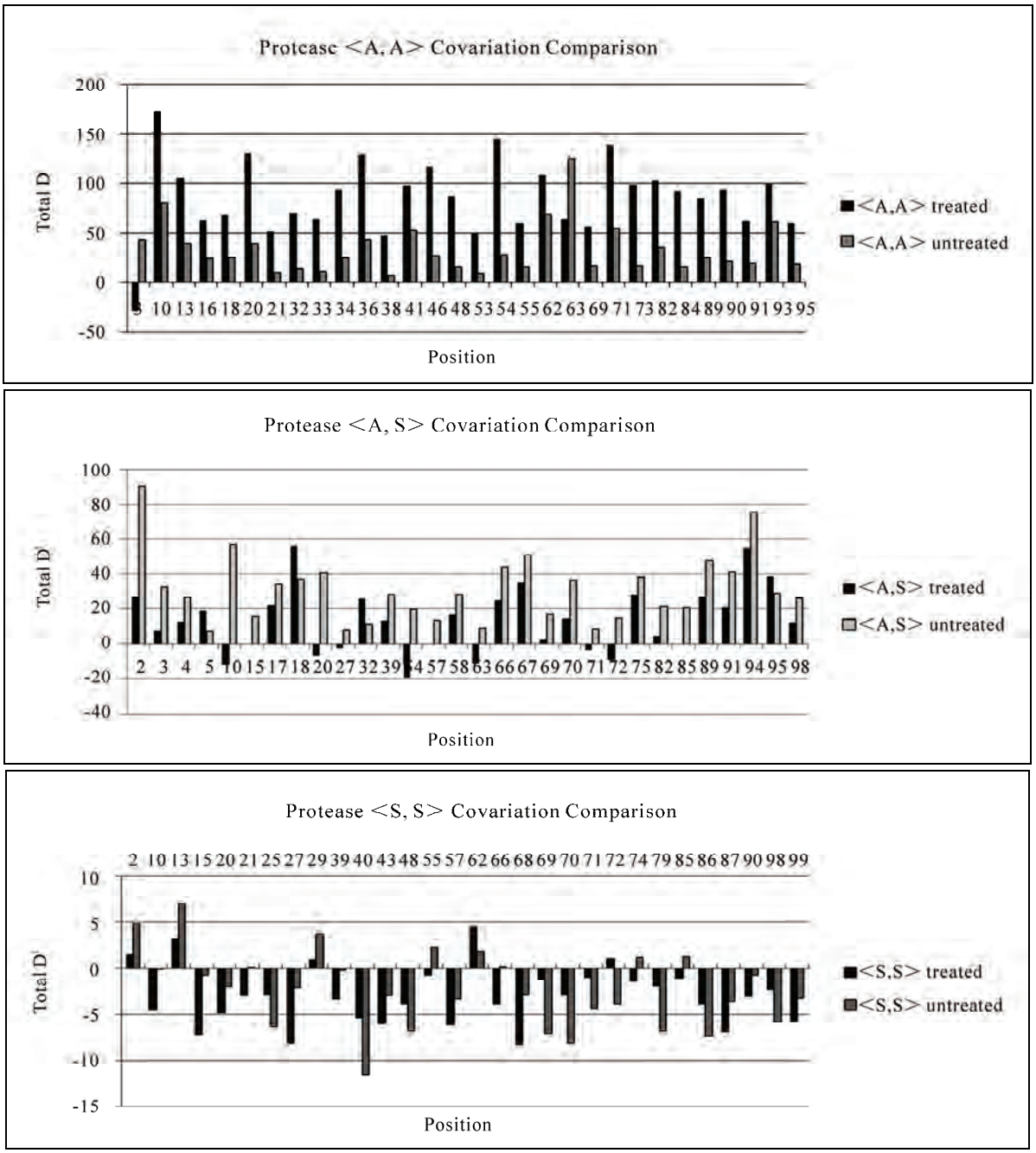

Figure 6. Treated/Untreated covariation comparison for protease. These three plots show the thirty positions whose covariation was most effected by treatment. These positions were selected because they had the largest difference in their total D' values between treated and untreated. The <A, A> mutation show that frequently D' values were higher after treatment, trend that was not as clear in <A, S> and <S, S> plots. D' values for <A, A> covariation are higher than those of <A, S> covariation, and much higher than those of <S, S> covariation. <S, S> covariation seems not to have been effected by treatment very much: the highest difference between before and after was less than 6.5.

Casting these histograms into a 2D contour plot revealed further information about the relationships between specific positions: we can see that covariation between positions is clearly related to the amount of covaration at a specific position. Two positions having high D' values will very likely have a high correlation. Both the histogram and the contour mapping of generically treated protease are shown in **Figure 7**.

Based on the position-covariation histogram of generally-treated subtype B protease as in **Figure 4**, we

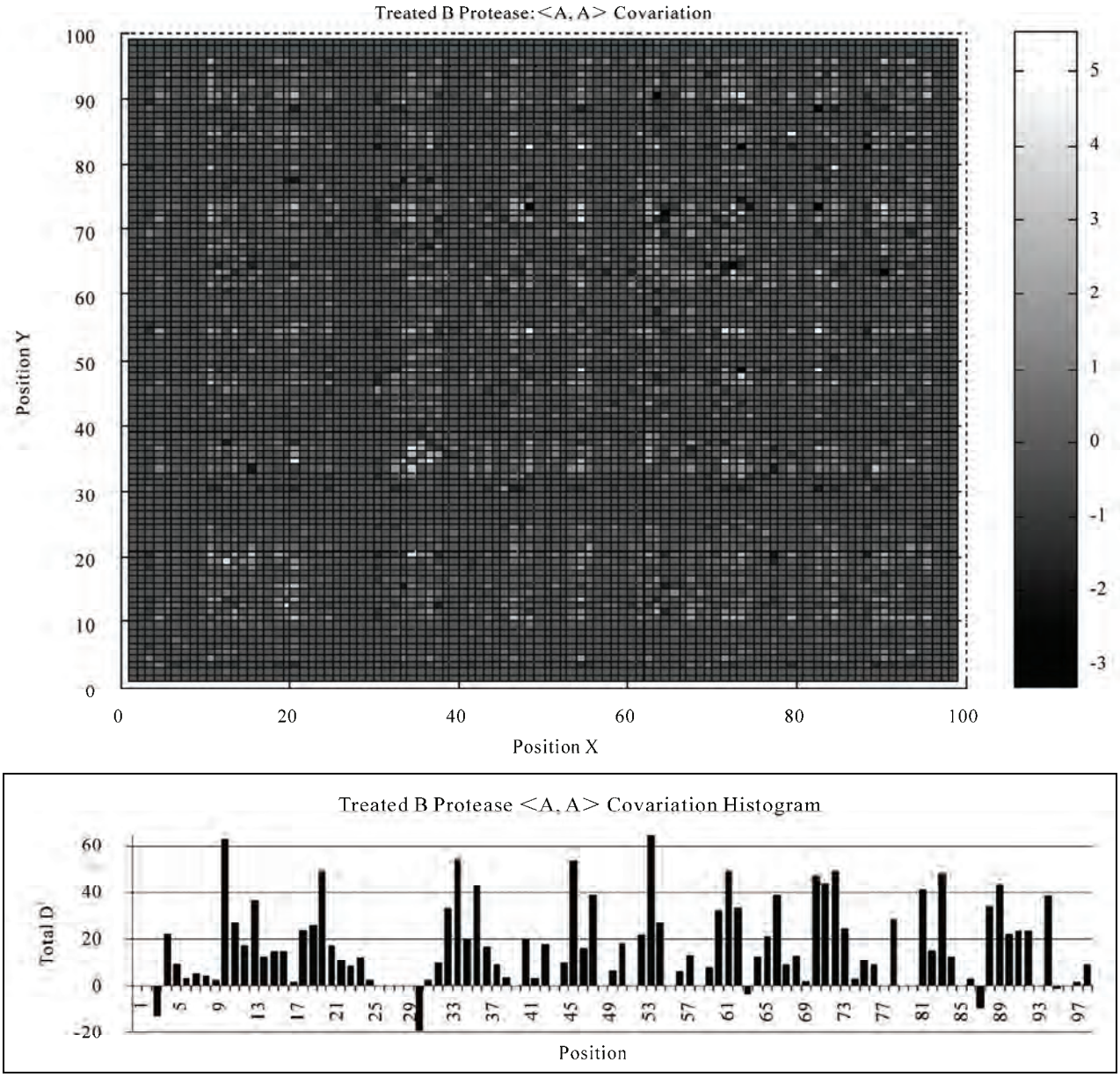

Figure 7. Treated B Protease. The top plot is a position relationship chart, with bright colors showing positions which are highly correlated with one another, and dark colors showing positions which are not. The shade of the grid at the left is representative of total D', the sum of the covariance values for all mutation pairs at that position. The bottom plot is a histogram of D' values for generally-treated B-subtype protease. Each column in the histogram is the sum of all values for a particular position in the 2D chart. These charts were generated from the statistically significant mutation pairs with a Fisher Test P value less than 0.05 and a ChiSQ Test P value less than 0.05.

selected the 20 most correlated statistically significant <A, A> positions according to D' value, which are: 10+^, 13+, 20+^, 33+^, 34, 36+^, 46+*, 48+*, 54+*, 62+, 63+^, 67, 71+^, 72, 73+^, 82+*, 84+*, 89, 90+*, and 95, with + positions having also been found in [1] using the θ value, and positions with * or ^ being sites of major or minor drug resistance respectively according to the Stanford HIV database. The D' analysis has an advantage of being able to find negative correlation effectively. We also found the negatively correlated positions: 3, 30+, 64, 88+, 96. We find clusters of covariation to occur near positions 10, 20, 37, 50, 73, and 90.

We also found top statistically significant correlated mutation pairs in our Treated Protease dataset. In order to do this, we sorted all <A, A> pairs according to the Fisher Test P value followed by the ChiSQ Test P value,

giving us the most statistically significant pairs. Then we chose the top thirty according to the highest D' value. Fisher's Exact Test and Pearson's Chi-Squared Test are done by calling the functions in R: fisher.test and chisq.test with their default values, such as the confidence interval = 95% in Fisher test and Yates's correction applied in Chi-Squared Test.

We selected the 34 most correlated position pairs from our Treated Protease dataset, which are: (10, 46), (10, 79), (12, 19), (13, 20), (13, 89), (15, 20), (20, 34), (20, 73), (20, 90), (33, 34), (33, 89), (34, 36) (34, 54), (34, 62), (34, 71), (36, 82), (47, 73), (48, 54), (48, 82), (54, 61), (54, 71), (54, 73), (54, 82), (63, 67), (63, 72), (63, 82), (71, 72), (71, 82), (72, 73), (72, 90), (73, 90), (79, 84), and (90, 95). The correlation of these positions is not reliant on a specific mutation, but all mutations associated with these positions. A list of the most correlated mutation pairs can be seen in **Table 1**.

Table 1. Top 30 highly covaried <A, A> mutation pairs.

Mut X	Mut Y	D'	Fisher Test P	ChiSQ Test P
<I62V(A)	I66L(A)>	0.818621	5.47E-08	1.01E-07
<L63P(A)	G73S(A)>	0.820203	1.66E-66	1.17E-50
<E35G(A)	M36I(A)>	0.829569	2.01E-17	2.77E-18
<L10I(A)	I54T(A)>	0.835171	4.23E-32	5.05E-31
<L10F(A)	P79N(A)>	0.841458	5.91E-06	1.14E-09
<T4A(A)	I84V(A)>	0.844762	6.99E-05	1.02E-05
<K20R(A)	M36I(A)>	0.846462	0	0
<L38W(A)	I62V(A)>	0.847875	5.81E-10	1.30E-09
<I13A(A)	M46I(A)>	0.850174	0.000136	8.07E-05
<E35N(A)	M36I(A)>	0.851419	2.58E-14	7.05E-15
<T12P(A)	G68D(A)>	0.85259	5.58E-09	7.51E-31
<I66V(A)	L90M(A)>	0.85367	2.77E-21	2.13E-19
<I54V(A)	Q61R(A)>	0.861101	7.84E-05	5.91E-05
<T4A(A)	L10F(A)>	0.861276	6.62E-07	1.35E-11
<N83S(A)	I84V(A)>	0.862011	4.14E-10	8.92E-13
<G73S(A)	90M(A)>	0.868072	5.87E-239	3.71E-218
<I72K(A)	L90M(A)>	0.881701	1.20E-12	2.27E-11
<I13M(A)	L90M(A)>	0.88433	5.17E-09	4.38E-08
<P79A(A)	I84V(A)>	0.8871	3.05E-42	6.05E-56
<L90M(A)	C95F(A)>	0.890186	9.91E-44	3.35E-39
<L63P(A)	I66V(A)>	0.905986	1.46E-08	2.09E-06
<L63P(A)	I72L(A)>	0.908414	5.33E-21	5.82E-15
<L63P(A)	I72E(A)>	0.913298	2.44E-09	5.93E-07
<G73T(A)	L90M(A)>	0.913535	6.34E-89	1.12E-78
<I72L(A)	L90M(A)>	0.926688	4.36E-65	4.96E-57
<G48A(A)	I54V(A)>	0.926895	1.50E-09	4.67E-10
<D30N(A)	K45Q(A)>	0.92856	4.25E-16	2.85E-38
<G73A(A)	L90M(A)>	0.931959	1.91E-16	2.09E-14
<I66L(A)	L90M(A)>	0.933267	6.96E-09	8.29E-08
<C67F(A)	L90M(A)>	0.985661	3.68E-44	1.14E-36

4. DISCUSSION

4.1. Biological Significance of <A> Type Mutations Versus <S> Type Mutations

Throughout the study, we can see a marked difference between the <A, A> category mutation pairs, the <A, S> category, and the <S, S> category. This is trend is consistent and universal. <A, A> pairs are, on average, the most covaried, <A, S> pairs are less so, and <S, S> pairs have even less covariation. This can be clearly seen in all plots which include the three different types of mutation pairs, but is most clearly seen in **Figure 6**.

We suggest the reason for this is that <A> mutations necessarily lead to greater covariance. Because an <A> mutation will have a more significant impact on an organism, it is more likely to be related to other changes within the genome. This is why <A, A> mutation pairs have such high covariance. However, an <A> type mutation might just as likely be related to a synonymous mutation as well. Thus <A, S> mutation pairs will also have a relatively high covariance, as opposed to <S, S> mutation pairs. <S> type mutations have a lesser impact on the organism at large, because the amino acid types are preserved.

We can further see this confirmed when we look at the general covariance of mutations at specific positions, as seen in **Figure 7**. <S> type mutations have a much higher occurrence frequency than <A> type mutations. The covariation of <A, A> and <A, S> pairs, however, is much higher than that of <S, S> pairs. This seems to imply that <A> type mutations have a greater effect on the genome itself.

4.2. Biological Importance of Individual Mutation Sites in Relation to Specific Treatments

We can see in **Figure 7** the effects which treatment has on the different mutation types. <A, A> mutation pairs in general have a dramatic increase of covariation after treatment. The mutation correlation patterns we discovered in the bottom plot of **Figure 6** are consistent to the single mutation patterns in [7]. We find that in [7], IDV-treated datasets negatively weight in positions 30 while NFV leads to highest positive weight among all the other weights. Similarely, Position 76 in IDV has the highest weight of all the other weights, while the NFV-treatment gives that position a negative weight. This is consistent with the findings of our plot. Note the distinct difference between IDV and NFV at positions 30 and 76 in the bottom plot of **Figure 7**.

Position 30 is an interesting case, as the overall correlation is negative, which seems to point out that other mutations are frequently absent when this mutation is present. However, we know that position 30 hosts a mutation, D30N, which is correlated with other mutations

when the specific PI treatment is neflinavir. This seems to hint that other treatment types have a steep inverse correlation at this mutation site. At the very least, we see that the treatment IDV gives a negative correlative weight at position 30 [7].

4.3. Differences in Covariation in Different Treatments and Subtypes

While the general trends we found were largely consistent throughout our comparison between the different treatments and subtypes, we found the differences in the covariation patterns between the subtypes and treatments interesting.

In **Figure 4**, we see that the increase in covariation between the untreated sequences and the the sequences which received any treatment whatsoever is far larger than the increase in covariation present in those sequences only treated with individual drugs. For example, the two drugs, NFV and IDV, have the most data within the Stanford database. In spite of this, neither the covariation increase from NFV or IDV alone is enough to cause the dramatic increase we see from generic treatment of B-subtype protease. The same is true of AZT-treated RT compared with generically treated RT. The generically treated datasets accounts for sequences treated with single drugs, such as NFV or IDV or AZT, as well as those treated with combinations of drugs. Our results, then, suggest that combinations of treatments lead to greater covariance than single treatments. This is further supported by the results of the RT treated with the combination of drugs, AZT, 3TC, and EFV, which have a greater increase in covariation than any single-treatment, but still not as much as the generically-treated sequences.

5. ACKNOWLEDGEMENTS

We would like to thank Houghton College for providing the funding for this research through the Summer Research Institute at Houghton, as well as Qi Wang for responding to our e-mails regarding his paper [1] both promptly and helpfully.

REFERENCES

[1] Wang, Q. and Lee, C. (2007) Distinguishing functional amino acid covariation from background linkage disequilibrium in HIV protease and reverse transcriptase. *PLoS ONE*, **2(8)**, 814.

[2] Liu, Y., Eyal, E. and Bahar, I. (2008) Analysis of correlated mutations in HIV-1 protease using spectral clustering. *Bioinformatics*, **24**, 1243-1250.

[3] Gilbert, P.B., Novitsky, V. and Essex, M. (2005) Covariability of selected amino acid positions for HIV type 1 subtypes C and B. *AIDS Research and Human Retroviruses*, **21(12)**, 1016-1030

[4] Hoffman, N.G., Schiffer, C.A. and Swanstrom, R. (2003) Covariation of amino acid positions in HIV-1 protease. *Virology*, **314**, 536-548.

[5] Rhee, S.Y., Liu, T.F., Holmes, S.P. and Shafer, R.W. (2007) HIV-1 subtype B protease and reverse transcriptase amino acid covariation. *PLoS Computational Biology*, **3(5)**, 87.

[6] Hedrick, P. (1987) Gametic disequilibrium measure: proceed with caution. *Genetics*, **117**, 331-341.

[7] Rhee, S.Y., Taylor, J., Wadhera, G., Ben-Hur, A., Brutlag, D. and Shafer, R.W. (2006) Genotypic predictors of human immunodeficiency virus type 1 drug resistance. *Proceedings of the National Academy of Sciences USA.* **103**, 17355-17360.

J. Biomedical Science and Engineering, 2010, 3, 300-303 **JBiSE**
doi:10.4236/jbise.2010.33040 Published Online March 2010 (http://www.SciRP.org/journal/jbise/).

Effect of static magnetic field on erythrocytes characterizations

Mohamed A. Elblbesy

Medical Biophysics Department, Medical Research Institute, Alexandria University, Alexandria, Egypt.
Email: mimizizo@yahoo.com

Received 29 November 2009; revised 15 December 2009; accepted 28 December 2009.

ABSTRACT

The interaction of static magnetic field (SMF) with living organisms is a rapidly growing field of investigation. Recently, exposure to moderate intensity SMFs (1 mT – 1 T) has attracted much attention for its various medical applications. This study was designed to show the microscopic effect of SMF on erythrocytes in vitro. For this purpose SMF system was constructed in my lab on basis of the idea of cell tracking velocimetry system. The changes in erythrocytes surface area, sphericity, and adhesion number for erythrocytes were calculated to quantify the effect of SMF on erythrocytes characterizations. The results showed that SMF increased erythrocytes surface area and reduced their sphericity. The adhesion number of erythrocytes under the influence of SMF showed the tendency of erythrocytes to adhere with each other. These findings indicate that more study on microscopic scales must be carried out in order to investigate the effect of SMF on erythrocytes.

Keywords: Static Magnetic Field; Erythrocytes; Surface Area; Shericity, Adhesion

1. INTRODUCTION

During the last few years there has been an increasing interest in the influence of magnetic field on biological cell [1]. Many attempts have been made to measure the magnetic effects. Historically, there are several significant studies in the field of erythrocyte rheology [2].

Reports from in vitro research indicate that low level high frequency fields may alter membrane structural and functional properties that trigger cellular responses. It was hypothesized that the cell membrane may be susceptible to low level high frequency fields, especially when these fields are amplitude modulated at extremely low frequencies [3]. There are abundant data on the effects of weak physical signals on cell functional activity. However cell targets for these signals are not established yet. Since water is the main component of biological systems and all metabolic processes take place in aqueous medium it was supposed that even minor changes in the physico-chemical properties of water could significant modify cell functional activity. The data about the effect of EMF on water specific electrical conductivity and wheat sprouting serve as an additional evidence for the hypothesis according to which the EMF-induced water structure changing is an important pathway through which the biological effect of EMF is realized [4].

Most of the theories addressing the mechanism of interaction between biological systems and MFs suggest that the plasma membrane, by virtue of its bioelectrical properties, is the site, where MFs exert their primary effects [5]. To investigate the effect of static magnetic on biological system, it is necessary to clarify interaction mechanisms of magnetic field with biological systems. Simple components of biological system, as cells, biomolecules, artificial membrane, are used in vitro studies that allow reducing of biological variables and more precisely defining and controlling the exposure parameters, compared with in vivo exposure. Erythrocytes are often used as model in exploring the structure and function of the biological cells as well as studying the effect of different physical and chemical factors on the cell. The present study was established to elucidate the changes in biological cells interaction and morphological characterization through in vitro exposure of human erythrocytes to SMF.

2. MATERIALS AND METHODS

2.1. Samples Collection and Preparation

Twenty blood samples of 5 ml were collected from healthy volunteers of the same age and gender. The blood samples were centrifuged and erythrocytes were separated. Erythrocytes were washed three times in 0.155 M NaCl (2,000 rpm for 10 min). After the final centrifugation suspension were diluted to final erythrocytes concentration 2% in phosphate buffer slain (PBS).

2.2. SMF System

The SMF system was constructed in my lab. SMF system is based on the idea of cell tracking velocimetry system. In this system the movement of cells in a well

defined magnetic field is videotaped [6]. Erythrocytes suspension were placed in a glass sample holder and viewed using an inverted optical microscope in conjunction with a computer linked via digital camera and image capture software. Two rod of iron to produce a magnetic field with large gradient, were placed on both sides of sample holder. The iron rods were alternately magnetized by solenoids controlled by a DC power supply. When magnetized, the magnetic field produced by each rod exerted a force on erythrocytes directed towards the edge of the rod.

2.3. Erythrocytes Surface Area and Sphericity

Erythrocytes were suspended in phosphate buffer saline (PBS) at concentration of 5%. The erythrocytes suspension was placed on the sample holder of SMF system. Image of unexposed erythrocytes (control) was taken then the magnetic field was turned on and the image of exposed erythrocytes was captured. For each value of B images of exposed erythrocytes were compared with control by imaging processing software in order to calculate the changes in erythrocytes surface area A_{ch} and sphericity of each erythrocyte in the image.

The change in erythrocytes surface area was calculated as the following:

$$A_{ch} = \frac{A_{Ex}}{A_0} \quad (1)$$

where A_{ch} is the change in erythrocytes surface area, A_{Ex} is the surface area of the erythrocytes after exposed to SMF, and A_0 is the surface area of unexposed erythrocytes.

A_{ch} was calculated as the average of 100 erythrocytes for each image. It was taken that if A_{ch} greater than one there was an increase in erythrocytes surface area, and if A_{ch} smaller than 1 there was a decrease in erythrocytes surface area.

The sphericity of an erythrocyte is a dimensionless parameter first described by Canham and Burton [7] and is a measure of how spherical a cell is, with values between 0 and 1, for a sphere and laminar disk, respectively. It was calculated as the following:

$$\text{Sphericity} = 4.84\frac{V^{2/3}}{A_{Ex}} \quad (2)$$

where V is the volume of erythrocytes and is taken to be 88.5 μm^3.

2.4. Erythrocytes Adhesion Number

Five volume fractions (0.00001, 0.00003, 0.00005, 0.00007, 0.00009) of erythrocytes suspensions in PBS were prepared by further dilution of the main erythrocytes suspension. The erythrocytes suspension was placed in sample holder of SMF system. For each sample counting of doublets erythrocytes (N_2) and singlet erythrocytes (N_1) was performed. The plot of doublet to singlet ratio versus particle volume fraction should yield a straight line passing through the origin. The gradient of the line is a measure of the adhesion number. The same previous procedure was performed with SMF turned on to calculate the adhesion number of exposed erythrocytes.

2.5. Statistical Analysis

The data was present as the mean ± SD. For each plot, correlation (R^2) was calculated using Microsoft Excel.

3. RESULTS

The erythrocytes surface area increased as the value of magnetic field intensity increased (**Figure 1**). A strong correlation was found between A_{ch} and B (mT) (R^2 = 0.95). At low magnetic field the increased in erythrocytes surface area was slightly small. At higher values of magnetic field the increased in erythrocytes surface area raised.

The sphericity of the erythrocytes is inversely proportional to the applied SMF (**Figure 2**). Under the influence of SMF, the sphercity of erythrocytes was reduced by about 35 % in comparison with unexposed erythrocytes. The decrease in erythrocytes sphericity was reduced rapidly when SMF was applied. A small decrease in sphericity was recorded at higher values of B.

As indicated in **Figure 3**, The adhesion number increased under the influence of SMF. Acute increase in adhesion number was indicated at 15 mT. A strong relation between adhesion number and B was pointed out (R^2 = 0.96).

4. DISCUSSION

It is generally known that morphological and structural changes to the plasma membrane interfere with many functional and structural features of the cells, leading,

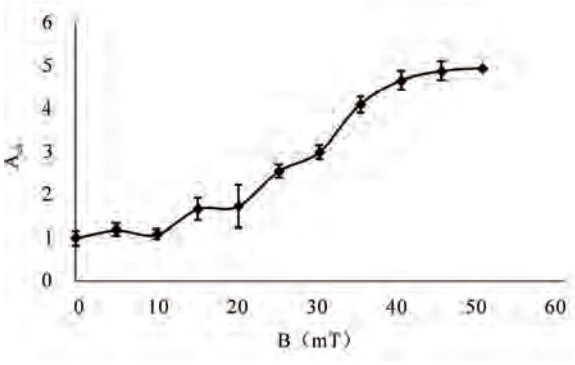

Figure 1. Erythrocytes surface area increased as the values of SMF intensity increased. Strong correlation between A_{ch} and B was observed (R^2 = 0.95).

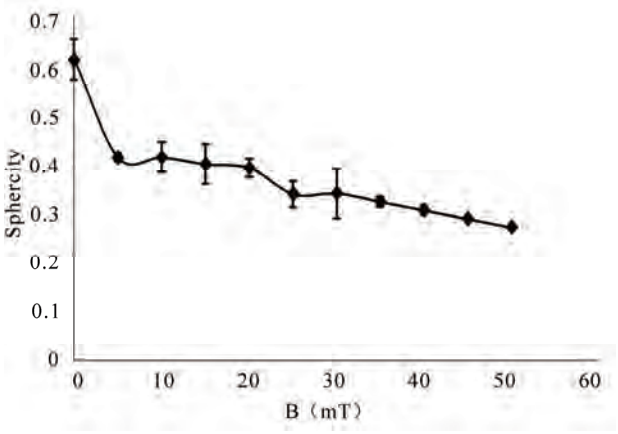

Figure 2. Sphericity of erythrocytes decreased under the influence of SMF. The correlation between sphericity and B is strong ($R^2 = 0.765$).

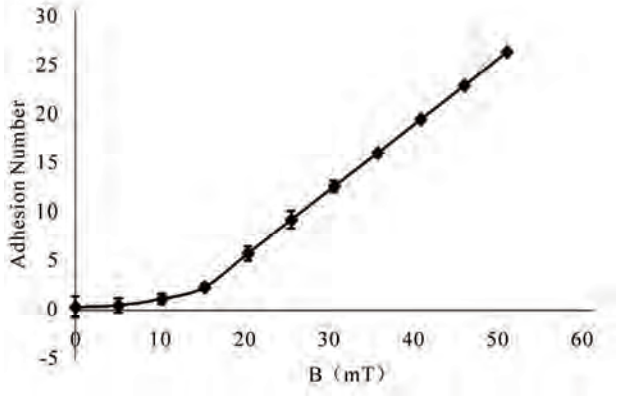

Figure 3. Sharp increase in erythrocytes adhesion number according to increase in SMF intensity (B).

for example, to changes in cellular shape, cytoskeleton arrangement, ion flux, receptor distribution, phagocytosis etc. Modifications in cell shape and plasma membrane as a consequence of exposure to MFs or EMFs have also been reported in many different cells [8,9,10]. Moderate-intensity (6 mT) SMFs exert a strong and replicable effect on cell shape and plasma membrane of different cell types [9]. In spite of the fact that this is not a high-intensity magnetic field, it is nevertheless able to produce changes in cell structure and function. Chionna *et al.* [9] focused their research on cell shape and cell surface modifications, providing evidence for time-related changes. As a general effect, cells growing in suspension lost their round shape and became irregularly elongated, while cells growing attached modified their shape and orientation or detached themselves, becoming freely suspended in the culture medium. Consistent with the previous studies increased in surface area and decreased in sphericity of the erythrocytes were found in the present study. The increased in erythrocytes surface area was at the expense of regular shape of the erythrocytes.

Dilek Ulker Cakir *et al.* [11] showed that long-term exposure to ELF-EMF decreased the mean volume of thrombocytes in the group of rats exposed for 50 days. Sanjay Jayavanth [12] showed that erythrocytes were monodisperse and with the formation and sedimentation of erythrocytes aggregates. In agreement of the previous studies our results showed that the adhesion of the erythrocytes increase under the influence of SMF compared to control.

From this study it can be concluded that studying the effect of SMF on the microscopic scale give a clear vision about the mechanisms of interaction between living cell and SMF. Also, it could be suggested that the SMF my increase the erythrocytes adhesion hence erythrocytes aggregation. It must be take in a count the changes of erythrocytes morphological structure when dealing with SMF.

REFERENCES

[1] Higashi, T., Ashida, N. and Takeuchi, T (1997) Orientation of blood cells in static magnetic field. *Physica B*, **237-238**, 616-620.

[2] Terumasa, H., Akio, Y., Tetsuya, T. and Muneyuki D. (1995) Effects of static magnetic fields on erythrocyte rheology. *Bioelectrochemistry and Bioenergetics*, **36**, 101-108.

[3] Repacholy, M.H. (2001) Review of health effects and gaps in knowledge. *Proceedings of WHO Meeting on EMF Biological Effects and Standard Harmonization in Asia and Okeania*, Seoul, 33-42.

[4] Hakobyan, S., Baghdasaryan, N., Amyan, A. and Ayrapetyan, S. (2001) The effect of EMF on water specific electrical conductivity and wheat sprouting. *Proceedings of WHO Meeting on EMF Biological Effects and Standard Harmonization in Asia and Okeania*, Seoul, 123.

[5] Rosen, A.D. (2003) Mechanism of action of moderate-intensity static magnetic fields on biological systems. *Cellular Biochemistry Biophysics*, **39**, 163-173.

[6] Lee, R.M., Maciej, Z., Masayuki, N., Kara, M., Sigalit, G., Merav, Z., Shlomo, M. and Jeffrey, J.C. (2000) The use of magnetite-doped polymeric microspheres in calibrating cell tracking velocimetry. *Journal of Biochemical and Biophysical Methods*, **44(1-2)**, 115-130.

[7] Canham, P.B. and Burton, A.C. (1968) Distribution of size and shape in populations of normal human red cells. *Circulation Research*, **22**, 405-422.

[8] Lisi, A., Pozzi, D., Pasquali, E., Rieti, S., Girasole, M., Cricenti, A., Generosi, R., Serafino, A.L., Congiu-Castellano, A., Ravagnan, G., Giuliani, L. and Grimaldi, S. (2000) Three dimensional (3D) analysis of the morphological changes induced by 50 Hz magnetic field exposure on human lymphoblastoid cells (Raji). *Bioelectromagnetics*, **21**, 46-51.

[9] Chionna, A., Dwikat, M., Panzarini, E., Tenuzzo, B., Carla`, E.C., Verri, T., Pagliara, P., Abbro, L. and Dini, L.

(2003) Cell shape and plasma membrane alterations after static magnetic fields exposure. *European Journal of Histochemistry*, **47**, 299-308.

[10] Rieti, S., Manni, V., Lisi, A., Giuliani, L., Sacco, D., D'Emilia, E., Cricenti, A., Generosi, R., Luce, M. and Grimaldi, S. (2004) SNOM and AFM microscopy techniques to study the effect of non-ionizing radiation on the morphological and biochemical properties of human keratinocytes cell line (HaCaT). *Journal of Microscopy*, **213**, 20-28.

[11] Dilek, U.C., Beran, Y., Mehmet, Z.A., Cemil, S. and Nuriye, M. (2009) Alterations of hematological variations in rats exposed to extremely low frequency magnetic fields (50 Hz). *Archives of Medical Research*, **40**, 352-356.

[12] Sanjay, J. and Megha, S. (2002) Influence of an inhomogeneous magnetic field on erythrocyte aggregation mechanism an analysis by He–Ne laser aggregometer. *Journal of Magnetism and Magnetic Materials*, **252**, 412-414.

J. Biomedical Science and Engineering, 2010, 3, 304-307 **JBiSE**
doi:10.4236/jbise.2010.33041 Published Online March 2010 (http://www.SciRP.org/journal/jbise/).

Tunable optical gradient trap by radial varying polarization Bessel-Gauss beam

Xiu-Min Gao[1,2], Song Hu[1], Jin-Song Li[3], Zuo-Hong Ding[2], Han-Ming Guo[2], Song-Lin Zhuang[2]

[1]Electronics & Information College, Hangzhou Dianzi University, Hangzhou, China;
[2]Optics & Electronics College, University of shanghai for Science and Technology, Shanghai, China;
[3]Optics & Electronics College, China Jiliang University, Hangzhou, China.
Email: xiumin_gao@yahoo.com.cn

Received 28 December 2009; revised 10 January 2010; accepted 12 January 2010.

ABSTRACT

Optical tweezers play an important role in many domains, especially in life science. And optical gradient force is necessary for constructing optical tweezers. In this paper, the optical gradient force in the focal region of radial varying polarization Bessel-Gauss beam is investigated numerically by means of vector diffraction theory. Results show that the beam parameter and vary rate parameter that indicates the change speed of polarization rotation angle affect the optical gradient force pattern very considerably, and some novel force distributions may come into being, such as multiple force minimums, force ring, and force crust. Therefore, the focusing of radial varying polarization Bessel-Gauss beam can be used to construct optical traps.

Keywords: Optical Gradient Force; Bessel-Gauss Beam; Radial Varying Polarization; Vector Diffraction Theory

1. INTRODUCTION

Optical tweezers technique has accelerated many major advances in numerous areas of science, especially in life science, since Ashkin developed optical tweezers system 1980s [1,2,3,4]. Optical tweezers can offer a very convenient, noninvasive, and non-contact access to processes at the microscopic scale [5], and a number of approaches have been proposed to constructing optical trap, such as generalized phase-contrast technique and holographic optical tweezers arrays [6,7]. In optical trapping system, it is usually deemed that the forces exerted on the particles in light field include two kinds of forces, one is the gradient force, which is proportional to the intensity gradient; the other is the scattering force, which is proportional to the optical intensity [8]. Therefore, optical gradient force is necessary for constructing optical tweezers, and the tunable focal intensity distribution predicts that the position of optical trap may be controllable.

It is well known that Bessel beams provide valid solutions to Helmholtz equation, and have attracted a lot of attention [9,10,11] for their non-diffracting property. And these beams are easily generated external to the laser cavity by illuminating an axicon with a Gaussian beam [12]. In this paper, the optical gradient force in the focal region of radial varying polarization Bessel-Gauss beam is investigated numerically by means of vector diffraction theory. The principle of the focusing this non-spiral vortex Gaussian beam is given in Section 2. Section 3 shows the simulation results and discussions. The conclusions are summarized in Section 4.

2. PRINCIPLE OF FOCUSING RADIAL VARYING POLARIZATION BESSEL-GAUSS BEAM PRINCIPLE OF THE FOCUSING GAUSSIAN

According the vector diffraction theory [13,14], the electric field in focal region of the radial varying polarization Bessel-Gauss beam can be written in the form as,

$$\vec{E}(r,\phi,z) = E_r\vec{e}_r + E_z\vec{e}_z + E_\varphi\vec{e}_\varphi \tag{1}$$

where $\vec{e}_r$, $\vec{e}_z$, and $\vec{e}_\varphi$ are the unit vectors in the radial, azimuthal, and propagating directions, respectively. E_r, E_z, and E_φ are amplitudes of the three orthogonal components and can be expressed as

$$E_r(r,z) = A\cos\phi\int_0^\alpha \cos^{1/2}\theta P(\theta)\sin(2\theta) \cdot J_1(kr\sin\theta)\exp(ikz\cos\theta)\,d\theta \tag{2}$$

$$E_z(r,z) = 2iA\cos\phi\int_0^\alpha \cos^{1/2}\theta P(\theta)\sin^2(\theta) \cdot J_0(kr\sin\theta)\exp(ikz\cos\theta)\,d\theta \tag{3}$$

$$E_\varphi(r,z) = 2A\sin\phi\int_0^\alpha \cos^{1/2}\theta P(\theta)\sin(\theta) \cdot J_1(kr\sin\theta)\exp(ikz\cos\theta)\,d\theta \tag{4}$$

where r and z are the radial and z coordinates of observation point in focal region, respectively. k is wave number. Here $P(\theta)$ is the pupil apodization function [15],

$$P(\theta) = J_1\left(\frac{2\beta_1 \sin\theta}{NA}\right)\cdot\exp\left[-\left(\frac{\beta_2 \sin\theta}{NA}\right)^2\right] \quad (5)$$

$\alpha = \arcsin(NA)$, which practically indicates the radius corresponding to each section zone of the cylindrical vector beam. ϕ is the polarization rotation angle from radial direction. As the function of convergence angle θ, and ϕ is in the form of,

$$\phi = C\cdot\frac{\sin(\theta)}{\sin(\alpha)}\cdot\pi \quad (6)$$

where C is viable rate parameter that indicates the change speed of polarization rotation angle. Based on the optical intensity distribution in focal region, the gradient force trap can be expressed as [1,16],

$$F_{grad} = \frac{n_b^2 r^3}{2}\cdot\left(\frac{m^2-1}{m^2+2}\right)\nabla\left|\vec{E}(r,\varphi,z)\right|^2 \quad (7)$$

where r is the radius of trapped particles, n_b is the refraction index of the surrounding medium, and m, the relative index of refraction, equals to the ratio of the refraction index of the particle n_p to the refraction index of the surrounding medium n_b. Gradient force points in the direction of the light intensity gradient when the diffractive index of particles is bigger than that of surrounding medium, *i.e.* $n_p > n_b$. Therefore, the gradient force pattern can be computed numerically by substituting **Eq. 1** into **Eq. 6**.

3. RESULTS AND DISCUSSIONS

Without losing generality and validity, it is supposed that $A=1$, $NA=0.95$, and $\beta_2=1$. It should be noted that in this paper Vr and Vz denote radial and axial coordinates, and the distance is k^{-1}, where k is wave number of the incident BG beam. The intensity distribution and corresponding optical gradient force pattern for $\beta_1=2.0$ and $C=1.0$ are firstly calculated and illustrated in **Figure 1**. Arrows in this figure indicate the force direction under condition of the diffractive index of particles is bigger than that of surrounding medium. It can be seen that the intensity distribution turns on the focal ring, as shown in **Figure 1(a)**, which can be used to construct ring-shape focal trap, given in **Figure 1(b)**.

Now the effect of the parameter β_1 on optical gradient is investigated. It is chosen that β_1 = 2.5 in the following calculation. The corresponding intensity distribution and gradient force pattern are given in **Figure 2**. We can see that the focal ring extends along optical axis, and there three weak on-axis peaks. From **Figure 2(b)**, it can be seen that there is one cylindrical crust trap, and multiple weak traps on axis. Therefore, parameter β_1 affects the Bessel-Gauss beam, in turn can alter the optical gradient force pattern considerably.

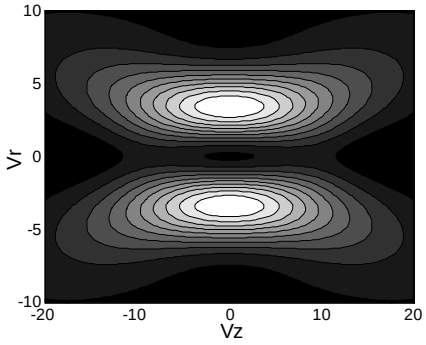

(a)

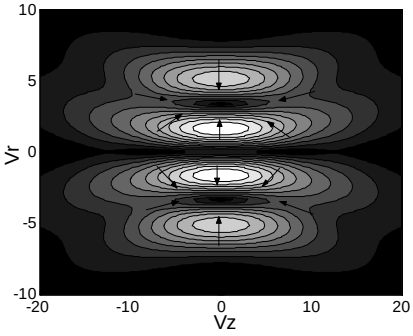

(b)

Figure 1. The (a) intensity distribution and corresponding (b) optical gradient force pattern for $\beta_1=2.0$ and $C=1.0$, respectively. Arrows indicate the force direction.

In order to get insight into the optical gradient force in the focal region of radial varying polarization Bessel-Gauss beam more deeply, different C is also considered in calculation. From **Figure 3(a)**, it can be seen that one optical intensity crust comes into being under condition of $C=0.2$, namely, one local intensity minimum occurs. **Figure 3(b)** illustrates the corresponding optical gradient force pattern that is in practice force crust pattern. So, the parameter C can be used to alter optical gradient force pattern in focal region of the Bessel-Gauss beam.

In our theoretical investigation, more values of β_1 and C are studied. And many novel optical gradient force patterns can occur. This paper only gives several typical cases. **Figure 4** illustrates the intensity distribution and corresponding optical gradient force pattern for $\beta_1=3.5$ and $C=1.0$. One intensity distorted cylinder

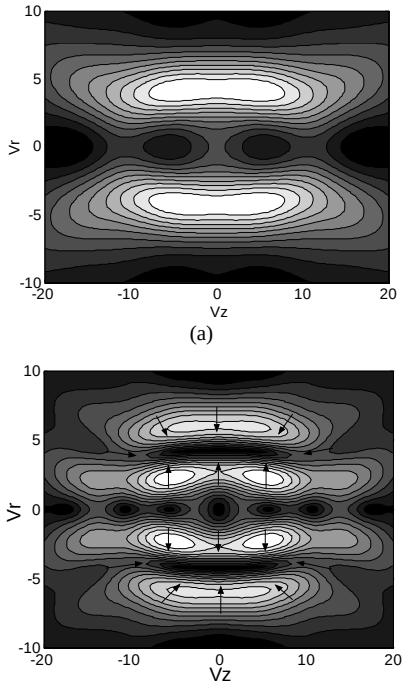

Figure 2. The (a) intensity distribution and corresponding (b) optical gradient force pattern for $\beta_1 = 2.5$ and $C = 1.0$, respectively. Arrows indicate the force direction.

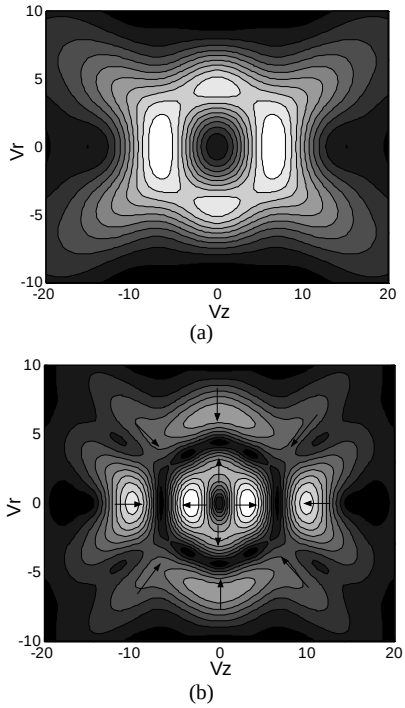

Figure 3. The (a) intensity distribution and corresponding (b) optical gradient force pattern for $\beta_1 = 2.5$ and $C = 0.2$, respectively. Arrows indicate the force direction.

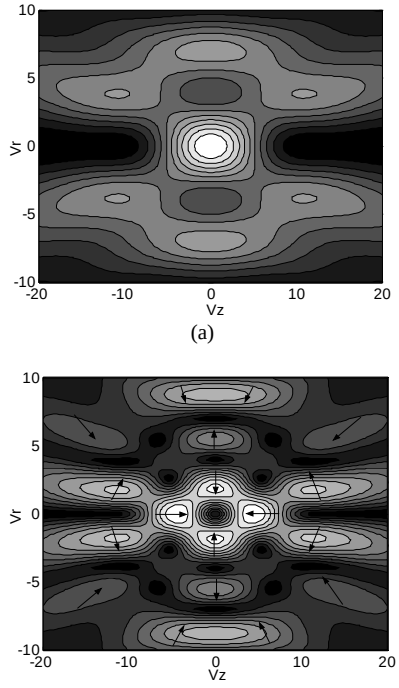

Figure 4. The (a) intensity distribution and corresponding (b) optical gradient force pattern for $\beta_1 = 2.5$ and $C = 1.0$, respectively. Arrows indicate the force direction.

appears outside of center main center intensity peak. **Figure 4(b)** shows that center optical trap comes into being, and simultaneously, more complicate force pattern also occur outside of this main trap. From above all optical gradient evolution process, it can be given that the beam parameter and vary rate parameter can be used to alter intensity and corresponding optical gradient force distributions in focal region of Bessel-Gauss beam remarkably.

4. CONCLUSIONS

The optical gradient force in the focal region of radial varying polarization Bessel-Gauss beam is investigated numerically by means of vector diffraction theory. Simulation results show that the beam parameter and vary rate parameter affect the optical gradient force pattern very considerably, and some novel force distribution patterns may come into being, which indicates that the focusing of radial varying polarization Bessel-Gauss beam can be used to construct optical traps.

5. ACKNOWLEDGMENTS

This work was supported by National Natural Science Foundation of China (60708002, 60878024, 60778022), China Postdoctoral Science Foundation (20080430086), Shanghai Postdoctoral Science Foundation of China (08R214141), and the Innovation Fund Project For Graduate Student of Shanghai (JWCXSL1002).

REFERENCES

[1] Ashkin, A., Dziedzic, J.M., Bjorkholm, J.E. and Chu, S. (1986) Observation of a single-beam gradient force optical trap for dielectric particles. *Optics Letters*, **11**, 288- 290.

[2] MacDonald, M.P., Paterson, L., Volke-Sepulveda, K., Arlt, J., Sibbett, W. and Dholakia, K. (2002) Creation and manipulation of three-dimensional optically trapped structures. *Science*, **296**, 1101-1103.

[3] Vladlen, G.S., Anton, S.D., Andrei, V.R., Wieslaw, K. and Yuri, S.K. (2009) Optical guiding of absorbing nanoclusters in air. *Optics Express*, **17**, 5743-5757.

[4] Grier, D.G. (2003) A revolution in optical manipulation. *Nature*, **424**, 810-816.

[5] Wang, M.D., Schnitzer, M.J., Yin, H., Landick, R., Gelles, J. and Block, S.M. (1998) Force and velocity measured for single molecules of RNA polymerase. *Science*, **282**, 902-907.

[6] Eriksen, R.L., Mogensen, P.C. and Glückstad, J. (2002) Multiple-beam optical tweezers generated by the generalized phase-contrast method. *Optics Letters*, **27**, 267-269.

[7] Curtis, J.E., Koss, B.A. and Grier, D.G.. (2002) Dynamic holographic optical tweezers. *Optics Communications*, **207**, 169-175.

[8] Visscher, K. and Brakenhoff, G.J. (1992) Theoretical study of optically induced forces on spherical particles in a single beam trap I: Rayleigh scatterers, *Optik*, **89**, 174-180.

[9] Durnin, J. (1987) Exact solutions for nondiffracting beams. I. The scalar theory. *Journal of the Optical Society America Associates*, **4**, 651-654.

[10] Li, Y., Gurevich, V., Kirchever, M., Katz, J. and Marom, E. (2001) Propagation of anistropic Bessel-Gaussian beams: sidelobe control, mode selection, and field depth. *Applied Optics*, **40**, 2709-2721.

[11] Yang, Y. and Li, Y. (2007) Spectral shifts and spectral switches of a pulsed Bessel-Gauss beam from a circular aperture in the far field. *Optics & Laser Technology*, **39**, 1478-1484.

[12] Igor, A. and Litvin Andrew, F. (2008) Bessel-Gauss resonator with internal amplitude filter. *Optics Communications*, **281**, 2385-2392.

[13] Zhan, Q. and Leger, J.R. (2002) Focus shaping using cylindrical vector beams. *Optics Express*, **10**, 324-330.

[14] Youngworth, K.S. and Brown, T.G. (2000) Focusing of high numerical aperture cylindrical-vector beams. *Optics Express*, **7**, 77-87.

[15] Elijah, Y., Yew, S., Colin, J. and Sheppard, R. (2007) Tight focusing of radially polarized Gaussian and Bessel-Gaussian beams. *Optics Letters*, **32**, 3417-3419.

[16] Garces-Chaves, V., McGloin, D., Melville, H., Sibbett, W. and Dholakia, K. (2002) Simultaneous micromanipulation in multiple planes using a self reconstructing light beam. *Nature*, **419**, 145-148.

J. Biomedical Science and Engineering, 2010, 3, 308-316 **JBiSE**
doi:10.4236/jbise.2010.33042 Published Online March 2010 (http://www.SciRP.org/journal/jbise/).

An index for evaluating distance of a healthy heart from Sino-Atrial blocking arrhythmia

Hossein Gholizade-Narm[1], Morteza Khademi[2], Asad Azemi[3], Masoud Karimi-Ghartemani[4]

[1]Electronic & Robotic Engineering, Shahrood University Technology, Shahrood, Iran;
[2]Ferdowsi University of Mashhad, Mashhad, Iran;
[3]College of Engineering, Penn State University, Philadelphia, USA;
[4]Sharif University of Technology, Tehran, Iran.
Email: Gholizade@shahroodut.ac.ir

Received 29 November 2009; revised 15 December 2009; accepted 28 December 2009.

ABSTRACT

In this paper, an index for evaluating Distance of a healthy heart from Sino-Atrial Blocking Arrhythmia (SABA) is presented. After definition of the main pacemakers' model of heart, Sino-Atrial (SA) and Atrio-Ventricular nodes (AV), the boundary of synchronization, which demonstrates the boundary of blocking arrhythmia, is obtained using perturbation method. In order to estimate of healthy heart characteristics, a parameter estimator is introduced. The distance from SABA is calculated using Lagrange method and Kohn-Tucker conditions. In addition, the maximum admissible decrease in the coupling intensity and the maximum admissible increase in the discrepancy between the natural frequencies of two pacemakers are determined in order to maintain the synchronization between the two pacemakers.

Keywords: Healthy Heart; Blocking Arrhythmia; Perturbation method; Synchronization Boundary; Optimization; Bifurcation

1. INTRODUCTION

The heart arrhythmias are the first cause of death according to World Health Organization (WHO) reports [1]. The lack of information about the health degree is one of the many factors for this. In other words, if people know their relative degree of health, the demise will be decreased. Fortunately, the medical science has the ability to measure the distance from illness in many issues. For instance, the fat and glucose of blood can be determined by some easy checks. The treatment could be initiated if it was near dangerous zone. Many works have also been done on cardiac arrhythmias' prediction to reduce the cardiac sudden death. Most of them have been done by physicians. The statistical methods are often used in those researches. In statistical methods, the QRS complex and QT interval and other segments of Electro Cardio Graph (ECG) are investigated and cardiac sudden death is predicted [2,3,4,5]. The nonlinear features such as fractal dimensions of Heart Rate Variability (HRV) are used by other methods to determine the risk of sudden death [6]. Finally, the General Regression Neural Network (GRNN), Learning Vector Quantization (LVQ) and wavelet transform are used to predict the life-threatening Ventricular tachycardia (VT) and Ventricular Fibrillation (VF) [7].

All of the works are based on signal processing and their result is a number which demonstrates the probability of being prone to arrhythmia or death. Unfortunately, signal processing based methods are not of enough accuracy to predict life-threatening cardiac arrhythmias (less than 70%) [6,7]. On the other hand, it cannot evaluate the relative degree of health if the heart is assumed healthy.

In this research, our goal is to evaluate the distance from SABA by observing action potential signals of SA and AV nodes. The blocking arrhythmias arise when two pacemakers are not in synchrony. The main reasons for asynchrony are either decreasing coupling intensity or increasing the discrepancy of two pacemakers' natural frequencies or both. For evaluation of distance from SABA, four stages should be passed. At first, a proper model should be considered for pacemakers. Then, the synchronization boundary must be obtained based on the model parameters. At the next stage, the model of parameters should be estimated from pacemakers' action potentials. Finally, by defining a cost function for distance from SABA and using optimization methods, the minimum distance is calculated.

Many models have been proposed for pacemakers and heart cells till now. Among the most well-known of them are Van der Pol [8,9,10,11], Fitzhugh-Nagumo [12,13,14], Hodgkin-Huxley [15], Beeler-Reuter [16] and Lou-Rudy [17] model. In this research, the Van der

Pol model is used as the model of SA and AV nodes for its simplicity and sufficiency for synchronization issues.

Synchronization and its boundary have dedicated many works of engineers and physicists to itself from the past decades. Synchronization can be divided into complete synchronization, lag synchronization, functional synchronization, phase synchronization and frequency synchronization [18,19]. The output signal of the oscillators must be exactly equal for complete synchronization. In other words, two signals should be identical in amplitude and frequency. The lag synchronization is similar to complete synchronization except that the output of one oscillator should be coincided on the delayed signal of another one. The complete and lag synchronization are accessible only for two identical oscillators. In functional synchronization, the output signal of one oscillator is a function of another one. This type of synchronization is defined for those oscillators whose parameters are related together. Any type of the aforementioned synchronization types will not be occurred if two oscillators are non-identical. However, most of the coupled oscillators are non-identical in nature. In this case, the phase and frequency synchronization is defined in which, the coincidence of the output signals of two oscillators is not necessary. In phase synchronization, the phase difference of signals should be fixed for all the time and for frequency synchronization, it is enough that the phase difference of two oscillators to be bounded. The heart pacemakers are in phase synchrony in normal mode. When they tend to asynchrony, they pass frequency synchronization at first and then become asynchrony. Therefore, the boundary of synchronization is determined by frequency synchronization, but since it is difficult to find the frequency synchronization boundary (it can only be obtained by simulation [20]) and on the other hand, its distance from phase synchronization boundary if very tiny [20,21], the phase synchronization has been taken as arrhythmia boundary in this research.

Perturbation methods, specially averaging method and bi-variant expansion are more applied in synchronization boundary determination [20,21,22]. The dynamical equations of two coupled oscillators are mapped to polar space using perturbation method. In polar space, the phase difference of two oscillators is a state variable. Therefore, the stability of new dynamical system is sufficient for phase synchronization because, in this case, the phase difference tends to a fixed point.

Unfortunately, there is not any background about measuring distance from arrhythmia. Our goal in this research is to evaluate this distance using synchronization boundary and pacemakers' parameters. In addition, we will answer to two questions: 1) How much the coupling intensity can be decreased subject to synchronization? 2) How much the natural frequency difference of two pacemakers can be increased subject to synchronization?

The paper is organized as follow: After introduction in Section 1, the synchronization boundary is obtained using perturbation method in Section 2. A state and parameter estimator is introduced in Section 3 for two coupled pacemakers system. The distance from SABA is evaluated in Section 4 and the maximum permitted value of natural frequency difference and minimum permitted value of coupling intensity are calculated in Section 5. Simulation results are demonstrated in Section 6 and the conclusion is discussed in Section 7.

2. THE PACEMAKER MODEL AND SYNCHRONIZATION BOUNDARY

The asynchrony between two vital pacemakers, SA and AV nodes, is the basic reason of blocking arrhythmias. In a healthy heart, the relationship between these two pacemakers is unidirectional coupling (from SA node to AV node) according to physicians' opinion; however, some physiologists suggest that the relationship is bidirectional but the effect of AV node on SA node is very smaller than vice versa [23]. According to the feedback of automatic nerves, the second idea is more acceptable. Here, we take the coupling as bidirectional, which is the general form. To change bidirectional case to unidirectional case, it is sufficient to equate the correspondence coefficient to the effect of AV node on SA node to zero. The model of two coupled pacemakers using Van der Pol Equations are,

$$\ddot{x}_t - \mu_1\left(1-x_t^2\right)\dot{x}_t + \omega_1^2 x_t = \alpha_1'\left(y_t - x_t\right) \quad (1)$$

$$\ddot{y}_t - \mu_2\left(1-y_t^2\right)\dot{y}_t + \omega_2^2 y_t = \alpha_2'\left(x_t - y_t\right) \quad (2)$$

were μ_1 and μ_2 are damping coefficients, ω_1 and ω_2 are natural frequencies, and α_1' and α_2' are coupling coefficients which demonstrate coupling intensity. Assume **Eqs. 1** and **2** are the SA and AV nodes' model respectively. According to relation between two coupled pacemakers, we take $\alpha_1' = \delta\alpha_2'$, $\delta << 1$. For using perturbation method, the system should be transformed to perturbation standard form. By scaling the time as $t = \varepsilon t_1$ which results $\dot{x} = \frac{dx}{dt} = \frac{dx}{dt_1}\frac{dt_1}{dt} = \frac{1}{\varepsilon}\dot{x}_{t_1}$, $\ddot{x} = \frac{1}{\varepsilon^2}\ddot{x}_{t_1}$ the **Eqs. 1** and **2** change as,

$$\begin{aligned} &\ddot{x}_{t_1} - \varepsilon\mu_1\left(1-x_{t_1}^2\right)\dot{x} + x_{t_1} = \varepsilon\delta\alpha_2\left(y_{t_1} - x_{t_1}\right) \\ &\ddot{y}_{t_1} - \varepsilon\mu_2\left(1-y_{t_1}^2\right)\dot{y}_{t_1} + \left(1+\varepsilon\Delta\right)y_{t_1} = \varepsilon\alpha_2\left(x_{t_1} - y_{t_1}\right) \end{aligned} \quad (3)$$

where $\varepsilon^2\omega_1^2=1$, $\varepsilon^2\omega_2^2=1+\varepsilon\Delta$ and $\alpha_2=\varepsilon\alpha_2'$. Suppose $\omega_1>>1$ therefore $\varepsilon<<1$. On the other hand, $\delta=k\varepsilon<<1$.

Remark: the natural frequency of SA node is greater than AV node in the healthy heart. Since our goal is the measurement of the distance of healthy heart from SABA, therefore $\Delta<0$ according to 3.

Consider variables x and y linear versus ε as $x=x_0+\varepsilon x_1$, $y=y_0+\varepsilon y_1$. By bi-variant expanding of **Eq. 3** versus time in the form of $\xi=t_1$, $\eta=\varepsilon t_1$ and eliminating higher order terms ($O(\varepsilon^2)$ and higher terms) we have,

$$\frac{\partial^2 x_0}{\partial\xi^2}+x_0=0 \tag{4}$$

$$\frac{\partial^2 x_1}{\partial\xi^2}+x_1=-2\frac{\partial^2 x_0}{\partial\xi\partial\eta}+\mu_1\left(1-x_0^2\right)\frac{\partial x_0}{\partial\xi} \tag{5}$$

$$\frac{\partial^2 y_0}{\partial\xi^2}+y_0=0 \tag{6}$$

$$\begin{aligned}&\frac{\partial^2 y_1}{\partial\xi^2}+x_1=-2\frac{\partial^2 y_0}{\partial\xi\partial\eta}+\mu_2\left(1-y_0^2\right)\frac{\partial y_0}{\partial\xi}\\&+\alpha_2\left(\frac{\partial x_0}{\partial\xi}-\frac{\partial y_0}{\partial\xi}\right)-\Delta y_0\end{aligned} \tag{7}$$

Considering x_0 and y_0 in periodic forms,

$$\begin{aligned}x_0&=A(\eta)\cos\xi+B(\eta)\sin\xi\\y_0&=C(\eta)\cos\xi+D(\eta)\sin\xi\end{aligned} \tag{8}$$

By substituting x_0 and y_0 at the right hand of **Eqs. 4** and **6** and equating secular terms (coefficients of $\sin\xi$ and $\cos\xi$) to zero we have,

$$\begin{aligned}2\frac{dA}{d\eta}&=\mu_1A-\frac{1}{4}\mu_1A\left(A^2+B^2\right)\\2\frac{dB}{d\eta}&=\mu_1B-\frac{1}{4}\mu_1B\left(A^2+B^2\right)\end{aligned} \tag{9}$$

$$\begin{aligned}2\frac{dC}{d\eta}&=\mu_2C-\frac{1}{4}\mu_2C\left(C^2+D^2\right)+\alpha_2(D-B)+\Delta D\\2\frac{dD}{d\eta}&=\mu_2D-\frac{1}{4}\mu_2D\left(C^2+D^2\right)+\alpha_2(A-C)+\Delta C\end{aligned} \tag{10}$$

Define A, B, C and D as follow,

$$\begin{aligned}&A=R_1(\eta)\cos\theta_1(\eta)\ ,\ B=R_1(\eta)\sin\theta_1(\eta)\\&C=R_2(\eta)\cos\theta_2(\eta)\ ,\ D=R_2(\eta)\sin\theta_2(\eta)\end{aligned} \tag{11}$$

Therefore, x_0 and y_0 are,

$$\begin{aligned}x_0(\xi,\eta)&=R_1(\eta)\cos\left(\xi-\theta_1(\eta)\right)\\y_0(\xi,\eta)&=R_2(\eta)\cos\left(\xi-\theta_2(\eta)\right)\end{aligned} \tag{12}$$

By substituting A, B, C and D in 9 and 10 and rearranging them,

$$\begin{aligned}2\dot{R}_1&=\mu_1R_1\left(1-\frac{1}{4}R_1^2\right)\\2R_1\dot{\theta}_1&=0\\2\dot{R}_2&=\mu_2R_2\left(1-\frac{1}{4}R_2^2\right)-\alpha_2R_1\sin(\theta_1-\theta_2)\\2R_2\dot{\theta}_2&=-\Delta-\alpha_2+\alpha_2R_1\cos(\theta_1-\theta_2)\end{aligned} \tag{13}$$

where $\dot{R}_1=\frac{dR_1}{d\eta},\dot{R}_2=\frac{dR_2}{d\eta},\dot{\theta}_1=\frac{d\theta_1}{d\eta},\dot{\theta}_2=\frac{d\theta_2}{d\eta}$. Assume $\Phi=\theta_1-\theta_2$, the slow flow dynamical Equations are,

$$\begin{aligned}2\dot{R}_1&=\mu_1R_1\left(1-\frac{1}{4}R_1^2\right)\\2\dot{R}_2&=\mu_2R_2\left(1-\frac{1}{4}R_2^2\right)-\alpha_2R_1\sin\Phi\\2\dot{\Phi}&=\Delta+\alpha_2-\left(\alpha_2\frac{R_1}{R_2}\right)\cos\Phi\end{aligned} \tag{14}$$

where $\dot{\Phi}=\frac{d(\theta_1-\theta_2)}{d\eta}$. The synchronization boundary is achieved by determining the Saddle-Node (S-N) and Hopf bifurcation condition curves of 14 [20]. The first step is to find the equilibrium points curve. Equate the left hand of 14 to 0,

$$\mu_1R_1\left(1-\frac{1}{4}R_1^2\right)=0\Rightarrow R_1=2 \tag{15}$$

$$\begin{aligned}&\mu_2R_2\left(1-\frac{1}{4}R_2^2\right)-\alpha_2R_1\sin\Phi=0\\&\Rightarrow\sin\Phi=\frac{\mu_2R_2\left(1-\frac{1}{4}R_2^2\right)}{\alpha_2R_1}\end{aligned} \tag{16}$$

$$\Delta+\alpha_2-\left(\alpha_2\frac{R_1}{R_2}\right)\cos\Phi=0$$
$$\Rightarrow\cos\Phi=\frac{(\Delta+\alpha_2)R_2}{\alpha_2 R_1} \quad (17)$$

By summing the square of 16 and 17 and substituting R_1=2 we have,

$$\left(\mu_2 R_2\left(1-\frac{1}{4}R_2^2\right)\right)^2+\left((\Delta+\alpha_2)R_2\right)^2=4\alpha_2^2 \quad (18)$$

Replace $R_2^2=p$ and rearrange 18 according to power of *p*,

$$\frac{1}{16}\mu_2^2 p^3-\frac{1}{2}\mu_2^2 p^2+\left((\Delta+\alpha_2)^2+\mu_2^2\right)p-4\alpha_2^2=0 \quad (19)$$

Eq. 19 shows the curve of equilibrium points vs. the system's parameters. Using Descartes' rule of signs we see that (19) has either one or three positive roots for p. At bifurcation, there will be a double root which corresponds to requiring the derivative of (19) to vanish:

$$\frac{3}{16}\mu_2^2 p^2+\mu_2^2 p+\left((\Delta+\alpha_2)^2+\mu_2^2\right)=0 \quad (20)$$

Eliminating *p* from (19) and (20) gives the condition for S-N bifurcation as,

$$4\Delta^6+24\Delta^5\alpha_2+\left(60\alpha_2^2+8\mu_2^2\right)\Delta^4+\left(32\mu_2^2\alpha_2+80\alpha_2^3\right)\Delta^3$$
$$+\left(60\alpha_2^4+4\mu_2^4+12\mu_2^2\alpha_2^2\right)\Delta^2$$
$$+\left(8\mu_2^4\alpha_2+24\alpha_2^5-40\mu_2^2\alpha_2^3\right)\Delta+4\alpha_2^6-\mu_2^2\alpha_2^4=0 \quad (21)$$

Eq. 21 plots as two curves intersecting at cusp points in the (α_2,Δ) plane. At the cusp point, a further degeneracy occurs and there is a triple root in **Eq. 19**. Derivation from 20 gives,

$$p=\frac{8}{3} \quad (22)$$

By substituting *p* from (22) to (19) and (20) gives cusp points.

$$\left(\alpha_2^*=0.544\mu_2\ ,\ \Delta_1^*=0.033\mu_2\right),$$
$$\left(\alpha_2^*=0.544\mu_2\ ,\Delta_2^*=-1.122\mu_2\right) \quad (23)$$

Next we look for Hopf bifurcations in the slow flow system 14. Let R_{10}, R_{20}, Φ_0 be an equilibrium point. The behavior of the system linearized in the neighborhood of this point is determined by the eigenvalues of the Jacobian matrix.

$$J=\frac{1}{2}\begin{bmatrix}-\frac{3R_{10}^2-4}{4}\mu_1 & 0 & 0\\ -\alpha_2\sin(\Phi_0) & -\frac{3R_{20}^2-4}{4}\mu_2 & -R_{10}\alpha_2\cos(\Phi_0)\\ -\frac{\alpha_2}{R_{20}}\cos(\Phi_0) & \frac{\alpha_2 R_{10}}{R_{20}^2}\cos(\Phi_0) & \frac{\alpha_2 R_{10}}{R_{20}}\sin(\Phi_0)\end{bmatrix} \quad (24)$$

Substituting $\sin(\Phi_0),\cos(\Phi_0),R_{10}$ from (15–17) in 24 and after simplification,

$$J=\frac{1}{2}\begin{bmatrix}-2\mu_1 & 0 & 0\\ -\frac{1}{2}\mu_2 R_2\left(1-\frac{1}{4}R_2^2\right) & \left(1-\frac{3}{4}R_{20}^2\right)\mu_2 & -(\Delta+\alpha_2)R_{20}\\ -\frac{(\Delta+\alpha_2)}{2} & \frac{(\Delta+\alpha_2)}{R_{20}} & \mu_2\left(1-\frac{1}{4}R_{20}^2\right)\end{bmatrix} \quad (25)$$

For Hopf bifurcation, it is necessary that matrix *J* contains 2 pure imaginary and 1 real eigenvalue.

$$|\lambda I-J|=0\Rightarrow$$

$$(\lambda+\mu_1)\left(\lambda^2+\left(\frac{1}{2}\mu_2 R_{20}^2-\mu_2\right)\lambda+J_{22}J_{33}-J_{23}J_{32}\right)=0 \quad (26)$$

It can be seen from 26 that the coefficient of λ must be 0 for Hopf bifurcation.

$$\frac{1}{2}\mu_2 R_{20}^2-\mu_2=0\Rightarrow p=R_{20}^2=2 \quad (27)$$

Substituting p from 27 in **Eq. 19** gives the Hopf bifurcation condition curve.

$$\Delta^2+2\alpha_2\Delta+\frac{1}{4}\mu_2^2-\alpha_2^2=0 \quad (28)$$

Eqs. 21 and **28** identify the phase synchronization boundary. A typical sample for synchronization boundary is brought in **Ex. 1**.

Synchronization boundary Equations show that the boundary depends on coupling coefficients, damping coefficients and discrepancy of two pacemakers' natural frequency. Therefore, they should be estimated in practice for distance evaluation from SABA.

3. THE STATE-PARAMETER ESTIMATOR

Measurement of all states and parameters of the cardiac pacemakers is impossible in practice but the measurement of only their action potentials is practical using two implantable leads. In this section, a state-parameter estimator (adaptive observer) is introduced which is able to

estimate necessary parameters from pacemakers' action potentials for distance evaluation. This estimator uses the high-gain method. The high-gain method is very effective in state estimation [24]. When the parameters are unknown in addition to states, the estimator is modified which is called adaptive observer. An adaptive observer is introduced in [25] which can estimate parameters and states simultaneously. We use an adaptive observer which is introduced in [25] in this research. The system form is as follow,

$$\dot{x}(t)=\begin{pmatrix} A_1 & 0 \\ 0 & A_1 \end{pmatrix}x(t)+\begin{pmatrix} \phi_1(x(t),u(t)) \\ \phi_2(x(t),u(t)) \end{pmatrix}$$

$$+\begin{pmatrix} \psi_1(x(t),u(t)) \\ \psi_2(x(t),u(t)) \end{pmatrix}\theta \qquad (29)$$

$$y(t)=\begin{pmatrix} C_1 & 0 \\ 0 & C_2 \end{pmatrix}x(t)$$

where $x\in\Re^n$, $y\in\Re^2$, and $\theta\in\Re^q$ are the state vector, output vector and the unknown parameters vector respectively. The matrices C_i, ψ_i, A_i, i = 1, 2 are,

$$A_i=\begin{bmatrix} 0 & 1 & & 0 \\ & & \ddots & \\ & & & 1 \\ 0 & & & 0 \end{bmatrix},$$

$$\psi_i(x,u)=\begin{bmatrix} 0 & \cdots & 0 \\ \vdots & & \vdots \\ 0 & \cdots & 0 \\ \psi_{in_i,1}(x,u) & \cdots & \psi_{in_i,q}(x,u) \end{bmatrix} \qquad (30)$$

$$C_i=\begin{bmatrix} 1 & 0 & \cdots & 0 \end{bmatrix}_{1\times n_i},\ n=\sum_{i=1}^{2} n_i$$

The adaptive rules are,

$$\dot{\hat{\Gamma}}(t)=\lambda(A-KC)\hat{\Gamma}(t)+\lambda\psi(\tilde{x}(t),u(t))$$

$$\dot{\hat{x}}(t)=A\hat{x}(t)+\phi(\tilde{x}(t),u(t))+\psi(\tilde{x}(t),u(t))\tilde{\theta}(t)$$

$$+\Lambda(\lambda)^{-1}\left[\lambda K+\Gamma(t)\Gamma^T(t)C^T\right]\left[y(t)-C\tilde{x}(t)\right] \qquad (31)$$

$$\dot{\hat{\theta}}(t)=I_\lambda\Gamma^T(t)C^T\left[y(t)-C\tilde{x}(t)\right]$$

$$\tilde{x}=\hat{x}\ if\ \|\hat{x}\|\le X,\ \frac{\hat{x}}{\|\hat{x}\|}X\ otherwise.$$

$$\tilde{\theta}=\hat{\theta}\ if\ \|\hat{\theta}\|\le\Theta,\ \frac{\hat{\theta}}{\|\hat{\theta}\|}\Theta\ otherwise.$$

where Θ, X are the $\theta(0), x(0)$ upper bound,

$$K=\begin{bmatrix} K_1 & 0 \\ 0 & K_2 \end{bmatrix}$$

and $K_{1,2}$ are selected such that the $A_i-K_iC_i$ matrix be stable.

$$\Lambda^{-1}{}_{i=1,2}(\lambda)=diag\left(1,\lambda,\lambda^2,\cdots,\lambda^{n_i-1}\right)\ (\lambda>0),$$

and

$$\Lambda=\begin{bmatrix} \Lambda_1 & 0 \\ 0 & \Lambda_2 \end{bmatrix}$$

$$I_\lambda=\begin{bmatrix} \lambda^{n_1}I & 0 \\ 0 & \lambda^{n_2}I \end{bmatrix}$$

For using the introduced adaptive observer, the system 1 and 2 must be mapped to state space representation.

$$\dot{x}(t)=Ax(t)+\phi(x(t),u(t))+\psi(x(t),u(t))\theta$$
$$y(t)=Cx(t) \qquad (32)$$

where,

$$C=\begin{bmatrix}1&0&0&0\\0&0&1&0\end{bmatrix},\ A=\begin{bmatrix}0&1&0&0\\0&0&0&0\\0&0&0&1\\0&0&0&0\end{bmatrix},\ x(t)=\begin{bmatrix}x_1(t)&x_2(t)&x_3(t)&x_4(t)\end{bmatrix}^T$$

$$\theta=\begin{bmatrix}\mu_1&\omega_1^2&\alpha_1'&\mu_2&\omega_2^2&\alpha_2'\end{bmatrix}^T,\ \phi(x,u)=0 \tag{33}$$

$$\psi(x,u)=\begin{bmatrix}0&0&0&0&0&0\\(1-x_1^2(t))x_2(t)&-x_1(t)&-x_1(t)+x_3(t)&0&0&0\\0&0&0&0&0&0\\0&0&0&(1-x_3^2(t))x_4(t)&-x_3(t)&x_1(t)-x_3(t)\end{bmatrix}$$

The performance of introduced estimator is demonstrated in **Ex. 2**.

4. DISTANCE EVALUATION FROM SABA

In this section, our goal is to evaluate the distance from SABA using synchronization boundary and pacemakers' parameters. As it was mentioned in Section 2, the boundary is determined by S-N and Hopf bifurcation conditions. If $-1.122\mu_2 \le \Delta < 0$, the boundary is determined by S-N bifurcation condition curve. Otherwise, the synchronization boundary is identified by Hopf bifurcation condition curve. For distance evaluation, at first, the pacemakers' parameters should be mapped from $(\alpha',\mu,\omega_1,\omega_2)$ space to (α,μ,Δ) space.

$$\varepsilon=\frac{1}{\omega_1},\Delta=\varepsilon(\omega_2^2-\omega_1^2),\alpha_2=\varepsilon\alpha_2' \tag{34}$$

The second step is to find a point on synchronization boundary in which has the minimum distance from (α,μ,Δ). Assume the point $(\alpha_2^*,\mu_2^*,\Delta^*)$ is the desired point. By inverse transformation of this point using (35), the minimum distance from SABA can be obtained.

$$\omega_{2\min}^2=\omega_1^2+\frac{1}{\varepsilon}\Delta^*,\alpha_2'^*=\frac{1}{\varepsilon}\alpha_2^* \tag{35}$$

$$\text{Min. Dist. from Blocking Arrh.} = \sqrt{(\omega_2-\omega_{2\min})^2+(\alpha_2'-\alpha_2'^*)^2+(\mu_2-\mu_2^*)^2} \tag{36}$$

The crucial point is how to find the desired point. The **Eq. 21** contains two curves that one of them pass through origin point (0, 0, 0) and forms the first part of synchronization boundary. For simplicity, we approximate this curve by a line which passes from origin and cusp point.

$$\alpha_2=-0.48485\Delta \tag{37}$$

Therefore, the synchronization boundary is defined by **Eqs. 28** and **37**. Suppose $P=(\alpha_{2P},\mu_{2P},\Delta_P)$ is the pacemakers' parameters which is transformed to (α,μ,Δ) space. Define the distance of a point on boundary $Q=(\alpha,\mu,\Delta)$ from P as,

$$Dis^2=(\alpha_2-\alpha_{2P})^2+(\mu_2-\mu_{2P})^2+(\Delta-\Delta_P)^2 \tag{38}$$

By minimizing 38 subject to 37 and again subject to 28 individually and taking into account their minimum value, the desired point $(\alpha_2^*,\mu_2^*,\Delta^*)$ is achieved. Therefore, two minimization problems should be solved.

$$\begin{aligned}&Minimize\ Dis^2\\&S.T.\quad f_1(\alpha_2,\mu_2,\Delta)=\alpha_2+0.48485\Delta=0\\&\qquad -1.122\mu_2\le\Delta\le 0\end{aligned} \tag{39}$$

Using Lagrange coefficient and Kohn-Tucker method for considering inequality constraints we have,

$$L_1=Dis^2-\lambda f_1(\alpha_2,\mu_2,\Delta)+\upsilon_1\Delta-\upsilon_2(\Delta+1.122\mu_2) \tag{40}$$

$$\begin{aligned}&\nabla_{(\alpha_2,\mu_2,\Delta)}L_1=0\\&\nabla_\lambda L_1=0\\&\upsilon_1\Delta=0\\&-\upsilon_2(\Delta+1.122\mu_2)=0\end{aligned} \tag{41}$$

The parameters $(\alpha_2, \mu_2, \Delta, \lambda, \upsilon_1, \upsilon_2)$ are gained by solving 41. If conditions 42 and 43 are satisfied, the distance is evaluated from obtained $(\alpha_2, \mu_2, \Delta)$, otherwise, the extremum of those parameters which do not satisfy the conditions is substituted to evaluate distance.

$$\begin{aligned} &\Delta \le 0 \\ &-(\Delta + 1.122\mu_2) \le 0 \end{aligned} \tag{42}$$

and

$$\begin{aligned} &\upsilon_1 \ge 0 \\ &\upsilon_2 \ge 0 \end{aligned} \tag{43}$$

In second time, the desired point is sought on the (37) surface.

Minimize Dis^2

$$S.T. \quad f_2(\alpha_2, \mu_2, \Delta) = \Delta^2 + 2\alpha_2\Delta + \frac{1}{4}\mu_2^2 - \alpha_2^2 = 0 \tag{44}$$
$$\Delta \le -1.122\mu_2$$

Again, using Lagrange coefficient and Kohn-Tucker method, $(\alpha_2, \mu_2, \Delta)$ values are obtained and distance is evaluated. By comparing the two evaluated distance and considering the minimum value, the desired point is identified. By inverse transformation of this point to $(\alpha', \mu, \omega_1, \omega_2)$ space according to **Eq. 35**, the minimum distance from SABA is evaluated using (36). The distance evaluation is illustrated in **Ex. 3** for a typical sample.

5. IDENTIFICATION OF MAXIMUM ADMISSIBLE VARIATION OF PACEMAKERS' PARAMETERS

In this section, our goal is to evaluate the maximum variation of a parameter subject to remaining synchronization whiles other parameters are fixed. For instance, how much the coupling coefficient can be decreased whiles two pacemakers remain in phase synchrony or how much the discrepancy of two natural frequencies can be increased and the synchronization remain unchanged.

5.1. Maximum Admissible Decrease of Coupling Coefficient

For identification of maximum admissible variation of coupling coefficient, at first, we transform the pacemakers' parameters to same usable form in synchronization boundary equations using **Eq. 34**. Now, we consider coupling coefficient as unknown parameter and obtain it from **Eq. 37**. If the condition (42) is satisfied, the obtained value is the desired coefficient otherwise we will compute it from **Eq. 28**. In any way, assume the desired coefficient is α_2^*. Therefore the maximum admissible decrease of coupling coefficient is,

$$\delta_{\max}\alpha_2 = \alpha_2' - \frac{\alpha_2^*}{\varepsilon} \tag{45}$$

In other words, the minimum of coupling coefficient subject to remaining synchronization is,

$$\alpha_{2\min}' = \frac{\alpha_2^*}{\varepsilon} \tag{46}$$

5.2. Maximum Admissible Increase Discrepancy between Two Pacemakers' Natural Frequencies

For identification of maximum admissible increase discrepancy between two Pacemakers' natural frequencies, like Section 5-1, at first, we transform the pacemakers' parameters from $(\alpha', \mu, \omega_1, \omega_2)$ space to (α, μ, Δ) space using **Eq. 34**. Now, we assume that Δ is the unknown parameter and obtain it from **Eq. 37**. If the condition (42) is satisfied, the obtained value is desired Δ otherwise we compute it from **Eq. 28**. In any way, assume the desired value is the Δ^*. Therefore the maximum admissible increase of discrepancy between two Pacemakers' natural frequencies is,

$$\begin{aligned} &\delta_{\max}\omega = \omega_1 - \omega_{2\min} \\ &\omega_{2\min}^2 = \omega_1^2 + \frac{1}{\varepsilon}\Delta^* \end{aligned} \tag{47}$$

The damping coefficient is one of the determinative parameters for synchronization boundary but we ignore to find its maximum admissible variation for its little importance.

6. SIMULATION

The distance evaluation from SABA is completed in 3 steps: at first, the synchronization boundary is determined, and then the pacemakers' parameters estimated. Finally, the minimum distance from boundary is computed. In this section, the synchronization boundary is obtained for a typical sample and plotted (**Ex. 1**). Afterward, the performance of introduced adaptive observer is illustrated in **Ex. 2**. Then the distance from SABA is shown in **Ex. 3**. As a final point, the maximum admissible variation of parameters is calculated in **Ex. 4**.

Ex. 1. Assume $\mu_2 = 1$, the synchronization boundary is determined by (21) and (28). **Figure 1** shows the synchronization boundary and highlights the cusp points.

Ex. 2. Assume pacemakers' parameters as $\mu_1 = 2$, $\omega_1^2 = 64$, $\alpha_1' = 4$, $\mu_2 = 1, \omega_2^2 = 25$, $\alpha_2' = 22$. The parameters are chosen such that the synchronization frequency is 70 per minute and the natural frequency of pacemakers equal to 76 and 47 per minute for SA and AV nodes respectively. **Figure 2** illustrates the state-

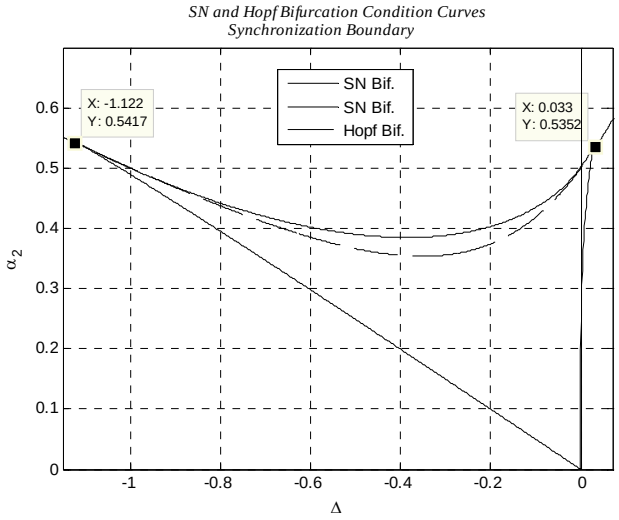

(a)

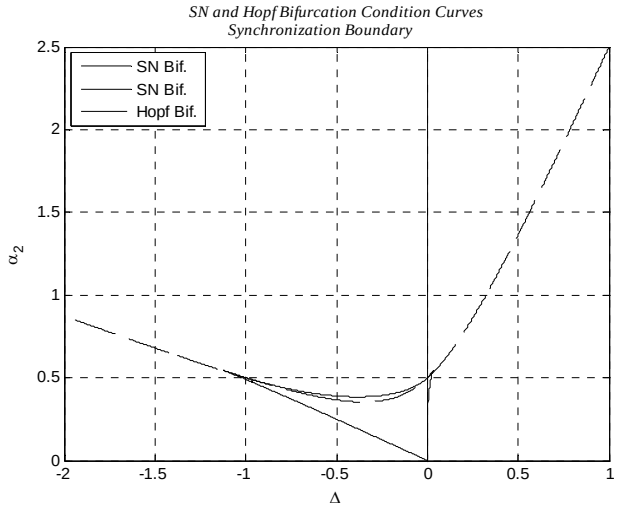

(b)

Figure 1. Phase synchronization Boundary. a. small discrepancy of natural frequency b. big discrepancy of natural frequency.

parameter estimator performance.

Ex. 3. Suppose pacemakers' parameters as **Ex. 2** for using synchronization boundary to evaluate distance from SABA, we should transform parameters at first.

$$\varepsilon = 0.125\ ,\delta = 0.05,$$
$$P = \left(\alpha_{2P} = \varepsilon\alpha_2', \mu_{2P}, \Delta_P\right) = \left(2.75, 1, -4.875\right)$$

Since $\Delta_P = -4.875 << -1.122$, therefore the desired point is on Hopf bifurcation condition curve. By solving (44) we have, $\alpha_2^* = 2.1409$, $\mu_2^* = 1.0214$, $\Delta^* = -5.1252$. We see that condition (44) is satisfied. The distance from SABA is,

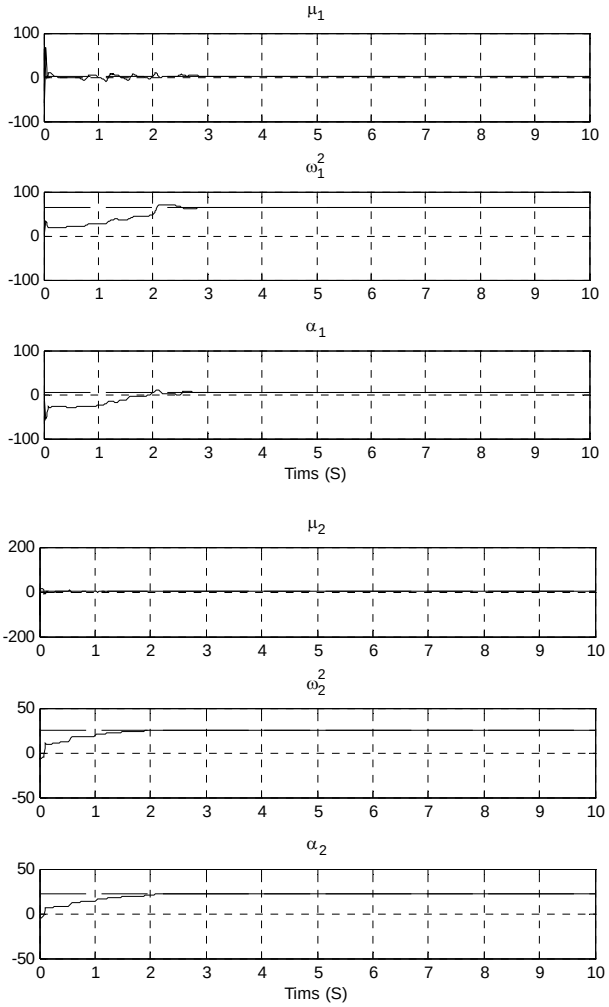

Figure 2. System's parameter estimation.

$$\omega_{2\min}^2 = 64 - 8\times 5.1252 = 22.9284,$$
$$\alpha_2^* = 8\times 2.1409 = 17.1272,\ \ \mu_2^* = 1.0214$$

Min. Dist. from Blocking Arrh.

$$= \sqrt{\left(\omega_2 - \omega_{2\min}\right)^2 + \left(\alpha_2' - \alpha_2^*\right)^2 + \left(\mu_2 - \mu_2^*\right)^2} = 23.7894$$

Ex. 4. The maximum admissible variation for **Ex. 3** parameters are,

$$\alpha_2^* = 2.0374 \Rightarrow \alpha_2'^* = \frac{1}{\varepsilon}\alpha_2^*$$
$$= 16.2992 \Rightarrow\ \delta_{\max}\alpha_2' = 5.7008$$
$$\Delta^* = -6.61 \Rightarrow \delta_{\max}\Delta = -1.7318, \omega_{2\min}^2$$
$$= 11.1456 \Rightarrow \delta_{\max}\omega_2 = \omega_2 - \omega_{2\min} = 1.6615$$

7. CONCLUSIONS

The evaluation of distance from SA blocking arrhythmia for a healthy heart was investigated in this paper. To do

this, the synchronization boundary was obtained using perturbation method. The synchronization boundary defines the illness boundary approximately. To compute the distance from this boundary, an estimator was introduced which can estimate SA and AV nodes' parameters from their action potential signals. Using optimization methods, the minimum distance from SABA was evaluated. This value can be considered as an alarm when it is very small. The coupling intensity and discrepancy of natural frequency of two pacemakers play a crucial role in synchronization of two basic pacemakers. Hence, a method was proposed to evaluate the maximum admissible variation of these parameters. The maximum variation value demonstrates the confidence margin.

REFERENCES

[1] World Helth Organization (WHO), Internet Available: www.who.int.

[2] El-Sherif, N., Denes, P., Katz, R., Capone, R., Brent , L., Carlson, M. and Reynolds, R. (1995) Definition of the best prediction criteria of the time domain signal-averaged electrocardiogram for serious arrhythmic events in the post infraction period. *Journal of American Collection Cardiology*, **25(4)**, 908-914.

[3] Tsagalou, E. P., Anastasiou-Nava, M. I., Karagounis, L. A., Alexopoulos, G. P., Batziou, C., Toumanidis, S., Papadaki, E. and Nanas, J. N. (2002) Dispersion of QT and QRS in patients with severe congestive heart failure: Relation to cardiac and sudden death mortality, *Hellenic Jornal of Cardiology*, **43**, 209-215.

[4] Thong, T., McNames, J., Aboy, M. and Goldstein, B. (2003) Paroxysmal atrial fibrillation prediction using isolated premature atrial events and paroxysmal atrial tachycardia. *Proceedings of IEEE International Conference on Biomedical Engineering*, EMBC, 163-166.

[5] Thong, T., McNames, J., Aboy, M. and Goldstein, B. (2004) Prediction of paroxysmal atrial fibrillation by analysis of atrial premature complexes. *IEEE Transactions On Biomedical Engineering*, **51(4)**, 561-569.

[6] Owis, I., Abou-Zied, H. and Youssef, M. (2002) Study of Features Based on Nonlinear Dynamical Modeling in ECG Arrhythmia Detection and Classification. *IEEE Transactions On Biomedical Engineering*, **49(7)**, 733-736.

[7] Abbas, R., Aziz, W. and Arif, M. (2004) Prediction of ventricular Tachyarrhythmia in Electrocardiograph Signal Using Neuro-wavelet Approach. *National Conference on Emerging Technologies*, 82-87.

[8] Van der Pol, B. and Van der mark, J. (1927) Frequency demultiplication. *Nature*, **120**, 363-364.

[9] Van der Pol, B. and Van der mark, J. (1928) The Heartbeat considered as a relaxation oscillation and electrical model of heart. Phil. Mag. Supll., **6**, 763-775.

[10] Grudzinsky, K. and Zebrowski, J. (2004) Modeling cardiac pacemakers with relaxation oscillators. *Physica A: Statistical Mechanics and its Applications*, 153-162.

[11] Sato, S., Doi, S. and Nomura, T. (1994) Bonhoffer-van der pol oscillator model of the Sino-Atrial node: A possible mechanism of heart rate regulation. *Method of Information in Medicin*, 116-119.

[12] Fitzhugh, R. (1961) Impulses and physiological in theoretical models of nerve membranes. *Biophysical Journal*, **1**, 445-466.

[13] FitzHugh, R. (1969) Mathematical models of excitation and propagation in nerve. In: Schwan H.P. Ed., *Biological Engineering*, McGraw Hill, New York.

[14] Nagumo, J., Arimoto, S. and Yoshizawa, S. (1962) An active pulse transmission line simulating nerve axon. *Proceedings of the IRE*, **50**, 2061-2070.

[15] Hodgkin, A. L., Huxley, A. F. and Katz, B. (1952) Measurement of current-voltage relations in the membrane of the giant axon of Loligo, *The Journal of physiology*, **116**, 424.

[16] Beeler, G.W. and Reuter, H. **(**1977**)** Reconstruction of the action potential of ventricular myocardial fibres. *The Journal of physiology*, **268**, 177-210.

[17] Lou, C.H. and Rudy, Y. (1994) A dynamic model of the cardiac ventricular action potential I. *Circulation Research*, **74**, 1071-1096.

[18] Pikovsky, A., Rosenblum, M. and Kurths, J. (2002) Synchronization: A universal concept nonlinear science, Cambridge University Press.

[19] Santos, A. M., Lopes, S. R. and Viana, R. L. (2004) Rhythm synchronization and chaotic modulation of couplead van der pol oscillatiors in a model for the heartbeat. *Physica A*, **338**, 335-355.

[20] Rand R. H. (2004) Lecture notes in nonlinear vibrations. 45 version, The Internet-First University Press, Ithaca. http://dspace.library.cornell.edu/handle/1813/79.

[21] Rompala, K., Rand, R. and Howland, H. (2007) Dynamics of three coupled van der Pol oscillators with application to circadian rhythms. *Communications in Nonlinear Science and Numerical Simulation*, **12**, 794-803.

[22] Nayfeh, A. H. (1973) Perturbation Methods, John Wiley & Sons Ltd., Chichester.

[23] Grudzinski, K., Zebrowski, J.J. and Baranowski, R. (2006) Model of the sino-atrial and atrio-ventricular nodes of the conduction system of the human heart. *Biomedical Technology*, **51**, 210-214.

[24] Gauthier, J. P., Hammouri, H. and Othman, S. (1992) A simple observer for nonlinear systems – applications to bioreactors. *IEEE Transactions on Automatic Control*. **37(6)**, 875-880.

[25] Besancon, G., Zhang, Q. and Hammouri, H., (2002) High-Gain observer based state and parameter estimation in nonlinear systems. International Federation of Automatic Control.

J. Biomedical Science and Engineering, 2010, 3, 317-321 **JBiSE**
doi:10.4236/jbise.2010.33043 Published Online March 2010 (http://www.SciRP.org/journal/jbise/).

A mixture model based approach for estimating the FDR in replicated microarray data

Shuo Jiao, Shun-Pu Zhang

Department of Statistics University of Nebraska Lincoln, NE, USA.
Email: szhang3@unl.edu

Received 5 November 2009; revised 27 November 2009; accepted 3 December 2009.

ABSTRACT

One of the mostly used methods for estimating the false discovery rate (FDR) is the permutation based method. The permutation based method has the well-known granularity problem due to the discrete nature of the permuted null scores. The granularity problem may produce very unstable FDR estimates. Such instability may cause scientists to over- or under-estimate the number of false positives among the genes declared as significant, and hence result in inaccurate interpretation of biological data. In this paper, we propose a new model based method as an improvement of the permutation based FDR estimation method of SAM [1] The new method uses the *t*-mixture model which can model the microarray data better than the currently used normal mixture model. We will show that our proposed method provides more accurate FDR estimates than the permutation based method and is free of the problems of the permutation based FDR estimators. Finally, the proposed method is evaluated using extensive simulation and real microarray data.

Keywords: FDR; T-Mixture Model; Microarray; Genes

1. INTRODUCTION

Genome-wide expression data generated from the microarray experiments are widely used to uncover the functional roles of different genes, and how these genes interact with each other. A key step to achieve this is to identify the differentially expressed (DE) genes under different experimental conditions. Such information can be used to identify disease biomarkers that may be important in the diagnoses of different types of diseases. Earlier statistical approaches for detecting DE genes focused mostly on parametric methods which are easily subject to model misspecification problems. Some of the well-known parametric methods for detecting DE genes include the two sample *t*-test [2], the analysis of variance approach [3], a regression approach [4], the regularized t-statistic method (Bayes-t test) [5,6]), the semi-parametric hierarchical mixture method [7], and the parametric EB method [8]. Recently, the availability of replicated microarrays has made it possible to use the nonparametric methods to detect the DE genes. The nonparametric methods require much less stringent dis-tributional assumptions, and thus can provide more robust results than the parametric methods. Some of the well-known nonparametric methods for analyzing microarrays include the Significance Analysis of Microar-ray (SAM) of [1], the nonparametric EB method [9,10], the non-parametric t-test with adjusted p-value [11], the Wilcoxon Rank Sum test [12], samroc [13] and the normal mixture model method (MMM) of [14].

In this paper, we will focus our attention on SAM, one of the most popular methods in microarray data analysis. SAM indentifies DE genes by computing a modified *t*-statistic as the test score of a gene and finding the genes with test scores exceeding an adjustable threshold. The false discovery rate (FDR) was then estimated by a permutation based method. More specifically, the number of false positive (FP) genes among the significant genes is estimated as the median of the numbers of scores exceeding the cutoffs in each permuted set of null scores.

Since the permutation based approach estimates the FDR by counting the number of FP genes exceeding some cutoffs, we will call it the empirical method in this paper. Due to its nature, there are two drawbacks with the empirical method: 1) the granularity problem – the FDR estimates based on the counted number of FP genes tend to be unstable when the actual number of FP genes is small; 2) the zero FDR problem – the estimated FDR may be zero when the range of the permuted null scores is smaller than that of test scores and when the cutoffs are more extreme than the endpoints of permuted null scores. These two drawbacks are illustrated in the **Figures 1, 2** and **3**.

In this paper, we will propose a *t*-mixture model based approach as an improvement of the empirical FDR estimation method of SAM. Our method aims to solve the two aforementioned drawbacks of the current empirical

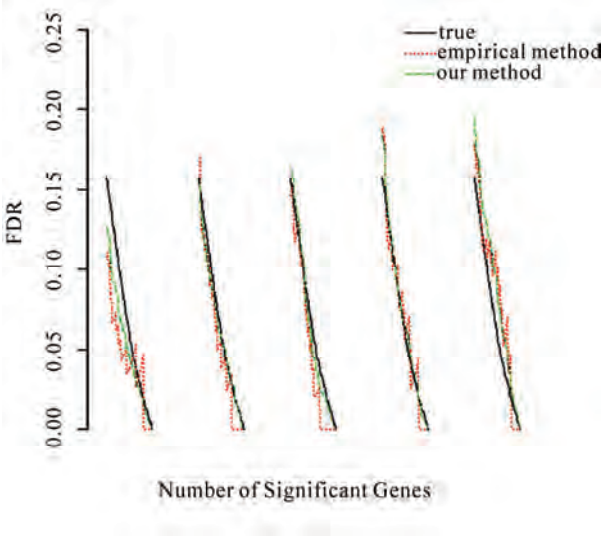

Figure 1. Comparison of true FDR, the empirical FDR estimator $\widehat{FDR}$ and the model based FDR estimator $\widehat{FDR}_1$ for two sample microarray data. 5 replicates are listed. Total number of significant genes is decreasing from 100 to 1 (left to right) for each replicate.

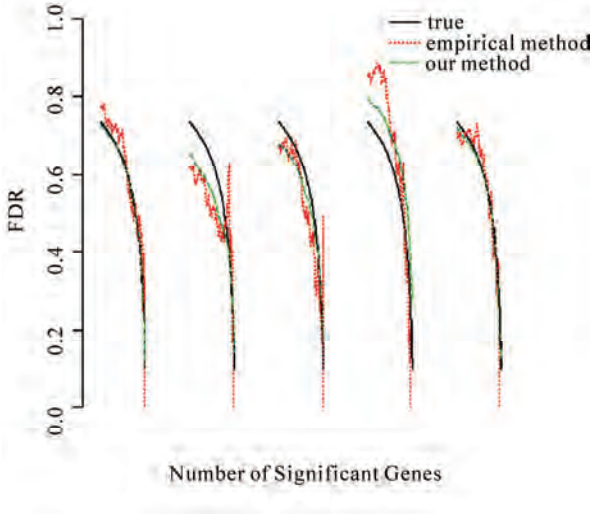

Figure 2. Comparison of true FDR, the empirical FDR estimator $\widehat{FDR}$ and the model based FDR estimator $\widehat{FDR}_1$ for two sample microarray data. 5 replicates are listed. Total number of significant genes is decreasing from 150 to 1 (left to right) for each replicate.

FDR estimation method: the granularity and the zero FDR problems. The performance of our method is assessed by applying them to simulated and real microarray data.

2. METHODS

2.1. SAM

2.1.1. SAM algorithm

Let Y_{ij} be the expression levels of genes *i* under array *j*

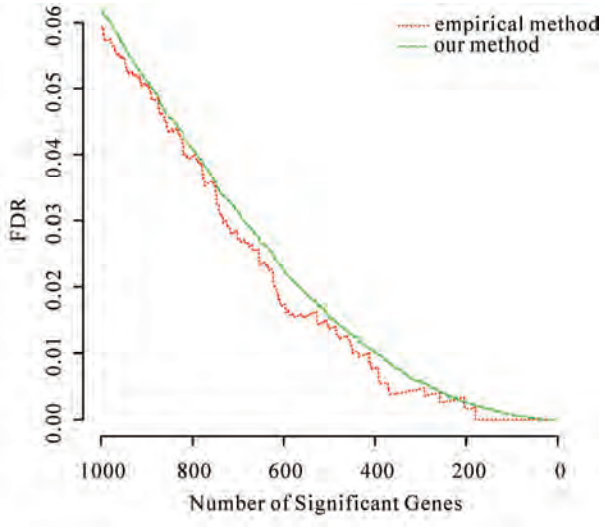

Figure 3. Comparison of the empirical FDR estimator $\widehat{FDR}$ and the model based FDR estimator $\widehat{FDR}_1$ for Leukemia microarray data.

(i=1,…,n; j=1,… j_1, j_1+1,…, $j_1+j_2=J$), and the first j_1 and last j_2 arrays are obtained under two conditions. We need to test if gene *i* has differential expressions under the two conditions.

In SAM, the test statistic is defined as:

$$Z_i = \frac{Y_{i(1)} - Y_{i(2)}}{\sqrt{(1/j_1 + 1/j_2)s_i^2 + s_0}},$$

where $Y_{i(1)}$, $Y_{i(2)}$ are the sample means under two conditions; s_i^2 is the pooled sample variance; s_0 is the fudge factor. The null score z_i^b is then computed by applying the test statistic to the *b-th* set of permuted data.

In the SAM manual [15], the following algorithm is given to detect DE genes. First, all genes are ranked by the magnitude of their test scores Z_i so that $Z_{(1)}$ is the largest test score and $Z_{(i)}$ is the *i-th* largest test score. For the *b-th* set of null scores, the same procedure is applied so that $z_{(i)}^b$ is the *i-th* largest null score in the *b-th* set of null scores. The expected relative difference is then defined as $z_{(i)}^E = \sum_{b=1}^{B} z_{(i)}^b / B$. After that, a scatter plot of $Z_{(i)}$ vs. $z_{(i)}^E$ is plotted. In the scatter plot, some points are displaced from the $Z_{(i)} = z_{(i)}^E$ line with a distance greater than Δ, a pre-specified threshold. In [16], the author pointed out that the estimated total number of significant (TS) genes and FP genes obtained using the SAM algorithm can be written as:

$$\widehat{TS} = \#\{i; Z_{(i)} > \delta_U \text{ or } Z_{(i)} < \delta_L\}, \text{ and} \quad (1)$$

$$\hat{FP} = \sum_{b=1}^{B} \#\{i; z_{(i)}^b > \delta_U \text{ or } z_{(i)}^b < \delta_L\} / B, \quad (2)$$

where δ_U and δ_L are the upper and lower cutoffs decided by the pre-specified threshold Δ. For simplicity, we only consider symmetric cutoffs ($|\delta_U| = |\delta_L|$) in this paper though extensions to asymmetric cutoffs are straightforward. Under symmetric cutoffs, (1) and (2) can be written as:

$$\hat{TS}(\delta) = \#\{i; | Z_{(i)} | > \delta\} \quad (3)$$

$$\hat{FP}(\delta) = \sum_{b=1}^{B} \#\{i; | z_{(i)}^b | > \delta\} / B \quad (4)$$

2.1.2. Empirical FDR Estimator of SAM

Given a gene-specific significance level $\alpha \in (0, 1]$ and assume that we have obtained the *p*-values for all the genes under consideration, the FDR of [17] is defined as:

$$FDR = E[\frac{N(\alpha)}{TS(\alpha)}], \quad (5)$$

where $N(\alpha)$ is the number of genes among the EE genes whose *p*-values are less than or equal to α, and $TS(\alpha)$ is the number of genes among all the genes whose *p*-values are less than or equal to α (or it is the total number of significant genes). Instead of controlling gene-specific significance level α, SAM usually controls the total number of significant genes by setting a corresponding cutoff δ, hence (5) can be re-written as:

$$FDR = E[\frac{N(\delta)}{TS(\delta)}], \quad (6)$$

where $N(\delta)$ is the number of EE genes with absolute value of Z_i greater than δ, and $TS(\delta)$ is the total number of genes with absolute value of Z_i greater than δ.

It was shown in [18] that the FDR can be approximated by

$$FDR \approx \frac{E[N(\delta)]}{E[TS(\delta)]}. \quad (7)$$

Since $N(\delta)$ is the number of false positive among the EE genes, denote the proportion of EE genes by π_0, (7) becomes

$$FDR \approx \frac{\pi_0 E[FP(\delta)]}{E[TS(\delta)]}, \quad (8)$$

where $FP(\delta)$ is the number of FP if all the genes are EE. $FP(\delta)$ and $TS(\delta)$ can be estimated by $\hat{FP}(\delta)$ and $\hat{TS}(\delta)$ in (3) and (4), respectively. As a result, the empirical FDR estimator of SAM is

$$\hat{FDR} = \frac{\hat{\pi}_0 \hat{FP}(\delta)}{\hat{TS}(\delta)}, \quad (9)$$

As mentioned before, this empirical FDR estimator of SAM has the granularity problem and the zero FDR problem. In the following sections, we solve these problems by proposing a model based FDR estimation method.

2.2. The *T*-mixture Model (TMM) Based FDR Eestimation Approach

Let f be the probability density of the test score Z_i and f_0 be the density of null score z_i^b. In TMM, it is assumed that the data are from several components with distinguished *t*-distributions. In other words, both f and f_0 are considered to be a mixture of the *t*-distributions with probability density function:

$$h(z; \psi_g) = \sum_{i=1}^{g} \pi_i \phi(z; \mu_i, \Sigma_i, \nu_i), \quad (10)$$

where $\phi(z; \mu_i, \Sigma_i, \nu_i)$ denotes the *t*-distribution density function with mean μ_i, variance Σ_i, and degrees of freedom ν_i. The coefficients π_i are the mixing proportions and g is the number of components, which can be selected adaptively. ψ_g denotes all the unknown parameters (π_i, μ_i, Σ_i, ν_i) $| i = 1,...g$ in (5). The mixture model is fitted by maximum likelihood using an expectation conditional maximization (ECM) algorithm [19]. The final model is selected based on Bayesian Information Criterion (BIC). More details on how to fit the TMM to microarray data can be found in [20]. It was reported in their paper that not only does the TMM approach provide more accurate estimates of the densities, but also it enjoys computational efficiency since it was demonstrated in [20] that one only needs to use one set of permuted null scores to fit the *t*-mixture model. More specifically, instead of using all z_i^b's *(size=n*B)* to fit the *t*-mixture model, a random sample with size *n* can be drawn from $\bigcup_{b=1}^{B} \bigcup_{i=1}^{n} z_i^b$ and used as the null statistics.

Since the test statistic Z_i and the null statistic z_i (because only one set of null score is used now, we will denote the null statistic as z_i instead of z_i^b) have the densities f and f_0, respectively, it is easy to see from (8) that

$$FDR \approx \pi_0 \frac{E[FP(\delta)/n]}{E[TS(\delta)/n]}$$

$$= \pi_0 \frac{E\sum_{i=1}^{n} I(|z_i| \geq \delta)/n}{E\sum_{i=1}^{n} I(|Z_i| \geq \delta)/n}$$

$$= \pi_0 \frac{P(|z| \geq \delta)}{P(|Z| \geq \delta)}$$

$$= \pi_0 \frac{\int_{|z| \geq \delta} f_0(z)dz}{\int_{|z| \geq \delta} f(z)dz} \quad (11)$$

where δ is chosen such that a given number of significant genes is detected. Equation (11) can be viewed as the model based formula of FDR.

Assume that we have available the estimators $\hat{f}$ and $\hat{f}_0$ of f and f_0 from the TMM, respectively, then the corresponding model based FDR estimator for (11) is

$$\widehat{\text{FDR}}_1 = \pi_0 \frac{\int_{|z| \geq \delta} \hat{f}_0(z)dz}{\int_{|z| \geq \delta} \hat{f}(z)dz}, \quad (12)$$

The model based FDR estimator (12) has the following advantages compared to the empirical FDR estimator of SAM:

1) It does not have the granularity problem of the empirical FDR estimator (9);

2) It provides non-zero FDR estimate for any δ, while (9) only provides non-zero FDR when cutoffs are within the two endpoints of the range of the permuted null scores;

3) Unlike (9), the numerator and the denominator of (12) are not subject to the sampling variability.

3. RESULTS

3.1. Simulated Data

In the simulation, $j_1 = j_2 = 4$ replicates and n = 5,000 genes are generated while 200 of them are assumed to be differentially expressed. For the DE genes, the data under condition 1 are generated from $N(2,1)$ and the data under condition 2 are generated from $N(0,1)$. The EE genes are generated from $N(0,1)$ regardless of the conditions. For the generated data, we calculate the true FDR and estimated FDR for a grid of total number of significant genes ranging from 100 to 1 (in decreasing order). This procedure is repeated for five times. **Figure 1** shows comparisons of true FDR, empirical FDR estimator $\widehat{FDR}$ defined by (9), and the model based FDR estimator $\widehat{FDR}_1$ defined by (12).

As we can see, the instability of empirical $\widehat{FDR}$ increases significantly as it decreases to 0, which shows its granularity problem. Another fact worth noticing is that $\widehat{FDR}$ tends go to zero faster than the true FDR, which is the zero FDR problem. It can be seen that the true FDR strictly decreases as the total number of significant genes decreases. However, the empirical $\widehat{FDR}$ does not show this characteristic. In contrast, $\widehat{FDR}_1$ captures the decreasing trend very well and does not have the erratic jumps of $\widehat{FDR}$. To check how well these two FDR estimators approximate the true FDR, we calculate the mean squared error for both of them. MSE for $\widehat{FDR}$ is 0.00045 and MSE for $\widehat{FDR}_1$ is 0.00021, which shows that our method outperforms the empirical method.

Next, we compare the performances of the two methods when the two populations for the DE and EE genes are not so well separated. For this purpose, we conduct another simulation which tries to mimic the real data. The expression levels for the EE genes under the two conditions are generated from $N(\mu_{i1}, \sigma_i^2)$ and $N(\mu_{i1}, \sigma_i^2)$ with $\mu_{i1} = \mu_{i2} \sim N(0,2)$ $\sigma_i^2 \sim Gamma(4,2)$. The expression levels for the DE genes are generated similarly as the EE genes, except that μ_{i1} and μ_{i2} are generated from $N(0,2)$ separately. In this case, the grid of total number of significant genes ranges from 150 to 1 (in decreasing order). Comparison results are displayed in **Figure 2**.

It is seen from **Figure 2** that $\widehat{FDR}$ is very unstable and approximates true FDR poorly, which makes the estimates highly inaccurate. On the other hand, $\widehat{FDR}_1$ has a much smoother curve than $\widehat{FDR}$ and seems to be able to capture the decreasing trend of the true FDR very well. In addition, the fact that MSE for $\widehat{FDR}$ is 0.025 and for $\widehat{FDR}_1$ is 0.015 shows that our method gives a significantly better fit to the true FDR.

3.2. Real Data

The Leukemia data of [21] is one of the most studied gene expression data sets. This data set includes 27 acute lymphoblastic leukemia (ALL) samples and 11 acute myeloid leukemia (AML) samples for 7129 genes. In **Figure 3**, we estimate the FDRs for different number of significant genes using both our proposed model based FDR estimator and the empirical FDR estimator. As we expect, the model based FDR estimator gives a more stable estimate.

4. DISCUSSION

In this paper, we have proposed a *t*-mixture model based approach to improve the performance of SAM's empirical FDR estimator. We demonstrate that our method does not have the granularity and zero FDR problems as the

empirical method. The results also show that our estimator provides more stable and accurate estimates of the FDR. The advantage of our method is more evident in the case when DE genes are not well separated with EE genes and the variances of expression levels for every gene are different. This is due to the fact that the permutation FDR estimator is more easily affected by the sampling variability.

REFERENCES

[1] Tusher, V.G., Tibshirani, R. and Chu, G. (2001) Significant analysis of microarrays applied to the ionizing radiation response. *PNAS*, **98**, 5116-5121.

[2] Long, A. D., Mangalam, H. J., Chan, B. Y. P., Tolleri, L., Hatfield, W. G. and Baldi, P. (2001) Improved statistical inference from DNA microarray data using analysis of variance and a Bayesian statistical frame work, **276**, 19937-19944.

[3] Kerr, M.K., Martin, M. and Churchill, G. (2000) Analysis of variance for gene expression microarray data, *Journal of Computational Biology*, **7**, 819-837.

[4] Thomas, J.G., Olson, J.M., Tapscott, S.J. and Zhao, L. P. (2001) An efficient and robust statistical modelling approach to discover differentially expressed genes using genomic expression profiles. *Genome Research*, **11**, 1227-1236.

[5] Baldi, P. L. and Long, A. D. (2001) A Bayesian framework for the analysis of microarray expression data: Regularized t-test and statistical inference of gene changes. *Bioinformatics*, **17**, 509-519.

[6] Kendziorski, C. M., Newton, M. A., Lan, H. And Gould, M. N. (2003) On parametric empirical Bayes methods for comparing multiple groups using replicated gene expression profiles. *Statistics in Medicine*, **22**, 819-837.

[7] Newton, M., Noueiry, A., Ahlquist, P., Sarkar, D. (2004) Detecting differential gene expression with a semiparametric hierarchical mixture method. *Biostatistics*, **5(2)**, 155-176.

[8] Smyth, G. K. (2004) Linear models and empirical Bayes methods for assessing differential expression in microarray experiments. *Statistical Applications in Genetics and Molecular Biology*, **3(1)**, Article 3.

[9] Efron, B., Tibshirani R., Storey, J. D., Tusher, V. (2001) Empirical Bayes analysis of a microarray experiment, *Journal of the American Statistical Association*, **96**, 1151-1160.

[10] Efron, B., Tibshirani, R., Gross, V. and Chu, G. (2000) Microarrays and their use in a comparative experiment, Technical report, Statistics Department, Standard University.

[11] Dudoit, S., Yang, H. Y., Callow, J. M. and Speed, P. T. (2002) Statistical methods for identifying differentially expressed genes in replicated cDNA microarray experiments. *Statistica Sinica*, 111-139.

[12] Troyanskaya, O. G., Garber, M. E., Brown, P. O., Botstein, D. and Altman, R. B. (2002) Nonparametric methods for identifying differentially expressed genes in microarray data. *Bioinformatics*, **18**, 1454-1461.

[13] Broberg, P. (2003) Ranking genes with respect to differential expression, *Genome Biology*, **4**, R41.

[14] Pan, W., Lin, J. and Le, C. (2003) A mixture model approach to detecting differentially expressed genes with microarray data. *Functional & integrative genomics*, **3**, 117-124.

[15] Chu, G., Narasimhan, B., Tibshirani, R. and Tusher, V. SAM "significance analysis" of microarrays-users guide and technical document, http://www-stat.stanford.edu/~tibs/SAM/sam.pdf.

[16] Zhang, S. (2007) A comprehensive evaluation of SAM, the SAM R-package and a simple modification to improve its performance, *BMC Bioinformatics*, **8**, 230.

[17] Benjamini, Y. and Hochberg, Y. (1995) Controlling the false discovery rate: a practical and powerful approach to multiple testing. *Journal of the Royal Statistical Society*, **57**, 289-300.

[18] Storey, J.D. and Tibshirani, R. (2003) Statistical significance for genomewide studies. *PNAS*, **100**, 9440-9445.

[19] Liu, C. and Rubin, D. (1995) ML estimation of the t distribution using EM and its extensions ECM and ECME. *Statistica Sinica*, **5**, 19-39.

[20] Jiao, S. and Zhang, S. (2008) The t-mixture model approach for detecting differentially expressed genes in microarrays. *Functional & Integrative Genomics*, **8**, 181-186.

[21] Golub, T. R., Slonim, D. K., Tamayo, P., Huard, C., Gaasenbeek, M., Mesirov, J. P., Coller, H., Loh, M. L., Downing, J.R. and Caligiuri, M. (1999) Molecular classification of cancer: class discovery and class prediction by gene expression monitoring. *Science*, **285**, 531-537.

J. Biomedical Science and Engineering, 2010, 3, 322-326 **JBiSE**
doi:10.4236/jbise.2010.33044 Published Online March 2010 (http://www.SciRP.org/journal/jbise/).

Cyclogram and cross correlation: A comparative study to quantify gait coordination in mental state

Deepak Joshi[1,2], Sneh Anand[1,2]

[1]Center for Biomedical Engineering, IIT Delhi, India;
[2]Center for Biomedical Unit, AIIMS, New Delhi, India.
Email: joshideepak2004@yahoo.co.in

Received 19 December 2009; revised 28 December 2009; accepted 4 January 2010.

ABSTRACT

The purpose of this study to evaluate the effect of mental task on gait coordination. The comparison between two techniques Crosscorrelation and Cyclogram has been performed. A set of gait experiments was developed and conducted to evaluate the effect of mental task on gait coordination. The perimeter derived from the geometric figure, cyclogram perimeter (CP), of the knee-knee cyclogram is the main descriptor considered in this study. For crosscorrelation it is the peak value of cross correlation coefficient (CCC) that has been taken for comparison. The sensitivity of both the techniques in terms of percentage has been calculated. Crosscorrelation is highly sensitive (mean=20.4 S.D.=2.3), towards the change in gait coordination with mental task, in comparison to cyclogram perimeter (mean=2.2 S.D.=1.2). The results have strength to assess the progress of rehabilitation among Parkinson patients.

Keywords: Gait Coordination; Cyclogram; Crosscorrelation; Mental Task

1. INTRODUCTION

It is no longer sufficient to consider gait as a mostly automatic motor activity, but rather one that requires the integration of motor function with cognitive processes such as attention, memory and planning. The evidence of improvement in gait disturbance in Parkinson's disease patients after giving training in mental singing also supports this concept. A focus on high level gait performance therefore requires a focus on cognition [1,2].

1.1. Dual Task Interference

Walking, Running, Swimming and other similar locomotive activities involve gross motor skills and the coordination to perform this is gross motor coordination. Gross motor coordination is left-right coordination, which refers to the alternating left and right limb movement. The basic neuronal circuits that generate this type of coordinated activity are located in the spinal cord. Similar to the lower limb there is left-right coordination in upper limb as well e.g., playing piano, drumming. In walking humans, arm to leg coordination is a well established phenomenon. It could be derived from the intrinsic organization of the human CNS (central Nervous System), but it could also consist of a movement induced epiphenomenon [3]. Arm and hand movements are mainly controlled by the motor cortical regions, whereas locomotion is thought to be regulated mainly at brain-stem, spinal, and cerebellar regions, with descending input from the cortex. Gait consists of highly preprogrammed movements, whereas some upper-extremity movements are more novel and thought to require attention, visual guidance, and somatosensory feedback to control their performance [4]. Interference between cognitive tasks and motor control activities such as gait is a problem in neurological rehabilitation settings. Interference between cognition and locomotor tasks may be important in assessing a neurological patients' ability to function independently, and in designing therapies for both cognitive and motor rehabilitation.

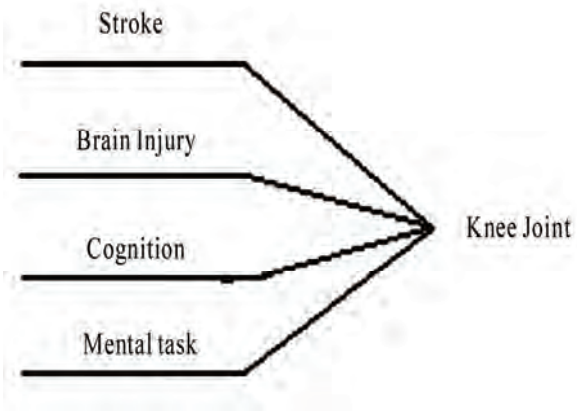

Figure 1. Cognitive aspects that affect knee joint motion.

Quantification of the extent of interference between gait and cognitive tasks after brain injury has been reported. The walking speed of Alzheimer's disease patients slowed more than that of elderly subjects during the dual task. This may contribute to the risk of falls [5, 6]. People with chronic stroke incidence cope well with the challenges of varied environments and can maintain their gait speed while performing a secondary task. Despite moderate levels of gait impairment, gait automaticity may be restored over time to a functional level [7]. So many gait parameters has been studied for assessment of dual task interference. A recent research shows the gait parameters velocity, step time, swing time, and stance time have a significant interaction between complexity of mental task and articulation, with articulation having a greater effect at higher levels of complexity [8]. Very few researchers have taken the kinematic variables for the assessment of same. Knee joint has its leading role in most of the locomotion like walking, running squatting and sitting crossed leg (SCL). So knee angle can be the most affected parameter while monitoring dual task assessment. **Figure 1** shows the knee joint cognition aspects. Time histories of neuromuscular and mechanical variables of human motion are often compared by using discrete timing events (onset, offset, time to peak, zero crossing, etc.). The determination of these discrete timing points is often subjective and their interpretation can cause confusion when attempting to compare patterns [9].

1.2. Crosscorrelation

Keeping in mind the matching of pattern of knee angle trajectories for various locomotion tasks has been monitored to assess the effect on mental task on locomotion activity. Crosscorrelation is a well-known and elegant method of detecting common periodicities between two signals of interest. Crosscorrelation is a measure of similarity of two waveforms as a function of a time-lag applied to one of them. For discrete functions, the crosscorrelation is defined as:

$$(f * g)[n] = \sum_{-\infty}^{+\infty} f[m] * g[n+m] \qquad (1)$$

where f and g are two time series, having m samples each. The n variable corresponds to the lag (in number of samples) by which the time series is shifted. The crosscorrelation gives an indication of pattern similarity between the two sets of data. In that sense Crosscorrelation is an objective means of pattern recognition and comparison. Crosscorrelation has been used to quantify coordination between joints of the same and different limbs during spontaneous kicking in 7 to 8 week old infants [10]. Study has been conducted to compare EMG signals from different walking trails, different test sessions, and different individuals in able-bodies adults. The results shows that crosscorrelation may be useful for evaluating changes in an individual patient's muscle activation patterns [11]. Another potential application of crosscorrelation was in monitoring the adaptations in interlimb and intralimb coordination to asymmetric loading in human walking. Changes in coordinative patterns were quantified utilization both crosscorrelation and root-mean-square difference (RMS) measures. Crosscorrelation measures were utilized to assess differences in the temporal evolution between coordination patterns [12].

1.3. Cyclogram

A cyclogram is formed by ignoring the time axis angle and directly plotting knee angle of one leg VS knee angle of other leg (**Figure 3**). Cyclograms reflect the gait kinematics during the total gait cycle which is different from having other discrete measures such as the step length, or walking speed, which are more common in literature. The geometrical features of cyclogram have been used to study the human walking in slope surface [13]. Simple iterative algorithm has been proposed for the computation of moments from a polygon approximation of the boundary, like in cyclogram. A discrete version of Green's theorem, which evaluates a double sum over a two dimensional discrete object by a simple summation along the discrete boundary of the object, was implemented [14,15]. The cyclograms are readily adaptable to clinical purposes by overlay of normal and abnormal gait traces. In human the pattern is speed dependent, highly predictable, and dramatically affected in the case of gait abnormalities. Comparison between bipedal and quadrupedal locomotion has been done by cyclogram [16]. Neural network approach was used to classify three gait patterns using the features of hip-knee cyclogram. Three gait patterns were generated from normal gait, a simulation of leg length difference, and a simulation of leg weight difference [17]. Cyclogram is also used for gait signature. If it is use as the signature in gait recognition and verification, it could lead to an automatic person recognition system using video footage from security cameras. To compare the signatures between two gaits, the difference of shape and phase of the cyclograms were calculated using the point projection method and extreme points of curves [18].Hip range, knee range, ratio of hip range/knee range, ratio of knee range/hip range, area of cyclogram, circularity, eccentricity, orientation, and cusp orientation [19]. No literature is available that reports use of cyclogram for assessing the dual task interference. Authors used the perimeter of knee-knee cyclogram to see the eefect of mental task on gait coordination. Further the results are compared with the previous work of authors in which the crosscorrelation between knee angles was used to assess the effect of mental task on gait coordination [20].

To compare the performance of both techniques the sensitivity of both, for gait with mental task is calculated as follows:

$$\% \text{ sensitivity (CC)} = \{CCC(NW) - CCC(MT)\}/CCC(NW) \quad (2)$$

$$\% \text{ sensitivity (CP)}) = \{CP(NW) - CP(MT)\}/CP(NW)\} \quad (3)$$

Where CCC- peak of crosscorrelation coefficient, CP-Cyclogram Perimeter, NW-Normal Walk, MT-walking with mental task, CC-Crosscorrelation.

Besides Crosscorrelation and Cyclogram, Artifical Neural Network (ANN) can be most powerful tool to evaluate the coordination in different gait patterns [21,22]. Though ANN needs more computational power and is quite complex to be calculated in comparision of Crosscorrelation and Cyclogram, in real time. So authors compared the sensitivity of Crosscorrelation and cyclogram for this study.

2. EXPERIMENTAL METHOD

Six male healthy subjects (mean age=26 years, S.D. =4.6years) without any history of lower extremity injury participated voluntarily for the experiment. All of them provided written consent to participate. Subjects were educated enough to carry out the mental task exercise. Data was collected in a 3 D motion analysis system using six CCD Cameras. EVA 7.0 and Orhtotrak 6.2 software were used for data recording and gait analysis respectively. Twenty five Cleveland markers were placed on the subjects.

2.1. Experiment Protocol

Subjects were introduced to the various locomotive tasks initially, except walking with a mental task. This was done to avoid any biasing to the mental state while only walking. Data recording began 2-3 minutes after the subjects began walking. This was done to habituate the subjects to maintain constant speed. This speed was preferred speed. Seven to eight trials were performed for each locomotive task to get sufficient amount of data for comparison and analysis. After completing all locomotive tasks, they were asked to perform a mental task exercise along with walking. The mental task assigned to them was naming of months from December to January. Subjects were instructed not to skip any month in between and if they commit any mistake they should improve it. Thus difficulty level of the task was maintained.

2.2. Data Collection

Data was collected at the sampling frequency of 120 Hz. The time duration to record the data for every trial was 3 seconds, except walking with mental task. Therefore the total sample for a trial was 360. While having mental task the subjects was instructed to walk until they complete it. Some of the trials were not included for analysis as they were corrupted due to incomplete information or noise. A low pass Butterworth filter with cut off of 6.0 Hz was used to remove the noise from data. The Orthotrak software produced output in Excel format. The data from Orthotrak was imported to Matlab 7.0 for analysis. Out of 360 samples, data which completes a gait cycle was taken for analysis i.e. heel strike to heel strike. The data in different planes was analyzed. The CCC between the knee angles was observed for every trial in all the planes. The knee angle was considered because the knee plays a leading role in walking.

2.3. Data Analysis

The maximum of CCC was calculated and noted down for each trail. The CCC in the other two planes Frontal and Transversal were also calculated. **Figure 2.1** shows the crosscorrelation coefficient profile for walking and walking with mental task. The CCC in these planes varied irregularly and was low too, thus, it was not possible to reach a conclusion. Therefore their values were ig-

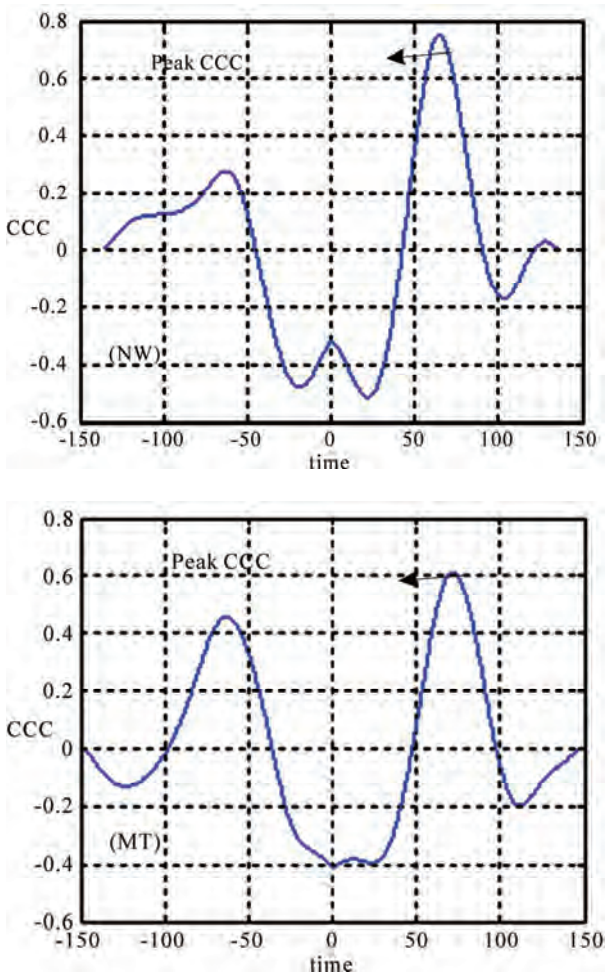

Figure 2 **NW** denotes Normal Walk and **MT** denotes walking with mental task.

nored. The CCC was calculated using **Eq. 1** where f and g are left and right knee angle time series, respectively. Cyclogram was drawn as right knee angle vs. left knee angle. **Figure 3** shows the cyclogram for while walking and walking with mental task. There was a possibility to synchronize both lower limb gait events, using the lag where peak CCC exists, to draw cyclogram. This was avoided to get any bias of CCC in cyclogram. Cyclogram perimeter is calculated from following Equation:

$$L_i = \{ (\emptyset_{lk}(i+1) - \emptyset_{lk}(i))^2 + (\emptyset_{rk}(i+1) - \emptyset_{rk}(i))^2 \}^{1/2} \quad (4)$$

where $\emptyset_{lk}$ represents the angle of left knee and $\emptyset_{rk}$ represents the angle of right knee. i represents a particular instant of time. $L = \sum_{i=1}^{n} (Li)$ gives the value of cyclogram perimeter.

The cyclogram perimeter is the total distance travelled in their respective joint spaces. Cyclogram area was not taken into consideration as it is more sensitive to noise comparative to perimeter.

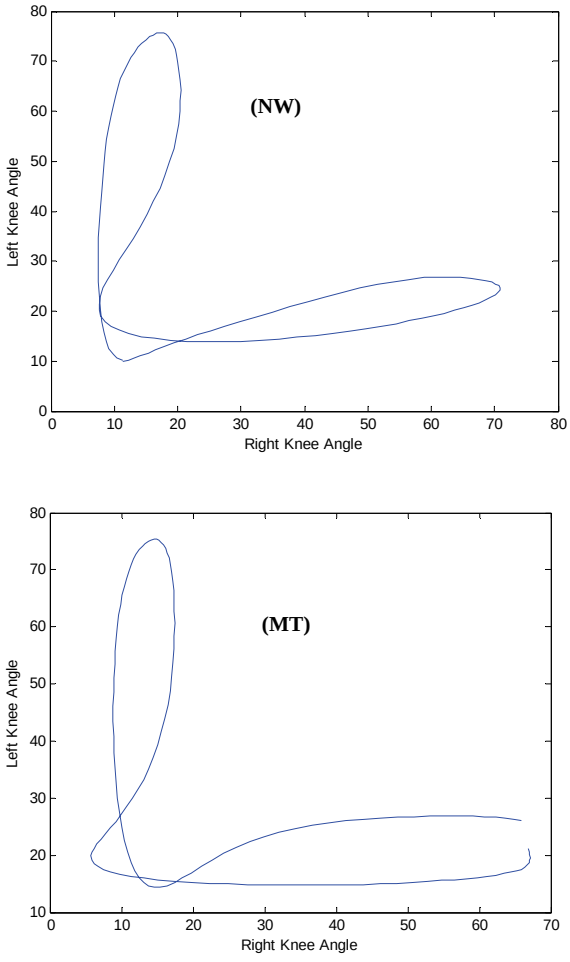

Figure 3 **NW** denotes Normal Walk and **MT** denotes walking with mental task.

3. RESULTS

3.1. Crosscorrelation

The CCC with walking is 0.78 (mean) SD = 0.03 which significantly decreases to 0.62(mean) SD = 0.01. The CCC in the other two planes Frontal and Transversal were also calculated. The CCC in these planes varied irregularly and was low too, thus, it was not possible to reach a conclusion. Therefore their values were ignored.

3.2. Cyclogram Perimeter

Cyclogram perimeter decreases with mental task. The normal walk knee-knee cyclogram perimeter matches with the range of hip-knee cyclogram (212.8 degree) calculated at 0 degree slope of walking [13]. The Cyclogram perimeter with walking is 268.2 (mean) SD = 13.2 which significantly decreases to 261.9 (mean) SD = 16.9.

In contrast to cyclogram perimeter, Crosscorrelation shows higher sensitivity (mean=21.5 S.D. =2.8) towards the mental task along with gait. The sensitivity calculated for cyclogram perimeter was mean=2.9 S.D. =1.5.

4. DISCUSSION AND CONCLUSIONS

Methods have been proposed to assess mental task while locomotion. CCC analysis in this research work shows CCC as a good marker to assess mental state. CCC decreases significantly as the walking goes along with the mental task. The results also shows that CCC is highly subjective but it follows the same decreases pattern with mental task. Using Knee angle is more direct measurement in comparision to EMG. Cross correlation and Cyclogram are independent techniques. Though both of them are well established technique to quantify coordination, this study shows CCC is highly sensitive to quantify the change in coordination of limbs, while with mental task. This may be due to the fact that in Crosscorrelation it is the strength of matching of signals to each other with respect to time irrespective of the range the signal (knee angle) covers while in cyclogram it is the sum of range covered by the knee angles trajectories. In terms of implementation in real time in hardware both are equal in terms of complexity. Finally, this study involved a limited number of healthy subjects and the level of education, of subjects, is not taken into account. This work was performed in the 3 D motion analysis lab, a portable , low cost embedded system can be design to calculate CCC and cyclograms of knee angles in the saggittal plane while walking and then can be dedicated for the assesment/toughness of mental task only.

5. ACKNOWLEDGEMENTS

The authors highly acknowledge Director, Defence Institute of Physiology and Allied Sciences (DIPAS) New Delhi for allowing the authors to collect data. A sincere acknowledgement to both the subjects for participating voluntarily.

REFERENCES

[1] Lord, S. and Rochseter, L. (2007) Walking in real world: Concepts related to functional gait. *NZ Journal of Physiotherapy*, **35(3)**.

[2] Satoh, M. and Kuzuhara, S. (2008) Training in mental singing while walking improves gait disturbance in parkinson's patients. *Journal of European Neurology*, **60(5)**.

[3] Wannier, T., Bastiaanse, C., Colombo, G. and Dietz, V. (2001) Arm to leg coordination in humans during walking, creeping and swimming activities. *Experimental Brain Research*, **141**, 375-379.

[4] o'Shea, S., Morris, M.E. and Iansek, R. (2002) Dual task interference during gait in people with parkinson disease: Effects of motor versus cognitive secondary tasks. *Journal of Physical Therapy*, **82(9)**.

[5] Patrick, H., Jaket, C., *et al.* (2000) Interference between gait and coginitive tasks in a rehabilitation neurological application. *Journal of Neurol Neurosurg Psychitary*, **69**, 479-486.

[6] Camicioli, R., Howieson, D., *et al.* (1997) Talking while walking: The effect of a dual task in aging and Alzheimer's disease. *Journal of Neurology*, **48(4)**, 955-958.

[7] Lord, S.E., Rochester, L., *et al*. (2006) The effect of environment and task on gait parameters after stroke: A randomized comparison of measurement condtions. *Archives of Physical Medicine and Rehabilitation*, **87(7)**, 967-973.

[8] Armieri, A., *et al*. (2009) Dual task performance in a healthy young adult population: Results from a symmetric manipulation of task complexity and articulation. *Gait and Posture*, **29**, 346-348.

[9] Li, L. and Caldwell, G.E. (1999) Coefficient of cross correlation and the time domain correspondence. *Journal of Electromyography and Kinesiology*, **9**, 385-389.

[10] Piek, J.P. (1996) A quantitative analysis of spontaneous kicking in two-month-old infants. *Human Movement Science* 15, 707-726.

[11] Wren, T.A.L., *et al*. (2006) Cross-correlation as a method for comparing dynamic electromyography signals during gait. *Journal of Biomechanics*, **39**, 2714-2718.

[12] Haddad, J.M., *et al*. (2006) Adaptations in interlimb and intralimb coordination to asymmetrical loading in human walking. *Gait and Posture*, **23**, 429-434.

[13] Goswami, A. (1998) A new gait parameterization technique by means of cyclogram moments: Application to human slope walking. *Gait and Posture*, **8**, 15-36.

[14] Jiang,X.Y. and Bunke, H. (1991) Simple and fast computation of moments. *Pattern Recognition*, **24(8)**, 801- 806.

[15] Yang, L. and Albregtsen, F. (1996) Fast and exact computation of cartesian geometric moments usig discrete green's theorem. *Pattern Recognition*, **29(7)**, 1061-1073.

[16] Charteris, J., Leach, D. and Taves, C. (1979) Comparative kinematic analysis of bipedal and quadrupedal locomotion: A cyclographic technique. *Jornal of Analomy*, **128(4)**, 803-819.

[17] Barton, J.G. and Lees, A. (1997) An application of neural networks for distinguishing gait patterns on the basis of hip-knee joint angle diagrams. *Gait and posture*, **5**, 28-33.

[18] Ma, Y.L., Pollick, F.E. and Turner, M. (2005) A statistical approach to gait recognition and verification by using cyclogram. *IEEE International Conference on Visual Information Engineering*, 425-432.

[19] Hollerbach, J.M., *et al*. (2001) Torso Force Feedback Realistically Simulates Slope on Treadmill Style Locomotion Interfaces. *The International Journal of Robotics Research*, **20**, 939-951.

[20] Joshi, D., *et al*. (2009) Gait Co-ordination: Potential marker for mental state. 2*nd International Conference in Biomedical Informatics and Signal Processing*, 12-14.

[21] Popovic, D. and Jonic, S. (1998) Determining synergy between joint angles during locomotion by radial basis function neural networks. *Proceedings of the* 20*th Annual Conference of the IEEE Engineering on Medicine and Biology Society*, **20(5)**.

[22] Dejnabadi, H., Jolles, B.M. and Aminian, K. (2008) A new approach for quantitative analysis of inter-Joint coordination during gait. *IEEE Transactions on Biomedical Engineering*, **55(2)**.

J. Biomedical Science and Engineering, 2010, 3, 327-329 **JBiSE**
doi:10.4236/jbise.2010.33045 Published Online March 2010 (http://www.SciRP.org/journal/jbise/).

Modelling of bionic arm

Amartya Ganguly

Department of Biomedical Engineering, JIS College of Engineering; Block 'A', Phase III, Kalyani, Nadia, India.
Email: ganguly.amartya@yahoo.in

Received 11 December 2009; revised 25 December 2009; accepted 29 December 2009.

ABSTRACT

The bionic arm is a prosthesis which will allow the amputees to control it with the help of their own brain instead of depending upon the mechanical functions of the artificial limbs which are at present available in the market. A complex design of control systems is embedded in the bionic arm which will receive and analyze the signals from the brain and convert the electrical energy to mechanical energy, making the bionic arm move.

Keywords: Neural Network; Bionic, Amputation; Upper Limb

1. INTRODUCTION

Bionic arm is a revolutionary idea for amputees across the globe. This is as close as we can get to our natural limb. The fundamental point is to make the arm move with our brain unlike previous prosthetic upper limbs. In the case of bionic arm we take the nerve conduction signals from the brain and amplify it so that we can register the signal and convert that electrical signal into mechanical energy so as to move the mechanical device i.e. the arm. Prosthesis is being used and constantly being perfected to suit human needs. Various types of prosthesis have been made to suit many actions but not all. But the bionic arm will be able to perform all kinds of movements of the human upper limb even the most difficult actions like unscrewing the cap of bottle or picking up a coin from the ground. This arm will also be able to judge the correct pressure required for any movement.

2. METHODS

The electrodes placed near the chest region will detect the strongest of the nerve impulses from the brain which is then fed to the biopotential amplifier to amplify the signals. The amplified signals are then routed to the transducer to convert this electrical energy to mechanical energy enabling the bionic arm to move as per the strength of the signal. This can be further explained by mathematics as given below.

This here is a mathematical model in order to simulate the function of the brain. For this purpose the NARMA L2 Controller has been used. To put it more generally neural networks have been used [1].

2.1. Model Components

The **Figure 1** above shows the arrangement of the circuit components of the Model of Bionic Arm. [2,3]The uniform random signal goes to the brain that is the Narma L2 Controller which goes to the subsystem of bionic arm which consists of the biopotential amplifier and the transducer, **Figure 2** shown below. The graphical result is viewed in the scope.

2.2. Narma L2 Controller

[4]The neurocontroller described in this section is referred to by two different names: feedback linearization control and NARMA-L2 control. It is referred to as feedback linearization when the plant model has a particular form (companion form). It is referred to as NARMA-L2 control when the plant model can be approximated by the same form. The central idea of this type of control is to transform nonlinear system dynamics into linear dynamics by canceling the nonlinearities. **Figure 3** represents the training to identify the Narma L2 controller. This section begins by presenting the companion form system model and demonstrating how you can use a neural network to identify this model. Then it describes how the identified neural network

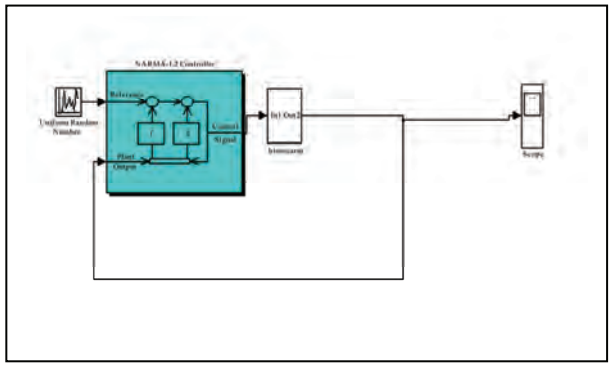

Figure 1. Block diagram of bionic arm. [5]

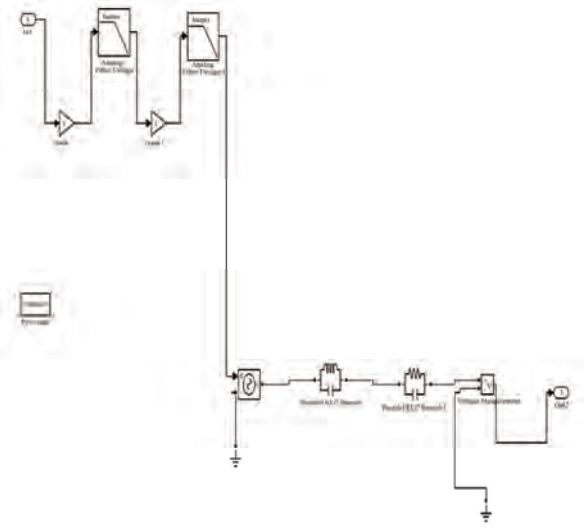

Figure 2. Circuit Diagram of Biopotential Amplifier and Transducer. [5]

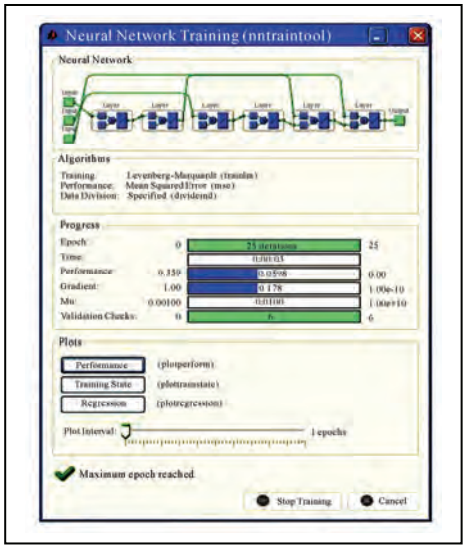

Figure 3. Neural Network Training to identify the Narma L2 controller. [5]

model can be used to develop a controller. This is followed by a demonstration of how to use the NARMA-L2 Control block, which is contained in the Neural Network Toolbox™ block set.

3. IDENTIFICATION OF NARMA-L2 MODEL

As with model predictive control, the first step in using feedback linearization (or NARMA-L2) control is to identify the system to be controlled. You train a neural network to represent the forward dynamics of the system. The first step is to choose a model structure to use. One standard model that is used to represent general discrete-time nonlinear systems is the nonlinear autoregressive-moving average (NARMA) model. The notation MA (q) refers to the moving average model of order q:

$$X_t = c + \varepsilon_t + \sum_{i=1}^{p} \varphi_i X_{t-i} + \sum_{i=1}^{q} \theta_i \varepsilon_{t-i}$$

Where the θ_1, ..., θ_q are the parameters of the model, μ is the expectation of X_t (often assumed to equal 0), and the, $\varepsilon_t, \varepsilon_{t-1}, \ldots$ are again, white noise error terms. The moving average model is essentially a finite impulse response filter with some additional interpretation placed on it. This is the identification procedure used for the NN Predictive Controller.

The only problem with using this controller is that if you want to train a neural network to create the function G to minimize mean square error, you need to use dynamic backpropagation ([NaPa91] or [HaJe99]). This can be quite slow. One solution, proposed by Narendra and Mukhopadhyay [NaMu97], is to use approximate models to represent the system. The controller used in this section is based on the NARMA-L2 approximate model.

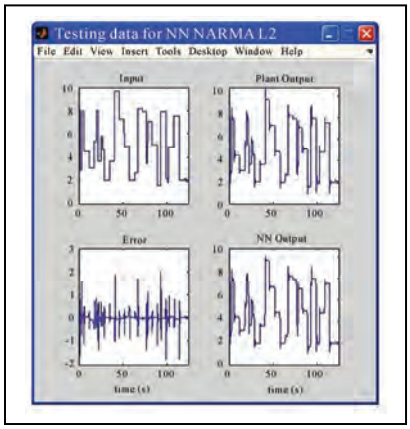

Figure 4. Testing the signals for the Narma L2 Controller.

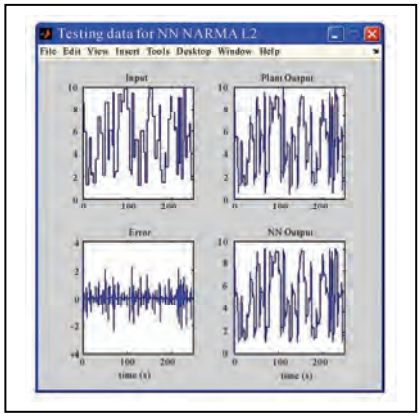

Figure 5. Training the signals for the Narma L2 Controller.

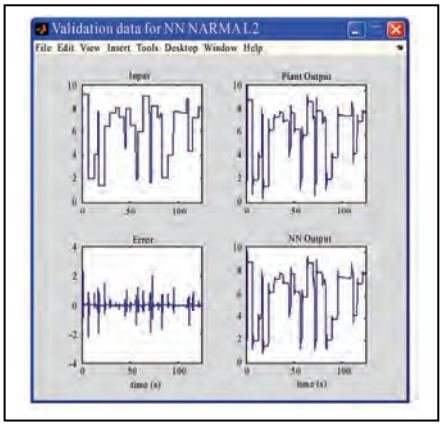

Figure 6. Validation of signals of Narma L2 Controller.

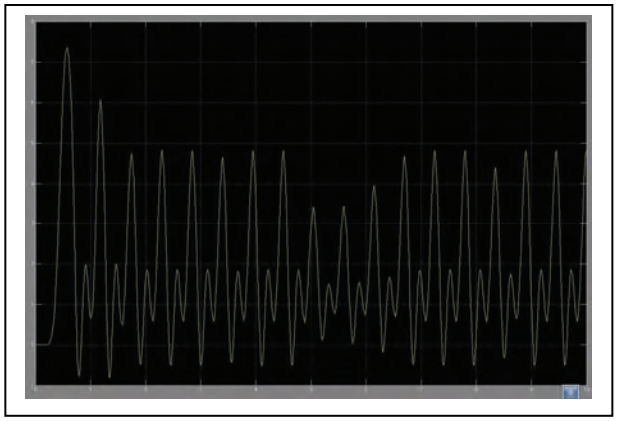

Figure 7. The final graphical result of the signal versus time of the bionic arm.

4. RESULTS

Since the brain receives various signals to perform a wide range of functions pertaining to different systems of the human body any unknown system would require training of the brain, in this case the NARMA L2 Controller. We have to train it so that it can identify which signals are exclusively for the movement of the upper limb. The **Figures 4, 5, 6** and **7** show us the various stages the controller has to go through before we can ascertain that the signals received are for the movements of the upper extremity. Here, random uniform signals have been taken as input data similar to the brain which constantly receives and emits various types of signals for different functions. The neural network will be able to identify the upper limb action signals after this training process has been completed.

5. CONCLUSIONS

The aim of this paper was to give a theoretical analysis of a concept which can be implemented in practice. This would also help to concentrate about the limitations of the artificial upper limbs which can only perform a very few actions making amputees all the more conscious of their developed deficiencies.

6. ACKNOWLEDGMENT

I would like to take this opportunity to thank Dr. Meghamala Dutta and Dr. Avijit Talukdar who had provided insightful knowledge regarding the hypothetical analysis of bionic arm.

REFERENCES

[1] Joseph, D.B. (2004) Handbook of biomedical engineering. CRC Press.
[2] George, B., Gwilym, M.J. and Gregory, C.R. (1994) Time series analysis: Forecasting and control, 3rd Edition, Prentice-Hall.
[3] Mills, T.C. (1990) Time series techniques for economists. Cambridge University Press, Cambridge.
[4] Pandit, Sudhakar M. and Wu, S.M. (1983) Time series and system analysis with applications. John Wiley& Sons, Inc.
[5] Mathworks-MatLab Software.

Call for Papers

Journal of Biomedical Science and Engineering (JBiSE)

www.scirp.org/journal/jbise

JBiSE, an international journal, publishes research and review articles in all important aspects of biology, medicine, engineering, and their intersection. Both experimental and theoretical papers are acceptable provided they report important findings, novel insights, or useful techniques in these areas. All manuscripts must be prepared in English, and are subject to a rigorous and fair peer-review process. Accepted papers will immediately appear online followed by printed in hard copy.

Subject Coverage

- Bioelectrical and neural engineering
- Bioinformatics and Computational Biology
- Biomedical modeling
- Biomedical imaging, image processing and visualization
- Clinical engineering, wearable and real-time health monitoring systems
- Biomechanics and biotransport
- Software, tools and application in medical engineering
- Biomaterials
- Physiological signal processing
- Biomedical devices, sensors, artificial organs and nano technologies
- NMR/CT/ECG technologies and electromagnetic field simulation
- Structure-based drug design

Editor-in-Chief

Editorial Board

Notes for Intending Authors

Submitted papers should not have been previously published nor be currently under consideration for publication elsewhere. Paper submission will be handled electronically through the website. All papers are refereed through a peer review process. For more details about the submissions, please access the website.

Website and E-Mail

www. scirp. org/journal/jbise
Email: jbise@scirp.org

ISSN 1937-6871 (Print), 1937-688X (Online)

Journal of Biomedical Science and Engineering, 2010, 3.
Published Online March 2010 in SciRes (http://www.scirp.org/journal/jbise).

TABLE OF CONTENTS

Volume 3, Number 3, March 2010

9771937687001014